61 /2/2023

JOURNAL OF THEORETICAL AND APPLIED MECHANICS

WARSAW 2023, QUARTERLY, VOLUME 61, INDEX 365238, ISSN 1429-2955

POLISH SOCIETY OF THEORETICAL AND APPLIED MECHANICS

POLISH SOCIETY OF THEORETICAL AND APPLIED MECHANICS

JOURNAL OF THEORETICAL AND APPLIED MECHANICS

No. 2 • Vol. 61

Quarterly

WARSAW, APRIL 2023

JOURNAL OF THEORETICAL AND APPLIED MECHANICS
(until 1997 Mechanika Teoretyczna i Stosowana, ISSN 0079-3701)

Beginning with Vol. 45, No. 1, 2007, *Journal of Theoretical and Applied Mechanics* (JTAM) has been selected for coverage in Thomson Reuters products and custom information services. Now it is indexed and abstracted in the following:

- **Science Citation Index Expanded** (also known as SciSearch®)
- **Journal Citation Reports/Science Edition**

* * * * *

Editorial Office

Al. Armii Ludowej 16, room 650; 00-637 Warszawa, Poland
phone (+48) 664 099 345, e-mail: biuro@ptmts.org.pl

www.jtam.pl

* * * * *

Publication supported by Ministry of Science and Higher Education of Poland

Rozwój kwartalnika naukowego *Journal of Theoretical and Applied Mechanics*, ISSN 1429-2955, jest dofinansowany ze środków Ministra Edukacji i Nauki przyznanych z pomocy *de minimis* w ramach programu „Rozwój czasopism naukowych", umowa RCN/SN/0056/2021/1.

JOURNAL OF THEORETICAL AND APPLIED MECHANICS
61, 2, pp. 207-218, Warsaw 2023
https://doi.org/10.15632/jtam-pl/159670

STUDY OF TRIAXIAL COMPRESSION MECHANICAL PROPERTIES AND PORE-FRACTURE CHARACTERISTICS OF COAL ROCKS IN THE YILI BASIN, XINJIANG

Cheng Shen, Ling Yue
Changzhou Vocational Institute of Engineering, Changzhou, China
Yang Liu
School of Civil and Transportation Engineering, Hebei University of Technology, Tianjin, China
e-mail: 201911601006@stu.hebut.edu.cn

Compressive mechanical properties and pore-fissure characteristics of coal rock specimens from three stably developed coal seams M_1, M_8 and M_{12} in the Xinjiang Yili Basin were investigated in detail by a series of tests. The results show that the compressive mechanical properties of coal rocks in the Yili Basin are significantly affected by the confining pressure. The peak axial stress increases and the peak modulus of elasticity decreases as the confining pressure increases. The peak axial strain increases and then remains constant, while the peak circumferential strain and peak volumetric strain increase and then decrease. The confining pressure has almost no effect on Poisson's ratio of the coal rock specimens. In addition, electron microscopy tests show that the microscopic fraction of the coal rock specimens is predominantly vitrinite, accounting for 83.1%-89.2%, while the percentage of the inertinite group is relatively small, at 10.3%-16.1%. The throat radius of the coal rock is mainly concentrated around 1-2 μm, while the pore radius of the coal rock is between 150-200 μm. The coal rock has an overall fine throat and low permeability, and the coal rock in the Yili Basin of Xinjiang is a typical low-permeability coal rock.

Keywords: triaxial compression, mechanical properties, mercury injection, pore-fissure characteristics

1. Introduction

Coal is currently one of the world's major energy sources, and its position will remain unchanged for a long time in the future. With gradual depletion of coal resources and gradual reduction of coal reserves at shallow depths, the mining of coal is subsequently moving deeper underground. Compressive mechanical properties of coal rocks are closely related to safe production of coal mines, and the study of the compressive mechanical properties of deeper coal rocks remains a priority (Wang *et al.*, 2013; Blondeel and van de Graaf, 2018; Haque *et al.*, 2018; Xu *et al.*, 2019; Shan *et al.*, 2021; Liu *et al.*, 2022).

The studies on the mechanical behavior of coal rocks have been extensively reported (Yin *et al.*, 2016; Chen *et al.*, 2019; Zhong *et al.*, 2022). Yin *et al.* (2016) studied physical and mechanical properties of coal rock after treatment at different temperatures under impact loading. Dynamic compression experiments were conducted by using a split Hopkinson pressure bar (SHPB). They found that the stress-strain curves under impact loading lacked the stage of micro-fissure closure and the slope of the elastic deformation stage was higher than that under static loading. Chen *et al.* (2019) investigated deformation and failure behavior of a coal-rock combined body under uniaxial compression by experiments and numerical simulations. Their experimental results showed that the mechanical properties and deformation failure characteristics of the coal-rock combined body were governed mainly by the coal. Zhong *et al.* (2022) investigated the role of

pore fluid in low-permeability coal away from the excavation boundary but still influenced by the periodic excavation disturbance, a series of undrained cyclic triaxial compressive tests were conducted on saturated coal. Their results showed that pore water had little effect on the axial strain evolution of coal, but has a significant effect on the radial and volumetric strain evolution.

The shape, size and surface characters of pore-fractures in coal are a basis for understanding of the occurrence and migration of coalbed methane (CBM), which requires quantitative characterization (Chen *et al.*, 2017; Zhu *et al.*, 2021; Xue *et al.*, 2022). Njiekak *et al.* (2018) studied porosity, shape and size of carbonates by a micro-computed tomography (CT) and scanning electron microscopy (SEM). Their results showed that as micro-CT porosity depended on the scan resolution and image segmentation processes, to rely solely today on micro-CT scanning for pore volume evaluation of heterogeneous carbonate samples should be considered with extreme caution. Wang *et al.* (2020) analyzed size distribution and volume contribution of pore-fractures in coal at three cohesive-scales (nanometer-scale, micrometer-scale and macro-scale) by using X-ray CT image. They found that the pore volume contribution measured using X-ray CT image analysis increased, then decreased with increasing pore diameter, and the specific surface area decreased rapidly with increasing pore diameter. Qajar and Arns (2022) studied the evolution of pore structure and permeability of a microporous carbonate rock during chemical dissolution using information provided from X-ray micro-computed tomography (μ-CT) and mercury intrusion porosimetry (MIP) techniques. They found that the permeability changes were controlled by macroporosity and critical pore diameter.

This study takes the Yili Basin, Xinjiang, as the study area, and investigates in detail the compressive mechanical properties and pore-fracture characteristics of coal specimens from three stably developed coal seams in the Yili Basin by triaxial compression tests, mercury compression tests and scanning electron microscopy tests. This will provide reference and guidance for the evaluation of recoverability and exploration and development of deep-seated coal rocks.

2. Experimental study

2.1. Sample preparation

The coal formations in the Yili Basin can be broadly divided into six systems from the bottom up, which are Triassic, Jurassic, Cretaceous, Palaeocene, Neoproterozoic and Quaternary. There are a total of 12 coal seams in the area, recorded as M_1-M_{12} from the bottom to top, of which the stable development is in seam 1 (M_1), seam 8 (M_8) and seam 12 (M_{12}). The test coal specimens were taken from each of these stable coal seams. Fresh and intact coal rock blocks were wrapped tightly in a plastic film and transported back to the laboratory, where they were then processed into standard cylindrical coal specimens of 2.5 cm diameter and 5 cm length, and numbered according to the location of the seam. The accuracy of the specimen is in accordance with the requirements of the International Society for Rock Mechanics (ISRM) (Fairhurst and Hudson, 1999), i.e. the permissible deviation of height, diameter or side length of the sample is ± 0.3 mm, the permissible deviation of unevenness of the two end faces of the sample is ± 0.05 mm, and the end faces should be perpendicular to the axis of the sample with a permissible deviation of $\pm 0.25°$.

2.2. Test methods

The M_8 coal seam is between the M_1 and M_{12} coal seams, the coal rock specimens for the triaxial compression tests were taken from the M_8 seam and the tests were repeated three times under the same confining pressure. Meanwhile, both the permeability test and the component test were repeated at least three times.

2.2.1. Triaxial compression testing

The triaxial compression tests and permeability tests are carried out using the TFD-2000L triaxial rheological testing machine, which has a maximum axial load of 2000 kN and a maximum confining pressure of 200 MPa (Fig. 1a). The specific test steps are as follows: 1) The coal rock specimen was fixed to the base of the loading system and wrapped with a heat-shrinkable tube. Then heated it with a heat gun to make it tight to the coal wall, and fixed the top and bottom ends of the coal sample with sealing rings to ensure its good sealing. Then, the confining pressure chamber was closed and silicone oil was added. 2) The confining pressure control system was started to increase the confining pressure at a rate of 0.5 MPa/min. According to the sampling depth of the coal rock specimens, the confining pressures were set at to 5, 10, 15 and 20 MPa, respectively. 3) When the confining pressure reached the specified size, the coal rock sample was at hydrostatic pressure. At this point, the axial stress was applied by displacement loading with 0.01 mm/s until the specimen failure (Determination method of physical and mechanical properties of coal and rock: GB/T23561.9-2009).

2.2.2. Permeability testing

The permeability test of the coal rock specimens was also performed using the TFD-2000 triaxial rheological testing machine, which has inlet and outlet pipes at the upper and lower ends (Fig. 1b). 1) The first step was the same as the first step of triaxial compression test. 2 The axial stress and confining pressure of the coal rock specimens were maintained at 5 MPa. The vacuum pump was turned on and the coal rock specimen was vacuumed for 6 hours and the temperature was maintained at 30°C by heating the silicone oil. 3) The gas inlet valve was opened and CH4 was introduced, and the gas pressure at the inlet end was adjusted to 1.2 MPa. Gas adsorption was carried out on the coal specimen until the adsorption equilibrium was reached, and the parameters to be measured were recorded. 4) Changed the inlet pressure (1.6, 1.2, 0.8 and 0.4 MPa) and repeated steps (2), (3) and (4). 5) Based on Darcy's law, the permeability K of the coal rock can be calculated (Lin and Zhou, 1987)

$$K = \frac{2qp\mu L}{(p^2 - p_0^2)S} \tag{2.1}$$

where K is the permeability [mD]; q is the CH4 percolation flow rate at standard conditions [cm^3/s]; μ is the CH4 gas dynamic viscosity, and $\mu = 1.1502 \cdot 10^{-5}$ Pa s; L is the length of the specimen [cm]; S is the cross-sectional area of the coal rock specimen [cm^2]; p_0 is the atmospheric pressure [Pa]; p is the air pressure at the inlet end of CH4 [Pa].

2.2.3. Coal rock component testing

1) The coal specimens were crushed to less than 1.00 mm and the proportion of coal samples made less than 0.10 mm not and more than 10%. The pulverized coal was mixed with the shellac in a certain proportion, and the coal brick was made by the hot glue method, which was ground, polished and dried in order to be ready for determination. 2) The coal brick was placed under a polarized light microscope, and the difference in the characteristics of the coal rock components under the microscope was determined, and the percentage of the statistical points of each coal rock component to the total effective points was used as the final measurement result. (Method of microscopic determination of the reflectance of vitrinite in coal: GB/T 6948-2008; Determination of maceral group composition and minerals in coal: GB/T 8899-2013).

Furthermore, the Coretest ASPE730 constant velocity mercury piezometer used for mercury injection testing is capable of feeding mercury at up to 900 psi with a constant feed rate of 0.00005 ml/min and a high resolution pressure sensing acquisition device with a resolution of

0.001 psi. (Determination of pore size distribution and porosity of solid materials by mercury pressure and gas adsorption: GB/T21650-2008).

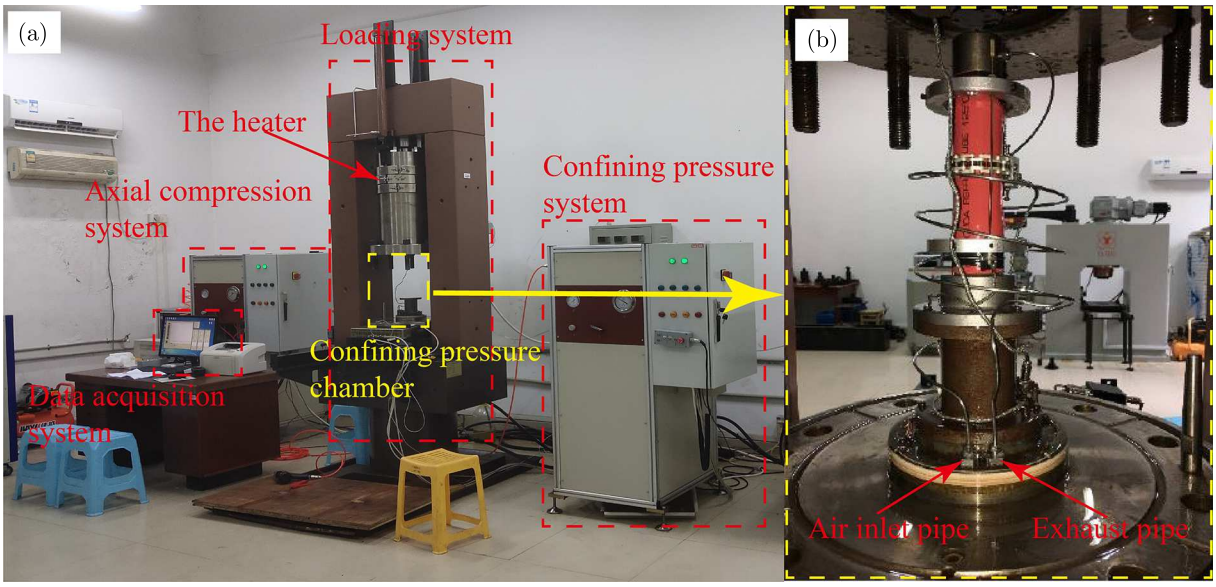

Fig. 1. Equipment for triaxial compression and penetration tests: (a) TFD-2000L triaxial rheological testing machine, (b) confining pressure chamber

3. Triaxial compression test results

3.1. Stress-strain curves

The triaxial compressive total stress-strain curves of the coal rock specimens under different confining pressures are shown in Fig. 2. It can be found that the confining pressure has a significant effect on the characteristics of the total stress-strain curves of the coal rock specimens. As shown in Fig. 2a, when the coal specimen is in uniaxial compression, the full stress-strain curve can be roughly divided into four stages, namely the initial compression-density stage, the elastic stage, the failure stage and the residual stress stage. When the coal rock specimen is in uniaxial compression, its initial stress increases rapidly, while the axial strain increases slowly, and the stress-strain curve is initially straight and then slightly curved. When the coal sample enters the second stage, the elastic state, the stress-strain curve is a straight line segment. When the specimen reaches the peak load and damage occurs, the axial stress drops significantly, followed by the residual stress phase. As shown in Fig. 2b, the full stress-strain curve of a coal sample under confining pressure can be roughly divided into three stages, namely the initial compression-density stage, the plastic stage and the damage stage. The stress-strain curve for the coal rock under confining pressure conditions has no obvious elastic segment, and as the stress increases the curve shows a clear non-linearity with a typical plastic deformation phase. The coal sample then breaks down and the stress decreases with no residual stress stage.

3.2. Peak strain and peak stress

The peak mechanical parameters of the triaxial compression of the coal rock under different confining pressures are shown in Fig. 3, and the basic mechanical parameters are listed in Table 1. From Fig. 3a and Table 1, it can be seen that the influence of the confining pressure on the peak axial stress of the coal rock specimen is very obvious. When the confining pressure is 0 MPa, the peak axial stress is 2.85 MPa, and when the confining pressure is 5 MPa, the peak axial stress is

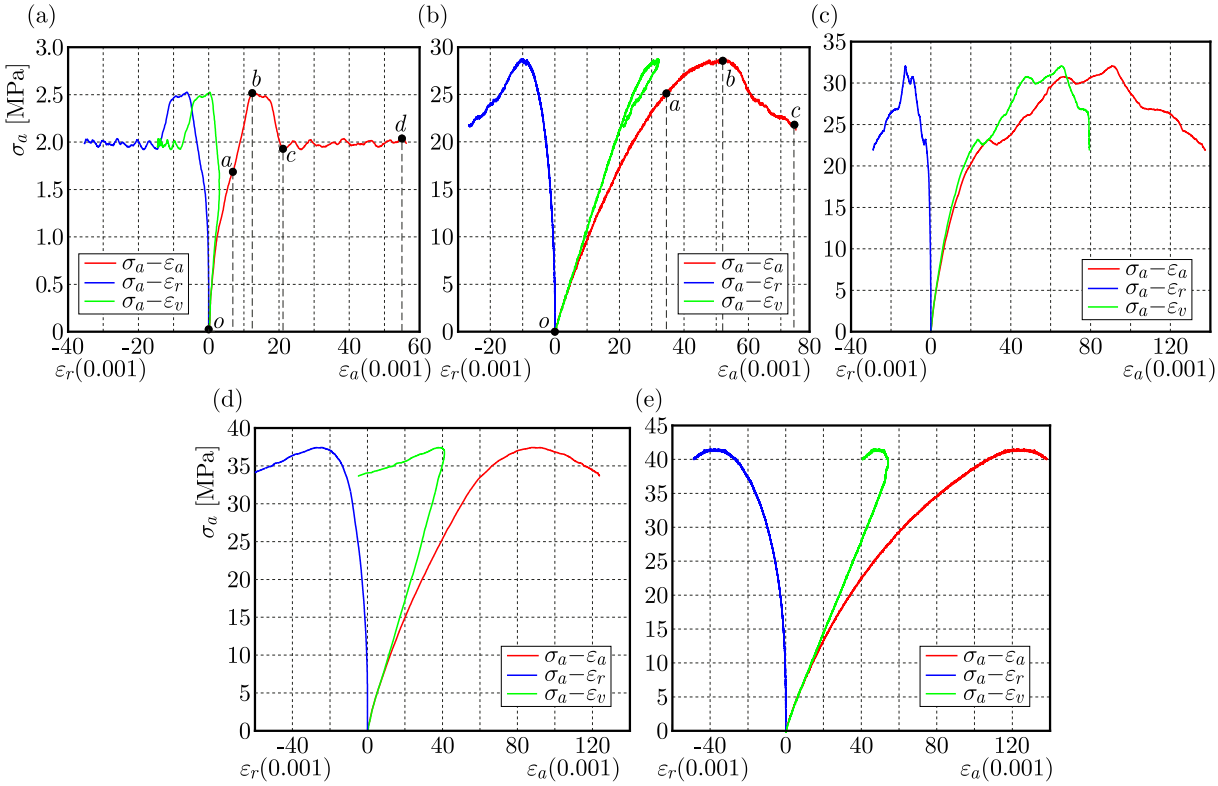

Fig. 2. Triaxial compression total stress-strain curves for coal rock specimens at different confining pressures: (a) 0 MPa, (b) 5 MPa, (c) 10 MPa, (d) 15 MPa, (e) 25 MPa

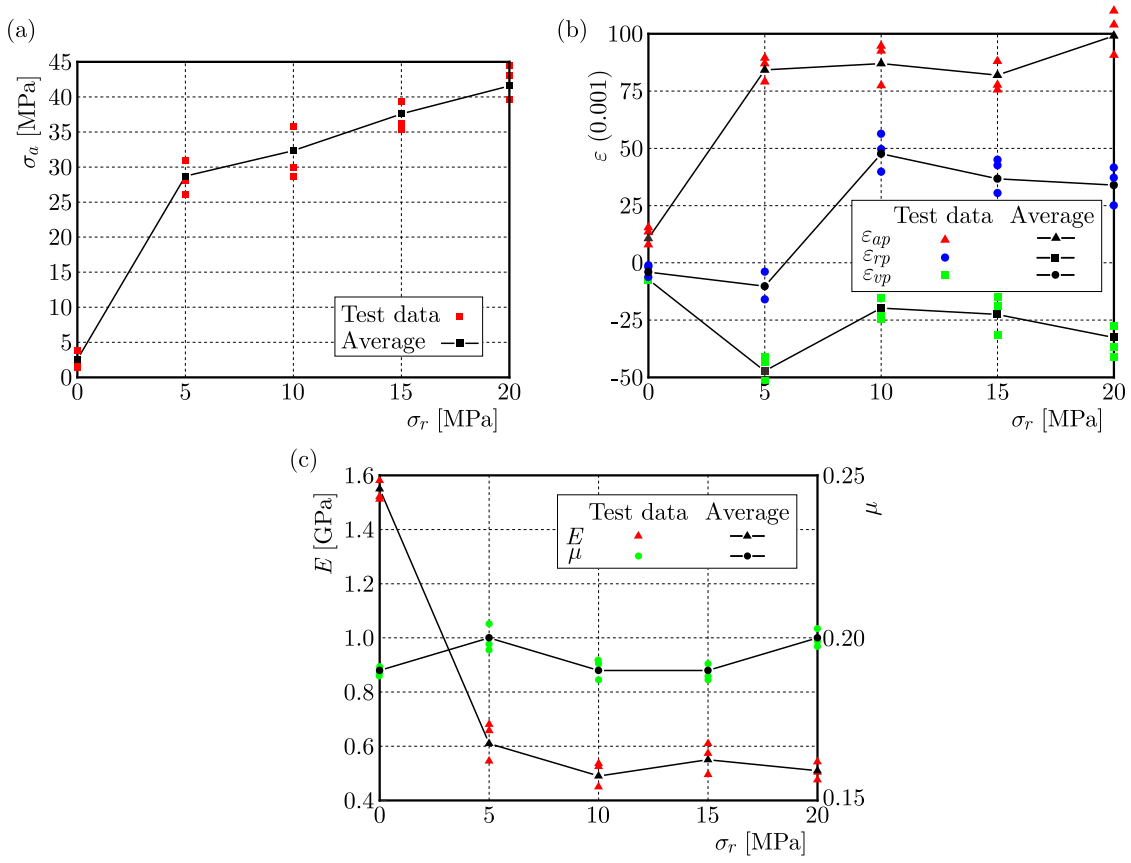

Fig. 3. Relationship between peak mechanical parameters and confining pressure: (a) axial stress, (b) strain, (c) elastic modulus and Poisson's ratio

27.81 MPa, which is an increase by 9.76 times. At the same time, it can be found that the rate of increase of the peak axial stress in the coal rock decreases significantly with the gradual increase of the confining pressure. This indicates that although the confining pressure can significantly increase the peak axial stress in the coal rock, the rate of increase is limited.

The trend of the peak strain of the coal rock with the confining pressure is shown in Fig. 3b. The peak axial strain increases rapidly with an increase of the confining pressure and then remains almost constant. The peak circumferential strain, on the other hand, increases first and then decreases with increasing confining pressure, reaching a maximum value when the confining pressure is 5 MPa. The peak volumetric strain increases from negative to positive with the increasing confining pressure, which indicates that the peak volumetric strain is determined by the peak circumferential strain at 0-5 MPa and the peak volumetric strain is determined by the peak axial strain when the confining pressure is 10-20 MPa.

The relationship among the peak modulus of elasticity and the peak Poisson's ratio and the confining pressure is shown in Fig. 3c. The peak modulus of elasticity of the coal rock decreases significantly with an increase of the confining pressure, i.e. the peak modulus of elasticity of the coal rock achieves the maximum value at 0 MPa, which is due to the presence of the confining pressure which makes the axial strain of the coal rock increase significantly during the compression process, however, the axial stress cannot increase proportionally with the axial strain. For Poisson's ratio of the coal rock, which remains between 0.18 and 0.21, the effect of the confining pressure on the modulus of elasticity of the coal rock is relatively small.

Table 1. Basic mechanical parameters of coal rock specimens under different confining pressures

σ_r [MPa]	σ_{ap} [MPa]	ε_{ap} [0.001]	ε_{rp} [0.001]	ε_{vp} [0.001]	E [GPa]	μ
0	2.85	11.76	−7.63	−4.23	1.51	0.18
5	27.81	82.21	−46.68	−12.36	0.58	0.20
10	33.25	85.69	−18.74	45.51	0.51	0.19
15	36.98	82.73	−24.37	34.24	0.54	0.21
20	42.37	98.48	−35.89	31.61	0.56	0.20

Note: σ_r is the confining pressure
σ_{ap} is the peak axial strength
ε_{ap} is the peak axial strain
ε_{rp} is the peak circumferential strain
ε_{vp} is the peak volume strain
E is the elastic modulus, μ is Poisson's ratio

3.3. Ultimate failure pattern

The triaxial compression damage pattern of the coal rock specimens is shown in Fig. 4. Oblique shear damage and vertical splitting damage are the main forms of damage to the coal rock. Moreover, the degree of coal rock fragmentation significantly increases with an increase of the confining pressure. This indicates that although high confining pressure can effectively increase the load capacity and deformation capacity of the coal rock, once the coal rock is damaged, the energy released and the degree of fragmentation will also increase significantly. As a result, the coal rock needs to be mined more safely and cautiously under high confining pressure.

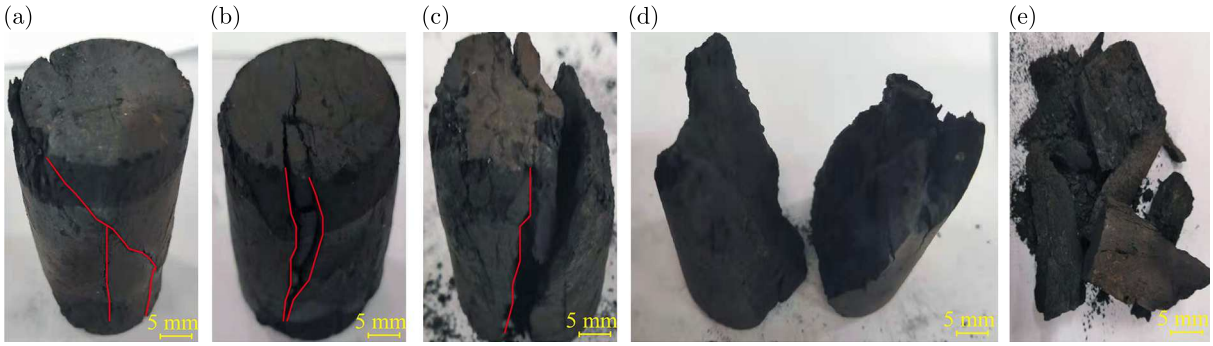

Fig. 4. Triaxial compression failure patterns of coal rock under different confining pressure

4. Mercury pressure testing and pore-fracture characterisation

4.1. Capillary pressure

The capillary pressure curves of the coal rocks obtained from the mercury pressure tests are shown in Fig. 5. The capillary pressure curve of the coal specimen is generally located in the upper left part of the figure, which indicates that the physical properties of the coal rocks in the Yili Basin of Xinjiang are generally poor and the permeability is small. The capillary pressure curve increases significantly with increasing mercury saturation, with no obvious flattening trend throughout the process. The rate of capillary pressure increase is significantly faster when the mercury saturation is between 0-20%. When the mercury saturation is above 20%, the rate of capillary pressure increase slows down significantly, indicating poor pore radius sorting in the coal rock specimens. This differs significantly from the capillary pressure curves obtained for other more common higher-order coal and sandstone reservoirs, which typically have more significant flat segments. Furthermore, the overall sortability of the conventional sandstone and high-order coal reservoirs is better and is usually dominated by the development of pore fractures, the main feature being the larger volume and greater number of pores within their coal rocks. In contrast, for the lower-order coals, the microfractures within the coal specimens are relatively underdeveloped and the pore-fissure radii are overall poorly sorted, forming a curve pattern that projects to the upper left.

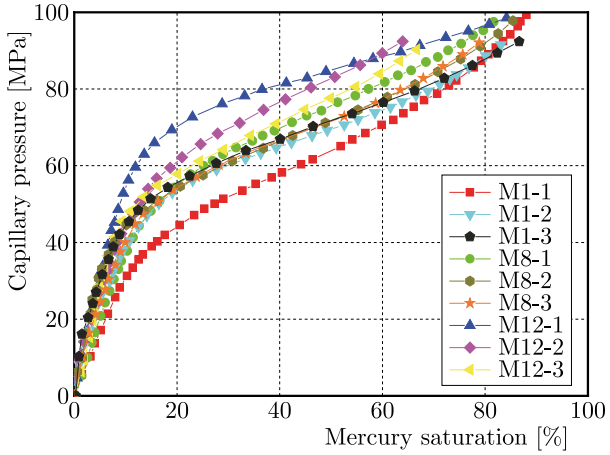

Fig. 5. High pressure mercury capillary pressure curve for 9 coal specimens

The input and output mercury curves of the coal rock specimens are shown in Fig. 6. The input and output mercury curves from the three stably developed coal seams in the Yili Basin, Xinjiang, are generally similar. Among them, the cumulative mercury intrusion of the coal rock

specimens is in descending order for the M_8, M_1 and M_{12} seams. This indicates that the pore space in the M_8 seam is slightly larger than that in the M_1 and M_{12} seams. In addition, all three groups of coal rock specimens have a small portion of the mercury withdrawal curve overlapping with the mercury ingress curve at the beginning of the mercury withdrawal, and the hysteresis loop formed by the mercury ingress and egress curves is small, indicating that the coal rock specimens have fewer open pores and are less connected.

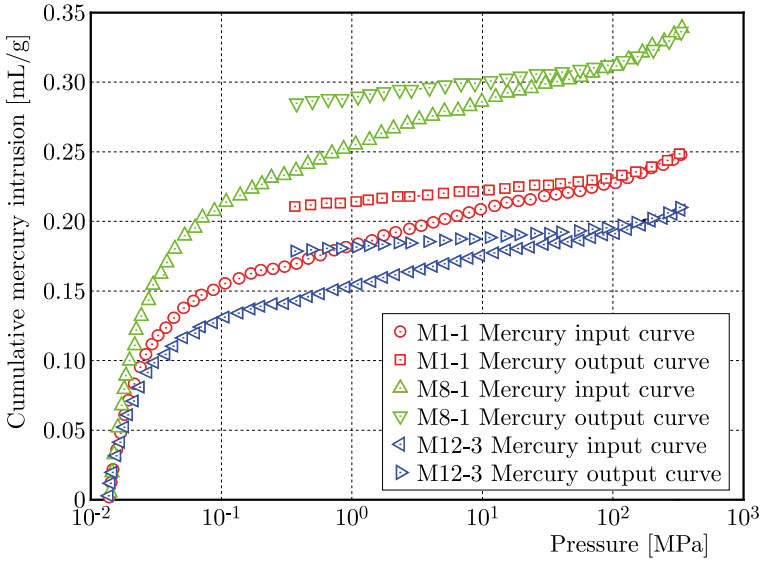

Fig. 6. Mercury-dehydration curves of three coal rock specimens

4.2. Throat and pore distribution characteristics

The pore volumes of the three groups of coal specimens are shown in Fig. 7, which shows a typical single-peak structure with peaks mainly in the range of 104-105 nm. The pore volumes of the three groups of coal specimens are significantly different, with the pore volumes from the M_8 seam being significantly larger than those from the M_1 and M_{12} seams. This trend is consistent with the variation pattern of the pressure-relief curve in Fig. 6. The analysis by the Hodot quadratic method (Yang *et al.*, 2020) shows that the pore volume of coal rock specimens from the Yili Basin, Xinjiang, is 38.6% microporous, 36.8% small porous, 11.5% medium porous and only 13.1% large porous, and the pores of coal rocks are dominated by microporous and small pores.

Based on the mercury-pressure tests, the distribution of throat radii and pore radii of coal rocks in the Yili Basin, Xinjiang, is shown in Figs. 8 and 9. From Fig. 8 it can be seen that the throat radii of the three stably developed coal seams, M_1, M_8 and M_{12}, are mainly concentrated around 1-2 μm, which indicates that the overall throat radii of coal rocks are on the fine side, thus leading to the overall low permeability of coal rocks. On the other hand, the pore radius is between 150-200 μm, which indicates that the small micropores and medium are more developed in the coal rocks, while the fine throat channels are more distributed and the pores are mostly fine necked bottle pores with poor pore connectivity, which is not conducive to the storage and desorption of coalbed methane (CBM). Figure 10 shows the pore-throat ratio of coal rock specimens. The pore-throat ratio reflects the configuration relationship between pore and throat. The distribution of the pore-throat ratio is opposite to that of throat channel, the higher the permeability of coal rock specimens, the more concentrated the distribution of the pore-throat ratio.

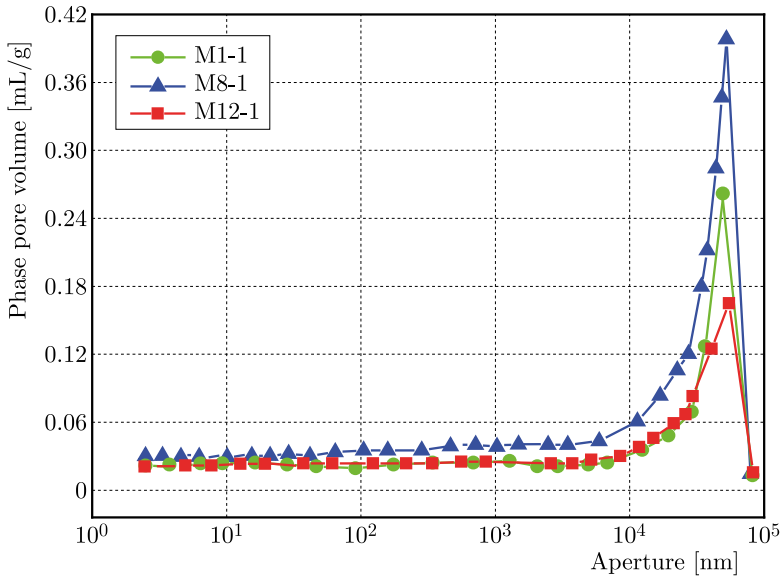

Fig. 7. Pore volume relationship for three sets of coal rock specimens

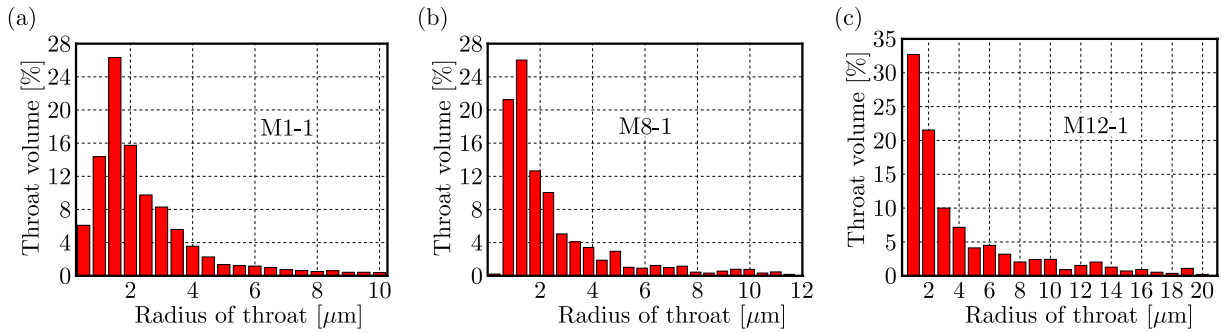

Fig. 8. Characteristics of the distribution of throat radii in coal rock specimens

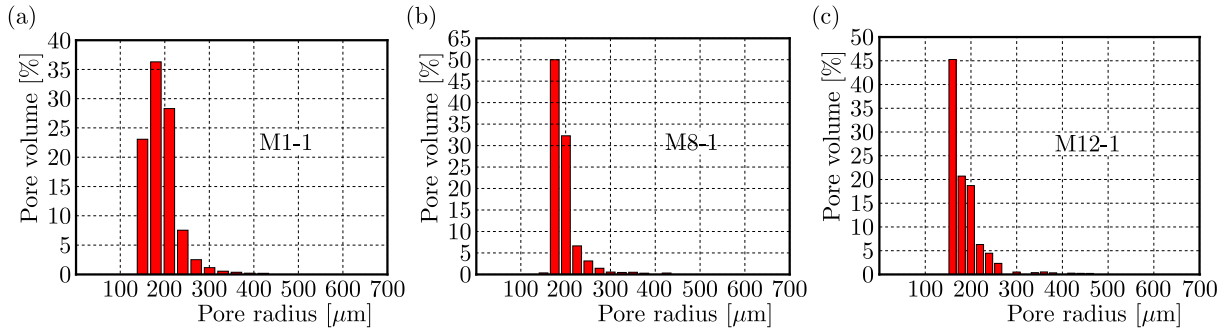

Fig. 9. Pore radius distribution characteristics of coal rock specimens

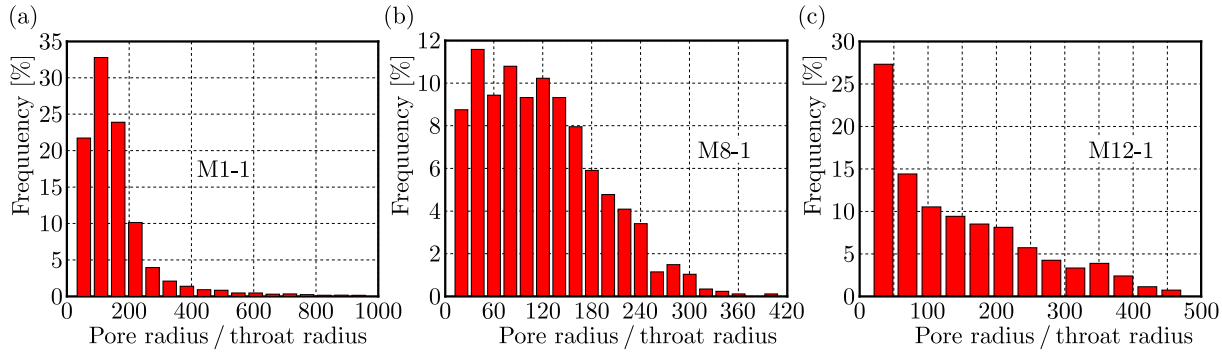

Fig. 10. The pore-throat ratio of coal rock specimens

4.3. Maximum reflectance characteristics of the coal rock microfraction and specular group

The basic physical parameters of the coal specimens are shown in Table 2. Among them, the permeability of the six coal rock specimens in the M_1 and M_{12} seams ranged from 0.11-0.19 mD, which is a medium permeability reservoir. The permeability of the coal rock specimens in the M_8 seam ranged from 0.06-0.09 mD, which is typical for low permeability reservoirs. In addition, the porosity of the nine coal rock specimens ranged from 4.1% to 5.5%, with an average porosity of 4.98%, which is typical for low porosity reservoirs. The porosity range of the coal sample specimens indicates that the overall physical properties of the coal rocks in the Yili Basin of Xinjiang are poor.

Table 2. Basic physical parameters of coal specimens

Specimen number	Porosity [%]	Penetration rate [mD]	Density [g/cm^3]	Maximum specular body reflectance [%]	Vitrinite [%]	Inertinite [%]	Chitinous [%]
M_1-1	4.9	0.11	0.92	3.52	83.1	16.1	0.8
M_1-2	5.2	0.13	0.84	2.67	86.7	13.0	0.3
M_1-3	4.1	0.14	0.88	3.62	86.3	13.2	0.5
M_8-1	5.3	0.07	0.96	3.13	84.5	15.1	0.4
M_8-2	4.5	0.09	0.91	3.47	86.5	13.1	0.4
M_8-3	5.5	0.06	0.89	3.59	89.2	10.3	0.5
M_{12}-1	4.8	0.18	0.87	3.64	88.2	11.4	0.4
M_{12}-2	5.1	0.17	0.93	3.17	85.6	14.3	0.1
M_{12}-3	5.4	0.19	0.97	3.01	86.4	13.1	0.6

Meanwhile, the test results show that the microscopic fraction of the coal rocks in the Yili Basin, Xinjiang, is dominated by vitrinite, with a percentage of 83.1%-89.2 and an average of 86.27%, while the percentage of the inert group is relatively small, with its percentage ranging from 10.3%-16.1%. It can also be seen that for the coal rock specimens tested, the chitinous group is very small, at just 0.1%-0.8%. In addition, small amounts of carbonate minerals and clay minerals were found in the coal specimens.

5. Discussion

A large amount of gas is formed during formation of coal, and effective gas extraction can reduce the gas content and pressure to a safe range, thus reducing the possibility of gas disaster accidents. As the depth of the coal seam increases, the confining pressure on the coal rock increases. There is a large number of original defects (micro-fractures and micro-porosity) inside the coal rock specimens, and these original defects are highly susceptible to compressive deformation under the action of external stress. As the confining pressure continues to increase, the original defects are further compressed and closed, and the coal matrix squeezes the micro-pore fracture space inward, which leads to the narrowing of the seepage channel and the obstruction of gas transport in the micro-pore fracture space (Gray, 1987). The coal seam permeability characteristics will directly affect the gas extraction efficiency of the mine. In this study, the permeability of coal rock specimens under fixed confining pressure conditions was investigated, however, the effect of different confining pressure on the permeability of coal rock specimens was not considered. Therefore, the influence of different confining pressure on the permeability of coal rock specimens will be emphasized in the next work.

6. Conclusion

In this paper, the triaxial mechanical properties and pore-fracture characteristics of coal rocks in the Yili Basin, Xinjiang, were investigated by triaxial compression tests, mercury compression tests and scanning electron microscopy tests. The following main conclusions were obtained.

- Confining pressure has a significant effect on the compressive mechanical properties of coal rocks in the Yili Basin, Xinjiang. As the confining pressure increases, the axial peak stress of coal rocks increases, while the peak elastic modulus decreases significantly. The axial peak strain increases and then remains constant, while the circumferential peak and volumetric peak strains increase and then decrease. The confining pressure has almost no effect on Poisson's ratio of the coal rock specimens.
- Oblique shear damage and vertical splitting damage are the main forms of damage to the coal rock. Furthermore, the degree of coal rock fragmentation increases significantly with the increase of the confining pressure.
- The microscopic fraction of coal rocks in the Yili Basin of Xinjiang is dominated by the mirror mass, with a proportion of 83.1%-89.2, while the proportion of the inert group is relatively small, with its proportion ranging from 10.3%-16.1%. In addition, the coal rocks are generally typical low-permeability coal rocks with permeabilities ranging from 0.06-0.19 mD and poor pore connectivity.

It is worth noting that the micro fissure-pores of coal rock specimens are closely related to their petrographic composition. Therefore, enough attention should be paid in the related future studies.

Acknowledgments

This work was supported by the National Natural Science Foundation of China (No. 51638002), and the Natural Science Foundation of Jiangsu Province Universities Project (No. 19KJD410001).

References

1. Blondeel M., van de Graaf T., 2018, Toward a global coal mining moratorium? A comparative analysis of coal mining policies in the USA, China, India and Australia, *Climatic Change*, **150**, 89-101
2. Chen S., Yang T., Ranjith P.G., Wei C., 2017, Mechanism of the two-phase flow model for water and gas based on adsorption and desorption in fractured coal and rock, *Rock Mechanics and Rock Engineering*, **50**, 571-586
3. Chen Y.L., Zuo J.P., Liu D.J., Wang Z., 2019, Deformation failure characteristics of coal-rock combined body under uniaxial compression: experimental and numerical investigations, *Bulletin of Engineering Geology and the Environment*, **78**, 3449-3464
4. Fairhurst C.E., Hudson J.A., 1999, Draft ISRM suggested method for the complete stress--strain curve for the intact rock in uniaxial compression, *International Journal of Rock Mechanics and Mining Sciences*, **36**, 3, 279-289
5. Gray I., 1987, Reservoir engineering in coal seams, Part 1 – The physical process of gas storage and movement in coal seams, *SPE Reservoir Engineers*, **2**, 1, 28-34
6. Haque E., Reza S., Ahmed R., 2018, Assessing the vulnerability of groundwater due to open pit coal mining using DRASTIC model: a case study of Phulbari Coal Mine, Bangladesh, *Geosciences Journal*, **22**, 359-371
7. Lin B.Q., Zhou S.N., 1987, Experimental study on gas permeability of coal sample, *Journal of China University of Mining and Technology*, **16**, 2, 21-28

8. Liu Y., Lu C.P., Xiao Z.Y., Guo Y., 2022, Mechanisms underlying the slip and failure of coal-rock parting-coal sructures under unloading conditions, *Rock Mechanics and Rock Engineering*, **55**, 4913-4928

9. National Standardization Administration Committee, 2008, Determination of pore size distribution and porosity of solid materials by mercury pressure and gas adsorption: GB/T21650-2008. Beijing: Standards Press of China

10. National Standardization Management Committee, 2008, Method for microscopic determination of specular reflectance of coal: GB/T6948-2008. Beijing: Standards Press of China

11. National Standardization Administration Committee, 2009, Determination method of physical and mechanical properties of coal and rock: GB/T23561.9-2009. Beijing: Standards Press of China

12. National Standardization Administration Committee, 2013, Determination of maceral group composition and minerals in coal: GB/T 8899-2013. Beijing: Standards Press of China.

13. Njiekak G., Schmitt D.R., Kofman R.S., 2018, Pore systems in carbonate formations, Weyburn field, Saskatchewan, Canada: Micro-tomography, helium porosimetry and mercury intrusion porosimetry characterization, *Journal of Petroleum Science and Engineering*, **171**, 1496-1513

14. Qajar J., Arns C.H., 2022, A comparative study of micro-CT and mercury intrusion techniques for predicting permeability and surface area evolution during chemical dissolution, *Advances in Water Resources*, **168**, 104301

15. Shan R.L., Li Z.L., Wang C.H., Wei Y., Tong X., Liu S., Shan Z., 2021, Study on the distribution characteristics of stress deviator in the surrounding rock when mining closely spaced coal seams, *Environmental Earth Sciences*, **80**, 602

16. Wang L., Cheng Y.P., Xu C., An F.H., Jin K., Zhang X.L., 2013, The controlling effect of thick-hard igneous rock on pressure relief gas drainage and dynamic disasters in outburst coal seams, *Natural Hazards*, **66**, 1221-1241

17. Wang X.L., Pan J.N., Wang K., Ge T., Wei J., Wu W., 2020, Characterizing the shape, size, and distribution heterogeneity of pore-fractures in high rank coal based on X-ray CT image analysis and mercury intrusion porosimetry, *Fuel*, **282**, 15, 118754

18. Xu C., Fu Q., Cui X.Y., Wang K., Zhao Y., Cai Y., 2019, Apparent-depth effects of the dynamic failure of thick hard rock strata on the underlying coal mass during underground mining, *Rock Mechanics and Rock Engineering*, **52**, 1565-1576

19. Xue Y., Liu J., Ranjith P.G., Gao F., Xie H., Wang J., 2022, Changes in microstructure and mechanical properties of low-permeability coal induced by pulsating nitrogen fatigue fracturing tests, *Rock Mechanics and Rock Engineering*, **55**, 74697488

20. Yang J., Zhang Z., Zhao L.F., 2020, Study on pore-fracture characteristics of coal rocks in the Buri Basin, *Coal Mine Safety*, **51**, 12, 214-218

21. Yin T.B., Wang P., Li X.B., Shu R.H., Ye Z.Y., 2016, Effects of thermal treatment on physical and mechanical characteristics of coal rock, *Journal of Central South University*, **23**, 2336-2345

22. Zhong C.L., Zhang Z.Y., Ranjith P.G., Zhang C., Xue K., 2022, The role of pore pressure on the mechanical behavior of coal under undrained cyclic triaxial loading, *Rock Mechanics and Rock Engineering*, **55**, 1375-1392

23. Zhu H.X., Han L.J., Meng Q.B., Liu J., Meng L., Dong W., 2021, The split-permeation grouting mechanism of loose and broken coal rock masses considering the temporal and spatial characteristics of slurry viscosity, *KSCE Journal of Civil Engineering*, **25**, 1887-1900

Manuscript received September 11, 2022; accepted for print December 7, 2022

JOURNAL OF THEORETICAL AND APPLIED MECHANICS
61, 2, pp. 219-232, Warsaw 2023
https://doi.org/10.15632/jtam-pl/159728

INVESTIGATION OF THE PAD STIFFNESS EFFECTS ON THE INITIATION OF BRAKE SQUEAL PHENOMENON

Akif Yavuz, Osman Taha Sen
Istanbul Technical University, Department of Mechanical Engineering, Istanbul, Turkey
e-mail: yavuza15@itu.edu.tr (corresponding author); senos@itu.edu.tr

The main objective of this study is to investigate pad stiffness effects on the instability of a nonlinear brake squeal model. Hence, a nonlinear mathematical model is developed. The nonlinear model is linearized to check the system stability through complex eigenvalue analysis. The results of linear stability analyses are compared to the numerical solution of the nonlinear model, and it is observed that the dynamic behavior predicted by the linear stability analysis is in accordance with the numerical solutions. Though, a discrepancy may occur at the predicted squeal frequencies with both approaches, especially at high pad stiffness levels.

Keywords: disc brake squeal, mode coupling phenomenon, linear stability analysis, nonlinear dynamics

1. Introduction

A wide variety of noise and vibration problems are observed in automotive disc brake systems. In the traditional classification, these problems are classified based on dominant frequencies as shown in Fig. 1 (Stojanovic *et al.*, 2022). Though, a phenomenological classification is also given in the literature, where the problems are classified based on physical mechanisms such as forced vibrations, vibrations primarily due to friction characteristics, and resonance effects (Jacobsson, 2003).

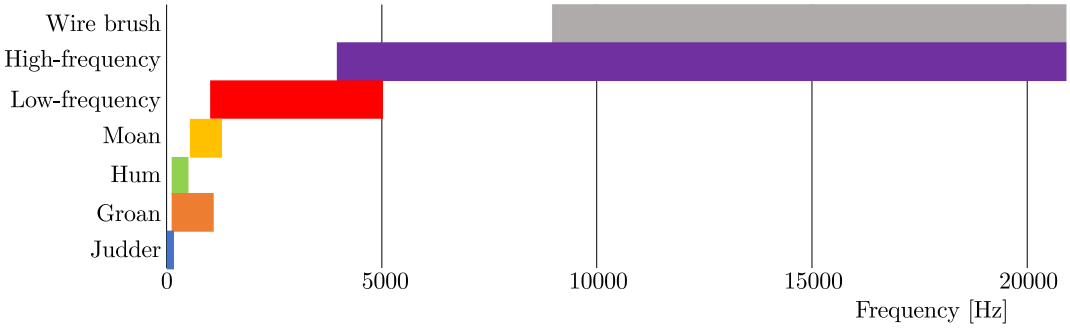

Fig. 1. Traditional classification of brake vibration and noise problems (Stojanovic *et al.*, 2022)

High frequency brake squeal noise has become an important vehicle comfort problem, even if it does not affect driving safety. Since the problem is in high frequency bands, these vibrations spread in the form of acoustic modes leading to brake noise problem (Kinkaid *et al.*, 2003). Although the problem of interest has been studied for nearly a century, and an extensive literature exists; a general solution to the brake squeal problem that can be applied to all automotive brake systems has not yet been developed (Papinniemi *et al.*, 2002). It is known that some proposed models are only suitable for certain systems and even in these systems they cannot always detect

the problem definitively. This is mainly due to the fact that the squeal phenomenon is mainly governed by friction which is not fully understood. Therefore, the mechanisms that cause the brake noise problem has not been adequately examined and the problem is still open to research.

The underlying physics leading to high frequency brake squeal noise is usually attributed to the resonance phenomenon, i.e., the natural frequency of the brake system is excited by nonconservative friction forces through several physical mechanisms; thus the system becomes dynamically unstable. In general, these physical mechanisms are defined as follows: 1) Stick-slip phenomenon with negative damping; 2) Sprag-slip phenomenon; 3) Self-excited vibrations with a constant friction coefficient; 4) Splitting or coupling of vibration modes; 5) Hammering (Kinkaid *et al.*, 2003).

In the existing literature, a wide variety of low order linear and nonlinear mathematical models are available, which are proposed for brake squeal investigation. In one study by Wang *et al.* (2014), the authors investigated squeal instability through numerical solutions of a four degree of freedom nonlinear disc brake system model. The results showed that the pad stiffness and disc velocity had significant effects on the initiation of squeal instability due to nonlinear effects of friction characteristics and contact loss. In another paper by Li *et al.* (2016), the authors developed a nonlinear mathematical model of a mass-sliding belt system and investigated the effects of preload and nonlinear contact stiffness on squeal instability. The authors observed that the surface separation between the mass and the sliding belt significantly altered the effects of preload and contact stiffness. In the study by Ghorbel *et al.* (2020), the validity of linear stability analysis was investigated through a two degree of freedom disc brake system model. The authors examined the effects of gyroscopic factors, damping and pad geometry via linear stability analysis, and obtained time domain solutions through numerical solutions of their nonlinear model. Consequently, the authors obtained a good match between the results of linear stability analysis and numerical solutions. In another study by Dakel and Sinou, where linear stability analysis was utilized, mode coupling instability was numerically investigated with a four degree of freedom system that exhibited friction nonlinearity (Dakel and Sinou, 2017). The linear stability analysis was carried out on through complex eigenvalue analysis of linearized governing equations, and the Hopf bifurcation points as a function of the kinetic friction coefficient were determined. Hochlenert used a linear stability analysis approach on a twelve degree of freedom disc brake model and investigated effects of the friction coefficient and disc angular velocity on stability of the system (Hochlenert, 2009). The author observed that the effect of the friction coefficient on dynamic instability vanished at high disc angular velocity and the effect of disc angular velocity disappeared at a high friction coefficient. Kang investigated the effect of friction coefficient characteristics on squeal instability on a two degree of freedom mathematical model (Kang, 2018). The author assumed a smooth friction-velocity curve (Stribeck type) and observed that the dynamic response of the system depended significantly on friction-velocity curve characteristics. Hoffmann *et al.* (2002) investigated the mode coupling instability through a two degree of freedom model by a time-series response and complex eigenvalue analysis.

Furthermore, the linear stability analysis approach on the investigation of squeal behavior was found to be misleading in some studies (Liu and Ouyang, 2020; Sinou, 2010; Zhang *et al.*, 2016). Liu and Ouyang studied the dynamics of a disc brake system with a five degree of freedom mathematical model by numerical and analytical means. The authors included the effects due to contact stiffness, stick-slip and geometrical nonlinearities in their model and concluded that a nonlinear stability analysis was crucial for detection of squeal instability (Liu and Ouyang, 2020). Sinou claimed that the stability analysis performed on the linearized system provided limited information about dynamic behavior of the system. Thus, the author suggested the use of numerical solutions of nonlinear governing equations for a precise investigation (Sinou, 2010). Zhang *et al.* (2016) stated that complex eigenvalue analysis applied to linearized models may lead to misinterpretations, probably due to inherent nonlinearities that have significant

effects on dynamics of the system. In yet another study by Belhocine and Ghazaly, the authors investigated the squeal phenomenon through a finite element model of the disc brake assembly, which was experimentally validated via modal testing. The authors performed stability analysis on the model and investigate the effect of Young's modulus of brake system components on the occurrence of high frequency squeal noise (Belhocine and Ghazaly, 2016).

In this study, the squeal phenomenon is investigated mathematically while utilizing a friction model obtained through experimentation on a mass-sliding belt test setup. First, a nonlinear mathematical model is developed to investigate the effect of preload on the system. Second, the nonlinear model is linearized, and its stability is assessed through complex eigenvalue analysis for different operating conditions, which are preload and belt velocity. The values of the critical pad stiffness at which the system switches from a stable to unstable regime are determined for various operating conditions, and the effects of the preload and belt velocity on the critical pad stiffness are determined. Third, the nonlinear governing equations are numerically solved for the same operating conditions; the results are compared to the linear stability analysis. It is observed that both models exhibit similar dynamic behavior from the perspective of predicting dynamic behavior of the system. Finally, the effect of pad stiffness on surface separation at the contact interface is numerically investigated through the nonlinear model, and the performance of the linear stability analysis is assessed by comparing the calculated squeal frequencies. It is observed that an increase of pad stiffness leads to significant surface separation effects, which leads to nonlinear dynamic behavior. Thus, the squeal frequencies predicted with linear stability analysis start to deviate from the numerical solutions of nonlinear equations at high pad stiffness levels.

The key assumptions in this current study can be listed as follows: 1) Damping is ignored in the mathematical modeling since there is no significant damping in a real physical brake system. 2) The springs utilized in the mathematical model are all assumed to have linear characteristics. This is a reasonable assumption due to minor deformations observed in these springs. 3) For linearization of the governing equations, the discontinuous 'sgn' function in nonlinear governing equations is replaced with a continuous 'tanh' function. This assumption may lead to a failure, especially at solution points near the discontinuity. However, this assumption is required for the linear stability analysis. 4) The surface separation effect is also ignored in the linear stability analysis. Though, it is shown in the study that squeal frequencies determined from the linearized model start to deviate from the nonlinear model as the surface separation effect becomes significant.

A flowchart of this study is shown below in Fig. 2, where the experimental and computational findings are depicted in detail. Furthermore, the novelty of this study is the fundamental understanding of the effects of operating parameters (angular configuration, preload and belt velocity) on the critical pad stiffness and the effect of pad stiffness on the surface separation at the contact interface.

2. Nonlinear two degree of freedom mathematical model

A nonlinear two degree of freedom mathematical model is developed as shown in Fig. 3. In the model, the pad is assumed as a mass m that performs planar motion in the vertical plane without any rotation. Thus, translations in x and y directions are defined as the two degrees of freedom. Furthermore, the brake disc is defined as a translating surface at constant velocity V underneath the mass. The pad is attached to the common ground with four linear springs. The two of these springs that represent stiffness of the brake pad k_1 and k_2 are positioned with arbitrary angles θ_1 and θ_2 with respect to the horizontal axis. The other springs k_3 and k_4 are parallel to the horizontal axis, and they represent elasticity of the clips between the pad and

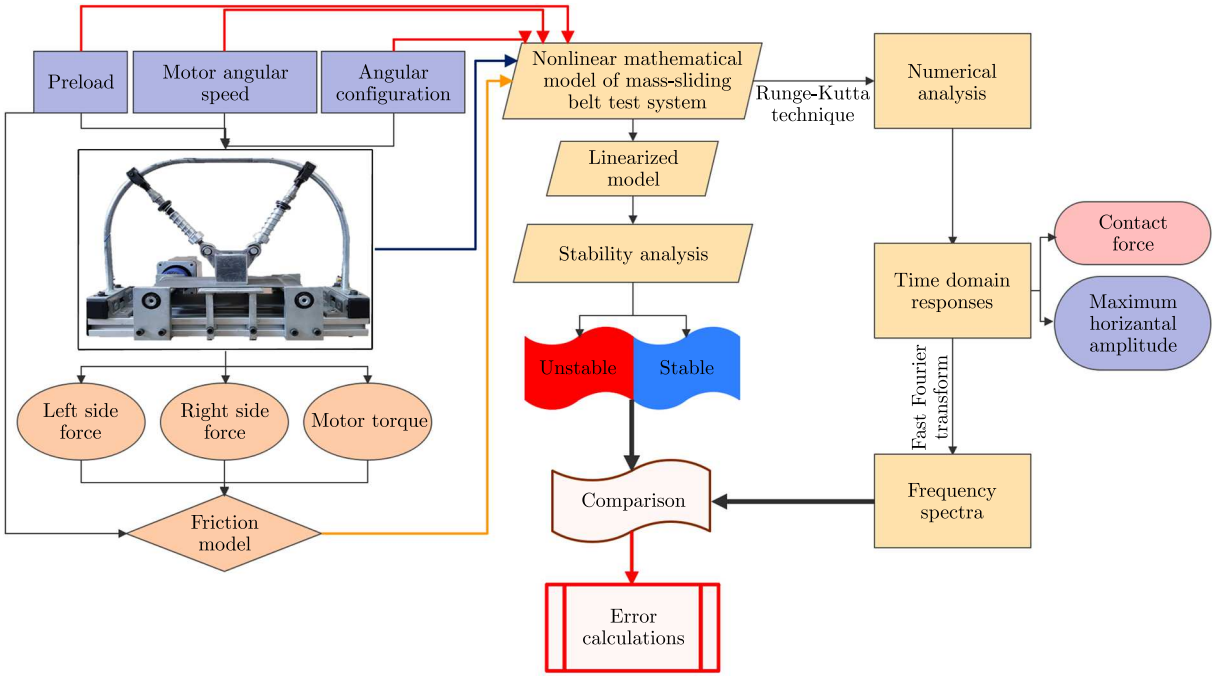

Fig. 2. The flowchart of the study

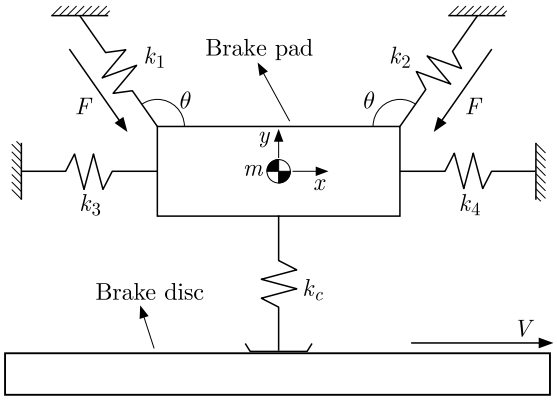

Fig. 3. Schematics of the nonlinear two degree of freedom mathematical model

the caliper. The contact between the pad and the disc is defined as a point contact where the stiffness at the contact interface is defined by another linear elastic element k_c, which can only generate a compressive force in y-direction. Furthermore, a pretension L_{pre} is defined on the contact spring k_c. The preload F is applied to springs k_1 and k_2 in order to mimic the effect of hydraulic brake pressure.

The dynamic friction coefficient μ at the pad/disc contact interface is obtained experimentally in a mass-sliding belt experiment (Fig. 4a), which has a similar structure to the model shown in Fig. 3. In this experiment, a mass is pushed on the sliding belt via two telescopic arms, which are supported by the springs k_1 and k_2, see Fig. 3. Note that the configurations of these springs are kept intact during the experiments, i.e., $\theta = (27/36)\pi$. The experiments are performed at different belt speeds and preload conditions. Restoring forces in springs k_1 and k_2 are measured with two force transducers, and the moment of the electric motor that drives the sliding belt is acquired from the inverter. Thus, the tangential force at the mass/sliding belt

interface is obtained, and the instantaneous dynamic friction coefficient $\mu_i(t)$ at the contact interface is calculated from the measured data as follows

$$\mu_i(t) = \frac{F_t(t)}{F_l(t)\sin\theta + F_r(t)\sin\theta + 2F\sin\theta} \tag{2.1}$$

where $F_t(t)$ is the instantaneous tangential force at the contact interface, and $F_l(t)$ and $F_r(t)$ are the instantaneous normal forces on the left and right telescopic arms, respectively. Furthermore, the term F is the constant preload applied to springs k_1 and k_2, respectively. In summary, the numerator in Eq. (2.1) is the tangential force at the brake pad and brake disc contact interface, which is calculated by dividing the measured motor torque by the radius of the drum. The denominator in Eq. (2.1) represents the total normal load at the brake pad and brake disc contact interface, which has a constant (due to the preload F) and time varying (due to $F_l(t)$ and $F_r(t)$) components. Though the forces F, $F_l(t)$ and $F_r(t)$ are not perpendicular to the disc surface, thus their projections on the vertical axis are calculated by multiplying these forces by $\sin\theta$.

Based on measurements, it is observed that the estimated dynamic friction coefficient $\mu_i(t)$ at a given parameter set does not alter significantly during tests. Hence, an average dynamic friction coefficient μ is defined by the mean value theorem for integrals in the closed interval of $[0, T]$ as below (Sawczuk *et al.*, 2021a,b)

$$\mu = \frac{1}{T}\int_0^T \mu_i(t)\, dt \tag{2.2}$$

Consequently, the dynamic friction coefficient is experimentally obtained as shown in Fig. 4b for two different preload levels, i.e., $F = 50\,\mathrm{N}$ and $F = 200\,\mathrm{N}$ with respect to V. Here, it should be emphasized that a two-dimensional linear regression model is utilized for derivation of the friction model depicted in Fig. 4b.

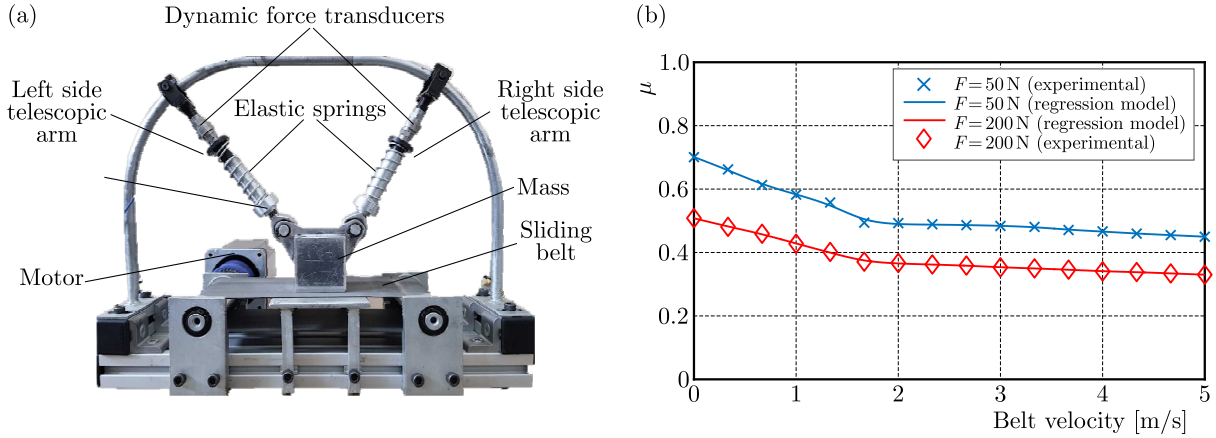

Fig. 4. (a) Mass-sliding belt test rig, (b) change of the dynamic friction coefficient with respect to V at two different preload levels

The nonlinear governing equations of the system shown in Fig. 3 are derived by calculating the elastic force vectors for each spring by Hooke's law. These force vectors are then projected on the x and y axes, and the force equilibria in these directions are obtained as shown in Eqs. (2.3)

$$
\begin{aligned}
&m\ddot{x} + k_1 \frac{\left(\sqrt{x^2+y^2-2L_1(x\cos\theta+y\sin\theta+L_1^2}-L_1\right)(x-L_1\cos\theta)}{\sqrt{x^2+y^2-2L_1(x\cos\theta+y\sin\theta)+L_1^2}} \\
&\quad + k_2 \frac{\left(\sqrt{x^2+y^2+2L_2(x\cos\theta-y\sin\theta)+L_2^2}-L_2\right)(x+L_2\cos\theta)}{\sqrt{x^2+y^2+2L_2(x\cos\theta-y\sin\theta)+L_2^2}} \\
&\quad + (k_3+k_4)x + \frac{1}{2}k_c\mu(y-L_{pre})[1+\operatorname{sgn}(L_{pre}-y)] = 0 \\
&m\ddot{y} + k_1 \frac{\left(\sqrt{x^2+y^2-2L_1(x\cos\theta+y\sin\theta)+L_1^2}-L_1\right)(y-L_1\sin\theta)}{\sqrt{x^2+y^2-2L_1(x\cos\theta+y\sin\theta)+L_1^2}} \\
&\quad + k_2 \frac{\left(\sqrt{x^2+y^2+2L_2(x\cos\theta-y\sin\theta)+L_2^2}-L_2\right)(y-L_2\sin\theta)}{\sqrt{x^2+y^2+2L_2(x\cos\theta-y\sin\theta)+L_2^2}} \\
&\quad + \frac{1}{2}k_c(y-L_{pre})[1+\operatorname{sgn}(L_{pre}-y)] + 2F\sin\theta = 0
\end{aligned}
\tag{2.3}
$$

The terms L_1 and L_2 in Eqs. (2.3) are the free lengths of the springs k_1 and k_2, respectively. Furthermore, the following nonlinearities are considered in the mathematical model: 1) Kinematic nonlinearity due to θ_1 and θ_2; 2) Contact loss nonlinearity due to piecewise linear 'sgn' function; and 3) Dynamic friction coefficient model μ obtained experimentally. For detailed derivation of the nonlinear governing equations, readers should refer to (Sen and Singh, 2021)

3. Linearization of the nonlinear governing equations

The stability of the system is assessed with complex eigenvalue analysis, which requires linearization of the governing equations. Consequently, the following assumptions are made in order to obtain a simplified linear mathematical model. First, the velocity of the disc is assumed to be greater than the velocity of the pad in the x direction, i.e., $\dot{x} < V$ for any time. Thus, the direction of the friction force vector does not change. Second, the pad and the disc are assumed to be in perpetual contact, i.e., $y < L_{pre}$. Third, the nonlinear terms due to the angular configuration θ in Eqs. (2.3) are linearized with Taylor series expansion around the point $(x, y) = (0, 0)$. Furthermore, the discontinuous piecewise linear 'sgn' function is approximated with a continuous 'tanh' function as $\operatorname{sgn}(z) = \tanh(\sigma z)$, where σ is a regularizing factor (Oberst *et al.*, 2013). Finally, the linearized equations are obtained as follows

$$
\begin{aligned}
&m\ddot{x} + (K_{aa}+k_3+k_4)x + (K_{ab}+\mu k_c)y = \frac{1}{2}\mu k_c L_{pre}[\tanh(\sigma L_{pre})+1] \\
&m\ddot{y} + K_{ab}x + (K_{bb}+k_c)y = -2F\sin\theta + \frac{1}{2}\mu k_c L_{pre}[\tanh(\sigma L_{pre})+1]
\end{aligned}
\tag{3.1}
$$

where K_{aa}, K_{ab} and K_{bb} are defined as

$$
\begin{aligned}
&K_{aa} = (k_1+k_2)\cos^2\theta \qquad K_{ab} = (k_1-k_2)\sin\theta\cos\theta \\
&K_{bb} = (k_1+k_2)\sin^2\theta
\end{aligned}
\tag{3.2}
$$

Using the above equations, the static equilibrium point (x^*, y^*) is obtained as

$$\begin{aligned} x^* &= \frac{1}{(K_{aa}+k_3+k_4)(K_{bb}+k_c)-K_{ab}(K_{ab}+\mu k_c)}\Big[(K_{bb}+k_c)\Big(\frac{1}{2}\mu k_c L_{pre}[\tanh(\sigma L_{pre})+1]\Big) \\ &\quad -\Big(-2F\sin\theta+\frac{1}{2}\mu k_c L_{pre}[\tanh(\sigma L_{pre})+1]\Big)(K_{ab}+\mu k_c)\Big] \\ y^* &= \frac{1}{(K_{aa}+k_3+k_4)(K_{bb}+k_c)-K_{ab}(K_{ab}+\mu k_c)}\Big[(K_{aa}+k_3+k_4)\Big(-2F\sin\theta \\ &\quad +\frac{1}{2}\mu k_c L_{pre}[\tanh(\sigma L_{pre})+1]\Big)-K_{ab}\Big(\frac{1}{2}\mu k_c L_{pre}[\tanh(\sigma L_{pre})+1]\Big)\Big] \end{aligned} \tag{3.3}$$

Finally, the linearized equations are shifted to the static equilibrium position via linear transformation $(\overline{x}, \overline{y}) = (x + x^*, y + y^*)$, and the Jacobian matrix is obtained to be used in complex eigenvalue analysis.

4. Stability analysis with complex eigenvalue solution

The stability of the system is assessed by the complex eigenvalue solution of the Jacobian matrix of the linearized model. Thus, the instability of the system is attributed to the complex eigenvalue λ with a positive real part. Particularly, the effect of preload F and disc velocity V on the instability is investigated. In the analysis, the angular configuration of k_1 and k_2 are selected to be $\theta = (27/36)\pi$ as in the experiments, and the complex eigenvalues are obtained over a broad range of brake pad stiffness levels (k_1 and k_2). Note that $k_1 = k_2$ is also assumed. The real and imaginary parts of the complex eigenvalues are depicted in Figs. 5-8 for different preload levels and disc velocities.

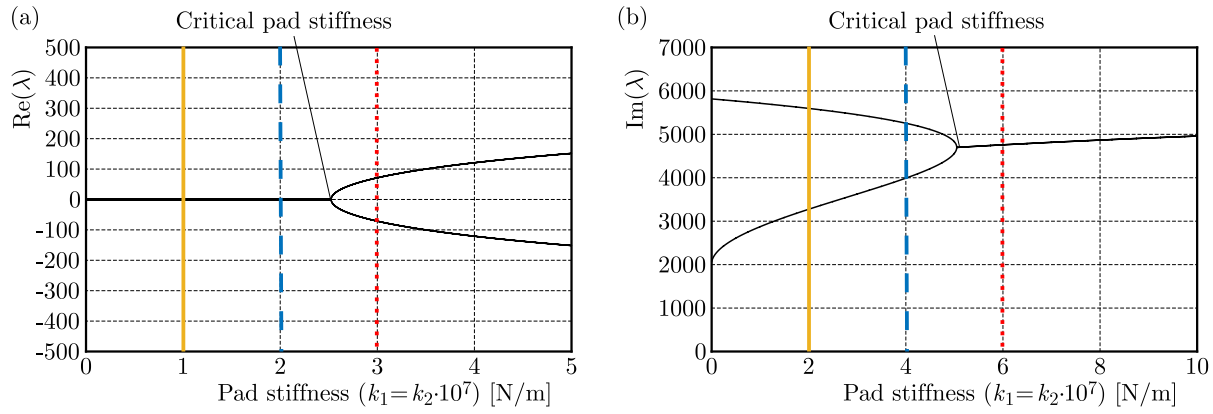

Fig. 5. Real and imaginary parts of the complex eigenvalues for $F = 50\,\mathrm{N}$ and $V = 1\,\mathrm{m/s}$: (a) Re(λ), (b) Im(λ)

As evident from Figs. 5-8, the system exhibits mode coupling behavior, i.e., the imaginary parts of the eigenvalues are coupled for one specific value of brake pad stiffness, which is called the critical pad stiffness k_{cr}, and the real part of one eigenvalue becomes positive. This dynamic behavior triggers the squeal phenomenon. Figure 5 shows the real and imaginary parts of the complex eigenvalues for $F = 50\,\mathrm{N}$ and $V = 1\,\mathrm{m/s}$. As seen in Figs. 5a and 5b, the system exhibits two purely imaginary eigenvalues up to $k_1 = k_2 = 5.16 \cdot 10^7\,\mathrm{N/m}$. Thus, $k_{cr} = 5.16 \cdot 10^7\,\mathrm{N/m}$, and the vibration modes occur at two distinct frequencies. At the point, when $k_1 = k_2 = 5.16 \cdot 10^7\,\mathrm{N/m}$, the vibration modes get coupled, and the real part of one of the eigenvalues becomes positive. Hence the system switches to an unstable state. In the second analysis depicted in Fig. 6, the value of belt velocity is increased to $V = 4\,\mathrm{m/s}$ while keeping F intact. Similarly,

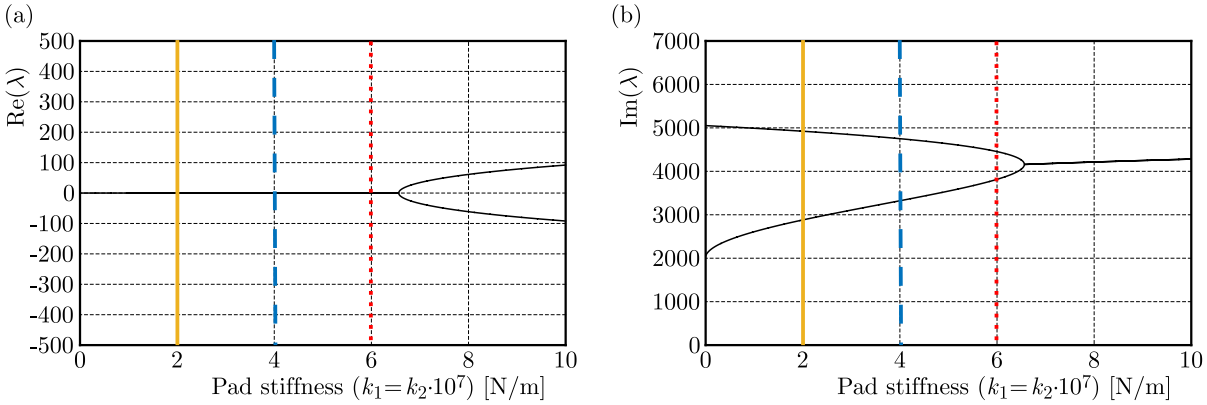

Fig. 6. Real and imaginary parts of the complex eigenvalues for $F = 50\,\mathrm{N}$ and $V = 4\,\mathrm{m/s}$: (a) Re(λ), (b) Im(λ)

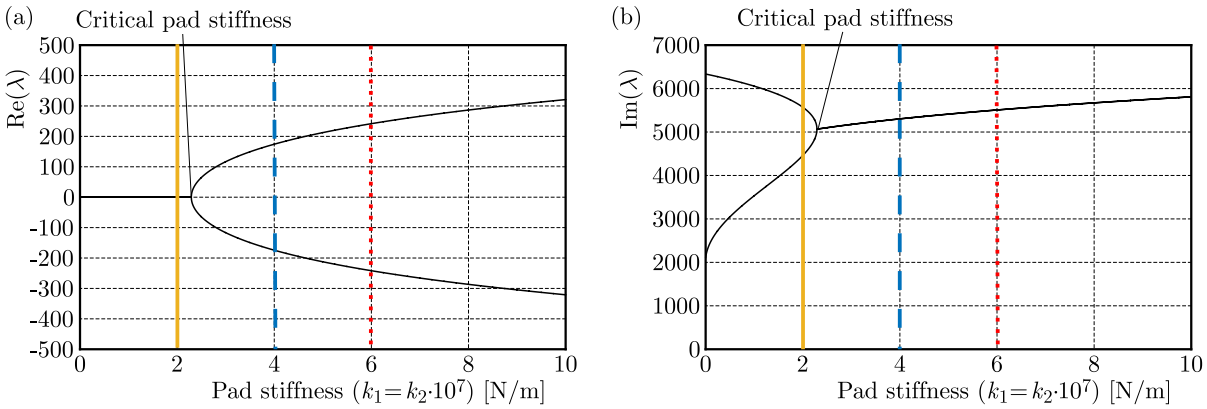

Fig. 7. Real and imaginary parts of the complex eigenvalues for $F = 200\,\mathrm{N}$ and $V = 1\,\mathrm{m/s}$: (a) Re(λ), (b) Im(λ)

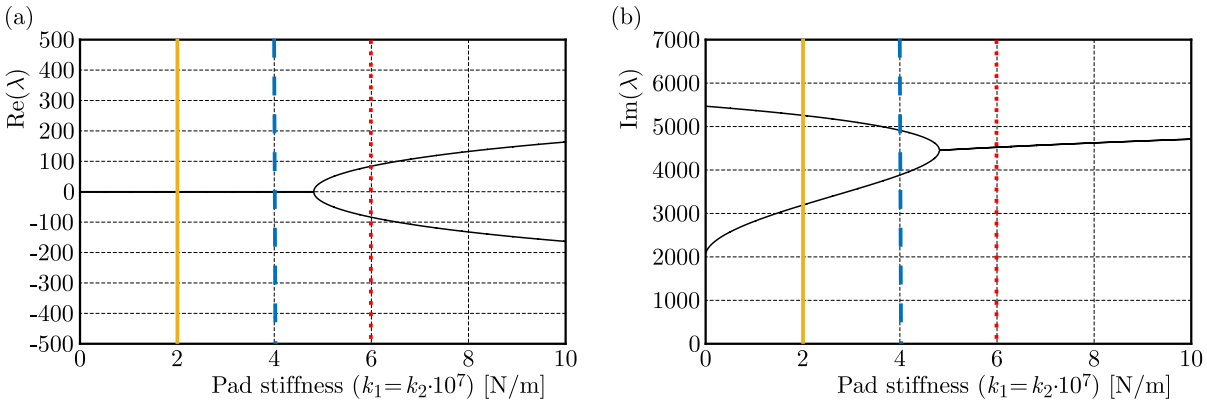

Fig. 8. Real and imaginary parts of the complex eigenvalues for $F = 200\,\mathrm{N}$ and $V = 4\,\mathrm{m/s}$: (a) Re(λ), (b) Im(λ)

the mode coupling behavior is again observed though for a higher k_{cr}, which is $6.71 \cdot 10^7\,\mathrm{N/m}$. The next analysis is run at $F = 200\,\mathrm{N}$ and $V = 1\,\mathrm{m/s}$ (Fig. 7), and it is seen that the value of k_{cr} is reduced to $2.10 \cdot 10^7\,\mathrm{N/m}$. Thus, the system is stable for the case shown with the yellow dashed line, but it performs unstable dynamics for the cases represented with blue and red dashed lines. In the last analysis (Fig. 8), which is run at $F = 200\,\mathrm{N}$ and $V = 4\,\mathrm{m/s}$ operating conditions, k_{cr} is increased to $4.97 \cdot 10^7\,\mathrm{N/m}$. Therefore, it is concluded that the increase of the preload extends the unstable regime, i.e., an increase in the preload leads to reduction in k_{cr}. On the

contrary, an increase at a given disc velocity reduces the unstable regime by increasing the value of k_{cr}.

In the next analysis, the effect of preload F on k_{cr} is investigated at two different disc velocities, and the change of k_{cr} with respect to F is depicted in Fig. 9. As seen in figures, the value of k_{cr} decreases with an increase of the preload. Furthermore, the area below the k_{cr} curves represent a stable region, and the area above the k_{cr} curves are the regions of instability. Though, at a given preload value, the critical pad stiffness value is increased with an increase of the disc velocity. Furthermore, observe the three vertical lines (solid yellow, dashed blue and dotted red) in Fig. 9, which correspond to $k_1 = k_2 = 2 \cdot 10^7\,\mathrm{N/m}$, $k_1 = k_2 = 4 \cdot 10^7\,\mathrm{N/m}$ and $k_1 = k_2 = 6 \cdot 10^7\,\mathrm{N/m}$, respectively. For the case of $V = 1\,\mathrm{m/s}$ (Fig. 9a), the preload values, where the stable/unstable regime transitions occur, are found to be 248 N, 79 N and 27 N. Note that the system is in an unstable regime when the preload is higher than the preload value where the transition occurs. Thus, for $F = 50\,\mathrm{N}$, the system exhibits unstable dynamics only for $k_1 = k_2 = 6 \cdot 10^7\,\mathrm{N/m}$. Though, the unstable dynamic behavior is observed for $k_1 = k_2 = 4 \cdot 10^7\,\mathrm{N/m}$ and $k_1 = k_2 = 6 \cdot 10^7\,\mathrm{N/m}$ when the preload is $F = 200\,\mathrm{N}$. This is also evident from vertical lines depicted in Figs. 5 and 7. For an other disc velocity $V = 4\,\mathrm{m/s}$, it is seen in Fig. 9b that unstable dynamic behavior is observed only for $k_1 = k_2 = 6 \cdot 10^7\,\mathrm{N/m}$ when the preload is greater than 128 N. Thus, for $F = 50\,\mathrm{N}$, the system is always in a stable state for the given k_1 and k_2 values. Though, when $F = 200\,\mathrm{N}$, unstable dynamic behavior is now observed. This claim is also observed from the vertical lines in Figs. 6 and 8.

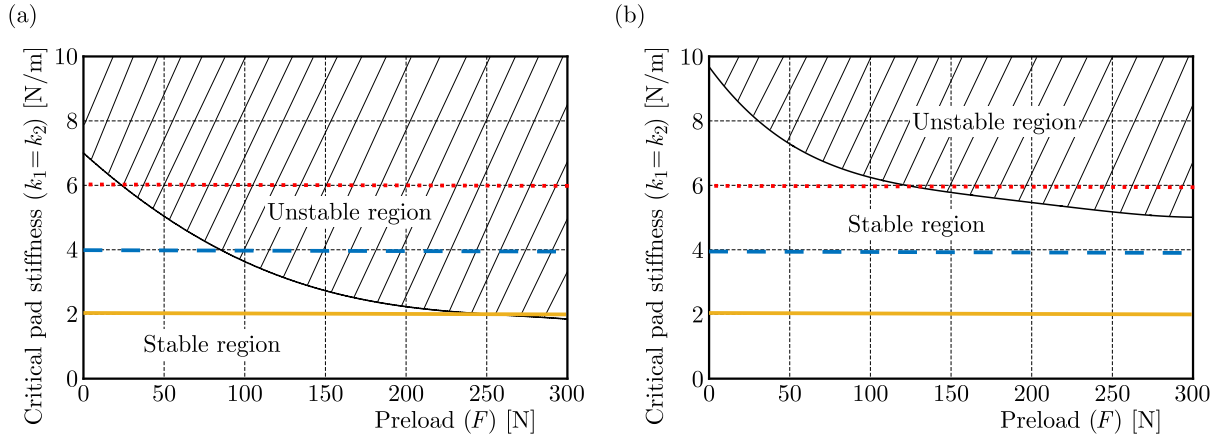

Fig. 9. The effect of preload on the critical pad stiffness: (a) $V = 1\,\mathrm{m/s}$, (b) $V = 4\,\mathrm{m/s}$

5. Numerical solution of nonlinear governing equations

In order to assess the results of linear stability analysis, the nonlinear governing equations are solved numerically with the 4th order explicit Runge-Kutta technique, and the responses in the time domain are obtained for the same operating conditions. Furthermore, the time domain responses are transformed to the frequency domain in order to assess the existence of nonlinearities. The time domain results are obtained for the three pad stiffness values of the prior analysis of Figs. 5-8, i.e., $k_1 = k_2 = 2 \cdot 10^7\,\mathrm{N/m}$, $k_1 = k_2 = 4 \cdot 10^7\,\mathrm{N/m}$ and $k_1 = k_2 = 6 \cdot 10^7\,\mathrm{N/m}$. Furthermore, the numerical results are obtained for the two preload levels, i.e., $F = 50\,\mathrm{N}$ and $F = 200\,\mathrm{N}$. The frequency spectra for these cases are shown in Figs. 10a and 10b, respectively. Note that the existence of super-harmonic peaks in the spectra are attributed to the significant contribution of nonlinearities, at which the squeal behavior is expected to occur. As seen from the spectra of Fig. 10a, the super-harmonic peaks arise only for the pad stiffness of $k_1 = k_2 = 6 \cdot 10^7\,\mathrm{N/m}$. Thus, it is claimed that it is highly possible to observe squeal behavior in

this particular case. Note that these two cases are also found to be the unstable cases in Figs. 5 and 9a. Increasing the preload to 200 N (Fig. 10b) makes the super-harmonic peaks emerge also for $k_1 = k_2 = 4 \cdot 10^7$ N/m. Thus, $k_1 = k_2 = 4 \cdot 10^7$ N/m case also now becomes a candidate at which the squeal occurrence is highly possible. Observe that these results are again coherent with the results of linear stability analysis depicted in Figs. 7 and 9a. Therefore, it is seen that similar dynamic behavior is observed with both stability analysis of the linearized model and numerical solutions of the nonlinear governing equations.

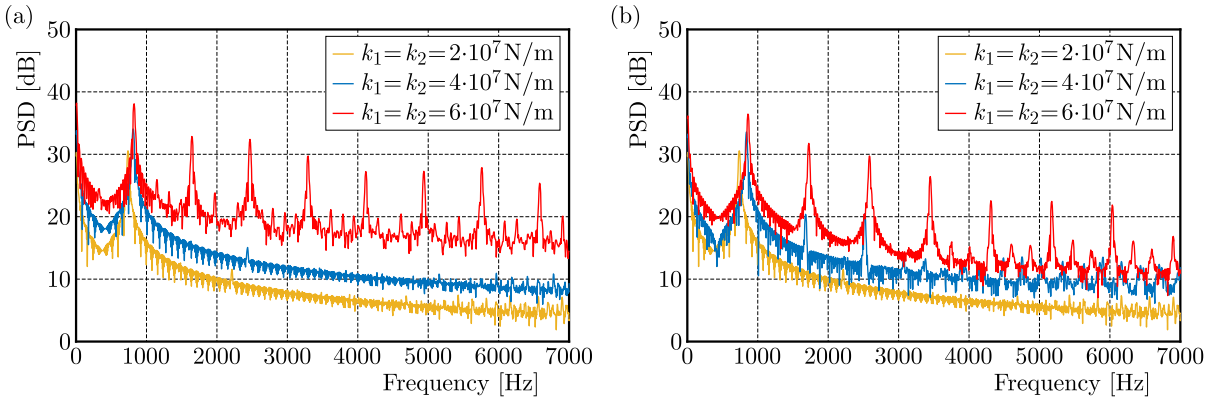

Fig. 10. Frequency spectra obtained from the numerical solutions of nonlinear governing equations for $V = 1$ m/s: (a) $F = 50$ N, (b) $F = 200$ N

Note that the linear stability analysis is based on the assumption of perpetual contact between the pad and disc surfaces. Though, the nonlinear governing equations consider the surface separation effect. In order to understand the effect of this simplification on the performance of linear stability analysis, squeal frequencies are obtained with both approaches for different pad stiffness values, and they are tabulated in Table 1. Here, the analysis is carried out for $F = 300$ N in order to guarantee squeal occurrence.

Table 1. Comparison of linear and nonlinear model results in terms of the squeal frequency ($V = 1$ m/s and $F = 300$ N)

Pad stiffness $k_1 = k_2$ [N/m]	Squeal frequency [Hz]		Error [%]	Contact loss duration [s]
	Nonlinear model	Linear model		
$2 \cdot 10^7$	964	958	0.62	0
$4 \cdot 10^7$	1095	1083	1.09	2.17
$6 \cdot 10^7$	1148	1119	2.52	3.02
$8 \cdot 10^7$	1302	1241	4.68	3.97
$10 \cdot 10^7$	1682	1538	8.56	5.79

Errors listed in Table 1 are the absolute percentage errors of squeal frequencies obtained via linear stability analysis with respect to the nonlinear model. Furthermore, the contact loss durations, which are calculated from the numerical solutions of the nonlinear governing equations, are also given in the table. Observe that the deviation between squeal frequencies increases as the value of pad stiffness increases; the same trend is also observed for the contact loss duration, which was also claimed by Aronov *et al.* (1984) based on their experimental studies. Hence, it is concluded that the performance of linear stability analysis worsens as the nonlinear effects (i.e., surface separation) dominate the dynamics of the system.

The numerically calculated time domain responses of the interfacial contact force between the brake pad and brake disc from the nonlinear model are depicted in Fig. 11 for two levels of pad stiffness. In the first case (Fig. 11a), where a smaller pad stiffness is assumed

($k_1 = k_2 = 2 \cdot 10^7$ N/m), the contact force is found to be always greater than zero. Hence, a perpetual contact is obtained at the contact interface, and the error on the predicted squeal frequencies is minimal as seen in Table 1. In the second case, the pad stiffness is set to a higher level ($k_1 = k_2 = 10 \cdot 10^7$ N/m), and it is observed that the surface separation starts to occur at the contact interface as evident from the time instances where the contact force is zero (Fig. 11b). Consequently, the deviation between the predicted squeal frequencies increases.

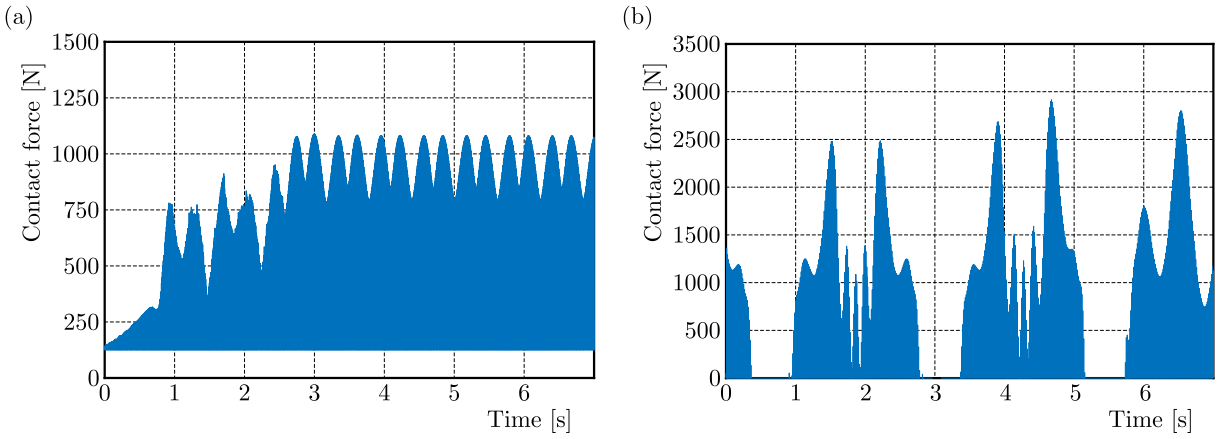

Fig. 11. Time domain results of the nonlinear model for $V = 1$ m/s and $F = 300$ N): (a) $k_1 = k_2 = 2 \cdot 10^7$ N/m, (b) $k_1 = k_2 = 10 \cdot 10^7$ N/m

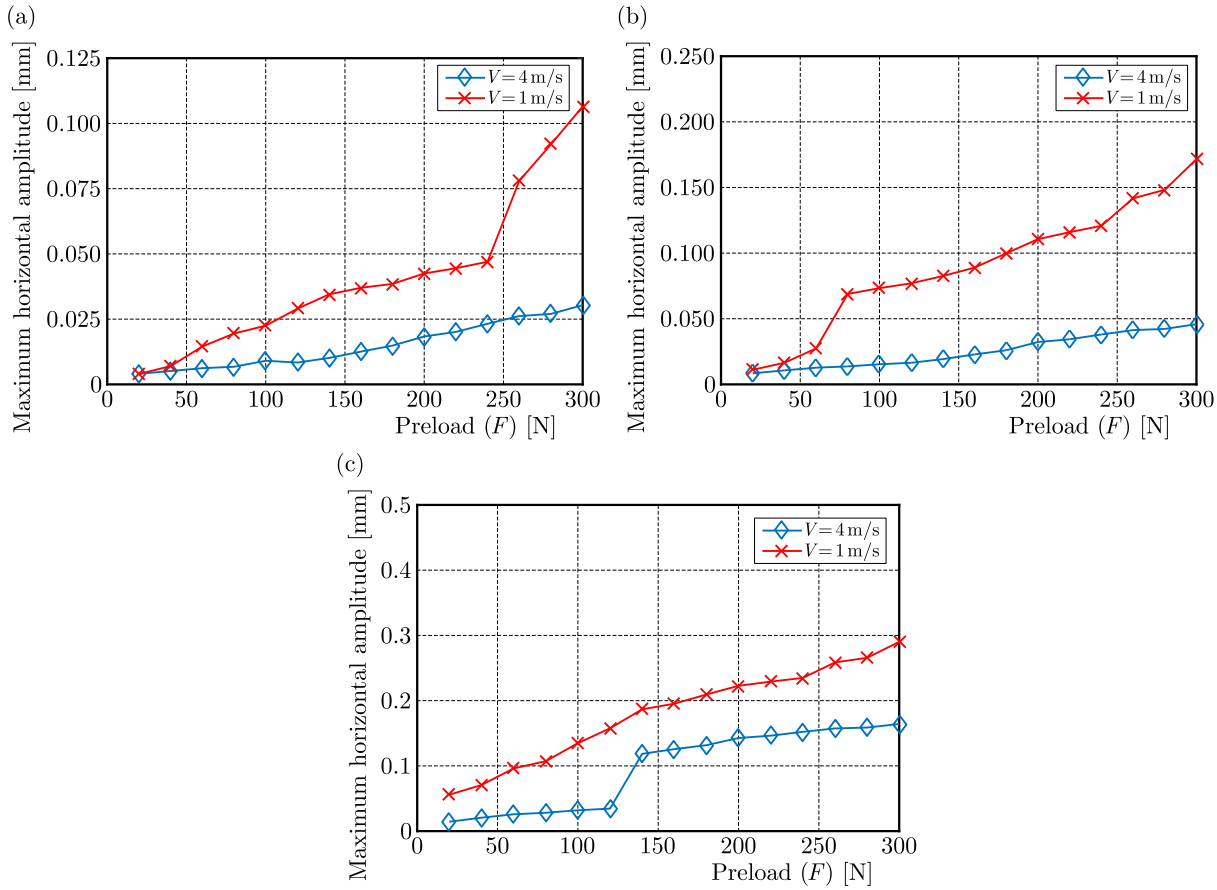

Fig. 12. Peak displacement amplitudes of the mass in x axis with respect to preload at different belt velocities: (a) $k_1 = k_2 = 2 \cdot 10^7$ N/m, (b) $k_1 = k_2 = 4 \cdot 10^7$ N/m, (c) $k_1 = k_2 = 6 \cdot 10^7$ N/m

In another analysis, numerical solutions are obtained at different preload levels for the same pad stiffness values of prior analyses. Furthermore, the results are obtained at two different levels of the disc velocity. The peak displacement amplitudes are gathered and scattered in Fig. 12. In the first case where $k_1 = k_2 = 2 \cdot 10^7\,\mathrm{N/m}$ (Fig. 12a), it is seen that the peak displacement amplitudes gradually increase for $V = 4\,\mathrm{m/s}$. Though, a sudden increase is observed around $F = 250\,\mathrm{N}$ at $V = 1\,\mathrm{m/s}$. Comparing this result with Fig. 9a, it is seen that $F = 250\,\mathrm{N}$ is at the vicinity of where the transition from the stable to unstable regime occurs. Similar results are also observed for the case of $k_1 = k_2 = 4 \cdot 10^7\,\mathrm{N/m}$ (Fig. 12b). Though, now a sudden increase in the displacement amplitude occurs around $F = 80\,\mathrm{N}$ for $V = 1\,\mathrm{m/s}$. Note that the stable to unstable regime transition occurs at $F = 79\,\mathrm{N}$ (Fig. 9a). Furthermore, the displacement amplitudes gradually increase for $V = 4\,\mathrm{m/s}$. These results are again in accordance with the results of the linear stability analysis of Fig. 9b. In the last case, where $k_1 = k_2 = 6 \cdot 10^7\,\mathrm{N/m}$ (Fig. 12c), the peak displacement amplitudes now gradually increase only for $V = 1\,\mathrm{m/s}$, while a sudden amplitude jump occurs around $F = 130\,\mathrm{N}$ for $V = 4\,\mathrm{m/s}$. As seen in Fig. 9b, this pad stiffness value is the only one where unstable dynamic behavior is observed when the preload level is greater than 128 N, and this value is close to the preload level where the jump occurs in Fig. 12c.

6. Conclusion

In this study, a nonlinear two degree of freedom mathematical model is developed for investigation of the brake squeal phenomenon with emphasis put on the brake pad stiffness. The nonlinear governing equations are linearized with further assumptions, and stability of the system is investigated by complex eigenvalue analysis. Furthermore, friction characteristics at the pad/disc contact interface are defined with a friction model derived through data obtained experimentally. Hence, the effect of pad stiffness on stability of the system is investigated for different preloads and belt velocities. Finally, the nonlinear governing equations are numerically solved for all operating conditions, and the results are compared to the linear stability analysis. Furthermore, the linear stability analysis of the predicted squeal frequencies are compared with the numerical solutions of nonlinear governing equations. Some of the major findings of this study are listed below:

- Mode coupling is found to be a significant mechanism that triggers unstable dynamic behavior and leads to the brake squeal phenomenon.
- An increase in the preload level leads to reduction of the critical pad stiffness for all disc velocities. Thus, it is concluded that the pad stiffness should be reduced at high preload conditions in order to guarantee stable dynamic behavior.
- An increase in the belt velocity leads to an increase of the critical pad stiffness for the same preload condition. Hence, the unstable region is found to be contracted as the disc velocity increases.
- The squeal frequencies obtained via linear stability analysis and from numerically calculated time histories of nonlinear governing equations are found to be similar.
- The frequency spectra calculated from time histories of the nonlinear governing equations exhibit super-harmonic peaks in the cases which are found to be unstable through linear stability analysis. Thus, it is shown that a similar dynamic response is obtained with both approaches, since the emergence of super-harmonic peaks is usually attributed to a nonlinear dynamic response.
- It is observed that the surface separation effects become significant at high pad stiffness levels.

- The predicted squeal frequencies from linear stability analysis start to deviate from the frequencies calculated from time histories of the nonlinear mathematical model as the surface separation effects become significant.
- The peak displacement amplitudes calculated numerically from the nonlinear governing equations exhibit a sudden jump at the boundaries of stable to unstable regime transition, which is attributed to the high amplitude oscillation behavior of the squeal response.

In conclusion, it is seen that the linear stability analysis successfully predicts the dynamic behavior of the system. Though the estimation of the squeal frequency may exhibit slight errors based on the strength of nonlinearity.

This study can be expanded by validating the major findings with experimentation. For example, experiments can be conducted at high pad stiffness levels, and the response of the system can be investigated experimentally. This requires the following slight modifications of the current experiment: 1) Two extra telescopic arms on both sides of the mass should be added in the experiment in order to mimic the developed mathematical model; and 2) Experiments at which different levels of spring stiffness are utilized should be performed. Though, in the current study an experimental validation is out of the scope. Thus, this validation remains as a future work.

References

1. Aronov V., D'Souza A.F., Kalpakjian S., Shareef I., 1984, Interactions among friction, wear, and system stiffness – Part 1: Effect of normal load and system stiffness, *Journal of Tribology*, **106**, 54-59
2. Belhocine A., Ghazaly N.M., 2016, Effects of Young's modulus on disc brake squeal using finite element analysis, *International Journal of Acoustics and Vibration*, **21**, 3, 292-300
3. Dakel M., Sinou J.J., 2017, Stability and nonlinear self-excited friction-induced vibrations for a minimal model subjected to multiple coalescence patterns, *Journal of Vibroengineering*, **19**, 1, 604-628
4. Ghorbel A., Zghal B., Abdennadher M., Walha L., Haddar M., 2020, Investigation of friction-induced vibration in a disk brake model, including mode-coupling and gyroscopic mechanisms, *Proceedings of the Institution of Mechanical Engineers, Part D: Journal of Automobile Engineering*, **234**, 2-3, 887-896
5. Hochlenert D., 2009, Nonlinear stability analysis of a disc brake model, *Nonlinear Dynamics*, **58**, 63-73
6. Hoffman N., Fischer M., Allgaier R., Gaul L., 2002, A minimal model for studying properties of the mode-coupling type instability in friction induced oscillations, *Mechanics Research Communications*, **29**, 4, 197-205
7. Jacobsson H., 2003, Aspects of disc brake judder, *Proceedings of the Institution of Mechanical Engineers, Part D: Journal of Automobile Engineering*, **217**, 6, 419-430
8. Li Z., Ouyang H., Guan Z., 2016, Nonlinear friction-induced vibration of a slider-belt system, *Journal of Vibration and Acoustics (ASME)*, **138**, 4, 041006
9. Liu N., Ouyang H., 2020, Friction-induced vibration considering multiple types of nonlinearities, *Nonlinear Dynamics*, **102**, 20572075
10. Kang J., 2018, Lyapunov exponent of friction-induced vibration under smooth friction curve, *Journal of Mechanical Science and Technology*, **32**, 8, 3563-3567
11. Kinkaid N.M., O'Reilly O.M., Papadopoulos P., 2003, Automotive disc brake squeal, *Journal of Sound and Vibration*, **267**, 105-166

12. Oberst S., Lai J.C.S., Marburg S., 2013, Guidelines for numerical vibration and acoustic analysis of disc brake squeal using simple models of brake systems, *Journal of Sound and Vibration*, **332**, 2284-2299

13. Papinniemi A., Lai J.C.S., Zhao J.Y., Loader L., 2002, Brake squeal: A literature review, *Applied Acoustics*, **63**, 391-400

14. Sawczuk W., Cañás A.M.R., Ulbrich D., Kowalczyk J., 2021a, Modeling the average and instantaneous friction coefficient of a disc brake on the basis of bench tests, *Materials*, **14**, 16, 4766

15. Sawczuk W., Ulbrich D., Kowalczyk J., Merkisz-Guranowska A., 2021b, Evaluation of wear of disc brake friction linings and the variability of the friction coefficient on the basis of vibroacoustic signals, *Sensors*, **21**, 17, 5917

16. Sen O.T., Singh R., 2021, Dynamics of a simplified nonlinear model offering insights into the hammering type brake squeal initiation process, *Noise Control Engineering Journal*, **69**, 3, 243-261

17. Sinou J.J., 2010, Transient non-linear dynamic analysis of automotive disc brake squeal – On the need to consider both stability and nonlinear analysis, *Mechanics Research Communications*, **37**, 96-105

18. Stojanovic N., Belhocine A., Abdullah O.I., Grujic I., 2022, The influence of the brake pad construction on noise formation, people's health and reduction measures, *Environmental Science and Pollution Research*, 1-12

19. Wang H., Liu X., Shan Y., He T., 2014, Nonlinear behavior evolution and squeal analysis of disc brake based on different friction models, *Journal of Vibroengineering*, **16**, 5, 2593-2609

20. Zhang Z., Oberst S., Lai J.C.S., 2016, On the potential of uncertainty analysis for prediction of brake squeal propensity, *Journal of Sound and Vibration*, **377**, 123-132

Manuscript received October 24, 2022; accepted for print December 12, 2022

JOURNAL OF THEORETICAL AND APPLIED MECHANICS
61, 2, pp. 233-244, Warsaw 2023
https://doi.org/10.15632/jtam-pl/160063

NUMERICAL STUDY ON COMPRESSION PROPERTIES OF SEMI-REENTRANT FILLED TUBULAR STRUCTURES

Dongquan Wu, Dinghe Li

Sino-European Institute of Aviation Engineering, Civil Aviation University of China, Tianjin, China

Corresponding author Dongquan Wu, e-mail: dqwu@cauc.edu.cn

Zhiqiang Zhang

Institute of Aviation Engineering, Civil Aviation University of China, Tianjin, China

Jiacheng Chen

The 18th Research Institute, China Electonics Technology Group Corporation, China

In this study, a semi-reentrant structure (SR) filled with different tubular structures, including tube, triangular and rectangle structures were designed. The tubular structures were perfectly assembled into semi-reentrant cells to avoid swaying in the semi-reentrant cell. The geometric relations and relative density for these structures were established. For the out-of-plane and in-plane compressions, SR filled tubular structures exhibited different deformation patterns compared to those of SR or pure fillers. A constraint effect was found between the filler tubular and container SR. With fillers contained inside the SR structures, the plateau stresses for three conditions were all promoted compared to those of SR. The best out-of-plane compression resistance occurred in the SR filled rectangle which might be caused by larger interaction areas between the SR and rectangular structures. The (specific) energy absorption of the SR filled tube compressed out-of-plane was the largest. The peak and plateau stress of the SR filled triangle was the largest compared to other structures when compressed in plane due to stability of the triangle. It was found that the plateau stress, energy absorption and specific energy absorption of SR filled triangle was the largest, while that of SR filled rectangle was the lowest.

Keywords: semi-reentrant (SR) structure, tubular fillers, out-of-plane, in-plane compression

1. Introduction

Skeletal or cellular structures with lightweight advantages, such as honeycomb with a positive Poisson's ratio, have been widely applied in the industry because of its outperformed mechanical properties and the perfect weight-to-cost ratio (Lu and Yu, 2003). Different from hexagonal honeycomb structures, auxetic structures with negative Poisson's ratios (Wang *et al.*, 2018b), such as Reentrant structures, exhibit synclastic curvature (Sevtsuk and Kalvo, 2014) and many superior mechanical properties (Wang *et al.*, 2018b). Another semi-reentrant structures are hybrids of hexagonal Honeycomb cells and Reentrant cells (see Fig. 1). A semi-reentrant structure exhibits zero Poisson's ratio in one in-plane direction and a higher elastic modulus in the other direction. It shows monoclastic surfaces (Davini *et al.*, 2017) when bending out-of-plane, thus it is suitable for applications with cylindrical shapes (Grima *et al.*, 2010). A lot of studies have focused on mechanical properties of these basic skeletal structures (Dong *et al.*, 2019). They have been used to develop components with better properties in the aerospace or automotive industries (Novak *et al.*, 2016). Although these structures have many advantages in applications, as lightweight, with good impact resistance or other properties, there is still an increasing requirement for a more superior enhancement in mechanical properties, especially about safety in the

aerospace or automotive industries. For safety reasons, in aerospace or automotive applications the large impact energy is always unwelcome and needs to be minimized or even dissipated, and crashworthiness is one of the most important properties to characterize this phenomenon. To achieve this purpose, many investigations have been conducted to create new geometrical configurations with excellent energy absorption capacity based on a honeycomb-shaped structure (Wang and Liu, 2019). It is widely known that the energy absorption of honeycomb structures depends on the non-linear plastic collapse of a unit cell with a thin wall (Wang and Liu, 2019). Hence, promoting energy absorption capacity of the unit cell could be effective in improving the energy absorption of the whole structure. For this aim, researchers have tried to fill foam materials into the spare space of honeycomb structures (Qin *et al.*, 2018) or used a double sidewall configuration. The latter method consists in filling skeletal structures into the unit cell (Wang and Liu, 2019).

Many investigations have been focused on filling foam materials into the spare space of outside container structures. The filled foam materials generally include polyurethane-foam (Yan *et al.*, 2014) or polyurethane closed-cell foam (Palanivelu *et al.*, 2010). Besides, glass/polyester composite, aluminum, lattice composite and CFRP tubes (Hussein *et al.*, 2018) have been used as the outside container materials. For geometrical configurations of the container structures, most are about tubular structures, such as thin-walled squares, circular/cylindrical, conical or hat sections tubes, and honeycomb or reentrant structures (Wang *et al.*, 2019) as well as grooved, tapered multi-cells (Wang *et al.*, 2018a). By filling foam materials into the container structure, the energy absorption ability of the structure would be substantially enlarged (Wang and Liu, 2019). However, there are still some disadvantages for filling foam materials into tubular structures, for example, to improve energy absorption, the structure should be fabricated into a long strip shape which may cause a waste of the structural space, cause an obvious increase of the structure weight and promote buckling rather than gradual folding deformation.

Therefore, to mostly utilize the hollow space of skeletal cells and to dissipate more plastic energy, filling skeletal structures into the unit cell has been proposed without sacrifice to the stability of the crash force or being lightweight. By now, there are some studies (Wang, 2019) about honeycomb filled skeletal structures. Al Antali *et al.* (2017) studied the influence of CFRP tubular-array density on specific energy absorption and characterized the dynamic response of the honeycomb core containing CFRP tubes and the rate-sensitivity. The advantages like simple preparation process and cost-effective energy absorption in dynamic applications were found. Sun *et al.* (2016) found that by incorporating an aluminium honeycomb into circular CFRP tubes, the composite structure outperformed pure aluminium honeycomb at quasi-static rates of strain, but its specific energy absorption would slightly decrease compared to the pure CFRP tubes. By filling aluminum honeycomb into square CFRP tubes, Hussein *et al.* (2016) also drew a similar conclusion after conducting experiments for a wide range of strain rates. Wang *et al.* (2019) and Wang and Liu (2019) studied out-of-plane compression performances of honeycomb cells filled with circular aluminum tubes (Wang and Liu, 2019) or CFRP tubes (Wang and Liu, 2018) (HFCT), and investigated the influence of tube fillers on deformation modes, energy absorption and interaction effects between the internal and outside container. Liu *et al.* (2018) also investigated the blast resistance performances of a sandwich panel filled with HFCT core, in which a considerable mass efficiency improvement concerning deflection resistance could be obtained.

In this study, a semi-reentrant structure filled with different skeletal structures, including tube, triangular and rectangular tubular structures were designed. To ensure the skeletal tube to be perfectly assembled into semi-reentrant cells and to avoid the oblique loadings or swaying of the skeletal tube in the semi-reentrant cell, the geometric relations of these structures were accurately calculated, and their relative density was also established. The out-of-plane and in--plane compression in two directions of these structures were investigated and compared. The

deformation mechanisms, stress against strain variations, plateau stress, densification strain and (specific) energy absorption were characterized and analyzed.

Table 1. Summary of geometrical details of different structures

Structures	Geometrical illustration	Parameters	Relative density ρ_c/ρ_A
Semi-reentrant (SR)	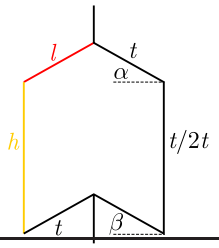	l – inclined arm length h – vertical arm length $t, 2t$ – cell wall thickness d – thickness of structure α, β – angles between arms $t = 0.08$ mm $\alpha = \beta = 30°$	$\dfrac{t\left(l + l\dfrac{\cos\alpha}{\cos\beta} + h\right)}{l\cos\alpha(l\sin\alpha + 2h - l\cos\alpha\tan\beta)}$
SR filled tube (SR-TU)	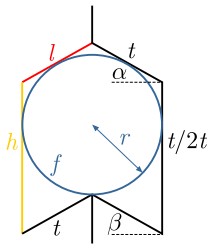	$r = 1$ mm – radius of circle f – cell wall thickness of filler $f = 0.008$ mm $l = \dfrac{r}{\cos\alpha} = \dfrac{2r}{\sqrt{3}}$ $h = \dfrac{r}{\cos\alpha} + r = \dfrac{2r}{\sqrt{3}} + r$	$\dfrac{t\left(l + l\dfrac{\cos\alpha}{\cos\beta} + h\right) + 2\pi r f}{l\cos\alpha(l\sin\alpha + 2h - l\cos\alpha\tan\beta)}$
SR filled triangle (SR-TR)	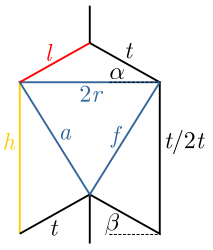	$2r = 2$ mm – length of edge 1 a – length of edge 2 and 3 $a = \sqrt{h^2 + l^2 - 2hl\cos\left(\dfrac{\pi}{2} - \beta\right)}$ $= r\sqrt{\dfrac{7 + 2\sqrt{3}}{3}}$	$\dfrac{t\left(l + l\dfrac{\cos\alpha}{\cos\beta} + h\right) + (2r + 2a)f}{l\cos\alpha(l\sin\alpha + 2h - l\cos\alpha\tan\beta)}$
SR filled rectangle (SR-RE)	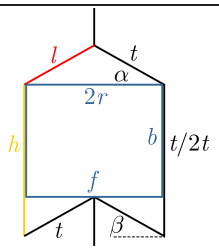	$2r = 2$ mm – length of edge 1 b – length of edge 3 $b = \sqrt{a^2 - r^2}$ $= r\sqrt{\dfrac{4 + 2\sqrt{3}}{3}}$	$\dfrac{t\left(l + l\dfrac{\cos\alpha}{\cos\beta} + h\right) + (4r + 2b)f}{l\cos\alpha(l\sin\alpha + 2h - l\cos\alpha\tan\beta)}$

2. Out of plane compression of semi-reentrant filled tubular structures

For compression simulation in Abaqus, width and height of the rigid compression walls are 25 mm and 25 mm, respectively, and thickness of the compression wall is 2 mm. A velocity of 50 mm/s is used to compress the structures. The cell wall thickness of SR is $t = 0.08$ mm, and the wall thickness of tubular fillers is $f = 0.008$ mm. In the simulation, the material properties of Al 3003 are used, as shown in Table 2, and the hardening of Al 3003 in quasi-static compression are considered as typical isotropic hardening, which is very commonly used for metal plasticity calculations, and it is simple and suitable for quasi-static compression conditions. Abaqus provides an isotropic hardening model that is useful for cases involving gross plastic straining or in cases where the straining at each point is essentially in the same direction in strain space throughout the analysis. The SR structures and filled structures are both built as shell models.

A specific velocity is applied in the reference point of the top grip, and the reference point of the bottom rigid grip is totally fixed. Two rigid grips are meshed with C3D8R solid elements, and the semi-reentrant structure are meshed by SR4 shell elements. The frictionless contact between the rigid grips and cell structures was introduced into Abaqus.

The stresses are calculated by the reaction forces F of the rigid grip section (S is the area of grip section, so stress is σ_1 or $\sigma_2 = F/S$). Strains $\varepsilon = U/d$ are computed from the displacements U of the top grip divided by thickness d of the structure (as shown in Fig. 1).

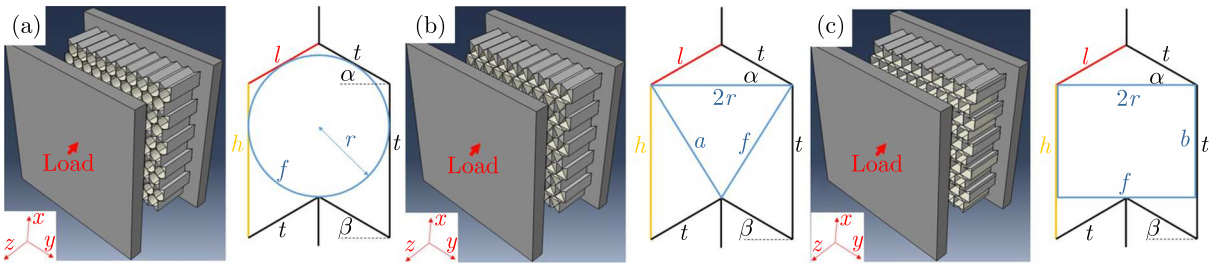

Fig. 1. Geometrical illustration of semi-reentrant structures filled with: (a) tube (SR-TU), (b) triangular (SR-TR), (c) rectangle (SR-RE) skeletal structures

Table 2. Mechanical properties of Al 3003

Materials	Elastic modulus [MPa]	Yield strength [MPa]	Ultimate strength [MPa]	Poison's ratio	Mass density ρ_A [kg/m^3]
Al 3003	70000	185	267	0.33	2700

2.1. SR filled tube structure

Figure 2 depicts deformation contours of SR, SR filled tube, SR filled triangle and SR filled rectangle compressed out-of-plane. For the SR structure, the deformation is focused on the central position in the out-of-plane direction. There is nearly no expansion in the in-plane direction of the cells. The SR filled tube exhibits a different deformation pattern compared to that of SR because the constraint effect is verified between the inner tube and the outer SR. With the influence of the filled tube, the SR filled tube deforms from the bottom section like the tube itself rather than from the middle side. And with the restriction of SR, the expansion of cells in the in-plane direction is not obvious. The SR filled triangle deforms from the top section, which is different from that of SR (deforms from the middle section), and there is an unobvious expansion of the cells in the in-plane direction due to the restriction of SR, and it could be observed that for the filled triangle, its collapse mode is compelled by the outside SR structure. The SR filled rectangle deforms both near the top and bottom sections, which is different from that of SR (deforms from middle section), and there is an unobvious expansion of the cells in the in-plane direction due to the restriction of SR, and a competitive collapse mode between the filled rectangle and outside SR is also observed.

Besides, it is concluded that the SR structure initially deforms from the middle section, and the SR filled tube deforms from the bottom side, the SR filled triangle deforms from topside, while the SR filled rectangle deforms both near the top and bottom sections, and there is no obvious expansion of the cells in the in-plane direction due to the restriction of SR.

Figure 3 compares the nominal stress versus strain curves for different structures. With fillers contained inside the SR structures, the plateau stresses for the three conditions are all promoted compared to those of SR. The plateau stress could be sorted as SR filled rectangle > SR filled tube > SR filled triangle > SR. Moreover, the densification strain could be ordered as: SR filled triangle > SR filled rectangle > SR filled tube > SR. A better compression resistance or larger plateau stress of the SR filled rectangle may be caused by larger interaction areas between the SR and rectangle structures, which will enhance the resistance of compressed deformation.

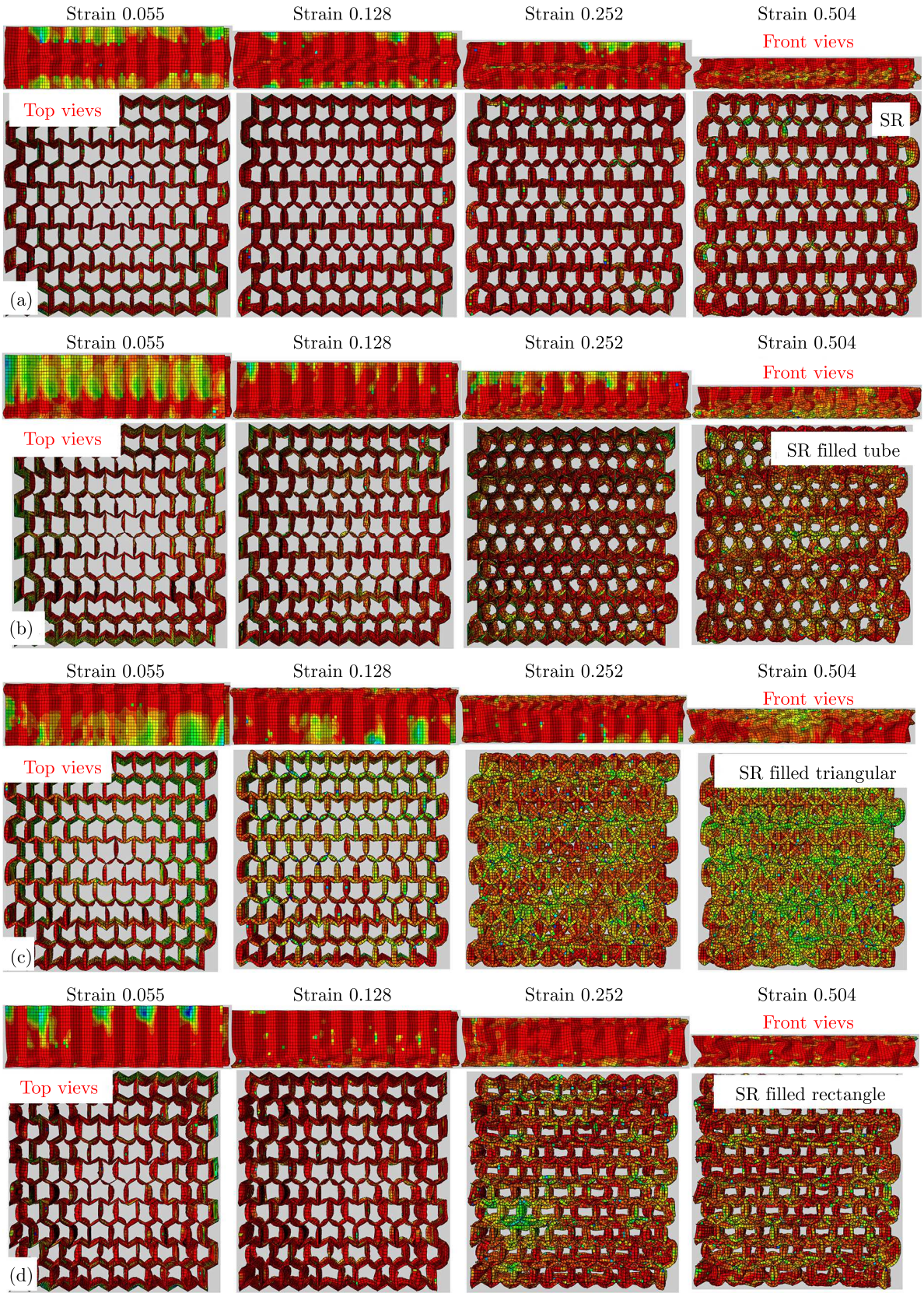

Fig. 2. Deformation contours of (a) SR, (b) SR-TU, (c) SR-TR, and (d) SR-RE

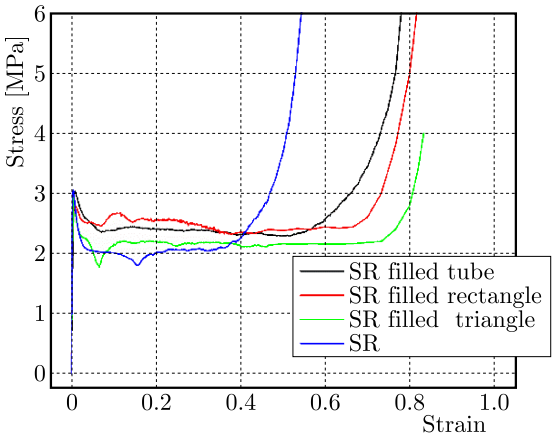

Fig. 3. Comparison of stress-strain curves among semi-reentrant structures with different fillers

Table 3 compares mechanical properties of SR filled different tubular structures. It is found that the energy absorption of SR filled tube is the largest, so is the specific energy absorption. The energy absorption and specific energy absorption have a similar order: SR filled tube > SR filled rectangle > SR filled triangular > SR.

Table 3. Mechanical properties of SR filled different tubular structures

	SR	SR-TU	SR-TR	SR-RE
Plateau stress σ_m [MPa]	2.06	2.43	2.4	2.5
Densification strain	0.54	0.866667	0.833333	0.833333
Energy absorption E [mJ]	1.1124	2.106	2	2.083333
Mass [Kg]	6.50E-04	7.31E-04	7.24E-04	7.24E-04
Specific energy absorption E_m [mJ/Kg]	1711.39	2880.99	2762.431	2877.53

3. In-plane compression of semi-reentrant filled tubular structures

For the in-plane compression of the structure, the rigid compression wall is similar to that for the out-of-plane compression. The structure is compressed along the x- or y-direction in the plane.

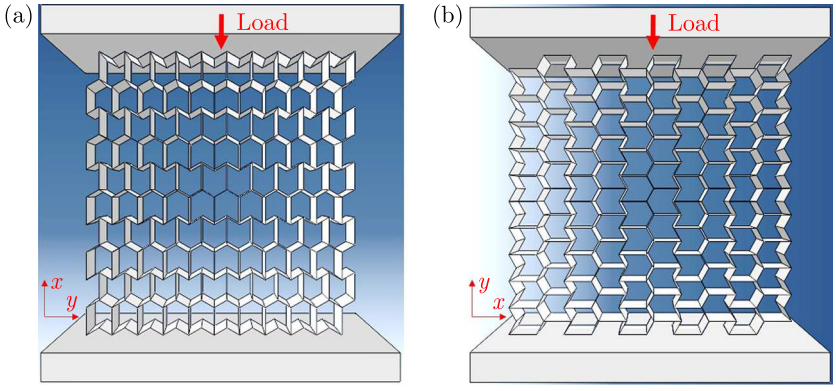

Fig. 4. Geometrical illustration of semi-reentrant structures compressed along x- or y-directions

The stresses are also calculated by the reaction forces F of the connection area between the rigid grip and structure S (so stress is σ_1 or $\sigma_2 = F/S$). Strains $\varepsilon = U/\text{width}$ are computed

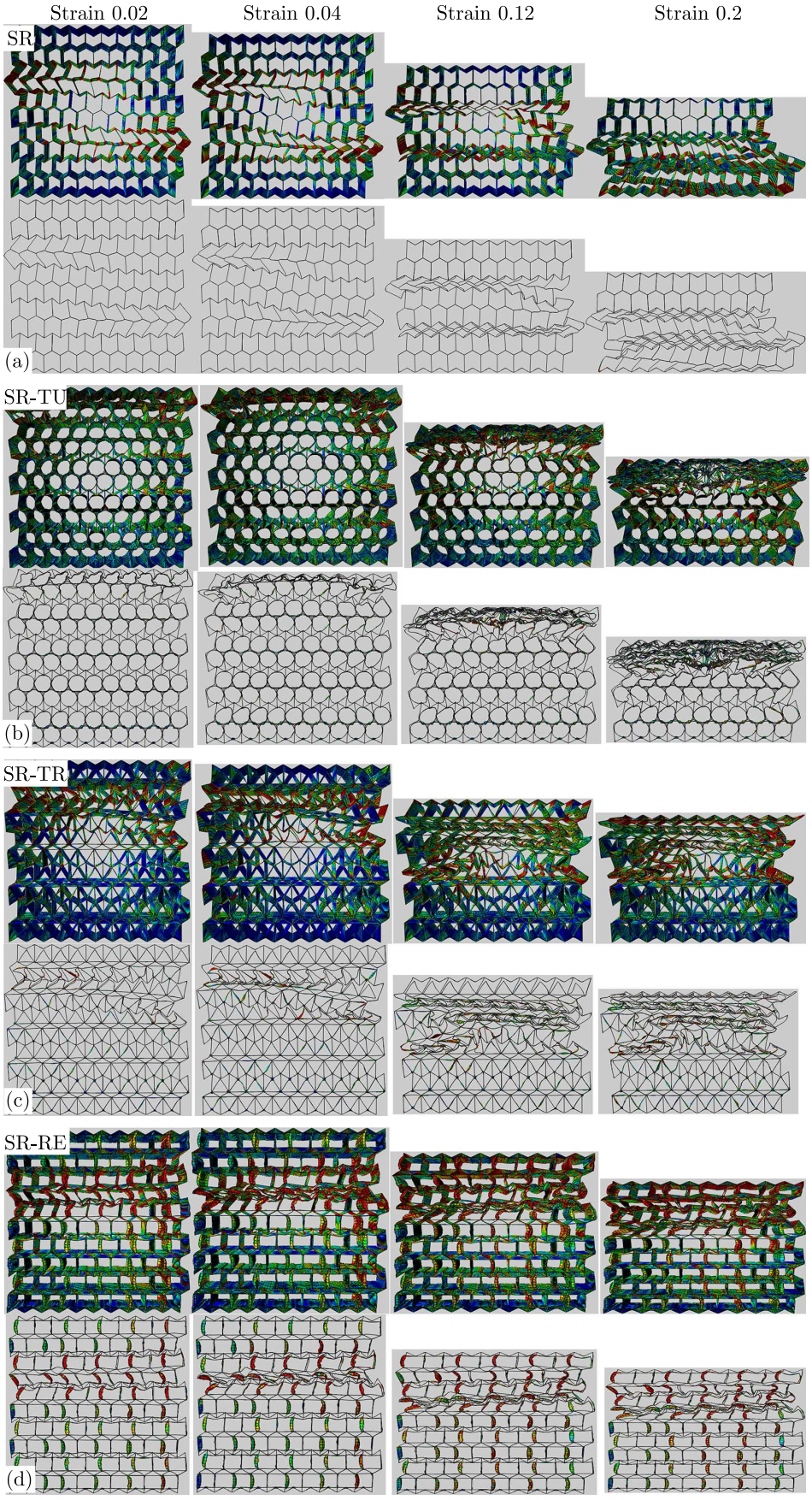

Fig. 5. Deformation contours of (a) SR, (b) SR-TU, (c) SR-TR and (d) SR-RE compressed in x-direction

from the displacements U of the top grip divided by width (compressed in x-direction) or height (compressed in y-direction) of structure (as shown in Fig. 4).

Figure 5 compares deformation contours for different structures compressed in the x-direction. For the SR structure, the deformation initially occurrs among the middle section, and with the compression distance increasing the middle and bottom sections fail and get stacked up together like a wave shape. The top section of SR keeps a good shape until the final deformation.

For the SR filled tube, the main deformation is accumulated on the top section layer by layer, and the bottom part keeps stable with few distortions. For the SR filled triangle, the major distortions are focused below the top layers, and the top layer shows a triangular shape in a long compression distance. Due to stability of the triangle, the bottom layers are very stable with nearly no deformation for the early compression process. In the SR filled rectangle, most of the deformation is located near the top layers, and the other layer is generally deformed into a rectangular shape as the compression process goes.

Figure 6 compares the nominal stress versus strain curves for different structures compressed in the x-direction. It could be found that SR with fillers will have a larger peak stress and plateau stress compared to those of the SR structures, especially for the SR filled triangle, which has better stability in the in-plane direction. The stability of the rectangular structure is also worse than that of the tube. Thus, the peak and plateau stress of these structures could be sorted as: SR-TR > SR-TU > SR-RE > SR.

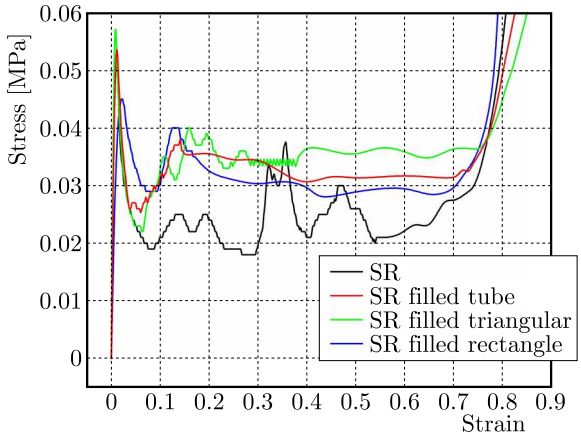

Fig. 6. Comparison of stress-strain curves among SR structures with different fillers in the x-direction

Table 4 compares the mechanical properties of SR filled different tubular structures when compressed in the x-direction. It is found that the plateau stress, energy absorption and specific energy absorption of the SR filled triangle are the largest, while these of SR filled rectangle are the lowest.

Table 4. Mechanical properties of SR filled different tubular structures compressed in x-direction

	SR	SR-TU	SR-TR	SR-RE
Plateau stress σ_m [MPa]	0.022	0.031	0.05	0.028
Densification strain	0.8	0.81	0.8	0.79
Energy absorption E [mJ]	0.0176	0.02511	0.04	0.02212
Mass [Kg]	6.50E-04	7.31E-04	7.24E-04	7.24E-04
Specific energy absorption E_m [mJ/Kg]	2.71E+01	3.44E+01	5.52E+01	3.06E+01

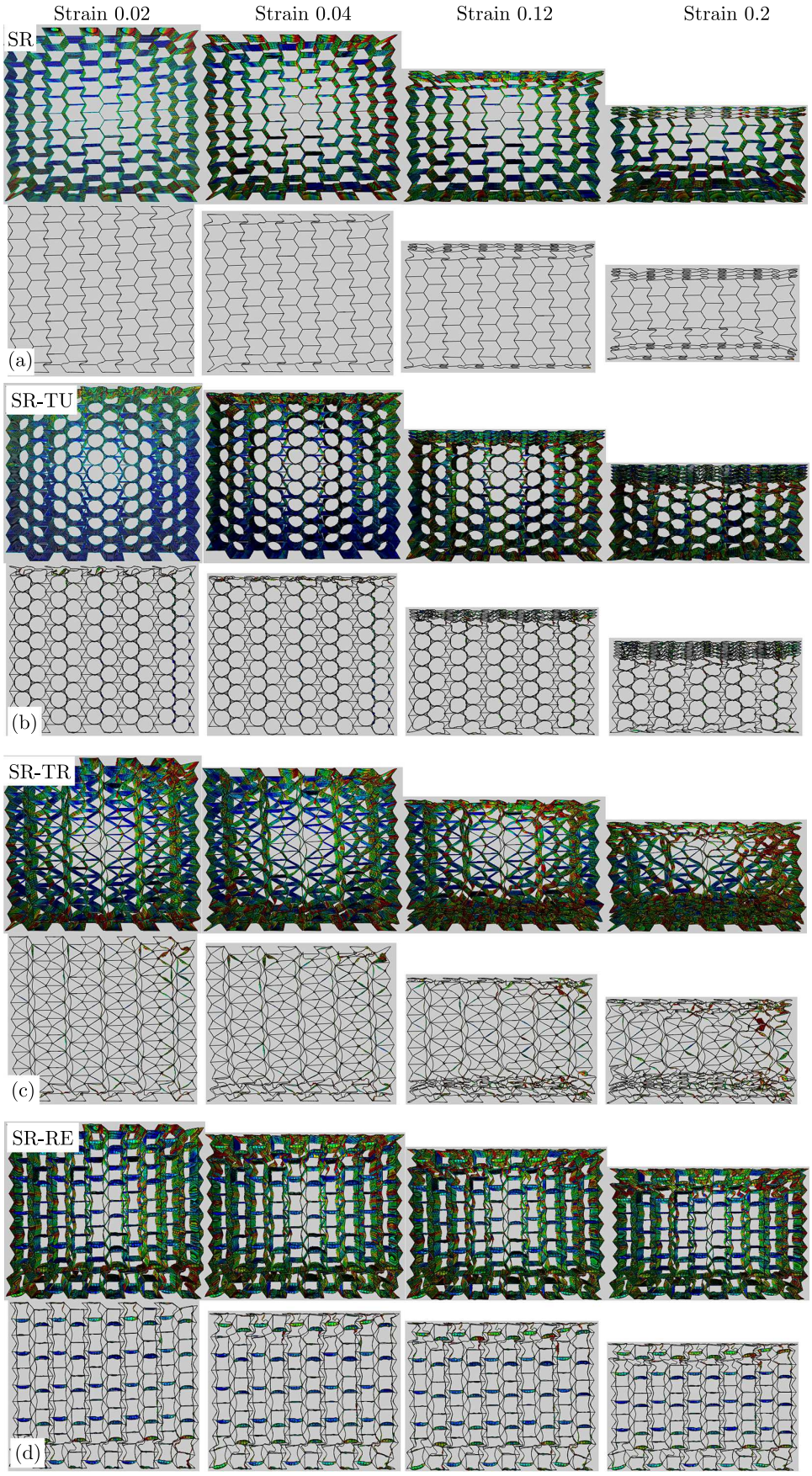

Fig. 7. Deformation contours of (a) semi-reentrant structures, (b) SR-TU, (c) SR-TR and (d) SR-RE compressed in the y-direction

Figure 7 compares deformation contours of different structures compressed in the y-direction. For the SR structure, the deformation occurs on the top and bottom sections, and the middle section is stable. The top section of SR keeps a good shape until the final deformation.

For the SR filled tube, the main deformation is accumulated on the top section layer by layer, and the bottom layer may deform a little as the compression increases. For the SR filled triangle, the major distortions are focused on the bottom layers, and a part of the top layer deforms above some compression strain load. The middle layers are very stable with nearly no deformation due to stability of the triangle. For the SR filled rectangle, most of the deformation is located near the top and bottom layers, and the other layers are already deformed into a rectangular shape.

Figure 8 compares the nominal stress versus strain curves for different structures compressed in the y-direction. It is also indicated that SR with fillers will have larger peak and plateau stressed compared to those of the SR structures, especially for the SR filled triangle. Hence, the peak and plateau stresses of these structures could be also sorted as: SR-TR > SR-TU > SR-RE > SR.

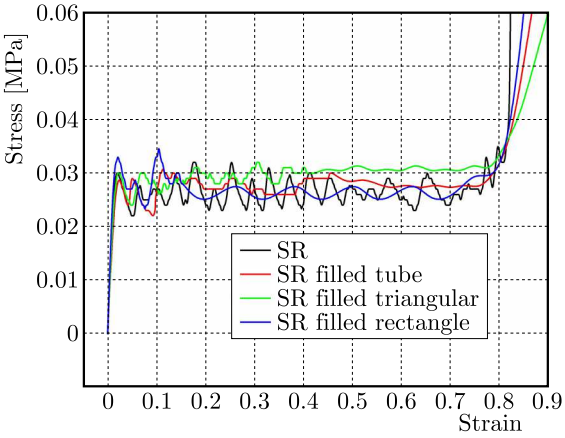

Fig. 8. Comparison of stress-strain curves among SR with different fillers in the y-direction

Table 5 compares mechanical properties of SR filled different tubular structures when compressed in the y-direction. It is found that the plateau stress, energy absorption and specific energy absorption of the SR filled triangle are the largest, while these of the SR filled rectangle are the lowest.

Table 5. Mechanical properties of SR filled different tubular structures compressed in y-direction

	SR	SR-TU	SR-TR	SR-RE
Plateau stress σ_m [MPa]	0.021	0.028	0.03	0.026
Densification strain	0.85	0.87	0.88	0.86
Energy absorption E [mJ]	0.01785	0.02436	0.0264	0.02236
Mass [Kg]	6.50E-04	7.31E-04	7.24E-04	7.24E-04
Specific energy absorption E_m [mJ/Kg]	2.75E+01	3.33E+01	3.65E+01	3.09E+01

4. Conclusion

In this study, semi-reentrant structures filled with different skeletal structures, including a tube, triangle and rectangle were designed. The out-of-plane and in-plane compression in two directions

of these structures were investigated and compared. The main conclusions are summarized as follows.

- For the out-of-plane compression, SR-TU exhibited a different deformation pattern compared to that of SR. SR initially deformed from the middle section, and SR-TU from the bottom side, SR-TR from topside, while SR-RE deformed both near the top and bottom sections, and there was no obvious expansion of the cells in the in-plane direction, meaning that a constraint effect appeared between the tubular filler and SR container. With the fillers contained, the plateau stresses for three conditions were all promoted compared to those of SR. The plateau stress were sorted as: SR-RE > SR-TU > SR-TR > SR. The densification strain was ordered as: SR-TR > SR-RE > SR-TU > SR. A better compression resistance or larger plateau stress of SR-RE may be caused by larger interaction areas between the SR and rectangular structures. The (specific) energy absorption of SR-TU was the largest.
- For the in-plane compression in the x-direction, SR initially deformed around the middle section and then the bottom failed in a wave-way. For SR-TU, the main deformation was accumulated on the top section layer by layer, while the bottom part kept stable. For SR-TR, major distortions were focused below the top layers and the top layer was compressed into a triangular shape after a large loading. Due to triangular stability, the bottom layers were quite stable at the initial stage. For SR-RE, deformation was located around the top layers and other layers were generally deformed into a rectangular shape. For the in-plane compression in the y-direction, SR deformed on the top and bottom sections, and its middle section was stable. For SR-TU, deformation was similar to that in the x-direction. For SR-TR, major distortions were focused on the bottom layers, and some top layers deformed after some compression strain, while the middle layers were stable. For SR-RE, deformation was located near the top and bottom layers. SR with fillers would have larger peak and plateau stresses compared to those of SR structures, especially for SR-TR. The peak and plateau stress of these structures could be sorted as: SR-TR > SR-TU > SR-RE > SR. The plateau stress, energy absorption and specific energy absorption of SR-TR were the largest, while that of SR-RE were the lowest.

Acknowledgement

The authors would like to acknowledge the support from the Scientific Research Program of Tianjin Education Commission (Grant No. 2021KJ053) and Aviation Science Foundation of China (Grant No. 20200038067001).

References

1. Al Antali A., Umer R., Zhou J., Cantwell W.J., 2017, The energy-absorbing properties of composite tube-reinforced aluminum honeycomb, *Composite Structures*, **176**, 630-639
2. Davini C., Favata A., Micheletti A., Paroni, R., 2017, A 2D microstructure with auxetic out-of-plane behavior and non-auxetic in-plane behaviour, *Smart Materials and Structures*, **26**, 12, 125007
3. Dong Z., Li Y., Zhao T., Wu W., Liang J., Xiao D., 2019, Experimental and numerical studies on the compressive mechanical properties of the metallic auxetic reentrant honeycomb, *Materials and Design*, **182**, 108036
4. Grima J.N., Oliveri N., Attard D., Ellul E., Gatt G., Cicala N., Recca G., 2010, Hexagonal honeycombs with zero Poisson's ratios and enhanced stiffness, *Advanced Engineering Materials*, **12**, 9, 855-862

5. Hussein R.D., Dong R., Lu G., Thomson R., 2018, An energy dissipating mechanism for crushing square aluminium/CFRP tubes, *Composite Structures*, **183**, 643-653

6. Hussein R.D., Ruan D., Lu G., Sbarski I., 2016, Axial crushing behaviour of honeycomb-filled square carbon fibre reinforced plastic (CFRP) tubes, *Composite Structures*, **140**, 166-179

7. Liu J., Wang Z., Hui D., 2018, Blast resistance and parametric study of sandwich structure consisting of honeycomb core filled with circular metallic tubes, *Composites Part B: Engineering*, **145**, 261-269

8. Lu G., Yu T.X., 2003, *Energy Absorption of Structures and Materials*, Elsevier, 1-424

9. Novak N., Vesenjak M., Ren Z., 2016, Auxetic cellular materials – a review, *Strojniški Vestnik – Journal of Mechanical Engineering*, **62**, 9, 485-493

10. Palanivelu S., Paepegem W.V., Degrieck J., Vantomme J., Kakogiannis D., Ackeren J.V., Hemelrijck D.V., Wastiels J., 2010, Comparison of the crushing performance of hollow and foam-filled small-scale composite tubes with different geometrical shapes for use in sacrificial cladding structures, *Composites Part B: Engineering*, **41**, 6, 434-445

11. Qin Q., Zhang W., Liu S., Li S., Zhang J., Poh L.H., 2018, On dynamic response of corrugated sandwich beams with metal foam-filled folded plate core subjected to low-velocity impact, *Composites Part A: Applied Science and Manufacturing*, **114**, 107-116

12. Sevtsuk A., Kalvo R., 2014, A freeform surface fabrication method with 2D cutting, *2014 Proceedings of the Symposium on Simulation for Architecture and Urban Design*, 109-116

13. Sun G., Li S., Liu Q., Li G., Li Q., 2016, Experimental study on crashworthiness of empty/aluminum foam/honeycomb-filled CFRP tubes, *Composite Structures*, **152**, 969-993

14. Wang T., Wang L., Ma Z., Hulbert G.M., 2018b, Elastic analysis of auxetic cellular structure consisting of re-entrant hexagonal cells using a strain-based expansion homogenization method, *Materials and Design*, **160**, 284-293

15. Wang Y., Lai H., Ren X.J., 2019, Enhanced auxetic and viscoelastic properties of filled reentrant honeycomb, *Physica Status Solidi*, **257**, 1900184

16. Wang Z., 2019, Recent advances in novel metallic honeycomb structure, *Composites Part B: Engineering*, **66**, 731-741

17. Wang Z., Liu J., 2018, Mechanical performance of honeycomb filled with circular CFRP tubes, *Composites Part B: Engineering*, **135**, 232-241

18. Wang Z., Liu J., 2019, Numerical and theoretical analysis of honeycomb structure filled with circular aluminum tubes subjected to axial compression, *Composites Part B: Engineering*, **165**, 626-635

19. Wang Z., Liu J., Yao S., 2018a, On folding mechanics of multi-cell thin-walled square tubes, *Composites Part B: Engineering*, **132**, 17-27

20. Yan L., Chouw N., Jayaraman K., 2014, Lateral crushing of empty and polyurethane-foam filled natural flax fabric reinforced epoxy composite tubes, *Composites Part B: Engineering*, **63**, 15-26

Manuscript received September 28, 2022; accepted for print December 14, 2022

JOURNAL OF THEORETICAL AND APPLIED MECHANICS
61, 2, pp. 245-258, Warsaw 2023
https://doi.org/10.15632/jtam-pl/160178

DYNAMIC ANALYSIS OF A MECHATRONIC DRIVE SYSTEM WITH AN INDUCTION MOTOR

Yongdi Cao, Xiaohong Liu

School of Mechanical Engineering, Yellow River Conservancy Technical Institute, Kaifeng, China
Corresponding author Yongdi Cao, e-mail: caoyongdi@yrcti.edu.cn

The paper presents research findings in the modelling and optimization of dynamic parameters of mechatronic systems with an induction motor. A mathematical model was developed to analyze currents in dynamic states of squirrel-cage rotors in the case of a line-to-line fault. The findings were verified experimentally using calculations for a 1.5 kW three-phase induction motor. The equations for a stationary $0x$, $0y$ coordinate system relating to the stator were derived. The set of design variables selected in the optimization process contained parameters describing design features of the gear shafts and control units settings.

Keywords: dynamic model, electromechanical system, vector control, optimization, rotor

1. Introduction

In most cases, a mechatronic control object is a set consisting of an actuator (drive) and a certain technological or technical device, the operation of which is evaluated by the monitoring of process variables. A simple example would be combination of an electric motor and a machine (Draganescu *et al.*, 2003). An assembled servomotor – the kinematic unit – is a more complex control object. Status control here refers, for example, to the static position, or static position and velocity, and sometimes acceleration of moving units. This control is accomplished with object sensors that track the process. The information from the sensors is transmitted through a negative feedback loop to the control system. The mechatronic device operations result from the interaction of control, sensor and drive systems, as well as device programming by the operator.

Physical models of real-world objects are used for dynamic study of mechatronic objects. The outcome and reliability of computer simulation depends on appropriate simplifying assumptions. The model should take into account both the system main dynamic properties and main external forces applied to it. Proper selection of machine dynamic properties is one of the ways to improve the reliability and durability. Optimization techniques are increasingly being used to support this process. This is due to effectiveness of this approach as well as development of professional software and digital tools (Panchenko *et al.*, 2020). The initial application of optimization procedures dealt mostly with static problems, such as cost minimization, dimensions or maximization of the transmitted power, etc. (Gautam *et al.*, 2019). Sensitivity analysis and optimization are becoming a tool for solving complex problems of machine system dynamics and supporting the design process (Zhu *et al.*, 2019). Focus areas and development of structural optimization methods, starting from static problems and ending with the solution of dynamics problems, were discussed in Yang *et al.* (2021).

Optimization of dynamic systems requires development of physical models to mathematically describe the investigated phenomena (Syromyatnikov *et al.*, 2021). The frequency response determined on their basis is widely used in optimization, vibration level control and model improvement (Zhong and Ma, 2021). Intended functions are developed using the superposition principle as well as more complex hybrid methods (Korohodskyi *et al.*, 2021). Optimization studies are used to solve complex statical and dynamical problems in the fastest growing engineering industries, such as aviation (Panchuk *et al.*, 2020) and automotive ones (Kryshtopa *et al.*, 2019).

Typically, sensitivity analysis serves as an introduction to optimization studies. Its results are used to justify the choice of decision variables (Omelchenko *et al.*, 2019) and to evaluate the quantitative and qualitative influence of parameters on the intended functions that determine dynamic parameters of the systems. The easiest way to find the intended function derivatives is to use the finite difference method (German-Galkin and Kozak, 2018). This method has a very simple algorithm, but the results may be affected by numerical errors. The accuracy of this method is sufficient for solving moderately complex problems. Semi-analytical methods are much more accurate and faster, but require more work to prepare the data. These methods include direct and conjugate methods (Atiyah and Sulc, 2020). The derivatives of the intended function determine the areas of greatest growth of the function and can be used to optimize the design features of machine systems (Fediakov *et al.*, 2020). Symak *et al.* (2021) investigated the effectiveness of using the vector control in an induction motor to reduce dynamic loads in the kinematic pairs of an electric drive system (Gryzlov and Grigorev, 2019). Modeling the shape of a machine as a complex dynamical system consisting of a number of simple interacting subsystems is one method for determining the dynamic status of the machine. Mathematical models of machine drive systems are complex dynamic systems with many degrees of freedom (Rosenberg, 1966). Modeling an electric drive system as a system with feedback between its electrical and mechanical parts is an example of such an approach (Qiao *et al.*, 2018). Voltage sags, short-term power outages and phase shifts in the supply voltage are now considered among the most unpleasant electromagnetic interferences, including those attributed to the adverse effect on the receiver operation (Karlov *et al.*, 2021).

The equipment operation is primarily affected by the magnitude of the phase shift as well as the amplitude and duration of the voltage sag. Cirrincione *et al.* (2003) described simulation tests of an induction motor model with the resulting phase shift after voltage sag and restoration, as well as after the phase shift of the supply voltage occurring in steady-state mode.

A line-to-line fault also affects the supply side and should be considered for safety reasons. A line-to-line fault in an induction motor designed by Berhausen and Boboń (2018) usually occurs when the stator winding insulation is damaged by an electrical breakdown in the adjacent phase. A short circuit between phases (line-to-line fault) is random in its location, and it is impossible to determine where it will occur. Line-to-line faults depend, among other things, on:

- anomalies (switching-on, windings, stresses) occurring in the motor winding insulation;
- operating conditions (frequency of transient processes, operating temperature of the insulation), etc.

Line-to-line faults occur on the machine external terminals (Lohrasbi and Sahai, 1988). Available solutions differ in the way the velocity and torque are controlled and in the way the motor condition is evaluated (German-Galkin and Kozak, 2020). However, field monitoring is the most common method. When designing mechatronic systems, it is important to study dynamic parameters of the system, especially the electric drive, to ensure reliable and efficient operation of the designed system.

This study aims at analyzing the operation of asynchronous electric motors intended for use as parts of mechatronic systems. The objectives of the study are (1) to develop a dynamic mathematical model of an asynchronous electric motor; (2) to solve the resulting model in MATLAB/Simulink; (3) to investigate the dynamic performance parameters of the asynchronous motor under normal and two-phase short circuit conditions.

2. Methods and materials

This paper discusses a methodology for calculating the line-to-line fault with short circuit currents for a squirrel-cage rotor of the vehicle wheel drive. The design of mechatronic drive systems is among the main challenges facing the development of modern electric vehicles. In this study, the proposed model is applied to a mechatronic system. The system includes an asynchronous electric motor and a mechanical drive system. The wheel speed is controlled by a motor controller regulating the speed of an asynchronous electric motor attached to each wheel. The structure of the proposed mechatronic system is depicted in Fig. 1.

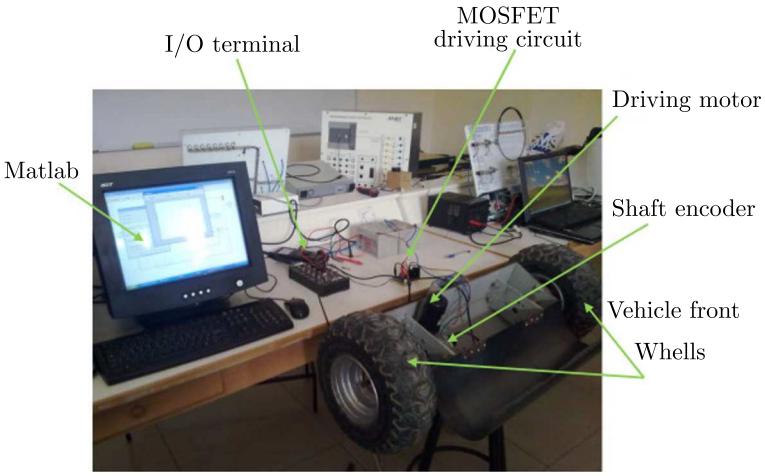

Fig. 1. Experimental mechatronic system

Mathematical modeling of the induction motor is based on the method of state variables. With this type of short-circuit, voltage spikes are important and are especially dangerous for the machine winding and the entire drive system (Rassõlkin *et al.*, 2020). The mathematical model of the motor has been developed in MATLAB to adopt dynamic parameters. The dynamic modeling of the line-to-line fault was based on the equations for state variables, chosen on the basis of the flux components:

- stator: $\psi_{s\alpha}(t)$, $\psi_{s\beta}(t)$,
- rotor output to the stator side: $\psi_{rs\alpha}(t)$, $\psi_{rs\beta}(t)$,
- velocity ω.

At each time point, the iterated state variables were determined by the fourth order Runge-Kutta method for positive and negative symmetric components. The fourth order Runge-Kutta method has been widely used because of its simple implementation, relatively simple formulas, quick response and the method high order. It makes it possible to obtain satisfactory calculation results with a small iteration step.

The calculation of parameters and visualization were performed in Comsol Multiphysics. Table 1 shows the motor parameters.

Table 1. Induction motor parameters

Name	Expression	Value	Description
f0	60[Hz]	60 Hz	Supply frequency
w0	2*pi*f0	376.99 Hz	Supply angular frequency
n0	1000	1000	Number of turns
L	0.50[m]	0.50 m	Length of motor
Omega	160[rad/s]	160 rad/s	Rotor angular velocity
coil_wire_current	2045.175[A]*sqrt(2)/n0	2.8923 A	Current amplitude in coil wire
r1	2[cm]	0.020 m	Outer radius of rotor steel
r2	3[cm]	0.030 m	Outer radius of rotor aluminum
r3	3.2[cm]	0.032 m	Inner radius of windings
r4	5.2[cm]	0.052 m	Inner radius of stator steel
r5	5.7[cm]	0.057 m	Outer radius of stator steel
win_angle	45[deg]	0.7854 rad	Angular span of winding
airgap	r3-r2	0.0020 m	Size of air gap

3. Mathematical model of the induction motor in the case of a line-to-line fault

The equations of state adopted for an induction motor with a squirrel-cage rotor. The general form of differential equations for positive and negative components is given by

$$\begin{aligned}
\frac{d\psi_{sx}(t)}{dt} &= -x\psi_{sx}(t) + xK_r\psi_{rsx}(t) + u_{sx}(t)\\
\frac{d\psi_{sy}(t)}{dt} &= -x\psi_{sy}(t) + xK_r\psi_{rsy}(t) + u_{sy}(t)\\
\frac{d\psi_{rsx}(t)}{dt} &= -y\psi_{rsx}(t) + yK_s\psi_{sx}(t) - \omega(t)\psi_{rsy}(t)\\
\frac{d\psi_{sy}(t)}{dt} &= -y\psi_{rsy}(t) + yK_s\psi_{sy}(t) + \omega(t)\psi_{rsx}(t)\\
\frac{d\omega}{dt} &= \frac{3p^2K_r}{2\sigma L_s J}\psi_{sy}(t) - \frac{3p^2K_r}{2\sigma L_s J}\psi_{sy}(t)\psi_{rsy}(t) - \frac{p}{J}M_z(t)
\end{aligned} \tag{3.1}$$

where: $\sigma = 1-(L_m^2/(L_sL_r)$ is the resulting dispersion coefficient; $K_s = L_m/L_s$ – stator coupling coefficient; $K_r = L_m/L_r$ – rotor coupling coefficient; $x = R_s/(\sigma L_s)$, $y = R_r/(\sigma L_r)$ – coefficients; $u_{sx}(t) = U_s\cos(2\pi ft)$, $u_{sy}(t) = U_s\sin(2\pi ft)$ – stator voltage along the x and y axis, respectively; R_s, R_r – stator and rotor active resistance, respectively [Ohm]; L_s, L_r, L_m – total stator, total rotor and magnetizing inductances [H].

The equivalent resistances and inductances for a serviceable asynchronous electric motor can be expressed as

$$R_e = R_s + R_rK_r^2L_e = L_s - \frac{L_m^2}{L_r} \tag{3.2}$$

In the case of a line-to-line fault, a part of the phase stator winding will be short-circuited. In this case, the equivalent resistances and inductances for a serviceable asynchronous electric motor would be

$$R_e = R_s - R_{cs} + R_rK_r^2 \qquad L_e = L_s - L_{cs} - \frac{L_m^2}{L_r} \tag{3.3}$$

where: R_{cs} is the faulty shorted part of the active resistance of the stator [Ohm]; L_{cs} is the faulty shorted part of the stator inductance [H].

In these equations, five independent variables were chosen as the state variables:

- stator flux along the x-axis: $\psi_{sx}(t)$;
- stator flux along the y-axis: $\psi_{sy}(t)$;
- rotor flux recalculated to the stator side along the x-axis: $\psi_{rsx}(t)$;
- rotor flux recalculated to the stator side along the y-axis: $\psi_{rsy}(t)$;
- the angular velocity, electric ω.

The excitation vector consists of the stator voltage along the x-axis and the stator voltage along the y-axis. The excitation vector consists of the moment loading the machine and the total moment of inertia which is assumed to be a constant for the purpose of line-to-line fault analysis. Hence, the excitation vector is a scalar (a given load torque). The angular velocity of the motor shaft Ω expressed as the angular electric velocity ω divided by the number of terminal pairs p is the output signal. The developed model takes into account both the possibility of setting the constant load torque and the load torque in the form of fan specifications depending on the machine rotational speed.

In the inductor motor model, the following simplifying assumptions are made:

- active resistances of the stator windings are identical;
- geometric axes of the sinusoidally distributed stator winding are separated by an angle of $2\pi/(mp_n)$, where p_n is the number of pole pairs;
- all phase m windings of the motor rotor (or m equivalent rotor windings) have identical active resistances R_r and identical quantities of pole pairs p_n;
- geometric angle between the axes of rotor windings is equal to the angle between axes of stator windings;
- all parameters of the rotor are given to the stator winding;
- the machine has a symmetrical structure and the stator winding arrangement;
- isotropic sheet with no hysteresis loop was used in the calculations (Zhuravlev and Grigor'ev, 2018);
- calculations took into account the magnetic core saturation only in the areas of the teeth;
- shifting of currents in the winding conductors, affecting the values of resistance and inductance of stator and rotor windings, with each iteration depending on the operating state of this machine (Solodkiy *et al.*, 2018).

By defining the state variables as fluxes, the electromagnetic torque coming from the positive and negative components may be calculated

$$M_e = \frac{3pL_m}{2(L_sL_r - L_m^2)}[\psi_{sy}(t)\psi_{rsx}(t) - \psi_{sx}(t)\psi_{rsy}(t)] \tag{3.4}$$

After calculating the magnetic fluxes, the stator and rotor currents can be determined as in the substitute two-phase motor in the $0x$ axis

$$i_{sx}(t) = \frac{\psi_{sx}(t) - K_r\psi_{rsx}(t)}{\sigma L_s} \qquad i_{rsx}(t) = \frac{-K_r\psi_{sx}(t) + \frac{K_r}{K_s}\psi_{rsx}(t)}{\sigma L_s} \tag{3.5}$$

and $0y$ axis

$$i_{sy}(t) = \frac{\psi_{sy}(t) - K_r\psi_{rsy}(t)}{\sigma L_s} \qquad i_{rsy}(t) = \frac{-K_r\psi_{sy}(t) + \frac{K_r}{K_s}\psi_{rsy}(t)}{\sigma L_s} \tag{3.6}$$

The currents for individual motor phases are determined by the following expressions

$$i_{r1}(t) = i_x(t) \qquad i_{r2}(t) = \frac{-i_{sx}(t)}{2} + \frac{\sqrt{3}}{2}i_{sy}(t) \qquad i_{r3}(t) = \frac{-i_{sx}(t)}{2} - \frac{\sqrt{3}}{2}i_{sy}(t) \tag{3.7}$$

The model of an induction motor with an inter turn fault of the stator winding was built in MATLAB/Simulink using the SimPowerSystems block library for electrical systems (Fig. 2). In the model, stator winding A is shorted to represent the inter turn short circuit fault. To compare the currents, a serviceable motor model with similar parameters and no short circuit was added. In the experiment with asynchronous electric motors, 1:30 of the total turns on a phase winding turns were short-circuited in advance. When examining the inter turn short circuit of the stator winding, the hardware part involved a frequency converter with an open architecture based on a TMS320F28335 microcontroller (Texas Instruments). The frequency converter software relies on a built-in MexBIOS environment. The architecture of this environment enables control and diagnostic algorithms to be combined. A scalar control system was used to control the asynchronous motor, but the Mexbios Development Studio also permits the use of any algorithms for sensor and sensorless systems. The current of the faulty phase winding I_z is calculated from the measured values of the stator currents I_x and I_y.

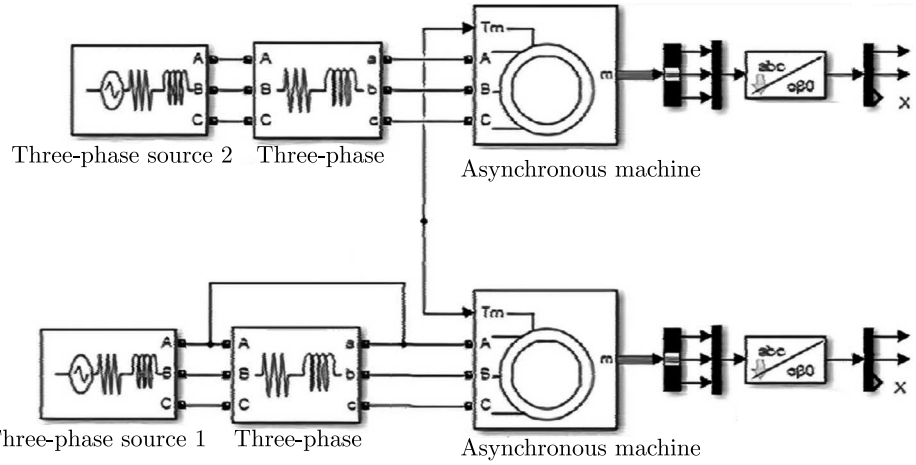

Fig. 2. Model of an asynchronous electric motor with an inter turn fault of the stator phase winding

4. Results

To build a physical model of the analyzed drive system mechanical part, a hybrid method is used, which is a combination of the finite element method and the rigid finite element method. The gearing is modeled as a system of shafts resting on bearings, the masses of which are concentrated in the form of disks at the location of the gears. The shafts are connected to each other through mating gears. Bar elements are adopted to discretize the shaft. Non-deformable disks of the model gears are rigidly fixed in the assemblies for splitting the shaft into rod elements. The system is driven by an induction motor.

The numerical calculations relied on a monoharmonic induction motor model in the xy coordinate system. The motor equations with independent variables – stator current and rotor flux – are represented in the canonical form by five equations of state

$$\frac{di_{sx}}{dt} = \frac{1}{L_z\sigma}\Big\{u_{sx} - R_s i_{sx} + \Omega_\phi\Big(\sigma L_s i_{sy} + \frac{L_m}{L_r}\psi_{ry}\Big) - \frac{L_m}{L_r}\Big[u_{rx} - R_r\Big(\frac{1}{L_r}\psi_{rx} - \frac{L_m}{L_r}i_{sx}\Big) + (\Omega_\chi - p\Omega_m)\psi_{ry}\Big]\Big\}$$

$$\frac{di_{sy}}{dt} = \frac{1}{L_z\sigma}\Big\{u_{sy} - R_s i_{sy} + \Omega_\chi\Big(\sigma L_s i_{sx} + \frac{L_m}{L_r}\psi_{rx}\Big) - \frac{L_m}{L_r}\Big[u_{ry} - R_r\Big(\frac{1}{L_r}\psi_{ry} - \frac{L_m}{L_r}i_{sy}\Big) + (\Omega_\chi - p\Omega_m)\psi_{rx}\Big]\Big\}$$

$$\frac{d\psi_{rx}}{dt} = u_{rx} - R_r\Big(\frac{1}{L_r}\psi_{rx} - \frac{L_m}{L_r}i_{sx}\Big) + (\Omega_\chi - p\Omega_m)\psi_{ry} \tag{4.1}$$

$$\frac{d\psi_{ry}}{dt} = u_{ry} - R_r\Big(\frac{1}{L_r}\psi_{ry} - \frac{L_m}{L_r}i_{sy}\Big) + (\Omega_\chi - p\Omega_m)\psi_{rx}$$
$$\frac{d\Omega_m}{dt} = \frac{1}{J}\Big[p\frac{L_m}{L_r}\Big(\psi_{rx}i_{sx} - \psi_{ry}i_{sy}\Big) - T_m\Big]$$
$$T_e = pL_m(\psi_{rx}i_{sy} - \psi_{ry}i_{sx})$$

where: u_{sx}, u_{sy} are components of the stator voltage vector (represented in the chosen Cartesian coordinate system); Ω_m – rotor angular velocity; Ω_χ – angular velocity of the rotating biaxial system; ψ_{rx}, ψ_{ry} – components of the rotor flux vector; i_{sx}, i_{sy} – components of the stator current; T_e – electromagnetic torque.

The three-phase induction motor model has been visualized in Comsol Multiphysics. Figure 3 shows the resulting diagram.

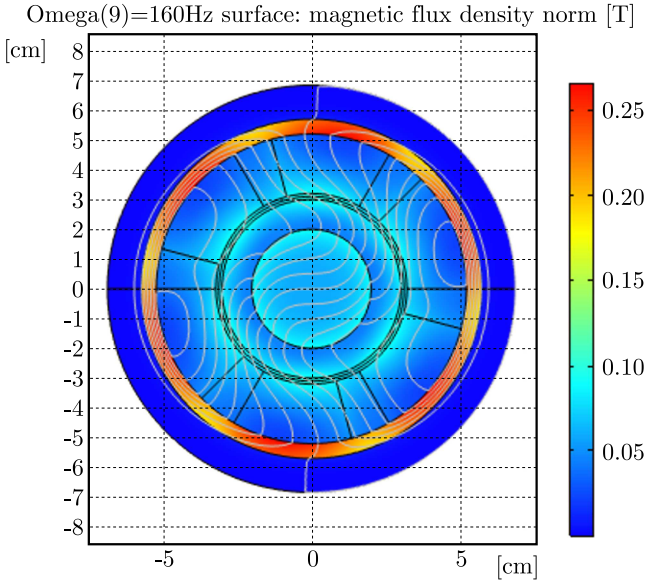

Fig. 3. Visualization of the magnetic field for the induction motor at $\Omega_m = 160\,\mathrm{rad/s}$

To solve the mathematical model of the drive system as an electromechanical system, a software written in MATLAB/Simulink has been used. The preliminary calculations for the purpose of construction of the inertia, stiffness and damping matrix of the gear transmission and its connection with the housing were performed in MATLAB. A modal analysis of the analyzed mechanical of the drive system part was also performed in MATLAB. The model simulating dynamic problems of the electromechanical system was created in Simulink (Fig. 4).

This model incorporates vector control for the angular velocity with an inverter supplying the algorithm f. The shaft angular velocity is controlled by changing the frequency in the motor windings (Jia and Yan, 2019).

Table 2 compares the first 10 natural frequencies of the mechatronic system before and after using the reduction drive. The table clearly demonstrates that the approximation error of the first eight frequencies is less than 6%. In the case of natural frequencies before and after crimping, their complete relevance is validated for all the first 10 frequencies.

Table 3 shows the first ten natural frequencies of the drive system, the housing itself, and the model consisting of a gear wheel connected to the housing.

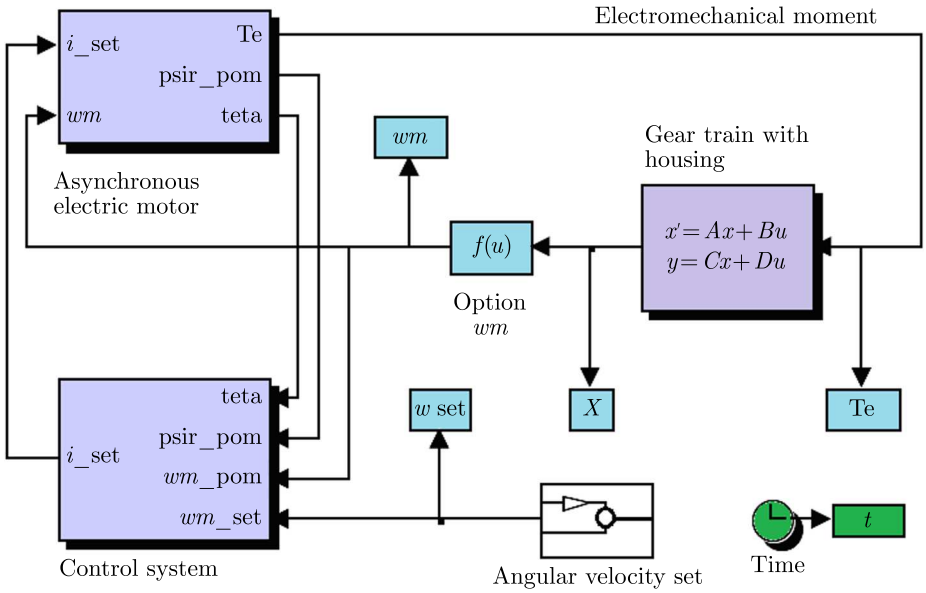

Fig. 4. Electromechanical model of a mechatronic system with an induction motor

Table 2. Comparison of natural frequencies of the housing model before and after reduction [Hz]

No.	Full model	Simplified model	Error [%]	χ^2	SSD	p
1	367.57	375.86	1.15	0.99837	34.3621	< 0.005
2	410.03	430.35	1.45	0.99816	206.451	< 0.005
3	567.58	584.18	4.70	0.99656	137.780	< 0.005
4	583.88	611.48	4.78	0.99598	380.880	< 0.005
5	658.71	687.18	4.68	0.99379	405.270	< 0.005
6	667.43	688.53	4.65	0.99655	222.605	< 0.005
7	698.03	701.80	5.10	0.99916	7.10645	< 0.005
8	695.17	705.88	4.55	0.99970	57.3521	< 0.005
9	794.13	800.76	8.41	1.00000	21.9785	< 0.005
10	841.80	851.17	8.61	1.00000	43.8985	< 0.005

Table 3. Natural frequencies of the drive system [Hz]

No.	Drive system	Housing of reduction drive	Drive + housing
1	0	405.86	0
2	254.46	440.45	254.46
3	296.05	594.29	296.05
4	296.05	622.49	296.05
5	296.14	687.29	295.24
6	296.14	689.54	295.24
7	599.19	702.90	495.62
8	712.19	705.99	441.09
9	712.52	900.76	599.20
10	712.73	942.27	614.99

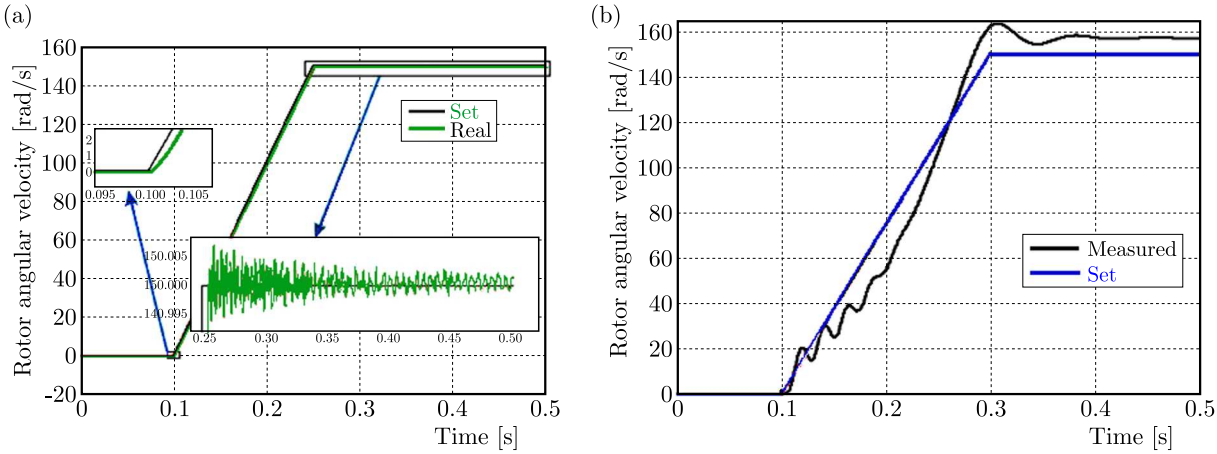

Fig. 5. Comparison of the set and actual rotational speed of the motor shaft

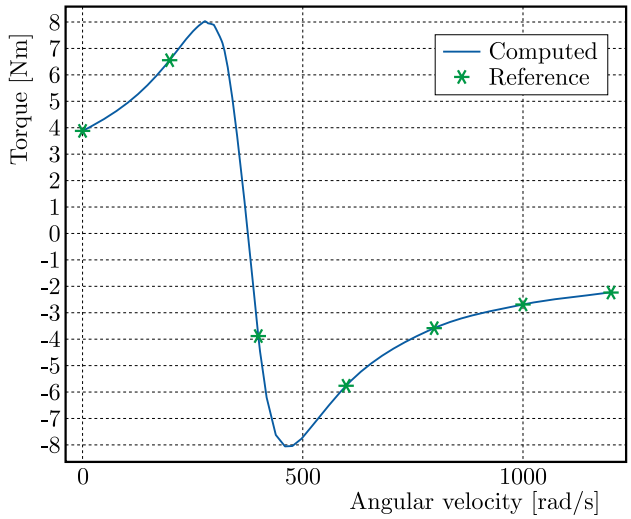

Fig. 6. Dependence of the torque on angular velocity

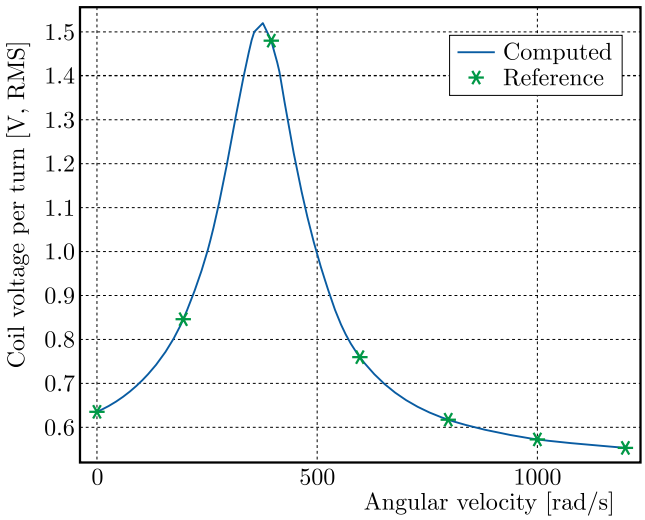

Fig. 7. Dependence of the coil voltage on angular velocity

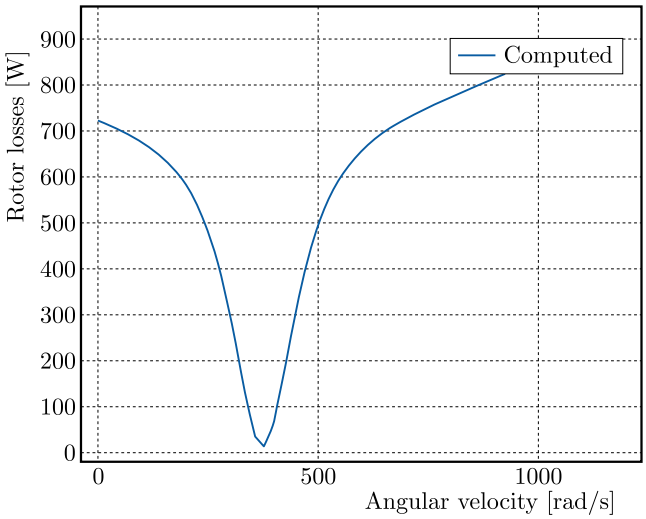

Fig. 8. Dependence of rotor losses on angular velocity

Figure 6 shows the calculated torque. Figure 7 shows the coil voltage, and Fig. 8 shows rotor losses as a function of rotational speed. The dependency graph shows the expected values for the induction motor. More specifically, the zero torque value, maximum voltage and minimum losses at the synchronous speed ($\Omega = 370\,\mathrm{rad/s}$).

5. Discussion

The innovation of this study with respect to the vector control of a three-phase asynchronous motor is that the proposed motor model is relative simple and allows calculation of the modulus and phase of the rotor flux vector. These advantages eliminate the need for additional mathematical blocks that other models of three-phase asynchronous motors require. The frequencies along the axes (x, y) are equal to zero, which enables higher accuracy and makes it easier to set up the circuits of three-phase asynchronous motors. The proposed model uses coordinate transformations that require knowledge of the position angle of the rotor flux vector calculated from the model. The coordinate transformation block operates with a delay of one sampling period, so this model requires a sufficiently high carrier frequency. In this case, the square root function is implemented through interpolation according to the table of reference points. It requires much more processor time and memory. Note that the presence of a block for calculating the amplitude and phase of the vector significantly complicates the implementation of the flux linkage meter.

Transient states occurring during dynamic operation of the induction motor depend on:

- machine power supply;
- changes in dynamic patterns of the applied external torque to the shaft (changes in the resulting moment of inertia of the entire system are possible) (Zhu *et al.*, 2019);
- mutual interaction of magnetic fluxes in transient states;
- form of voltage and current oscillations in specific phases of the stator and rotor windings, the currents associated with these windings.

With the discussed results of induction motor control in mind, the following properties of the drive system can be mentioned:

- the vector control enables full control of the motor torque and rotational speed;
- the rotational speed parameters are reproduced with high accuracy and small control deviations;

- control high quality is achieved with a constant value of the actual current component affecting the flux and with an adjustable imaginary component of the stator current which is proportional to the torque (Draganescu *et al.*, 2003).

The constant value of the rotor flux amplitude is achieved with a PI controller. The need to use coordinate transformation systems, which, unfortunately, affects the reliability and cost of such a system, constitutes the disadvantage of the chosen control method (Atiyah and Sulc, 2020). The resulting rotational speed and torque oscillograms reach a steady state after a short time without unnecessary oscillations. Starting the motor at the selected loads and the transition to the steady state takes a short time. The set speed is reached at idle speed in $t < 0.3$ seconds. The control system significantly reduces motor inrush currents, which translates into a lower torque value in the initial phase of motor operation but increases the durability of its windings (Abbasi *et al.*, 2021). A lower starting torque value does not allow the rotor resistance to be overcome, so that the motor remains stationary during the initial starting phase. The shape of the phase currents obtained in the control system is close to sinusoidal and is subject to little distortion, which is a significant advantage of IFOC (Zhong and Ma, 2021). The control system response to a step change in the load is satisfactory, and the transition time to the steady state is a few ms (He *et al.*, 2020). The presented system makes it possible to control idling, which is not possible with scalar control methods. When calculating the transient states, first of all, a machine model should be developed with simplifying assumptions that allow for a mathematical description of the motor (German-Galkin and Kozak, 2018). The adopted equations of state for a squirrel-cage rotor were obtained for a stationary coordinate system associated with the stator. They describe electromagnetic wave forms in an equivalent three-phase induction motor (Symak *et al.*, 2021). Such a stationary coordinate system associated with the stator makes a relatively simple iterative simulation of a line-to-line fault possible. Because of this, the next iteration can be determined for each iteration from the previous moment by making vector composition of the positive and opposite components of the simulated machine (Solodkiy *et al.*, 2018). In the case of an induction motor, a different coordinate system rotating with constant or variable speed rigidly connected with the rotor causes a significant complication of equations and difficulty of analysis. This is because each iteration for both components must take into account the fact that the rotor speed at each iteration alternates with slip, which makes it difficult to compose vectors and calculate them (Rosenberg, 1966). Such a model provides equations relating the dependencies of the assumed state variables representing rotor rotation with respect to excitation in the form of voltages, currents, magnetic fluxes as well as load torque and solution inertia (Bast *et al.*, 2020). At each iteration, the system with the positive component and the system of equations with the inverse sequence have the same state, on the basis of which the state variables are calculated. Therefore, in each iteration, different values of the state variables are determined (for positive and negative components) based on the previous step and the conditions of feeding the specific symmetric component (German-Galkin and Kozak, 2018). The paper also provides a comparative analysis of the current flow in a low-power motor in this type of short-circuit. At this stage of model development, nonlinearities such as backlash and variable grid stiffness are excluded, and a monoharmonic induction motor model is adopted (He *et al.*, 2020). The direct torque control and the ability to influence the torque make it possible to achieve strong dynamic patterns with a fast response to changes in the set value of angular velocity.

6. Conclusions

The paper presents a dynamical model of a mechatronic system driven by an induction motor with a squirrel-cage rotor and vector control. The mechanical part takes into account the shaft and housing match. A system of differential equations describing electromagnetic wave forms

in an equivalent three-phase induction motor has been formulated, replacing spatial vectors with the corresponding relations between their components along the $0x$ and $0y$ axes for the direct sequence and a similar system of equations for the negative sequence. MATLAB and Comsol multiphysics were used to solve the model. Dependency graphs for parameters of the mechatronic drive system with the induction motor in operating conditions and with the squirrel-cage rotor in the vector control mode and without control were built. The research findings suggest that for a motor synchronous speed $\Omega = 370\,\mathrm{rad/s}$ the torque is zero, the voltage reaches its maximum value and the minimum rotor losses are observed. The diagnostic methods discussed earlier require either more calculations or preliminary settings for the induction motor. However, the comparative analysis of those methods provides qualitative results that are very useful in assessing suitability of the method. The main advantages of the proposed method are as follows: it is simple and demands less data processing. The proposed system is not limited to a laboratory bench and wheel drives of electric vehicles. The proposed electric drive design can be used in manufacturing industries and other mechatronic systems (cranes, air cooling systems, pumping units, etc.)

Acknowledgments

This research did not receive any specific grant from funding agencies in the public, commercial or non-profit sectors.

References

1. Abbasi M.A., Husain A.R., Nik Idris N.R., Fasih ur Rehman S.M., 2021, Computationally efficient predictive torque control for induction motor drives based on flux positional errors and extended Kalman filter, *IET Electric Power Applications*, **15**, 6, 653-667

2. Atiyah A., Sulc B., 2020, Role of asynchronous motor modelling in driven railway wheelset dynamical simulation model, *2020 21th International Carpathian Control Conference (ICCC)*, 1-6

3. Bast D., Kulchytska-Ruchka I., Schöps S., Rain O., 2020, Accelerated steady-state torque computation for induction machines using parallel-in-time algorithms, *IEEE Transactions on Magnetics*, **56**, 2, 1-9

4. Berhausen S., Boboń A., 2018, Determination of high power synchronous generator subtransient reactances based on the waveforms for a steady state two-phase short-circuit, *Applied Mathematics and Computation*, **319**, 538-550

5. Cirrincione M., Pucci M., Cirrincione G., Capolino G.-A., 2003, A new experimental application of least-squares techniques for the estimation of the induction motor parameters, *IEEE Transactions on Industry Applications*, **39**, 5, 1247-1256

6. Draganescu F., Gheorghe M., Doicin C.V., 2003, Models of machine tool efficiency and specific consumed energy, *Journal of Materials Processing Technology*, **141**, 1, 9-15

7. Fediakov V.V., Kornienko M.N., Zhuravleva L.A., 2020, Features of loss calculation in mechatronic modules on the basis of synchronous reluctance and induction AC electric drives, *2020 IEEE Conference of Russian Young Researchers in Electrical and Electronic Engineering (EIConRus)*, IEEE, St. Petersburg and Moscow, Russia, 639-643

8. Gautam P.V., Kushwaha H.L., Kumar A., Kushwaha D.K., 2019, Mechatronics application in precision sowing: A review, *International Journal of Current Microbiology and Applied Sciences*, **8**, 4, 1793-1807

9. German-Galkin S., Kozak M., 2018, Structural model of the electric drive with double-fed asynchronous machine and direct torque control, *Multidisciplinary Aspects of Production Engineering*, **1**, 1, 41-45

10. Gryzlov A.A., Grigorev M.A., 2019, Frequency-response methods for synthesizing controlled high-speed electric drives of compressors, *Russian Electrical Engineering*, **90**, 5, 364-369

11. He S., Sui X., Liu Z., Kang M., Zhou D., Blaabjerg F., 2020, Torque ripple minimization of a five-phase induction motor under open-phase faults using symmetrical components, *IEEE Access*, **8**, 114675-114691

12. Jia J., Yan X., 2019, Development and application of on-line torque telemetry system for rolling mill based on WIFI signal transmission and high frequency induction power supply, *Proceedings of the 3rd International Conference on Mechatronics Engineering and Information Technology*, 861-868

13. Karlov D., Prokazov I., Bakshtanin A., Matveeva T., Kondratenko L., 2021, Optimizing neural network model performance for wind energy forecasting, *International Review on Modelling and Simulations*, **14**, 3, 185-193

14. Korohodskyi V., Voronkov O., Rogovyi A., Kryshtopa S., Lysytsia O., Fesenko K., Bezridnyi V., Rudenko N., 2021, Influence of the stratified fuel-air charge pattern on economic and environmental indicators of a two-stroke engine with spark ignition, *AIP Conference Proceedings*, **2439**, 020011

15. Kryshtopa S., Melnyk V., Dolishnii B., Korohodskyi V., Prunko I., Kryshtopa L., Zakhara I., Voitsekhivska T., 2019, Improvement of the model of forecasting heavy metals of exhaust gases of motor vehicles in the soil, *Eastern-European Journal of Enterprise Technologies*, **4**, 10 (100), 44-51

16. Lohrasbi J., Sahai V., 1988, Magnetohydrodynamic heat transfer in two-phase flow between parallel plates, *Applied Scientific Research*, **45**, 1, 53-66

17. Omelchenko E., Khramshin T., Tanich V., Kozhevnikov I., 2019, Dynamic computer model of traction asynchronous motor, *2019 IEEE Russian Workshop on Power Engineering and Automation of Metallurgy Industry: Research and Practice (PEAMI)*, 59-63

18. Panchenko A., Voloshina A., Titova O., Panchenko I., Caldare A., 2020, Design of hydraulic mechatronic systems with specified output characteristics, *Proceedings of the 3rd International Conference on Design, Simulation and Manufacturing: The Innovation Exchange*, Springer International Publishing, Cham, 42-51

19. Panchuk M., Kryshtopa S., Panchuk A., 2020, Innovative technologies for the creation of a new sustainable, environmentally neutral energy production in Ukraine, *International Conference on Decision Aid Sciences and Application, DASA 2020*, 9317165, 732-737

20. Qiao G., Liu G., Shi Z., Wang Y., Ma S., Lim T.C., 2018, A review of electromechanical actuators for More/All Electric aircraft systems, *Proceedings of the Institution of Mechanical Engineers, Part C*, **232**, 22, 4128-4151

21. Rassõlkin A., Belahcen A., Kallaste A., Vaimann T., Lukichev D.V., Orlova S., Heidari H., Asad B., Pando Acedo J., 2020, Life cycle analysis of electrical motor-drive system based on electrical machine type, *Proceedings of the Estonian Academy of Sciences*, **69**, 2, 162

22. Rosenberg R.M., 1966, On nonlinear vibrations of systems with many degrees of freedom, *Advances in Applied Mechanics*, Elsevier, Amsterdam, **9**, 155-242

23. Solodkiy E.M., Dadenkov D.A., Kostygov A.M., 2018, Sensorless vector control of asynchronous machine based on reduced order Kalman filter, *2018 17th International Ural Conference on AC Electric Drives (ACED), IEEE*, Piscataway, NJ, 1-5

24. Symak D., Sabadash V., Gumnitsky J., Hnativ Z., 2021, Kinetic regularities and mathematical modelling of potassium chloride dissolution, *Chemistry and Chemical Technology*, **15**, 1, 148-152

25. Syromyatnikov D., Druzyanova V., Beloglazov A., Bakshtanin A., Matveeva T., 2021, Evaluation of the economic profitability of using renewable energy sources in agro-industrial companies, *International Journal of Renewable Energy Development*, **10**, 4, 827-837

26. Yang J.Y., Ming Wang D., Ge Y.J., 2021, Design and implementation of hardware platform for bearingless induction motor control system, *2021 IEEE International Conference on Electrical Engineering and Mechatronics Technology (ICEEMT)*, Piscataway, NJ, 147-150

27. Zhong B., Ma L.L., 2021, Active disturbance rejection control and energy consumption of three--phase asynchronous motor based on dynamic system's decoupling, *Sustainable Energy Technologies and Assessments*, **47**, 101338

28. Zhu H., Nesler C., Divekar N., Ahmad M.T., Gregg R.D., 2019, Design and validation of a partial-assist knee orthosis with compact, backdrivable actuation, *IEEE International Conference on Rehabilitation Robotics*, Piscataway, NJ, 917-924

29. Zhuravlev A.M., Grigor'ev M.A., 2018, Calculation of electric drives with electric machines of unconventional design, *Russian Electrical Engineering*, **89**, 4, 222-227

Manuscript received August 4, 2022; accepted for print December 28, 2022

JOURNAL OF THEORETICAL AND APPLIED MECHANICS
61, 2, pp. 259-274, Warsaw 2023
https://doi.org/10.15632/jtam-pl/161688

A STUDY OF DYNAMIC HYSTERESIS MODEL FOR A MAGNETORHEOLOGICAL DAMPER

Kun-Yung Chen
Department of Aircraft Engineering, Air Force Institute of Technology, Taiwan R.O.C.
e-mail: 9615906@nkust.edu.tw
Ming-Lung Kung
Department of Avionics Engineering, Air Force Academy, Taiwan R.O.C.
e-mail: d993010015@nsysu.edu.tw

The paper proposes a new dynamic model based on the LuGre model and an electrical equation to describe the hysteresis phenomenon for a magnetorheological (MR) damper. In addition, a sliding mode observer (SMO) is proposed to estimate unmeasurable states of the MR damper. The parameters of the MR damper are successfully identified by using the self-learning particle swarm optimization (SLPSO) algorithm. The contributions of this paper are: i) a new dynamic model based on the LuGre model and an electrical equation for an MR damper is successfully formulated to fit for the hysteresis behavior, ii) the exerted damping force can be practically adjusted by using input voltage for the dynamic model, iii) the SMO is proposed to estimate the internal states and current, and iv) the unknown parameters of the MR damper are successfully identified by using the SLPSO algorithm with a numerical experiment.

Keywords: identification, LuGre model, magnetorheological damper, self-learning particle swarm optimization (SLPSO), sliding mode observer (SMO)

1. Introduction

The magnetorheological (MR) damper is a well known semi-active shock absorber which has been extensively studied and investigated recently. Characteristics of MR dampers include low power requirements, simple construction, quick response and adjustable damping force. Currently, they are widely applied in vehicle suspension systems and civil engineering to absorb shocks. However, the nonlinear hysteresis phenomenon of MR dampers is an inherent and complicated problem. Accordingly, how to correctly describe the hysteresis phenomenon with a simple dynamic model for the MR damper is a significant and interesting research area. Previously, the Bouc-Wen model has been widely implemented to characterize the hysteresis phenomenon (Ismail *et al.*, 2009; Ikhouane and Rodellar, 2005, 2007; Metered, 2010; Bhowmik, 2011; Ambhore *et al.*, 2013). Moreover, the development of the Bouc-Wen model to describe the hysteresis phenomenon in dynamically excited nonlinear structures has been reviewed (Ismail *et al.*, 2009). Moreover, standard and modified Bouc-Wen models have been proposed in the literature (Ikhouane and Rodellar, 2005; Metered, 2010; Bhowmik, 2011; Ambhore *et al.*, 2013). Recently, Ramli *et al.* (2019) proposed a Bouc-Wen model to describe the dynamic behavior of smart material-based actuators, then designed an adaptive controller to implement in a smart actuator. In (Naz *et al.*, 2021), a piezo-stage actuator that was modelled based on the nonlinear Bouc-Wen hysteresis model was numerically studied and presented. The performance of the positioning system model was validated through accuracy measurements and a regression analysis.

In (Balamurugan and Jancirani, 2013), a modified parametric algebraic model was presented that was able to control a semi-active suspension system, and the effectiveness and robustness of

the semi-active control approach was demonstrated in simulations. To investigate the dynamics of a damper filled with an MR fluid, a lumped mass thermo-mechanical model was proposed and studied in (Zalewski *et al.*, 2014). Several effects (including friction and temperature) were discussed in this model and the piston displacement coupled with the energy balance equation for temperature was analyzed. In (Boada *et al.*, 2018), an inverse MR damper model based on network inversion was proved in experimental tests to estimate the input current and voltage, and the damping force was exerted by an MR damper. In (Graczykowski and Pawłowski, 2017), the damper response of an MR fluid was modeled using thermodynamic equations which described reduced and parametric models in terms of relative phenomena. Recently, a generalized hysteretic bi-viscous operator was proposed in (Zhao *et al.*, 2018) for approximate description of hysteretic properties. In the aforementioned studies, different types of mathematical models were proposed to properly characterize the nonlinear hysteresis phenomenon in the input current. However, it is impractical to adjust the damping force using the input current for an MR damper. Therefore, a mathematical model using the input voltage is more practical for adjusting the damping force.

Determination of the unknown parameters in the proposed dynamic model is a significant task. Here, the parameter identification method is suitable for finding the unknown parameters of the dynamic model. Recently, some studies about parameter identification for MR dampers have been conducted. For example, parameter identification in typical loading cases was studied in (Peng *et al.*, 2018), and the authors established a functional relationship with the input current. Moreover, these parameters were defined and optimized by a genetic algorithm integrated with the Simulink toolbox in MATLAB. In (Pelliciari *et al.*, 2018), a pinched hysteretic system was modelled using a modified Bouc-Wen model. There, parameter identification for the hysteretic system was performed by using a genetic algorithm, and the numerical results were successful. A normalized Bouc-Wen model was employed in (Zhu *et al.*, 2019) to describe the hysteresis of an MR damper. Then, a genetic algorithm was utilized to identify the parameters of the MR damper, and the simulation results indicated that the proposed method was more accurate. A constrained unscented Kalman filter was proposed in (Niola *et al.*, 2019) to identify the parameters of the hysteresis model. There, the Bouc-Wen model was adopted to describe the hysteretic behavior for a seismic isolator. The results indicated that the proposed Kalman filter provided an improved parameter identification ability. A modified Bouc-Wen hysteresis model was adopted in (Bartkowski *et al.*, 2019) to describe nonlinear responses of tested specimens, and a genetic algorithm was applied to identify the model parameters. In (Nguyen *et al.*, 2022), a novel adaptive parameter identification method was proposed for a model consisting of an estimated model, a hysteresis observer, and adaptive algorithms. The mentioned models, including the Bouc-Wen one, LuGre and Dahl friction model for MR dampers, still have many unknown parameters to find to fit the real dampers. System parameter identification is a practical method that uses intelligence algorithms, including the particle swarm optimization algorithm, dynamic neural networks and genetic algorithms. If a fitness function (FF) is defined with an error function between the real and estimated damping force, these algorithms can randomly search for proper parameters to optimize (maximize or minimize) the FF, and these proper parameters are the final solutions.

In this paper, a modified LuGre friction model (Jiménez and Álvarez-Icaza, 2005) is implemented to characterize the nonlinear hysteresis phenomenon for an MR damper. The control input voltage can change the current to adjust the damping force. However, the control input voltage is more practical than the control input current for MR dampers during real operation. Therefore, an electrical equation including resistance, inductance and induced electromotive force is considered and integrated into the dynamic model. In other words, a new dynamic model with an electrical equation for MR dampers is formulated and presented in this paper. In addition, a sliding mode observer (SMO) is proposed to estimate unmeasurable states of the MR damper. Then, the self-learning particle swarm optimization (SLPSO) (Li *et al.*, 2012) is

proposed to identify the unknown parameters. An FF is defined as the absolute error between the real and estimated damping force. Three types of input voltage are implemented to verify the efficiency of the parameter identification, where it is revealed that a varying input voltage can excite more varying output responses, which are used to correctly identify the unknown parameters. From the simulation results, the new dynamic model was successfully formulated. The proposed identification method is practicable for dynamic modelling of an MR damper to identify the unknown parameters.

Finally, the remainder of this paper is organized as follows: Section 1 presents the introduction, Section 2 contains dynamic modeling of an MR damper, Section 3 presents parameter identification, whereas numerical experiments and conclusions are described in Sections 4 and 5, respectively.

2. Dynamic modeling

An MR damper is a shock absorber filled with a magnetorheological fluid, and the exerted damping force can be adjusted by the magnetic field via the input current. The damping characteristic of an MR damper can be continuously adjusted by changing the power of the electromagnet, whereby the fluid viscosity increases within the damper as the electromagnetic intensity increases. In traditional dampers, the relationship between the damping force f_d and velocity v is linear, which can be represented as $f_d = \mu v$, where μ is the damping coefficient. However, the relation of the damping force with input velocity and displacement for the MR damper is a nonlinear hysteresis phenomenon. Therefore, formulating an appropriate dynamic model of the MR damper that completely describes the hysteresis behavior is a significant challenge.

2.1. Mathematical model based on the LuGre model

In this study, one can find a dynamic model to describe the hysteresis phenomenon of the MR damper. The hysteresis phenomenon can also be found in various fields, including physics, chemistry, engineering, biology and economics. Moreover, previous models, such as the Preisach (Roussel *et al.*, 2022a,b) and Duhem models (Ahmed *et al.*, 2021; Xu *et al.*, 2022) have been proposed to describe nonlinear hysteresis systems. Many dynamic models have also been developed to describe such hysteresis behavior, and it is necessary to select and implement high-accuracy models to capture nonlinear hysteretic responses. For example, traditional and modified Bouc-Wen models (Ramli *et al.*, 2019; Naz *et al.*, 2021; Peng *et al.*, 2018; Pelliciari *et al.*, 2019) have been proposed to describe hysteretic responses of an MR damper. The Bouc-Wen model comprises three parts (spring, damper and Bouc-Wen block) and includes an evolutionary variable, internal displacement and external excitation displacement. However, the evolutionary variable and internal displacement are unmeasurable, which is a disadvantage in practical operations. A diagram of an MR damper is presented in Fig. 1, where I is the input current and terms x and v are the external excitation displacement and velocity, respectively. In this paper, the LuGre mathematical model (Jiménez and Álvarez-Icaza, 2005) has been adopted to describe the hysteretic behavior, which is written as follows

$$\dot{z} = v - \alpha|v|z \qquad f = \beta(I)v + \delta x + \varepsilon\dot{z} + \gamma(I)z + f_0 \tag{2.1}$$

where z is the internal state variable, f is the damping force exerted by the MR damper, α, δ and ε are the positive constants, and f_0 is the known damping force. The functions $\beta(I)$ and $\gamma(I)$ with the input current I are written as follows

$$\beta(I) = -p_1 I^2 + p_2 I + p_3 \qquad \gamma(I) = q_1 I + q_2 \tag{2.2}$$

where $p_{1,2,3}$ and $q_{1,2}$ are the positive constants. The mathematical model using the LuGre model of the MR damper is proposed in Eqs. (2.1). It is evident that the internal state of z is the only unknown variable in the mathematical model, which can be estimated by a state observer.

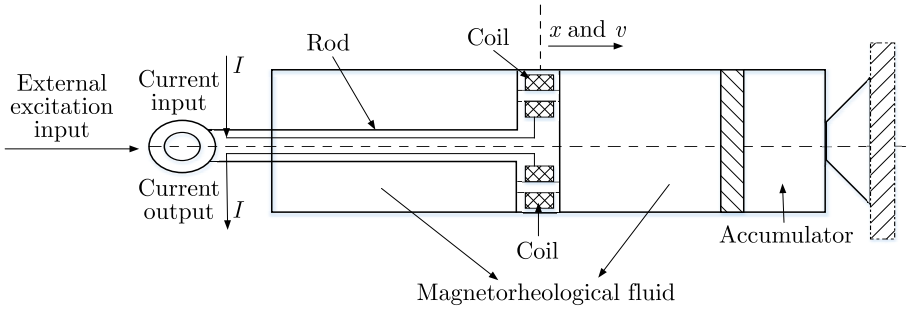

Fig. 1. A diagram of an MR damper

2.2. Electrical equation

Although the input current I is produced by the input voltage, it is easier to change the exerted damping force by adjusting the input voltage in practical applications of the MR damper. Then, an electrical equation that includes the control input voltage, resistance and inductance is necessary when formulating the dynamic model. The resistor-inductor circuit is the general electrical circuit that is suitable for the MR damper model. In particular, the induced electromotive force (EMF) that occurs between the coil and MR fluid is considered in the dynamic model. According to Faraday's law, the EMF $\mathcal{J}$ is formally defined as

$$\mathcal{J} = N\frac{d\Phi_B}{dt} \tag{2.3}$$

where $\mathcal{J}$ is the EMF, N is the number of turns on the coil, and Φ_B is the magnetic flux. It is known that MR fluids are filled with micrometer-sized magnetizable particles. When the magnetic field induced by the current in the coil and the magnetizable particles pass through the coil, the magnetic flux is directly proportional to the velocity of the magnetizable particles. According to this description, the following expression can be obtained

$$\mathcal{J} = \lambda v \tag{2.4}$$

where λ is the EMF constant. Therefore, the completed electrical equation that includes the input voltage, resistance, inductance and EMF is as follows

$$U = IR + L\frac{dI}{dt} + \lambda v \tag{2.5}$$

where U is the input voltage, R is the resistance, and L is the inductance. The electrical parameters R, L and λ are assumed constant without any temperature effect. The mathematical model with the LuGre model for the MR damper is proposed in Eqs. (2.1). In addition, the complete electrical equation is formulated in Eq. (2.5). To integrate the exerted damping force with the electrical equation, a diagram of an operational MR damper is presented in Fig. 2. When the external excitation displacement x and velocity v are applied to the MR damper, the exerted damping force f is produced, which can be adjusted with the input current I. Then, the damping force can be measured by using a load cell transferred to a personal computer (PC). Here, the PC receives signals including the damping force, external excitation displacement and velocity. Accordingly, the diagram of the MR damper is successfully designed, which can be extensively implemented in the system modeling, parameter identification and vibration control.

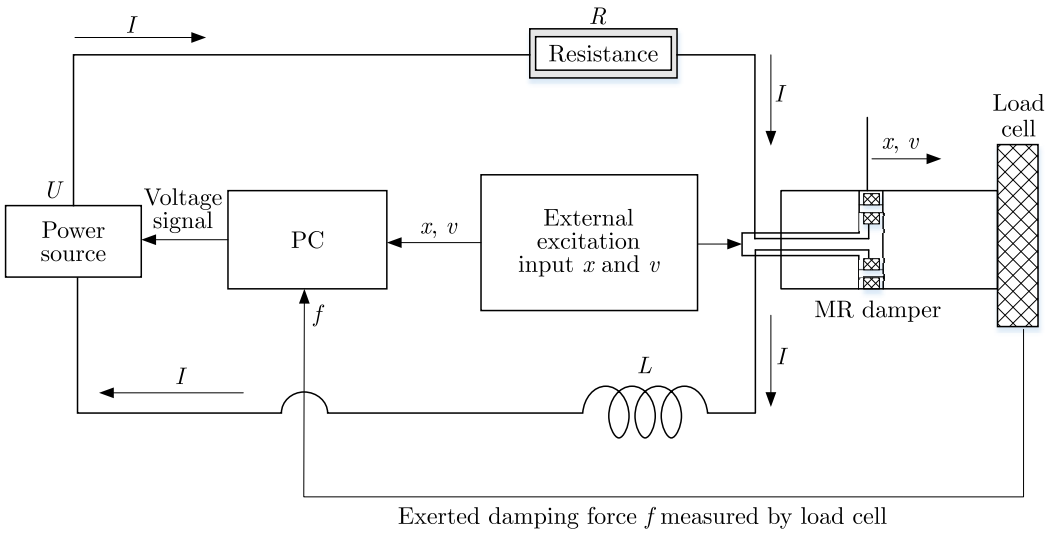

Fig. 2. A diagram of an operational MR damper

Finally, the proposed dynamic model with a state-space matrix form using Eqs. $(2.1)_1$ and (2.5) can be formulated as

$$\dot{\mathbf{X}} = \mathbf{AX} + \mathbf{BW} \qquad \mathbf{Y} = \mathbf{CX} \tag{2.6}$$

where

$$\mathbf{X} = \begin{bmatrix} x \\ z \\ I \end{bmatrix} \qquad \mathbf{A} = \begin{bmatrix} 0 & 0 & 0 \\ 0 & -\alpha|v| & 0 \\ 0 & 0 & \frac{-R}{L} \end{bmatrix} \qquad \mathbf{B} = \begin{bmatrix} 1 & 0 & 0 \\ 0 & 1 & 0 \\ 0 & \frac{-\lambda}{L} & \frac{1}{L} \end{bmatrix}$$

$$\mathbf{W} = [v, v, U]^{\mathrm{T}} \qquad \mathbf{C} = [1, 0, 0]$$

In particular, $\mathbf{X}$ is the system state vector, $\mathbf{Y}$ is the system output, $\mathbf{A}$ and $\mathbf{B}$ are the system matrices, $\mathbf{W}$ is the input vector, and terms v and U are the inputs.

3. Parameter identification

Dynamic modeling of a system is the first step toward analyzing an engineering problem. In Section 2, the dynamic model of an MR damper is formulated by Eqs. (2.6). The exerted damping force for an MR damper is also included in Eq. $(2.1)_2$. Moreover, there are 11 unknown parameters (α, δ, ε, $p_{1,2,3}$, $q_{1,2}$, R, L and λ) in the dynamic model using Eqs. $(2.1)_2$ and (2.6). In this study, parameter identification is proposed to identify these unknown parametersr. First, the SLPSO algorithm (Li *et al.*, 2012) is employed to find the unknown parameters. Then, the FF can be defined as an object function to be optimized by the SLPSO algorithm. When the SLPSO algorithm has optimized the FF with a set of parameters, the final parameters are the solutions for the unknown parameters.

3.1. Self-learning particle swarm optimization

Although the conventional PSO algorithm can find the local optimal solution to an optimization problem, the method is awkward when dealing with a complex and nonlinear optimization problem. Therefore, the SLPSO algorithm has been developed to deal with nonlinear systems and global optimization problems. The SLPSO has advantages including global optimization,

rapid convergence and searching ability, which are suitable for performing system parameter identification for the MR damper. First, the basic updated equation for the standard PSO for each particle j is described as follows

$$x_j'^{\,d} = x_j^d + v_j'^{\,d} \tag{3.1}$$

where $x_j'^{\,d}$ and x_j^d represent the current and previous positions in the d-th dimension for the particle j, respectively, while $v_j'^{\,d}$ is the current velocity. For the standard PSO algorithm, the updated equation of the particle velocity is as follows

$$v_j'^{\,d} = wv_j^d + \eta_1 r_1(x^d_{pbest_j} - x_j^d) + \eta_2 r_2(x^d_{gbest} - x_j^d) \tag{3.2}$$

where $w \in (0,1)$ is the inertia weight, v_j^d is the previous velocity for the particle j, η_1 and η_2 are positive acceleration constants, r_1 and r_2 are random numbers from 0 to 1, $x^d_{pbest_j}$ is the best position found for the particle j so far, and x^d_{gbest} is the best position found by the whole set of particles so far. When the current velocity $v_j'^{\,d}$ is updated, the new position $x_j'^{\,d}$ is updated to minimize the objective function for each iteration. However, the SLPSO has four velocity-updated strategies (exploitation, jumping out, exploration and convergence) to enable each particle to independently deal with different situations. For each particle j, the learning equations corresponding to the four operators are respectively given as follows:

1) Operator a: learning from its *pbest* position

$$\text{exploitation:} \quad v_j'^{\,d} = wv_j^d + \eta_3 r_j^d(pbest_j^d - x_j^d) \tag{3.3}$$

2) Operator b: learning from a random position nearby

$$\text{jumping out:} \quad x_j'^{\,d} = x_j^d + v_a vg^d N(0,1) \tag{3.4}$$

3) Operator c: learning from the *pbest* of a random particle

$$\text{exploration:} \quad v_j'^{\,d} = wv_j^d + \eta_3 r_j^d(pbest^d_{rand} - x_j^d) \tag{3.5}$$

4) Operator d: learning from the *abest* position

$$\text{convergence:} \quad v_j'^{\,d} = wv_j^d + \eta_3 r_j^d(abest^d - x_j^d) \tag{3.6}$$

where r_j^d is the random number for each particle j, η_3 is the acceleration constant, and $pbest^d_{rand}$ is the *pbest* of a random particle (which is better than $pbest_j$). The jumping step v^d_{avg} is the average speed of all particles in the d-th dimension, which is calculated using $v^d_{avg} = \sum_{j=1}^{N} |v_j^d|/N$, and N is the population size, where $N(0,1)$ is a random number generated from the normal distribution with a mean of 0 and a variance of 1. The *abest* position is an archive of the best position found so far. Finally, the position of each particle is updated to minimize the objective function.

In the SLPSO algorithm, each particle has its own velocity-updating strategy to address different situations for a nonlinear system. The cooperation of the four strategies is implemented by an adaptive learning framework at an individual level, which enables each particle to choose an optimal strategy according to its own local fitness landscape. The performing procedure for the SLPSO algorithm can be found in (Li *et al.*, 2012).

3.2. Sliding mode observer

For the dynamic model with the LuGre model in Eq. $(2.1)_1$, the variable z is an internal state and is unmeasurable. In addition, the current I is unknown. To solve the problem of estimating the states of z and I, a state observer can be implemented. The conditions are that the external excitation displacement x, velocity v and the input voltage U are known. Moreover, the system matrices $\mathbf{A}$ and $\mathbf{B}$ and the input vector $\mathbf{W}$ in Eq. $(2.6)_1$ are also known. The unknown states of z and I must be rapidly estimated to converge toward the real states. Therefore, a sliding mode observer (SMO) in accordance with Eq. $(2.6)_1$ is written as follows

$$\dot{\widehat{\mathbf{X}}} = \mathbf{A}\widehat{\mathbf{X}} + \mathbf{B}\mathbf{W} + \boldsymbol{\Delta} \tag{3.7}$$

where $\widehat{\mathbf{X}} = [\widehat{x}, \widehat{z}, \widehat{I}]^{\mathrm{T}}$, $\boldsymbol{\Delta} = \mathbf{K}\varepsilon$, $\mathbf{K} = [k_1, k_2, k_3]^{\mathrm{T}}$, $\varepsilon = |e|\,\mathrm{sgn}\,(e)$, and $e = \widehat{x} - x$, $\widehat{x}$, $\widehat{z}$ and $\widehat{I}$ are the estimated displacement, internal state and current, respectively. Terms k_1, k_2 and k_3 are known positive constants. The corresponding error dynamic equation between Eqs. $(2.6)_1$ and (3.7) is

$$\dot{\mathbf{E}} = \mathbf{A}\mathbf{E} + \boldsymbol{\Delta} \tag{3.8}$$

where $\mathbf{E} = \widehat{\mathbf{X}} - \mathbf{X} = [\widehat{x} - x, \widehat{z} - z, \widehat{I} - I]^{\mathrm{T}}$.

If Eq. (3.8) is an asymptotically stable system, then $\mathbf{E} \to \mathbf{0}$ with $t \to \infty$ and $\mathbf{A}$ is a stable matrix. Here, the term $\boldsymbol{\Delta}$ can be viewed as a control input for the stable system, which should be satisfied as follows

$$\|\boldsymbol{\Delta}\|_2 = \|\mathbf{K}\varepsilon\|_2 \leqslant \|\mathbf{K}\|_2\|\varepsilon\|_2 = \|\mathbf{K}\|_2|e| \leqslant \gamma\|\mathbf{E}\|_2 \tag{3.9}$$

where $\|\cdot\|_2$ is the Euclidean norm and γ is a positive constant. From the mentioned inequality equation, it is revealed that

$$|e| \leqslant \|\mathbf{E}\| \qquad 0 < \sqrt{k_1^2 + k_2^2 + k_3^2} \leqslant \gamma \tag{3.10}$$

To prove that the corresponding error dynamic equation is asymptotically stable, a Lyapunov candidate function L can be proposed as follows

$$L = \mathbf{E}^{\mathrm{T}}\mathbf{P}\mathbf{E} \tag{3.11}$$

where $\mathbf{P} \in \mathbb{R}^{3\times3}$ is the positive definite and diagonal matrix. The time derivative of L is

$$\dot{L} = \dot{\mathbf{E}}^{\mathrm{T}}\mathbf{P}\mathbf{E} + \mathbf{E}^{\mathrm{T}}\mathbf{P}\dot{\mathbf{E}} = \mathbf{E}^{\mathrm{T}}(\mathbf{A}^{\mathrm{T}}\mathbf{P} + \mathbf{P}\mathbf{A})\mathbf{E} + 2\mathbf{E}^{\mathrm{T}}\mathbf{P}\boldsymbol{\Delta} \tag{3.12}$$

If the homogeneous system $\dot{\mathbf{E}} = \mathbf{A}\mathbf{E}$ is asymptotically stable, there are positive definite matrices $\mathbf{P}$ and $\mathbf{Q}$ such that

$$\mathbf{A}^{\mathrm{T}}\mathbf{P} + \mathbf{P}\mathbf{A} = -2\mathbf{Q} \tag{3.13}$$

where $\mathbf{Q} \in \mathbb{R}^{3\times3}$ is the positive definite matrix. Then, Eq. (3.12) can be obtained as

$$\dot{L} = -2(\mathbf{E}^{\mathrm{T}}\mathbf{Q}\mathbf{E} - \mathbf{E}^{\mathrm{T}}\mathbf{P}\boldsymbol{\Delta}) \tag{3.14}$$

According to the Rayleigh principle (Andersen, 2000)

$$\lambda_{max}(\mathbf{Q})\mathbf{E}^{\mathrm{T}}\mathbf{E} \geqslant \mathbf{E}^{\mathrm{T}}\mathbf{Q}\mathbf{E} \geqslant \lambda_{min}(\mathbf{Q})\mathbf{E}^{\mathrm{T}}\mathbf{E} = \lambda_{min}(\mathbf{Q})\|\mathbf{E}\|_2^2 \tag{3.15}$$

where λ_{max} are the maximum eigen values of $\mathbf{Q}$ and λ_{min} are the minimum eigen values of $\mathbf{Q}$. Here, inequality equation Eq. (3.9) is used, from which the inequality expression is as follows

$$\mathbf{E}^{\mathrm{T}}\mathbf{P}\boldsymbol{\Delta} \leqslant \|\mathbf{E}\|_2\|\mathbf{P}\|_2\|\boldsymbol{\Delta}\|_2 = \lambda_{max}(\mathbf{P})\|\boldsymbol{\Delta}\|_2\|\mathbf{E}\|_2 \leqslant \gamma\lambda_{max}(\mathbf{P})\|\mathbf{E}\|_2^2 \tag{3.16}$$

where λ_{max} are the maximum eigen values of $\mathbf{P}$. If the condition satisfies $\mathbf{E}^{\mathrm{T}}\mathbf{Q}\mathbf{E} \geqslant \mathbf{E}^{\mathrm{T}}\mathbf{P}\boldsymbol{\Delta}$, then we can find an inequality equation by using Eqs. $(3.10)_2$, (3.15) and (3.16), as follows

$$0 < \sqrt{k_1^2 + k_2^2 + k_3^2} \leqslant \gamma \leqslant \frac{\lambda_{min}}{\lambda_{max}} \tag{3.17}$$

Constants k_1, k_2 and k_3 can be selected according to the above inequality equations. When the inequality equation $\mathbf{E}^{\mathrm{T}}\mathbf{Q}\mathbf{E} \geqslant \mathbf{E}^{\mathrm{T}}\mathbf{P}\boldsymbol{\Delta}$ exists, $\dot{L} \leqslant 0$ in Eq. (3.14) is obtained as

$$\dot{L} = -2(\mathbf{E}^{\mathrm{T}}\mathbf{Q}\mathbf{E} - \mathbf{E}^{\mathrm{T}}\mathbf{P}\boldsymbol{\Delta}) \leqslant 0 \tag{3.18}$$

Then, the error dynamic equation Eq. (3.8) is an asymptotically stable system, and $\mathbf{E} \to 0$ with $t \to \infty$. Hence, the proposed SMO can correctly and rapidly estimate the unknown states of z and I to converge toward the real states.

3.3. Parameter identification

In practical applications of MR dampers, the input voltage U, excitation displacement x, excitation velocity v and the output damping force f are known. However, the internal states of z and the current I are unavailable, and the parameters α, δ, ε, p_1, p_2, p_3, q_1, q_2, R, L and λ in the dynamic model of the MR damper are also unknown. In the process of identifying these parameters, we can find the identification parameters $\widehat{\alpha}$, $\widehat{\delta}$, $\widehat{\varepsilon}$, $\widehat{p}_1$, $\widehat{p}_2$, $\widehat{p}_3$, $\widehat{q}_1$, $\widehat{q}_2$, $\widehat{R}$, $\widehat{L}$ and $\widehat{\lambda}$. When $\widehat{\alpha}$, $\widehat{R}$, $\widehat{L}$ and $\widehat{\lambda}$ are found, the estimated states of $\widehat{z}$, $\dot{\widehat{z}}$ and $\widehat{I}$ can be obtained using the SMO. Then, the identified damping force $\widehat{f}$ can be obtained as follows

$$\widehat{f} = \widehat{\beta}(\widehat{I})v + \widehat{\delta}x + \widehat{\varepsilon}\dot{\widehat{z}} + \widehat{\gamma}(\widehat{I})\widehat{z} + f_0 \tag{3.19}$$

where $\widehat{\beta}(\widehat{I}) = -\widehat{p}_1\widehat{I}^2 + \widehat{p}_2\widehat{I} + \widehat{p}_3$ and $\widehat{\gamma}(I) = \widehat{q}_1\widehat{I} + \widehat{q}_2$.

If the estimated damping force $\widehat{f}$ is equal to the real damping force f, we can conclude that the dynamic model is successfully formulated with the identified parameters. Therefore, the FF is proposed as follows

$$\mathrm{FF} = \sum_{i=1}^{n} |f(t_i) - \widehat{f}(t_i)| \tag{3.20}$$

Finally, the process of parameter identification is combined with the SMO. The identified damping force $\widehat{f}$, FF and SLSO algorithms are proposed, and the diagram for parameter identification is displayed in Fig. 3. The real damping force $f(t_i)$ is produced by the external excitation input displacement, velocity and voltage. Then, the SLPSO randomly selects a set of proper parameters $\widehat{\alpha}$, $\widehat{\delta}$, $\widehat{\varepsilon}$, $\widehat{p}_1$, $\widehat{p}_2$, $\widehat{p}_3$, $\widehat{q}_1$, $\widehat{q}_2$, $\widehat{R}$, $\widehat{L}$ and $\widehat{\lambda}$ to minimize the FF at each iteration. When the FF converges toward the minimum value, the final identified parameters are the identification results presented by the SLPSO algorithm.

4. Numerical experiments

In the numerical experiments, there are two parts to execute. First, the system state of x of the MR damper is assumed to be available and the SMO is proposed to estimate the unavailable states of z and I. Then, the parameters of the mathematical model are unknown, and the SMO and SLPSO are implemented to identify the unknown parameters. The numerical parameters for numerical experiments are illustrated in Table 1. The dynamic model of the MR damper is solved by the Runge-Kutta method with the ODE 45 function using MATLAB. First, to verify the efficiency of the proposed dynamic model, the external excitation velocity is given as

Table 1. The given numerical parameters for numerical experiments

$\alpha = 3\,\mathrm{mm}^{-1}$,	$R = 5$,	$L = 0.1\,\mathrm{H}$,	$\lambda = 5 \cdot 10^{-5}\,\mathrm{Vs/mm}$	
$\varepsilon = 0.5\,\mathrm{Ns/mm}$,	$\delta = 1\,\mathrm{N/mm}$,	$q_1 = 800\,\mathrm{N/A}$,	$q_2 = 15\,\mathrm{N}$	
$p_1 = 1\,\mathrm{Ns/mmA}^2$,	$p_2 = 10\,\mathrm{Ns/mmA}$,	$p_3 = 0.5\,\mathrm{Ns/mm}$		

$v = 16\pi\cos(4\pi/5)t\,\mathrm{mm/s}$, and the input voltages are $U = 1\,\mathrm{V}$, $U = 10\,\mathrm{V}$ and $U = 50\,\mathrm{V}$. The phase plane of the damping force versys velocity with different input voltages is shown in Fig. 4, where it is evident that the proposed dynamic model can appropriately describe the hysteresis phenomena for a wide range of the external input velocities, voltages and current.

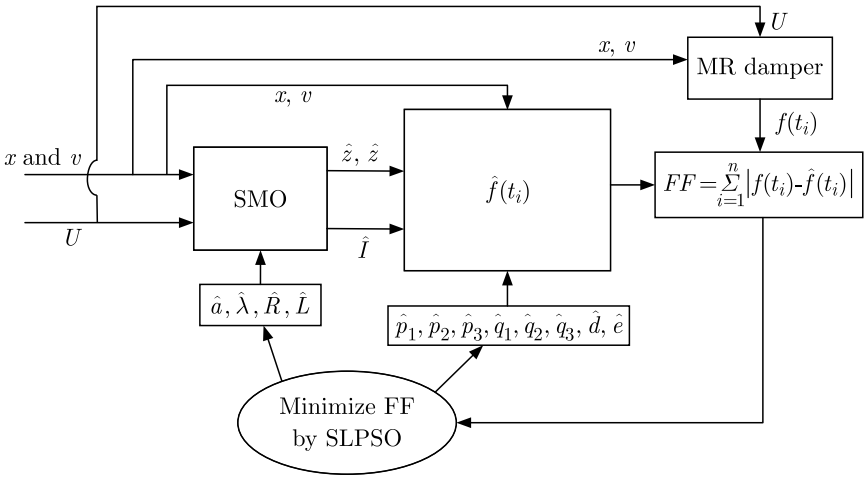

Fig. 3. Process of parameter identification using the SLPSO algorithm

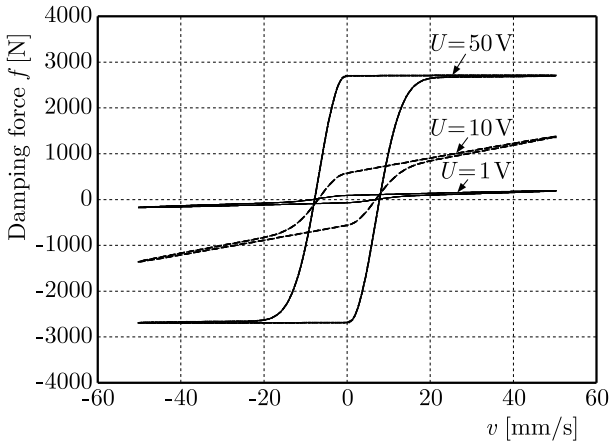

Fig. 4. Force-velocity plane for the variable input voltages

4.1. Sliding mode observer

To prove the estimation performance of the proposed SMO, the estimated results are demonstrated by using a numerical experiment in this Section. First, when the system matrices **A** and **B** are known, the input vector **W** is given as $v = 12\cos(\pi t)\,\mathrm{mm/s}$ and $U = 10\sin(\pi t/2)\,\mathrm{V}$. Therefore, the real states of z and I can be produced by using the above parameters and input vector in dynamic Eq. $(2.6)_1$. Nevertheless, for implementation of the SMO, the displacement x is available. The initial conditions of the estimation states are given as $\widehat{z}(0) = 1\,\mathrm{mm}$ and $\widehat{I}(0) = 2\,\mathrm{A}$.

The constants k_1, k_2 and k_3 for the SMO are selected according to inequality equations (3.17) to perform the best convergence performance between the real and estimated states. Figure 5 displays the responses between the real and estimated states by using the proposed SMO. A comparison between z and $\widehat{z}$ is displayed in Fig. 5a. Although the initial conditions of $z(0)$ and $\widehat{z}(0)$ are different, the estimation state of $\widehat{z}$ rapidly converges toward the real state of z in the initial period. Similarly, comparisons of I and $\widehat{I}$ are displayed in Fig. 5b. Although the initial conditions of $I(0)$ and $\widehat{I}(0)$ are different, the estimation state of $\widehat{I}$ rapidly converges toward the real state I in the initial period. In summary, the unknown states of z and I can be rapidly and correctly estimated by the SMO proposed in this paper.

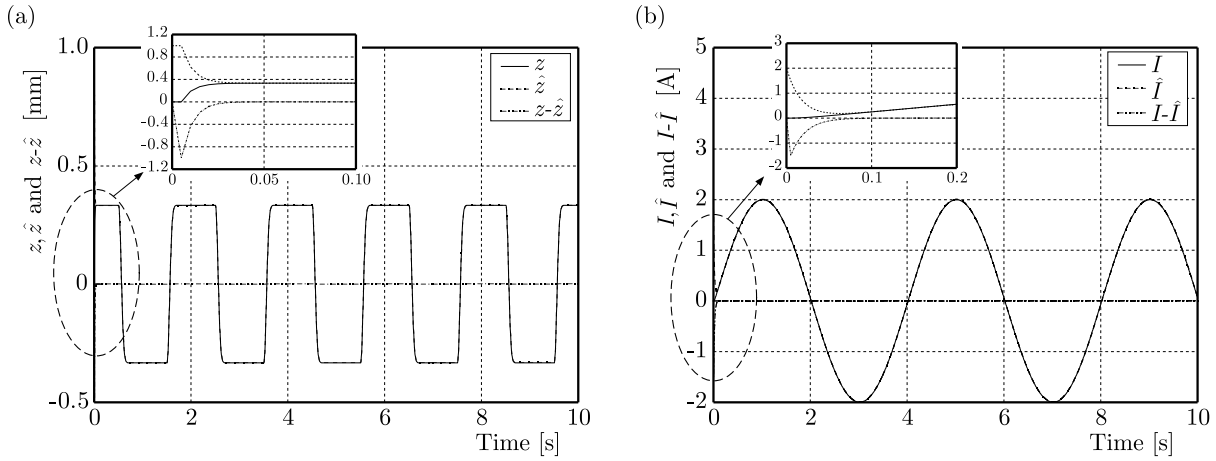

Fig. 5. Responses of the estimated states by using the SMO

4.2. Identification results

The external excitation displacement and velocity are respectively given as $x = 12\sin(2\pi/2.5)t$ mm and $v = (24\pi/2.5)\cos(2\pi/2.5)t$ mm/s, the operational duration of external excitation is 10 s, and the sampling time is $\Delta t = 5 \cdot 10^{-3}$ s. In the numerical experiments, the real exerted damping force f is obtained by using the given parameters, the external excitation displacement and external excitation velocity. However, the adjusting pf the damping force is dependent on the varying input current produced by the input voltage. Therefore, the input voltage plays a major role in producing the damping force. In the process of parameter identification for the MR damper, there are three kinds of input voltages: $U_1 = 10$, $U_2 = |10\sin(\pi/2.5)t|$ and $U_3 = t$. Accordingly, there are three types of damping forces produced by using U_1, U_2 and U_3. The processes of parameter identification using the SLPSO in Fig. 3 are implemented and performed. Table 2 lists the identification results by using U_1, U_2 and U_3. The feasible domains for each parameter are given, and the SLPSO algorithm can randomly search for the proper parameters in the feasible domains to minimize the FF. From the identification results, it is evident that the average of absolute error percentage by using U_1 is maximum, and the average absolute error percentage by using U_3 is minimum. A comparison of the responses of the FF by using U_1, U_2 and U_3 is shown in Fig. 6. Here, it is clear that the responses of the FF by using U_3 is minimum, and the responses of the FF by using U_1 is maximum. From these results, it can be determined that the identified parameters by using U_3 are equivalent to the real parameters. In the numerical experiments, the identified responses of displacement, velocity and damping force are respectively denoted as $\widehat{x}_1$, $\widehat{v}_1$ and $\widehat{f}_1$ by using the identified parameters with the input voltage U_1 in Table 2. The identified responses of displacement, velocity and damping force are respectively denoted as $\widehat{x}_2$, $\widehat{v}_2$ and $\widehat{f}_2$ by using the identified parameters by the input voltage U_2 in Table 2. Similarly, the identified responses of displacement, velocity and

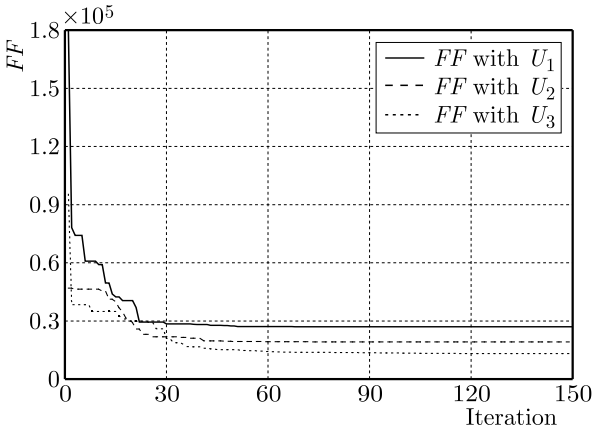

Fig. 6. Responses comparison of FF by using U_1, U_2 and U_3

Table 2. Identification results by using input voltages U_1, U_2 and U_3

Parameters	Given values	Feasible domain	Identified values/absolute error percentages		
			U_1	U_2	U_3
α	3	1.5-4.5	2.439/18.69%	2.360/21.31%	2.318/22.71%
R	5	2.5-7.5	7.500/50%	7.500/50%	6.299/25.98%
L	0.1	0.05-0.15	0.141/41%	0.150/50%	0.150/50%
$\lambda(10^{-5})$	5	2.5-7.5	7.500/50%	3.411/31.78%	7.185/43.70%
ε	0.5	0.25-0.75	0.716/43.2%	0.750/50%	0.750/50%
δ	1	0.5-1.5	1.500/50%	1.500/50%	1.500/50%
q_1	800	400-1200	1036.165/29.52%	1054.162/31.77%	869.212/8.65%
q_2	15	7.5-22.5	22.500/50%	18.716/24.77%	9.219/38.54%
p_1	1	0.5-1.5	1.500/50%	1.500/50%	1.215/21.50%
p_2	10	5-15	12.706/27.06%	11.853/18.53%	10.184/1.84%
p_3	0.5	0.25-0.75	0.750/50%	0.494/0.12%	0.750/50%
Average of absolute error percentages [%]			41.77% (Max)	34.39%	32.19% (Min)

damping force are respectively denoted as $\widehat{x}_3$, $\widehat{v}_3$ and $\widehat{f}_3$ by using the identified parameters by the input voltage U_3 in Table 2. In Fig. 7, the responses of real damping force f are produced with the given parameters $(\alpha, R, L, \ldots, p_2, p_3)$ in Table 2, whereas the responses of estimated damping forces $\widehat{f}_{1,2,3}$ are produced with the identified parameters $(\widehat{\alpha}, \widehat{R}, \widehat{L}, \ldots, \widehat{p}_2, \widehat{p}_3)$ by using the input voltages $U_{1,2,3}$, respectively. Comparing the responses of damping forces f and $\widehat{f}_{1,2,3}$ versus displacement in Figs. 7a, 7c and 7e, it is evident that the errors between f and $\widehat{f}_1$ are maximum (Fig. 7a), and the errors between f and $\widehat{f}_3$ are minimum (Fig. 7e). Figure 7b displays a comparison of the response between the real damping forces f and $\widehat{f}_1$ versus velocity. Figure 7d presents a comparison between the damping forces f and $\widehat{f}_2$ versus velocity, and Fig. 7f presents a comparison between the damping forces f and $\widehat{f}_3$ versus velocity. Comparing the damping forces between f and $\widehat{f}_{1,2,3}$ in Figs. 7b, 7d and 7f, it is clear that the errors between f and $\widehat{f}_1$ are maximum (Fig. 7b), and the errors between f and $\widehat{f}_3$ are minimum (Fig. 7f). From these comparisons, it is evident that the responses of $\widehat{f}_3$ with the identified parameters are similar to the real damping force f.

To confirm the values of the identified parameters in Table 2, the same external excitation displacement and velocity are used, and an other input voltage of $U(t) = 10\sin(\pi t/10)$, $0 \leqslant t \leqslant 10\,\mathrm{s}$ is applied to the MR damper. First, a comparison between the real internal state

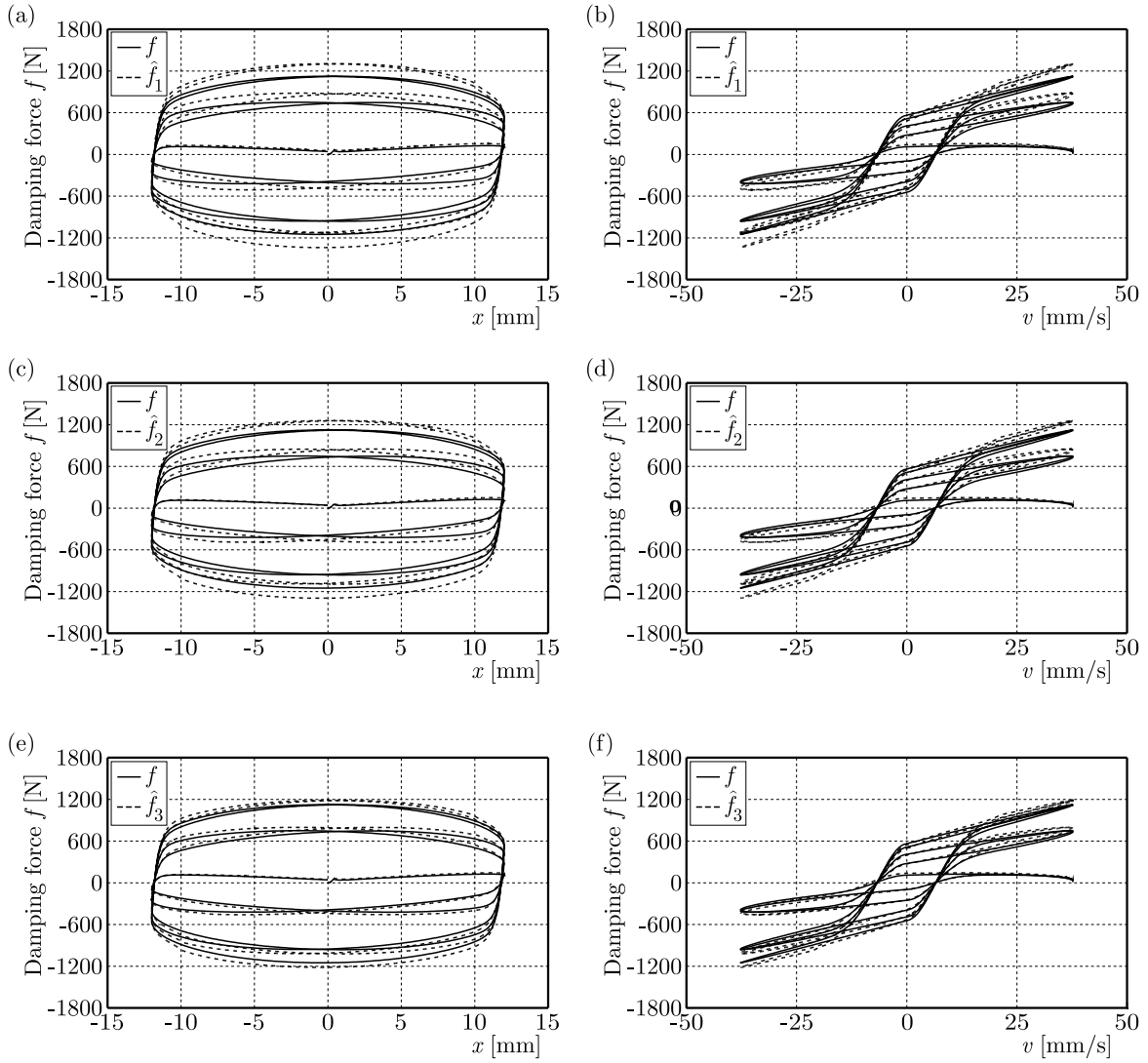

Fig. 7. Comparison of the response between f and $\widehat{f}_{1,2,3}$

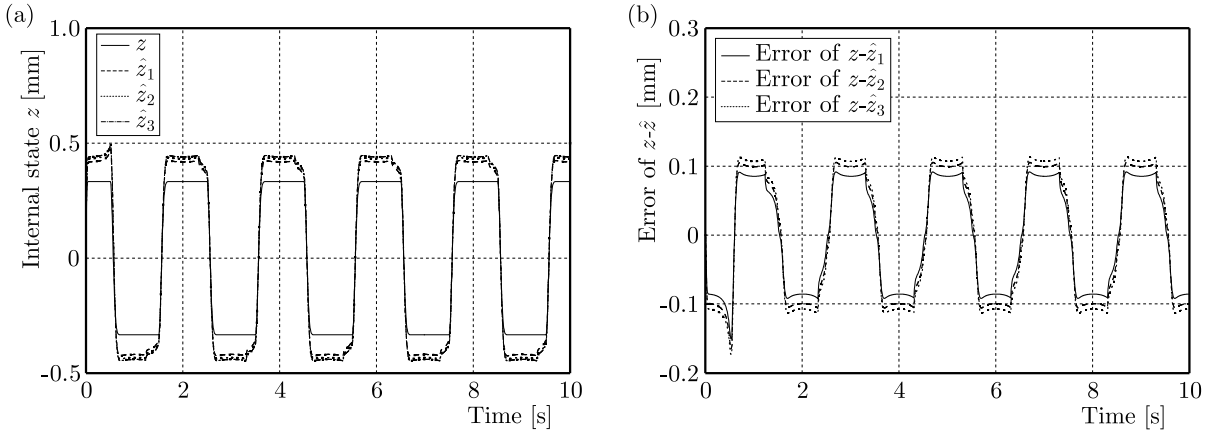

Fig. 8. Comparison of the responses between z and $\widehat{z}_{1,2,3}$ by the SMO

of z and the estimated internal state of $\widehat{z}$ by the SMO is shown in Fig. 8. The real internal state of z is obtained from Eq. $(2.1)_1$ with the given value of $\alpha = 3$. The estimated internal states $\widehat{z}_{1,3,3}$ are obtained by using the SMO with the identified values of $\widehat{\alpha}$ in Table 2. It is revealed that the errors of z and $\widehat{z}$ are between 0.1 mm. It is also evident that the estimated state of $\widehat{z}$ is successfully estimated by using the SMO. Figure 9 displays a comparison between the real damping f and estimated damping forces $\widehat{f}_{1,2,3}$. The error responses of $f - \widehat{f}_{1,2,3}$ versus displacement and velocity are respectively shown in Figs. 9a and 9b. Here, it can be observed that the error responses of $f - \widehat{f}_3$ are less than the other two errors. The error responses of $f - \widehat{f}_{1,2,3}$ versus time are respectively shown in Figs. 9c and 9d, where it is evident that the error responses of $f - \widehat{f}_{1,2,3}$ are also minimum.

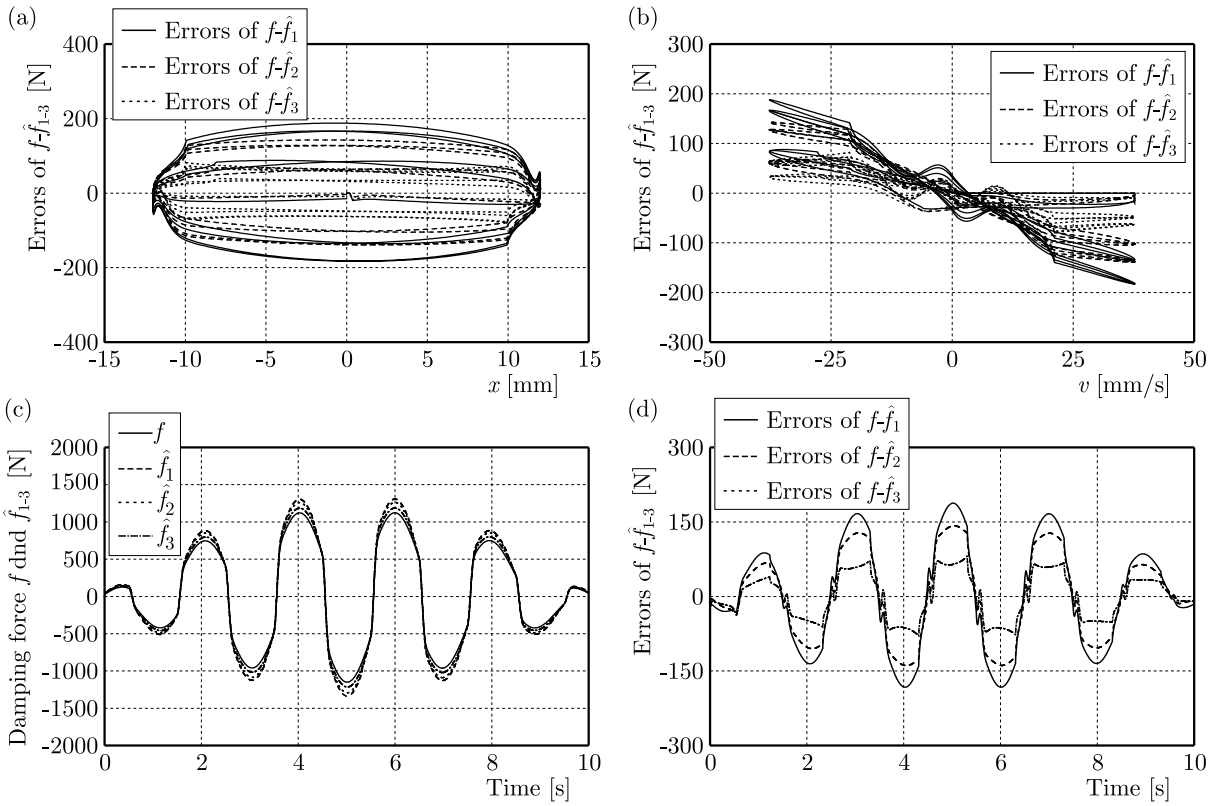

Fig. 9. Comparison of the responses between f and $\widehat{f}_{1,2,3}$ by using the input voltage $U(t) = 10\sin(\pi t/10)\,\mathrm{V}$

4.3. Discussion

In the numerical experiments, this paper proposes a methodology for parameter identification using the SLPSO for an MR damper with a new dynamic model. The real internal state, current and damping force are obtained from the dynamic model with given parameters and inputs. In practical conditions, the external excitation inputs (displacement and velocity) and input voltage are known, and the output is the exerted damping force. The parameters of the dynamic model are unknown. In this paper, three types of input voltages are implemented in the dynamic modeling. From the numerical experiments, three sets of parameters are revealed by three input voltages shown in Table 2. From a comparison of the response between the real damping force f and estimated damping forces $\widehat{f}_{1,2,3}$, it is revealed that the estimated damping force $\widehat{f}_3$ produced by the identified parameters is more similar to the real damping force f than the other two cases. Therefore, we can conclude that the responses found by using U_1 are dull,

and the responses by using U_2 are periodic, the two input voltages cannot excite the unknown parameters in the dynamic modelling. In contrast, the responses obtained by using U_3 are dynamic and varied, they can excite the unknown parameters by the SLPSO. Furthermore, the error responses between f and $\widehat{f}_3$ are smaller than the other two error responses shown in Fig. 9. Therefore, the parameters identified by using U_3 are equivalent to the real parameters of the MR damper when the identification conditions (e.g., U, x, v and feasible domain) are known and bound. Finally, the proposed dynamic model for the MR damper is practical for use with the input voltage. The method of parameter identification for the MR damper by using the SMO and SLPSO is feasible and successfully applied in this study. The advantage of the proposed dynamic model with the input voltage is the ability of adjusting the MR damper force.

5. Conclusions

In the dynamic response of an MR damper, the relationship between the exerted damping force and the external excitation input velocity is termed the hysteresis phenomenon. It is interesting to formulate a dynamic model for the MR damper. Therefore, in this paper, we proposed a dynamic model based on the LuGre model and an electrical equation for the MR damper. Then, the damping force can be practically adjusted by using the input voltage. However, there are some unknown parameters in the dynamic model of the MR damper. Accordingly, parameter identification by using the SLPSO algorithm is proposed to identify these unknown parameters, and the SMO is used to estimate the unmeasurable states. From numerical experiments, it is clear that the unmeasurable states are correctly estimated by the proposed SMO. Then, the unknown parameters of the dynamic model have been successfully identified by the SLPSO algorithm. The contributions of this paper are as follows:

- a new dynamic model based on the LuGre model and an electrical equation for MR dampers is formulated to fit for the hysteresis behavior,
- for the proposed dynamic model, the damping force can be practically adjusted by using the input voltage,
- the SMO is proposed to estimate the unmeasurable states,
- the unknown parameters of the MR damper are successfully identified by using SLPSO algorithm.

In the future work, the proposed dynamic model of MR dampers can be integrated into suspension systems to perform semi-active vibration control.

References

1. Ahmed K., Yan P., Li S., 2021, Duhem model-based hysteresis identification in piezo-actuated nano-stage using modified particle swarm optimization, *Micromachines*, **12**, 3, 315

2. Ambhore N., Hivarale S.D., Pangavhane D., 2013, A study of Bouc-Wen model of magnetorheological fluid damper for vibration control, *International Journal of Engineering Research and Technology (IJERT)*, **2**, 2, 1-6

3. Andersen K.M., 2000, An elementary proof of Rayleigh's principle, *International Journal of Mathematical Education in Science and Technology*, **31**, 3, 449-453

4. Balamurugan L., Jancirani J., 2013, Application of a new modified parametric algebraic model for magnetorheological damper in vehicle semi-active suspension, *International Journal of Automobile Engineering Research and Development*, **3**, 1, 1-14

5. Bartkowski P., Zalewski R., Chodkiewicz P., 2019, Parameter identification of Bouc-Wen model for vacuum packed particles based on genetic algorithm, *Archives of Civil and Mechanical Engineering*, **19**, 322-333

6. Bhowmik S., 2011, *Modelling and Control of Magnetorheological Damper: Real-Time Implementation and Experimental Verification*, Department of Mechanical Engineering Technical University of Denmark

7. Boada M.J.L., Boada B.L., Diaz V., 2018, A novel inverse dynamic model for a magnetorheological damper based on network inversion, *Journal of Vibration and Control*, **24**, 15, 3434-3453

8. Graczykowski C., Pawłowski P., 2017, Exact physical model of magnetorheological damper, *Applied Mathematical Modelling*, **47**, 400-424

9. Ikhouane F., Rodellar J., 2005, On the hysteretic Bouc-Wen model, *Nonlinear Dynamics*, **42**, 63-78

10. Ikhouane F., Rodellar J., 2007, *Systems with Hysteresis: Analysis, Identification and Control Using the Bouc-Wen Model*, John Wiley & Sons

11. Ismail M., Ikhouane F., Rodellar J., 2009, The hysteresis Bouc-Wen model, a survey, *Archives of Computational Methods in Engineering*, **16**, 2, 161-188

12. Jiménez R., Álvarez-Icaza L., 2005, LuGre friction model for a magnetorheological damper, *Structural Control and Health Monitoring*, **12**, 91-116

13. Li C., Yang S., Nguyen T.T., 2012, A self-learning particle swarm optimizer for global optimization problems, *IEEE Transactions on Systems, Man, and Cybernetics – Part B: Cybernetics*, **42**, 3, 627-646

14. Metered H., 2010, *Modelling and Control of Magnetorheological Dampers for Vehicle Suspension Systems*, School of Mechanical, Aerospace and Civil Engineering, University of Manchester

15. Naz S., Raja M.A.Z., Mehmood A., Zameer A., Shoaib M., 2021, Neuro-intelligent networks for Bouc-Wen hysteresis model for piezo stage actuator, *The European Physical Journal Plus*, **136**, 396

16. Nguyen X.B., Komatsuzaki T., Truong H.T., 2022, Adaptive parameter identification of Bouc-Wen hysteresis model for a vibration system using magnetorheological elastomer, *International Journal of Mechanical Sciences*, **213**, 106848

17. Niola V., Palli G., Strano S., Terzo M., 2019, Nonlinear estimation of the Bouc-Wen model with parameter boundaries: Application to seismic isolators, *Computers and Structures*, **222**, 1-9

18. Pelliciari M., Marano G.C., Cuoghi T., Briseghella B., Lavorato D., Tarantino A.M., 2018, Parameter identification of degrading and pinched hysteretic systems using a modified Bouc-Wen model, *Structure and Infrastructure Engineering*, **14**, 12, 1573-1585

19. Peng Y., Yang J., Li J., 2018, Parameter identification of modified Bouc-Wen model and analysis of size effect of magnetorheological dampers, *Journal of Intelligent Material Systems and Structures*, **29**, 7, 1464-1480

20. Ramli M.H.M., Minh T.V., Chen X., 2019, Pseudoextended Bouc-Wen model and adaptive control design with applications to smart actuators, *IEEE Transactions on Control Systems Technology*, **27**, 5, 2100-2109

21. Roussel R., Edelen A., Ratner D., Dubey K., Gonzalez-Aguilera J.P., Kim Y.K., Kuklev N., 2022a, Differentiable Preisach modeling for characterization and optimization of accelerator systems with hysteresis, *arXiv preprint*, arXiv:2202.07747

22. Roussel R., Edelen A., Ratner D., Dubey K., Gonzalez-Aguilera J.P., Kim Y.K., Kuklev N., 2022b, Differentiable Preisach modeling for characterization and optimization of particle accelerator systems with hysteresis, *Physical Review Letters*, **128**, 20, 204801

23. Xu S., Wu Z., Wang J., Hong K., Hu K., 2022, Generalized regression neural network modeling based on inverse Duhem operator and adaptive sliding mode control for hysteresis in piezoelectric actuators, *Proceedings of the Institution of Mechanical Engineers, Part I: Journal of Systems and Control Engineering*, **236**, 5, 1029-1037

24. Zalewski R., Nachman J., Shillor M., Bajkowski J., 2014, Dynamic model for a magnetorheological damper, *Applied Mathematical Modelling*, **38**, 2366-2376

25. Zhao X., Wu S., Pan H., 2018, A hybrid model of magnetorheological dampers based on generalized hysteretic biviscous operators, *Journal of Intelligent Material Systems and Structures*, **29**, 14, 2979-2985

26. Zhu H., Rui X., Yang F., Zhu W., Wei M., 2019, An efficient parameters identification method of normalized Bouc-Wen model for MR damper, *Journal of Sound and Vibration*, **448**, 26, 146-158

Manuscript received November 20, 2022; accepted for print February 2, 2023

JOURNAL OF THEORETICAL AND APPLIED MECHANICS
61, 2, pp. 275-287, Warsaw 2023
https://doi.org/10.15632/jtam-pl/162128

ON VISCOELASTIC FIBER JET FORMATION BY FORCESPINNING AT HIGH ROTATION RATE

Daniel N. Riahi

Department of Mechanical Science and Engineering, University of Illinois at Urbana-Champaign, Urbana, IL, USA, and School of Mathematical and Statistical Sciences, University of Texas Rio Grande Valley, Brownsville, Texas, USA

Saulo Orizaga

Department of Mathematics, New Mexico Institute of Mining and Technology, Socorro, New Mexico, USA

e-mail: saulo.orizaga@nmt.edu

We consider a nonlinear three-dimensional viscoelastic fiber jet that is generated during a forcespinning process. We provide a particular case for such a rotating jet at a high rotation rate. We use a viscoelastic constitutive model for the jet equations and then applying a new slender body approach, we continue with proper scaling and perturbation technique to develop a new model for such a jet system. We find that the profiles for jet quantities versus arc length are notably different from all those in related studies reported before for either high or low rotation rates. In particular, jet radius first rapidly decreases as the arc length decreases and then reaches its macro- or nano-scale size not far away from its exit section. The present model can predict a nano-fiber jet that is entirely based on proper scaling, perturbation technique and full fluid mechanics laws and equations.

Keywords: rotating flow, rotating jet, gravity effect, high rotating jet, polymeric fluid

1. Introduction

In a forcespinning process the fluid is driven through an orifice located in a spinneret that is rotating. This leads to formation of a jet flow. This is a process that has been developed and shown experimentally to generate macro- and nano-fiber jets. So far, there has been a number of studies that were either in theoretical and computational or in experimental areas of the mechanics of rotating fiber jet flows at low or high rotation rates (Sarkar *et al.*, 2010; Vazquez *et al.*, 2012; Altecor *et al.*, 2012; Padron *et al.*, 2013; Taghavi and Larson, 2014a,b; Noroozi *et al.*, 2017, 2020; Riahi, 2018a,b, 2020, 2021; Riahi *et al.*, 2018; Riahi and Orizaga, 2022). The studies were needed to understand how to produce fibers for possible use in various applications such as those in defense, energy, aerodynamics and health areas, etc. In the theoretical and computational modeling studies that have been done so far for such jet flows, an essential approach that has been used is based on the consideration that the jet is very thin. Such an approach is called a slender jet approach, and it is meant that the ratio of the fiber jet radius to its centerline scale is fixed to be small as compared to a value of one.

A notable experimental study done during a forcespinning process was due to Padron *et al.* (2011). These authors applied a high speed photography procedure to further insight into the nature of the whole mechanism that was involved in fiber jet formation by the forcespinning process. The authors noted that during the forcespinning process, a polymeric fluid was driven by rotational forces into an orifice that was located in a spinneret rotating and producing rotational forces. That resulted in a jet with a curved centerline moving forward in the three-dimensional space. The authors determined the effects at a high rotation rate of the rotational forces generated by the rotating spinneret. They also determined the effect of polymeric viscosity of the

fluid solution in their experiment, where they tested such an effect by using polymeric fluid solutions having different weight percentage of PEO (Polyethylene oxide) concentration in water. In addition, they determined a projection of the trajectory of the nano-fiber jet in a horizontal plane, speed of the jet and diameter of the nano-fiber jet.

The first investigation of the rotating jet flow generated by centrifugal spinning which developed the so-called regularization approximations were due to Taghavi and Larson (2014a,b). These authors studied a two-dimensional version of the steady jet flow of a Newtonian viscous fluid formed by centrifugal spinning. They introduced an approach referred to as a regularization procedure where the original dynamic equation for momentum of the fluid in the radial direction was strongly modified and changed. The authors introdused an additional term which was a third derivative with respect to the arc length of the curvature of the jet flow. They then determined computationally the solution of their regularized model with prescribed boundary conditions. However, there was no justification from a mathematical fluid mechanics point of view for such changes and modifications of the original fluid dynamical equations in the steady and two-dimensional version. But the authors explained the reasoning for using their regularization approach as numerically divergent and lacking solutions for rotating driven jet quantities. Some authors in the past studies on such rotating jet flow problems at high rotation rates tried using asymptotic techniques. Noroozi *et al.* (2017) investigated a three-dimensional steady rotating polymeric jet at a high rotation rate using and extended the regularization procedure (Taghavi and Larson, 2014a,b). The authors made a strong additional extension to the regularization procedure by, in particular, including third derivatives in the jet arc length of two local curvature functions in the radial component of the momentum equation. The authors then determined the solution to their new regularization model using a collocation method and calculated some jet quantities such as radius of the jet flow.

It should be also noted that the work by Noroozi *et al.* (2020) extended the regularization approach (Taghavi and Larson, 2014a,b) to investigate the steady rotating fiber jet flow of a viscous Newtonian fluid at a large rate of rotation. The authors also took into account the effects due to mass diffusion and an approximated form of the drag force exerted by the ambient air. The authors also performed some experimental work for a fluid solution of a polymeric nature. Regarding their regularization approximations, they notably needed to restrict the applicability of their model by disregarding all higher order terms in their regularization system. This resulted in the validity of their findings only to apply to a very thin interval for the arc length just in the vicinity of the exit section of the fiber jet flow.

Although the emphasis of the present article is mostly on the high rotation regime for the rotating viscoelastic jet. We find useful to briefly state several research investigations that were completed by Riahi and his co-authors (Riahi, 2018a, 2020, 2021; Riahi *et al.*, 2018; Riahi and Orizaga, 2022). In the last several years, even though those studies were at a low rotation rate regime because a number of different aspects were rather similar to those presented in this paper, which include methodology and type of the fiber jet determined based on an experimentally tested variable viscosity formula (Riahi *et al.*, 2018; Riahi, 2020; Riahi and Orizaga, 2022) or viscoelastic type of the jet flow (Riahi, 2018a; Riahi, 2021). However, there are some new aspects of our research on the rotating viscoelastic fiber jet that we included in the present investigation.

In the present paper, we include our newly developed slender body approach where the aspect ratio of radius of the jet at the orifice to the jet centerline scale is assumed to be a considerably small and positive constant ε. We also restrict the jet centerline domain to begin at a location very close to the orifice center but not at a such center in order to avoid possible numerical divergence and singularity there (Taghavi and Larson, 2014a). In addition, in contrast to the previous studies (Riahi, 2018a,b, 2020, 2021; Riahi *et al.*, 2018; Riahi and Orizaga, 2022), we employ proper scaling and perturbation techniques to investigate forcespinning of a three--dimensional nonlinear viscoelastic jet system at high rotation rates, on the basis of full fluid

equations of motion and dynamical laws. We were successfully able to determine macro and nano--fiber jet quantities at high rotation rates. This is the first time that such a proper scaling and perturbation approach, based on firm mathematical and fluid mechanics foundations, is capable for selected values of the parameters in the experimental range to predict macro- and nano-fiber jets at a moderate value of the arc length from the exit section of the jet flow. Our calculated results indicated, in particular, new profiles for the fiber jet radius and other jet quantities, which are notably different from the corresponding ones for low rotation rates (Riahi, 2018a, 2021) or those at high rotation rates determined by the regularization approach (Noroozi *et al.*, 2017, 2020) which involved severe approximations to the fluid mechanics equations for the jet.

2. Mathematical formulation

We show where the rotating viscoelastic jet flow begins by describing the original form of the governing fluid mechanics equations (Riahi, 2021) provided in a coordinate system rotating with the spinneret at the same rotational speed. Such a coordinate frame is attached and totally fixed to the spinneret (Fig. 1) for a forcespinning system (Altecor *et al.*, 2012; Riahi, 2021). In this figure, the Cartesian coordinate (X, Y, Z) system attached to the rotating spinneret is shown. In addition, its angular velocity of rotation is Ω, which is the same as that of the rotating spinneret, and whose axis along the vertical axis opposite to the gravity force $\mathbf{g}$. In addition, o is the spinneret centre and c is a half length of the spinneret. The coordinate of the jet centreline at the jet exit is $X = c$ and $Y = Z = 0$.

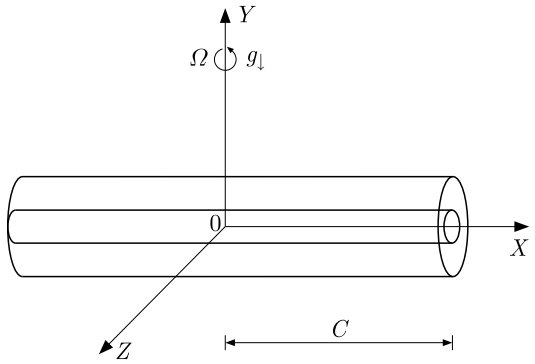

Fig. 1. Coordinate system and spinneret rotating about the vertical axis

We consider the original fluid mechanics equations for the continuity and momentum in the already described rotating frame for the non-Newtonian jet flow for, where we represent the stress tensor $\mathbf{T}$ by the upper convected Maxwell model as it is appropriate for the viscoelastic jet (Riahi, 2018a; Bird *et al.*, 1987; Larson, 1998). These equations were given in (Riahi, 2021), but are recalled below for sake of the readers' satisfaction

$$\begin{aligned}
&\nabla \cdot \mathbf{u} = \mathbf{0}\\
&\frac{\partial \mathbf{u}}{\partial t} + \mathbf{u} \cdot \nabla \mathbf{u} + \frac{1}{\rho}\nabla P - \frac{1}{\rho}\nabla \cdot \mathbf{T} + \boldsymbol{\omega} \times (\boldsymbol{\omega} \times \mathbf{r}) + 2\boldsymbol{\omega} \times \mathbf{u} + \mathbf{g} = \mathbf{0}\\
&\mathbf{T} = \boldsymbol{\tau} + \eta_s(\nabla \mathbf{u} + \nabla \mathbf{u}^{\mathrm{T}})\\
&-\lambda \frac{\partial \boldsymbol{\tau}}{\partial t} - \boldsymbol{\tau} + \lambda(-\mathbf{u} \cdot \nabla \boldsymbol{\tau} + \nabla \mathbf{u}^{\mathrm{T}} \cdot \boldsymbol{\tau} + \boldsymbol{\tau} \cdot \nabla \mathbf{u}) + \eta_p(\nabla \mathbf{u}^{\mathrm{T}} + \nabla \mathbf{u}) = \mathbf{0}
\end{aligned} \tag{2.1}$$

where all the symbols were already defined in (Riahi, 2021), but here we briefly describe them so that the readers have a self-contained article. Here $\mathbf{u}$ is velocity vector of the jet, P is pressure, $\mathbf{T}$ is stress tensor, ρ is density of the fluid, $\mathbf{g}$ is the gravity force per mass unit, t is time variable,

$\boldsymbol{\omega}$ is the angular velocity vector with magnitude Ω (Padron *et al.*, 2013; Riahi *et al.*, 2018), $\mathbf{r}$ is the position vector, η_p and η_s are viscosities of polymer and solvent, respectively, and λ is relaxation time. The cartesian coordinate system (X, Y, Z) is already described and shown in Fig. 1. As in (Riahi, 2021) and in experiments (Padron *et al.*, 2013), the present model is three--dimensional in space and, thus, includes the effect of gravity. The condition for the fiber jet arc length is given below

$$\Big(\frac{\partial \mathbf{X}}{\partial s}\Big)^2 + \Big(\frac{\partial \mathbf{Y}}{\partial s}\Big)^2 + \Big(\frac{\partial \mathbf{Z}}{\partial s}\Big)^2 - 1 = 0 \tag{2.2}$$

Here s is arc length along the centerline of the jet. Thus, $\mathbf{X}$, $\mathbf{Y}$ and $\mathbf{Z}$ are the components of $\mathbf{r}$ of a point on the centerline of the jet with respect to the coordinate (X, Y, Z) system.

Original Eqs. (2.1) and (2.2) are subjected to the known kinematic and dynamic conditions at the boundary of the free surface of the jet flow (Chhabra *et al.*, 2008), which are

$$\begin{aligned} &-\frac{\partial \beta}{\partial t} = \mathbf{u}\cdot\nabla\beta \qquad\qquad \beta \equiv n - R(s,\phi,t) \\ &(\mathbf{T} - P\mathbf{I})\cdot\mathbf{n} + \sigma\kappa\mathbf{n} = \mathbf{0} \end{aligned} \tag{2.3}$$

These boundary conditions are already given in (Riahi *et al.*, 2018; Riahi, 2021), and so here the new symbols are defined briefly. Here, n and ϕ are radial and azimuthal variables, respectively, in a polar coordinate in a plane perpendicular to the jet centerline, $\mathbf{n}$ is a unit normal vector in outward direction to the surface of the jet, $\mathbf{I}$ is the unit matrix, R is radius of the jet, σ is surface tension, and $\kappa \equiv \nabla\cdot\mathbf{n}$ is a double mean curvature of the boundary of the jet. Here (2.3) are given by independent variables (s, n, ϕ) of local orthogonal curvilinear coordinates. We also have the following main boundary conditions at the boundary of the orifice

$$\begin{aligned} &\mathbf{X} = \mathbf{Y} = \mathbf{Z} = \frac{\partial \mathbf{Y}}{\partial s} = \frac{\partial \mathbf{Z}}{\partial s} = \mathbf{0} \qquad\qquad \frac{\partial \mathbf{X}}{\partial s} - 1 = \mathbf{0} \\ &u - U = 0 \qquad\quad 0 = R - r_o \quad \text{at} \quad s = s_1 \end{aligned} \tag{2.4}$$

where r_0 is the orifice surface at the exit section of the fiber jet, U is the centerline velocity at the orifice's boundary and s is taken as the jet centerline from the orifice boundary in order to avoid presence of any singularity that may exist at the orifice center (Taghavi and Larson, 2014a). So, based on the value for $r_o = 1\,\text{mm}$ (Padron *et al.*, 2013) and our selected value for ε, which will be described below, we choose $s_1 = 0.001\,\text{m}$.

Equations (2.1)-(2.4) are then made in a non-dimensional form, and such a procedure is given in (Riahi, 2021). Thus, we describe it briefly here. We use the scaling U for $\mathbf{u} = (u, v, w)$, ρU^2 for pressure, r_0 for n and R, s_0 for s and (X, Y, Z), C/U for t and $(\eta_s + \eta_p)U/r_0$. Here s_0 is the centerline scale for the jet. For simplicity, we present the resulting non-dimensional variables in terms of the same original symbols. The resulting system contains several non-dimensional parameters, which are as follows. Rossby number $\text{Ro} = U/(\Omega s_0)$ is a rotational parameter, Froude number $\text{Fr} = U/\sqrt{s_0 g}$ represents the gravity effect, Weber number $\text{We} = \rho U^2 r_o$ is a surface tension parameter, Reynolds number $\text{Re} = U s_0/(\eta_s + \eta_p)$ represents the viscosity effect, Deborah number $\text{De} = \lambda U/s_0$ is a viscoelastic parameter, $\eta = \eta_p/(\eta_s + \eta_p)$ is the viscosity ratio, and a small aspect ratio is given by $\varepsilon = r_o/s_0$ ($\varepsilon \ll 1$), where λ is the relaxation time.

Typical values of units in the SI system for constants and scales described above have been chosen in the range of values which are in agreement mostly with those in the experimental studies (Padron *et al.*, 2013; Noroozi *et al.*, 2020) and are given as follows. The velocity scale is $U = 0.3\text{-}2.0\,\text{m/s}$, jet radius scale $r_0 = 0.2\text{-}0.3\,\text{mm}$, fluid density $\rho = 1000.0\text{-}1070.0\,\text{kg/m}^3$, surface tension $\sigma = 2.0\text{-}2.5\dot{\text{N}}/\text{m}$, angular velocity $\Omega = 200.0\text{-}2200.0\,\text{rad./s}$, viscosity of the polymer $\eta_p = (1.2\text{-}3.5)(10^{-3})\,\text{Ns/m}^3$, viscosity of the solvent $\eta_s = (0.8\text{-}1.4)(10^{-3})\,\text{Ns/m}^3$, relaxation time $\lambda = (0.001\text{-}100.0)\,\text{s}$, and acceleration due to gravity is $g = 9.81\,\text{m/s}^2$.

We already assumed that the fiber jet is a long and very slender jet, then the aspect ratio ε is a quite small parameter ($\varepsilon \ll 1$), so that we take its value to be $\varepsilon = 0.001/3$. Such a value is chosen for our scaling analysis in order to make sure that our modeling system, which will be determined based on the leading order terms in powers of ε for original Eqs. (2.1)-(2.3), is sufficiently accurate. The scaling analysis is based on the expansions for the dependent variables that are given below

$$\begin{aligned}
&(u, v, w) = [u_0 + \varepsilon n u_1 + \ldots, \varepsilon n v_1 + \ldots, \varepsilon n w_1 + \ldots] \\
&(P, R) = [P_0 + \varepsilon n P_1 + \ldots, R_0 + \varepsilon R_1 + \ldots] \\
&(X, Y, Z) = [X_0 + \varepsilon X_1 + \ldots, Y_0 + \varepsilon Y_1 + \ldots, Z_0 + \varepsilon Z_1 + \ldots] \\
&\tau_{ij} = \tau_{0ij}\delta_{ij} + \varepsilon n \tau_{1ij} + \ldots
\end{aligned} \tag{2.5}$$

where u_i, P_i, R_i, X_i, Y_i, Z_i ($i = 0, 1, \ldots$) and v_i and w_i ($i = 1, 2, \ldots$) are, in general, functions of s, ϕ and t. The subscripts ij for τ_{ij}, which are functions of s and ϕ, in $(2.5)_4$, mean that normal stress components in the directions of s and n are for $i = j = 1, 2$. However, the tangential components of stress are if $i \neq j$. Here, δ equal to 1 for $i = j$ and 0 for $i \neq j$.

Using (2.5) in the system, we apply the small and constant parameter ε to properly scale variables of the system. System (2.1) and (2.2) is then simplified and reduced for the steady case. We retain only the leading order terms and make additional simplifications to arrive at a final simplified and reliable system which is found to be dependent only on u_0, R_0, X_0, Y_0, Z_0 and normal stress terms. Dropping the subscripts for simplicity, the resulting form of the modeling system is given below

$$\begin{aligned}
&u\frac{\partial u}{\partial s} = \frac{1}{\mathrm{We}R^2}\frac{\partial R}{\partial s} - \frac{E_9}{\mathrm{Fr}^2} + \frac{2u}{\mathrm{Ro}}\Big(E_8\frac{\partial Z}{\partial s} - E_{10}\frac{\partial X}{\partial s}\Big) + \frac{1}{\mathrm{Ro}^2}[E_8(X+1) + E_{10}Z] \\
&\quad + \frac{1-\eta}{\mathrm{Re}}\Big(\frac{6}{R}\frac{\partial R}{\partial s}\frac{\partial u}{\partial s} + 2\frac{\partial 2u}{\partial s}^2\Big) + \frac{1}{\mathrm{Re}R^2}\frac{\partial R^2(\tau_{11} - \tau_{22})}{\partial s} \\
&u\frac{\partial R}{\partial s} = -\frac{R}{2}\frac{\partial u}{\partial s} \\
&\Big(\frac{\partial X}{\partial s}\frac{\partial^3 X}{\partial s^3} + \frac{\partial Y}{\partial s}\frac{\partial^3 Y}{\partial s^3} + \frac{\partial Z}{\partial s}\frac{\partial^3 Z}{\partial s^3}\Big)\frac{\partial u}{\partial s} + \frac{2}{3}\frac{\partial E_0}{\partial s} = 0 \\
&\Big(-u^2 + \frac{1}{\mathrm{We}R}\Big)E_0 - \frac{2u}{\mathrm{Ro}}\Big(E_{11}\frac{\partial Z}{\partial s} - E_{13}\frac{\partial X}{\partial s}\Big) + \frac{E_{12}}{\mathrm{Fr}^2} + \frac{1}{\mathrm{Ro}^2}[E_{11}(X+1) - E_{13}Z] \\
&\quad + \frac{1}{\mathrm{Re}}\Big(2\frac{\partial \eta}{\partial s}uE_0 + \frac{7\eta E_0}{3}\frac{\partial u}{\partial s} + \frac{(5\eta u}{3}\frac{\partial E_0}{\partial s}\Big)
\end{aligned} \tag{2.6}$$

and

$$\tau_{11} + \mathrm{De}\Big(u\frac{\partial \tau_{11}}{\partial s} - 2\tau_{11}\frac{\partial u}{\partial s}\Big) = 2\eta\frac{\partial u}{\partial s} \qquad \tau_{22} + \mathrm{De}\Big(u\frac{\partial \tau_{22}}{\partial s} + \tau_{22}\frac{\partial u}{\partial s}\Big) = -\eta\frac{\partial u}{\partial s} \tag{2.7}$$

where the expressions for E_0-E_{13}, which are functions of X, Y and Z, and together with their derivatives with respect to s and are very lengthy, will not be given here. The boundary conditions are

$$\begin{aligned}
&X = Y = Z = \frac{\partial Y}{\partial s} = \frac{\partial Z}{\partial s} = u - 1 = R - 1 = \frac{\partial X}{\partial s} - 1 = 0 \qquad \text{at} \quad s = s_1 \\
&\tau_{11} - 2\eta\frac{\partial u}{\partial s} = \tau_{22} + \frac{\partial u}{\partial s} = 0 \qquad \text{at} \quad s = s_1
\end{aligned} \tag{2.8}$$

The above modeling system of equations and the boundary condition are based on the leading order terms in powers of the aspect ration ε in our scaling and perturbation procedure. Thus, it is important to make sure that higher order terms in our procedure will affect the results based

on our above modeling system, and we can achieve such assurance by keeping the aspect ration ε as small as we think it should. We already provided a very small value for ε that can make higher order terms, which are of the order ε^n $(n \geqslant 2)$, extremely small without any influence on the outcome of our modeling system. Hence, the modeling system based on the proper scaling and perturbation procedure very much relies on the way we adjust the aspect ratio. Even though such an adjustment is not unique, it provides reasonably assurance that the results of the modeling system can be reliable.

The imposed stress conditions at the exit section $s = s_1$ of the jet are chosen to be simply Newtonian since our early results based on numerical testing of our computational outcome indicated that changes of the stress condition were rather insensitive to the final results. This outcome is also consistent with the assumption that the molecules of the polymeric fluid have not been able to be stretched right at the boundary of the orifice.

3. Results and discussions

We present in this Section the results and discuss the solutions to the modeling system of the jet flow given by Eqs. (2.6)-(2.8) found by a computational procedure solving the initial value problem. We first convert Eqs. (2.6) and (2.7) into a system which consists of thirteen first order ordinary differential equations, where the independent variable is the arc length of the jet centerline s. Treating this system as an initial value problem, we solve it using a Runge-Kutta scheme of the fourth order, which is quite efficient (Ascher *et al.*, 1995). Since Eqs. (2.6) and (2.7) contain higher derivatives for some dependent variables, and Eqs. (2.8) does not have enough conditions at $s = s_1$ for solving the above stated 13 equations, we first carry out an asymptotic procedure in the limit of $s \to s_1$, which is similar to that applied before the two-dimensional approximation case where the rotation rate was low (Riahi, 2018) to determine the asymptotic solutions for a very small s $(0 < s \ll 1)$ in Eqs. (2.6) and (2.7). Then, we found the leading order expressions for the dependent variables, which were used to find some needed boundary conditions at $s = s_1$. We determined the solutions for such an initial value problem numerically and generated data for the jet quantities for different parameter values that were chosen to be in the range of experimental studies (Padron *et al.*, 2013; Noroozi *et al.*, 2017) during the forcespinning process. We were also careful that our numerical scheme did not lead to numerical instability by choosing a sufficiently small step size of the adjacent grid point, etc.

We generated computational data for the jet centerline speed, radius of the jet, trajectory of the jet in three-dimensional space, rate of strain, tensile force and rate of stretching for different values of all non-dimensional parameters of our modeling system. As we described before, the values of parameters were chosen to be in the range of those reported by Noroozi *et al.* (2017) in the experiments by Padron *et al.* (2013).

Figure 2 shows the radius R of the fiber jet versus the arc length s of the jet for the Weber number $\mathrm{We} = 0.037$, Reynold number $\mathrm{Re} = 0.2$, Froude number $\mathrm{Fr} = 1.0$, viscosity ratio $\eta = 0.4$ and different values for Deborah number $\mathrm{De} = 0.1,\ 0.05$ and Rossby number $\mathrm{Ro} = 0.059,\ 0.061$. We can observe from this figure that the effects of viscoelasticity and forces due to rotation are destabilizing because the radius of the jet decreases as viscoelasticity and/or rotational effects increase. Such effects of the rotation and viscoelasticity are also seen to be enhanced rapidly as the arc length of the jet increases. The fiber radius can reach macro- and nano-scale values for the jet not too far away from the exit section as we will explicitly explain later in this Section by providing a figure and generated data. The profile for the radius of the jet versus the arc length of its centerline at a such higher rotation rate is found to be very different from the results obtained for the high rotation rate by using the regularization modeling approach (Noroozi *et al.*, 2017, 2020) and for the low rotation rate for the asymptotic procedure (Riahi, 2018b). At the

high rotation rate, the fiber radius rapidly decreases with the increasing arc length for the jet close to its exit section. Such a rate of decrease is enhanced by the increasing Deborah number, while the arc length rate with the increasing s decreases for the jet centerline beyond some distance from the jet exit section. Our present results indicate that in contrast to those reported in (Riahi, 2018b) for low rotation rate cases, the fiber radius decreases as either rotation rate or relaxation time increases at a relatively smaller rate.

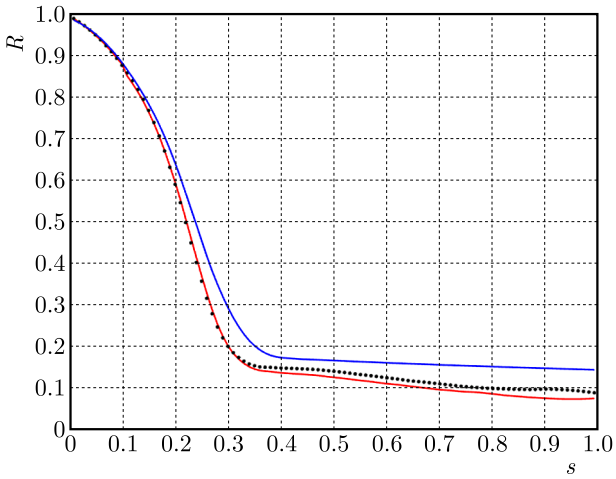

Fig. 2. Radius of the jet R versus arc length s of the jet centerline for the Weber number We = 0.037, Reynolds number Re = 0.2, viscosity ratio $\eta = 0.4$, Froude number Fr = 1.0, Deborah number De = 0.1 and Rossby number Ro = 0.059 (red line); De = 0.1 and Ro = 0.061 (dotted black line) and De = 0.05 and Ro = 0.061 (blue line)

The other noticeable observation in Fig. 2 is that at high rotation rates such as considered in this figure, the jet fiber significantly decreases with a very small increase in the rotation rate, and such rate of decrease is more noticeable for jets not too close to their exit section. An increase in the viscoelastic effect also decreases the jet radius but is less significant as compared to that due to the increase of the rotation rate.

Figure 3 presents the jet speed u versus arc length s for the Weber number We = 0.037, Reynolds number Re = 0.2, Froude number Fr = 1.0, viscosity ratio $\eta = 0.4$, Deborah number De = 0.05, 0.1) and Rossby number Ro = 0.059, 0.061. This figure shows that the value of speed gets higher as the rotation rate or viscoelasticity grows. In addition, the rate of such an increase is further enhanced when the jet moves away from its exit section. It is again apparent that the rotational forces or viscoelasticity tends to make the fiber jet more intensified which we refer to as some sort of destabilization effect exerted by either rotational or viscoelasticity effects on the speed of the fiber jet. However, a notable result shown in this figure is a significant increase of the jet speed with respect to a rather moderate increase in viscoelasticity. The value of the jet speed in also visibly higher for the jet not too close to its exit section. We also made some comparison between the present results at a high rotation rate with the results from the previous studies at a low rotation rate (Riahi, 2020, 2021). It is found that in the present case with high rotational forces, the speed of the jet and its rate of increase with respect to either arc length of the jet centerline, rotation rate or viscoelasticity takes higher values as the rotation rate, viscoelasticity or arc length takes higher values than those in the previous results (Riahi, 2020, 2021) in the case of a small rotation rate. In addition, the present profiles for the fiber jet speed are notably different from the previous results at small rotation rates as well as from those based on the high rotation rate model constructed by the regularization approximation. We can conclude by the combined results provided in Figs. 2 and 3 and our further data that the jets produced at a very high speed are in fact very thin.

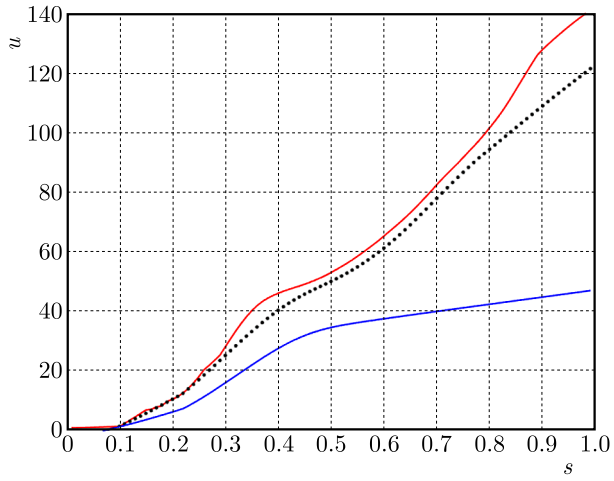

Fig. 3. Jet speed u versus arc length s of the jet centerline for Weber number We = 0.037, Froude number Fr = 1.0, Reynolds number Re = 0.2, viscosity ration $\eta = 0.4$, Deborah number De = 0.1 and Rossby number Ro = 0.059 (red line), De = 0.1 and Ro = 0.061 (dotted black line) and De = 0.05 and Ro = 0.061 (blue line)

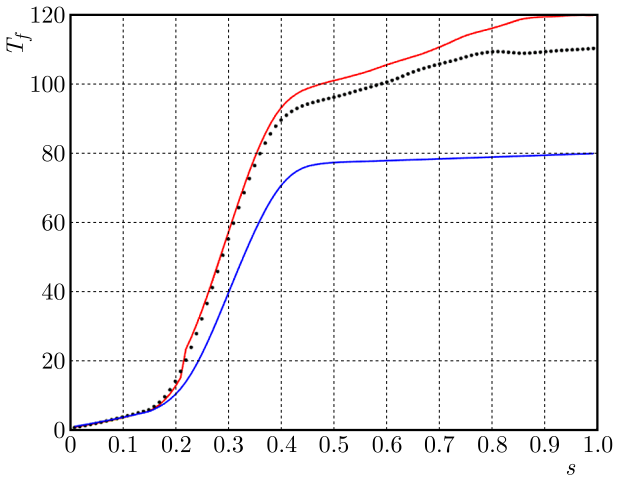

Fig. 4. Tensile force T_f versus arc length s of the jet centerline for the Weber number We = 0.037, Reynolds number Re, viscosity ratio $\eta = 0.4$, Froude number Fr = 1.0, Deborah number De = 0.1, Rossby number Ro = 0.059 (red line), De = 0.1 and Ro = 0.061 (dotted black line), De = 0.05 and Ro = 0.061 (blue line)

Figure 4 presents the tensile force T_f, whose expression is $R^2(\tau_{11} - \tau_{22})$ as provided in (Riahi, 2018a, 2021) versus the arc length s of the jet centerline for Weber number We = 0.037, Froude number Fr = 1.0, viscosity ratio $\eta = 0.4$, Reynolds number Re = 0.2, Deborah number De = 0.1, Rosby number Ro = 0.059 (red line), De = 0.1 and Ro = 0.061 (dotted black line), De = 0.05 and Ro = 0.061. This figure shows that the effect of the tensile force is intensified remarkably as the magnitude of rotational forces or viscoelasticity effects increase when the arc length of the fiber jet moves away further from its original exit section. We also noted that the rate of change of the tensile force with respect to the arc length of the fiber jet centerline takes higher values as the fiber jet moves away shortly from the orifice. Then it appears that the rate of increase drops as the fiber jet moves much further away from its original exit section. The reduction of the effect of relaxation time is observable in the case of the tensile force as it reduces more deeply and becomes very weakly dependent on the wave length of the jet centerline for jet locations not too close to its exit section. We also made calculation for the fiber jet parameters such as radius, etc. for several Weber numbers. In particular, we found that the radius of the fiber decreases

as the surface tension decreases. This result agrees with physical understanding of the surface tension as it generally exerts some stabilizing effect to slows down the fiber jet, which implies thickening of the jet.

Figure 5 provides some typical results in the Cartesian coordinates (X, Y, Z) of the jet trajectory or, equivalently, of the jet centerline in the three-dimensional domain, where X and Z are in the horizontal plane and Y is in the vertical direction for the given values of Reynolds, Weber, Deborah and Rossby numbers as well as the viscosity ratio η listed in the figure caption and for the Froude number Fr $= 0.1$ and 1.0. From the results shown in this figure, it can be seen that the local curvature of the jet centerline curve as well as its tightness increase as the effect of the gravity force becomes more significant. This result indicates that the force of gravity tends to speed up the fiber jet since the resultant rotational and gravity forces enhance jet effectiveness, and we refer this to as a kind of destabilizing effect exerted by the gravity force. It can also be seen from this figure that the effect of gravity force makes the jet centerline more three-dimensionally, which is expected since resultant force due to rotation and gravity becomes a more three-dimensional domain. In addition, we also calculated the jet centerline for several fixed values of the parameters Re, We, η and Fr but with different values of Ro and De. We observed that the curvature of the jet trajectory tends to locally increase as the rotational forces or viscoelasticity increase.

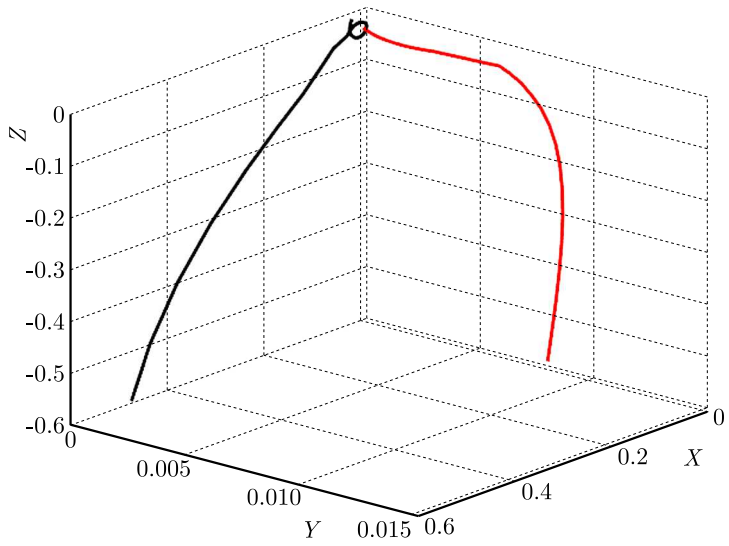

Fig. 5. Jet centerline in terms of the three-dimensional Cartesian coordinate (X, Y, Z) for the Reynolds number Re $= 0.1$, Weber number We $= 0.004$, Deborah number De $= 0.1$, Rossby number Ro $= 0.055$, viscosity ratio $\eta = 0.4$ and for two values of Froude number Fr $= 0.1$ (red line) and 1.0 (black line)

Figure 6 provides radius R of the fiber jet versus the arc length s of the jet centerline for Re $= 0.2$, Ro $= 0.06$, We $= 0.0039$, De $= 0.1$, Fr $= 1.0$ and viscosity ratio $\eta = 0.4$. We can observe from this figure that the fiber jet radius becomes very small fastly, approaching zero as the fiber jet moves away from its exit section by some rather small distance. The rate of decrease of the jet radius becomes large as the fiber jet moves further away from its exit section. To provide a more explicit demonstration for the fiber jet that reaches a nano-scale level, we also provide in Table 1 some generated data for this figure.

From the experimental studies (Padron *et al.*, 2013; Noroozi *et al.*, 2020), for the production of the polymeric fiber jet we set $r_0 = 0.29\,\text{mm}$ and our already chosen $\varepsilon = 0.001/3$) to make our model sufficiently accurate. The results are given in Table 1. Since both s and R are non-dimensional quantities, we use values given in Table 1 and proceed ih the way we made non--dimensional system in Section 2. We have dimensional arc length $ss_0 = (\varepsilon/r_0)s$, where s_0 is the dimensional scale of the fiber jet and r_0 is the scale for the fiber jet, so dimensional jet radius

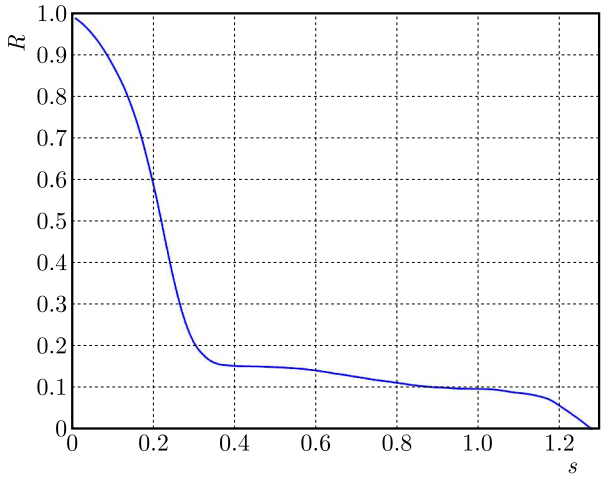

Fig. 6. Radius of the jet R versus the arc length for the jet centerline s for Re = 0.2, Ro = 0.06, We = 0.0039, De = 0.1, Fr = 1.0 and $\eta = 0.4$ with a nano-fiber jet achieved at a moderate distance from the jet exit section

is Rr_0. We now choose a value for the arc length from those listed in Table 1, that is $s = 1.10$, which corresponds to the fiber jet radius $R = 0.0776$. Then we find that the macro-scale jet is achieved at dimensional arc length of about 0.957 m with dimensional fiber radius of about 22.5 μm. Next, we choose from Table 1 $s = 1.30$, which corresponds to $R = 0.0003$. We then find that the nano-fiber jet is reached at dimensional arc length of about 1.131 m with dimensional fiber radius of about 87.0 nm.

Table 1. Generated data for Fig. 6, where s is the arc length of the jet centreline and R is the jet radius

s	0.0	0.2	0.4	0.6	0.8	1.0	1.10	1.20	1.275	1.30
R	1.0	0.591	0.152	0.133	0.108	0.0958	0.0776	0.0539	0.0019	0.0003

In addition to the above results for the radius of the fiber jet, we also calculated additional data for several other fiber jet quantities versus several parameters. We found that as compared to the already determined results for low rotation rates (Riahi, 2020, 2021), the present results at high rotation rates have notably higher speeds of the fiber jet, tensile force, rate of strain and rate of jet stretching. The corresponding arc length increases as the magnitude of rotational forces, viscoelasticity or the arc length of the fiber jet centerline increase.

We now compare the present results that we obtained based on proper scaling and perturbation methods at high rotation rates with the related studies done in the past (Noroozi *et al.*, 2017; Noroozi *et al.*, 2020) for fiber jets at high rotation rates, which are given as follows. Noroozi *et al.* (2017) extended the earlier developed regularization approach (Taghavi and Larson, 2014a,b) to study fiber jets generated by centrifugal spinning. Their extension included a number of additional assumptions and simplifications. They studied a non-Newtonian jet on the basis of a power-law model for the stress tensor, and they calculated the results numerically using a collocation method. Their calculated result for the radius and speed of the jet versus arc length of the jet centerline appeared to merge with the results for the inviscid case and remained as inviscid parameters for the arc length beyond some moderate value. These results qualitatively agree with the present results only for very small values of the arc length of the jet centerline. Noroozi *et al.* (2020) also extended the regularization procedure (Taghavi and Larson, 2014a,b) and studied centrifugal spinning of a Newtonian jet at high values of the rotation rate. The authors also included the presence of mass diffusion and an approximated version of the air-drag force in their jet modeling system. They significantly simplified their

model by discarding all higher order terms, so that their results appeared to become applicable only within the vicinity of the jet orifice. They ignored the presence of gravity by assuming that the rotational forces are much greater than the gravity force, and, in addition, they assumed that the jet centerline is in a fixed horizontal plane. They treated their modeling system as a boundary value problem and solved it numerically. Their graphical result for the fiber radius variation versus arc length was found to have some qualitative similarity with the present result only for sufficiently small values of the arc length. From the point of view of applied mathematics and fluid mechanics, we should note that a comparison between our present results presented in details in Section 3 and the results by Noroozi *et al.* (2017, 2020) indicated that our new findings are based on proper scaling. Our modeling system was based on original fluid mechanics laws and equations as well as perturbation technique, whereas the other related studies (Noroozi *et al.*, 2017, 2020) were basically based on the regularization approach, neglecting the gravity force and focusing mostly on a two-dimensional version of the fiber jet. Our present results take into account three-dimensionality of the jet in the presence of gravity force at high rotation rates, and we implemented a new slender body approach and a procedure to avoid the presence of numerical divergence. Our results predicted new fiber jet profiles for different jet quantities, and we were able to predict macro and nano-fiber jets at particular locations of the fiber jet at a moderate distance from the orifice.

4. Conclusions

We have considered a mathematical model describing the interesting and yet complicated dynamics of a thinning jet due to a rotating mechanism (forcespinning). We have presented simplifying assumptions and modeling conditions that are useful to treat such a complicated system of equations, and we believe that this approach provides a good point of reference fof such s problem. In this paper, we developed a theory based on full fluid mechanics laws and equations providing a model for a nonlinear three-dimensional viscoelastic jet system with the gravity force. It enables using of the upper convected Maxwell constitutive equations for the viscoelastic stress tensor in the momentum equations during the forcespinning process at high rotation rates. We applied a slender body assumption for the jet flow that started at a location very close to the orifice center and kept a sufficiently small value of the jet aspect ratio to maintain an accurate modeling system formed on the basis of the leading order terms in powers of a very small jet aspect ratio and with proper scaling of the jet variables. We determined numerically macro- and nano-fiber jet solutions for the modeling system. Our results for high rotation rates came from our newly developed model that for the first time predicted macro- and nano-fiber jets at a moderate distance from the jet initial formation. The results of our model were in contrast to the results found by regularization approximations (Noroozi *et al.*, 2017, 2020). The values of the fiber jet quantities and their rates of changes with respect to the arc length and parameters were found to be quite different from the corresponding ones from the regularization procedure at high rotation rates. We observed that the jet speed, stretching rate, strain rate, tensile force and jet curvature as well as their rates of increase with respect to the arc length of jet centerline were notably raised-up with the growing resultant rotational and gravity force, arc length and viscoelasticity after the jet moved away by a very small distance from the orifice. However, the jet radius and its rate of change with respect to the arc length were reduced significantly with the increasing arc length, resultant rotational and gravity force, viscoelasticity, and the jet radius reached a macro- and nano-scale size after some moderate distance from the jet exit section. The curvature of the fiber jet centerline was found to increase with the growing resultant rotational and gravity force, viscoelasticity and with the decreasing surface tension and the polymer

viscosity. Our overall results indicated that the fiber jet of a non-Newtonian fluid at a very high speed was very thin at the nano-scale level and was experienced by a strong tensile force.

Although the experimental observation of the nano-fiber formation at a high rotation rate have so far indicated that the nano-fiber jet began to form at a considerable time after jet initiation from the orifice. This actually means that after some considerable distance from the jet exit section, our predicted results showing that the initial location of the nano-fiber jet can not be far from the jet exit section opens two possible observations that are given as follows. Firstly, our result was based on particular and selected values of the jet parameters which were within the range from available experiments (Padron *et al.*, 2013; Noroozi *et al.*, 2017, 2020). This can stimulate new experimental efforts by searching selected parameters to determine if nano-fibers can be formed at a distance not far from the orifice, which, if so, it can agree with the present results and can be very valuable in fiber manufzcturing technologies to improve nano-fiber production of high yield. Secondly, an actual fiber jet system in the experiments contains other components that affect jet formation finalizing nano-fiber production, which include stabilizing effects of the ambient drag force, evaporation process of the solvent, temperature and humidity of the environment and the effect of presence of the collection device that collects the fiber. The authors plan to carry out such an additional work for a more completed model in the future, which may improve the present introductory model.

Finally, it should be noted that the present new theory and model for prediction of a nano--fiber scale jet at a moderate distance from the orifice, where computation is based on a rather simple numerical code, indicate that a future simulation of such a model incorporating a more sophisticated code could possibly lead to prediction of sub-nano fiber jets, which can bring a wide range of new ideas and exploration to develop new technologies with tremendous amount of benefits to the advancement of various factors for humanity.

Acknowledgments

S.O. thanks Anwar and Elizabeth from NMT for their continued support. The authors also thank the reviewers' comments and suggestions for an earlier version of this work that improved the quality of the present paper. In addition, S.O. thanks Cristina Villalobos, Timothy Huber and Elda Leal for the office space and hospitality at the University of Texas Rio Grande Valley (UTRGV).

References

1. Altecor A., Mao Y., Lozano K., 2012, Large-scale synthesis of tin-doped indium oxide nanofibers using water as solvent, *Functional Materials Letters*, **5**, 1250020
2. Ascher U.M., Mathheij R.M.M., Russell R.D., 1995, *Numerical Solution of Boundary Value Problems for Ordinary Differential Equations*, Philadelphia, PA, USA: SIAM Publication
3. Bird R.B., Curtiss C.F., Armstrong R.C., Hassager O., 1987, *Dynamics of Polymeric Liquids, vol. 1, Fluid Mechanics*, Wiley, New York
4. Chhabra R.P., Richardson J.F., 2008, *Non-Newtonian Flow and Applied Rheology*, 2nd Ed., Oxford, UK: Butterworth-Heinemann
5. Larson R.G., 1998, *The Structure and Rheology of Complex Fluids*, UK: Oxford
6. Noroozi S., Alamdari H., Arne W., Larson R.G., Taghavi S.M., 2017, Regularized string model for nanofibre formation in centrifugal spinning methods, *Journal of Fluid Mechanics*, **822**, 202-234
7. Noroozi S., Arne W., Larson R.G., Taghavi S.M., 2020, A comprehensive mathematical model for nanofibre formation in centrifugal spinning methods, *Journal of Fluid Mechanics*, **892**, A26-48

8. Padron S., Caruntu I.D., Lozano K., 2011, On 2d forcespinning modeling, *Proceedings of the 2011 ASME International Mechanical Engineering Congress and Exposition*, IMECE2011-64823, USA: ASME Publications, 821-830

9. Padron S., Fuentes A., Caruntu D., Lozano K., 2013, Experimental study of nanofiber production through forcespinning, *Journal of Applied Physics*, **113**, 024318

10. Riahi D.N., 2018a, Nonlinear rotating viscoelastic jets during forcespinning process, *Proceedings of the Royal Society, A: Mathematical, Physical and Engineering Science*, **474**, 20180346

11. Riahi D.N., 2018b, Rotating fiber jets during forcespinning with aerodynamic effect, *Journal of Engineering Mechanics*, **144**, 8, 04018069

12. Riahi D.N., 2020, On three-dimensional rotating polymeric fiber jets with gravity effect, *Fluid Dynamic Research*, **52**, 1-18

13. Riahi D.N., 2021, On forcespinning of nonlinear rotating jets of viscoelastic Boger fluids, *Journal of Non-Newtonian Fluid Mechanics*, **287**, 104442

14. Riahi D.N., Lozano K., Cremar L., Fuentes A., 2018, On nonlinear rotating polymeric jets during forcespinning process, *Fluid Dynamics Research*, **50**, 065507

15. Riahi D.N., Orizaga S., 2022, On rotationally driven nonlinear inclined polymeric jet with gravity effect, *Mathematics in Engineering*, **4**, 2, 1-18

16. Sarkar K., Gomez C., Zambrano S., Ramirez M., de Hoyos E., Vasquez H., Lozano K., 2010, Electrospinning to forcespinning, *Materials Today*, **13**, 11, 12-14

17. Taghavi S.M., Larson R.G., 2014a, Regularized thin-fiber model for nanofiber formation by centrifugal spinning, *Physical Review E*, **89**, 023011

18. Taghavi S.M., Larson R.G., 2014b, Erratum: Regularized thin-fiber model for nanofiber formation by centrifugal spinning, *Physical Review E*, **89**, 059903(E)

19. Vazquez B., Vasquez H., Lozano K., 2012, Preparation and characterization of polyvinylidene fluoride nanofibrous membranes by forcespinning, *Polymer Engineering and Science*, **52**, 2260-2265

Manuscript received October 22, 2022; accepted for print January 31, 2023

JOURNAL OF THEORETICAL AND APPLIED MECHANICS
61, 2, pp. 289-303, Warsaw 2023
https://doi.org/10.15632/jtam-pl/161683

RECOGNITION OF PICK WEAR CONDITION BASED ON GREY-MARKOV CHAIN MODEL

Qiang Zhang

School of Mechanical Engineering, Liaoning Technical University, Liaoning, China, and
School of Mechatronics, Shandong University of Science and Technology, Shandong, China

Jiayao Zhang

School of Mechanical Engineering, Liaoning Technical University, Liaoning, China
Corresponding author J. Zhang, e-mail: 1725157910@qq.com

An attempt is made in this paper to solve the pick wear problem of mining machinery and propose a pick wear degradation model based on the Grey-Markov chain by using generated characteristics signals and certain pick wear parameters to enhance the prediction accuracy. The vibration and acoustic emission signals generated during the catting pick are extracted and analyzed. The energy and the value of the characteristic signal are obtained by wavelet analysis to construct a characteristic sample library of the signals. Two kinds of signals are applied to the model to analyze the error between the real and the predicted values. The model prediction results demonstrate a 1.43% error of the vibration signal, 1.64% error of the acoustic emission signal with 98% prediction accuracy, thus offers a new method for monitoring the pick wear of mining machinery.

Keywords: pick wear, vibration acceleration signal, acoustic emission signal, Grey-Markov method

1. Introduction

The pick is one of the most important parts of mining machinery. Currently, the condition of coal quality is worsening day by day. The coal, rock and hard rock are in contact with each other over a prolonged period under a state of high impact and stress, thereby, damaging and shortening the life of the pick severely and warranting replacements of coal mining machinery parts. Therefore, the pick wear has become one of the main research problems in the coal mining (Bagri *et al.*, 2021; Boing *et al.*, 2020; Chen *et al.*, 2020; Fan *et al.*, 2020).

Several common signal-based wear methods are advocated by scholars to reduce the catting pick wear problem including the characteristic parameter method, time series analysis, and Fourier transform (Hu *et al.* 2019; Lan *et al.*, 2020; Li *et al.*, 2020). The signal quantity recorded by the characteristic parameter method is large, and the real-time analysis is strong. However, the connection between the acoustic emission waveform obtained and the acoustic emission source mechanism must be understood while using this method, otherwise the physical nature of the acoustic emission waveform cannot be found. Although the application of time series analysis in some cases have achieved some results, this method cannot explain the reason of calculating the auto-regressive coefficient and three catting pick factors as input variables of a neural network (Lubis *et al.*, 2020; Ma *et al.*, 2020). Fourier transformation embodies information of the signal in the frequency domain and does not change with time. For the wear method, it is common to study the wear condition between a metal and metal. Abaqus software and a dynamic model can accurately predict the wear condition. Similarly, these theoretical methods are also applicable to pick wear. (Shen *et al.*, 2020; Ouafik, 2020; Shadfar and Molatefi, 2017; Łuczak *et al.*, 2022).

In view of this, an attempt is made to adopt the Grey-Markov model prediction method based on the identification of pick wear degree of the vibration signal and the acoustic emission signal. The method is characterized by a small stable error in the calculation process by dividing the state parameters. The precise prediction of pick wear is realized by extracting a variety of feature information related to the pick wear state by analyzing and processing.

2. Online monitoring system for pick wear characteristic signals

2.1. Establishment of an experimental system for pick wear monitoring

The experimental system mainly consists of two parts: the pick and the multi-sensor testing subsystem. The pick consists of the pick mechanism, walking mechanism and control cabinet. The multi-sensor test system consists of the vibration signal acquisition system, acoustic emission signal acquisition system and current signal acquisition system. Its main form of composition is shown in Fig. 1.

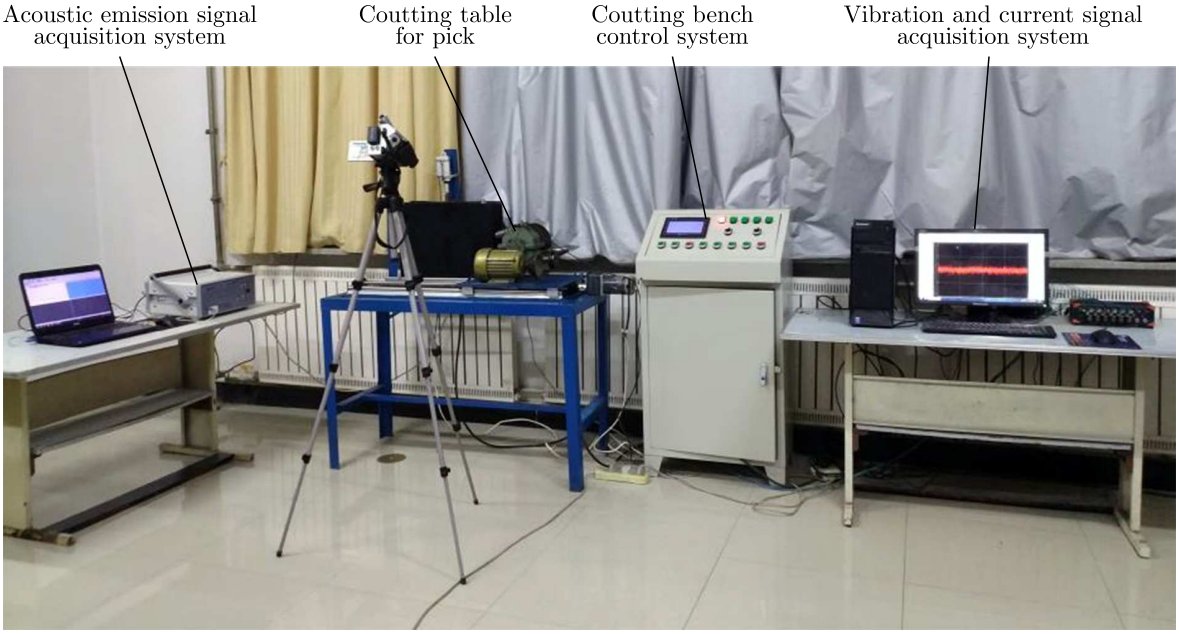

Fig. 1. Pick wear monitoring experimental system

2.2. Monitoring signal extraction

The pick wear can be divided into 6 states, namely, new pick, slight wear, medium wear, large wear, severe wear and failure pick (A1-A6), respectively.

2.2.1. Vibration signal extraction

The vibration signals in the pick process are collected, and the signal characteristics are analyzed to judge the wear degree of the picking gear. The vibration acceleration curves of X-axis in the pick process for different wear degrees are selected as characteristic signals. The vibration acceleration signals measured in picks with different wear degrees are shown in Fig. 2a-2f displaying vibration acceleration curves in X-axis direction.

It can be seen from Fig. 2 that with deterioration of the pick wear degree, the pick vibration is continuously intensified, and the vibration acceleration average peak of pick is steadily increasing.

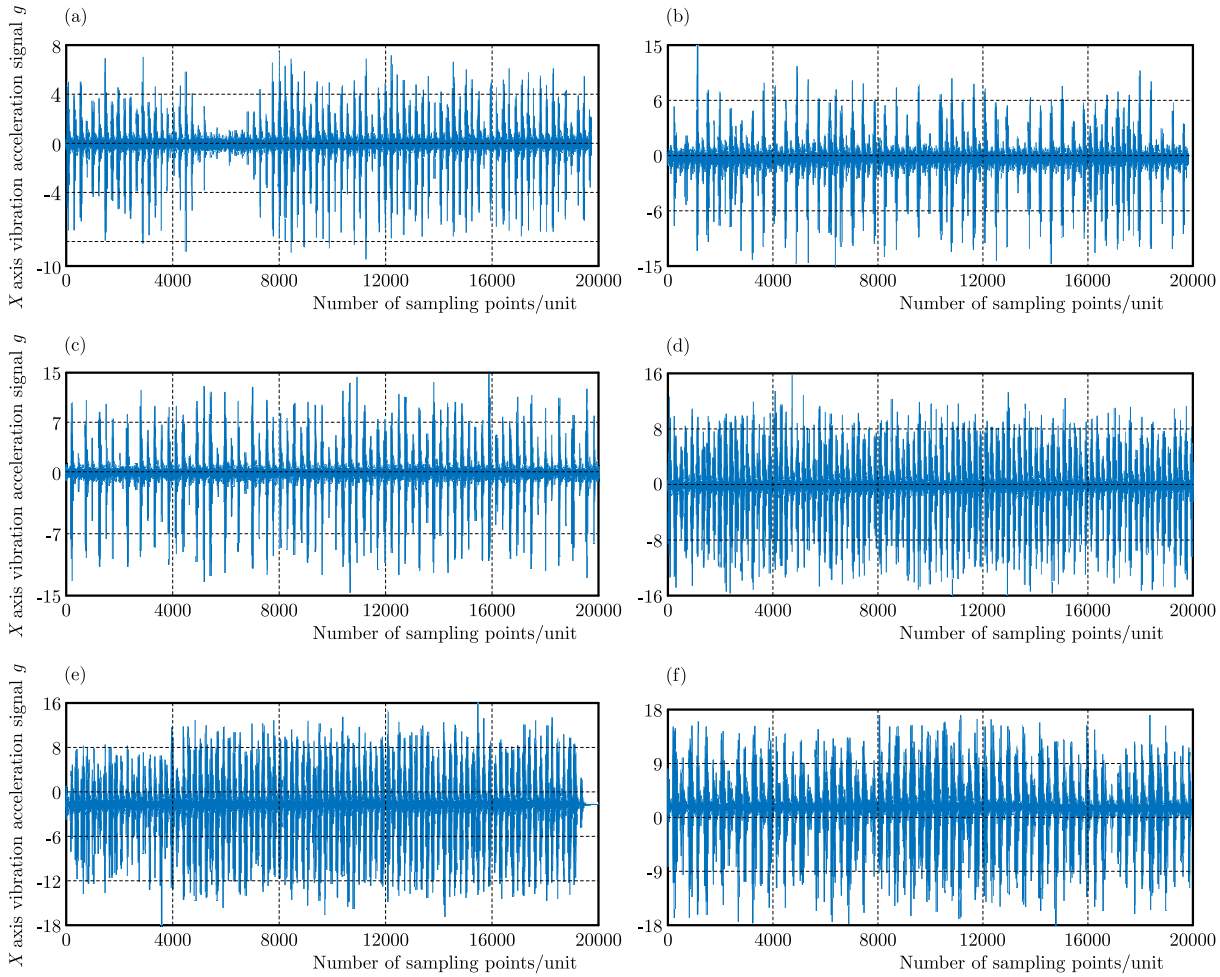

Fig. 2. X-axis vibration acceleration curves for different wear degrees: (a) new pick, (b) slight wear, (c) medium wear, (d) large wear, (e) severe wear, (f) failure pick

The average peak acceleration is 3.98 g, 4.52 g, 5.49 g, 6.51 g, 8.52 g and 9.52 g, respectively. The pick vibration acceleration corresponding to the failure pick is the largest. Through tests and extraction of the signal, it can be noticed that with the aggravation of the pick wear degree, the average peak vibration acceleration of the pick increases continuously and the change is more obvious. Hence, a change in the vibration acceleration signal change is taken as the characteristic signal.

2.2.2. Acoustic emission signal extraction

The frequency of the acoustic emission signal is high. Collisions, friction and plastic deformations in the pick process result in outward propagation of the energy and sound waves. According to the difference of acoustic emission signals in the pick process between picks with different wear degrees and coal rock, the wear degree can be determined as depicted in Fig. 3.

According to Fig. 3a-3f, with a change in the picking gear wear degree, the peak values of the acoustic emission signals correspond to 5.034 V, 3.94 V, 2.85 V, 1.44 V, 0.62 V and 0.43 V, respectively. Through testing and extraction, it can be seen that with the aggravation of picking gear wear, the acoustic emission signal gradually decreases, a change in the pick acoustic emission signal is obvious, and the amplitude fluctuates greatly, so the change of the acoustic emission signal of the picking gear is taken as the characteristic signal.

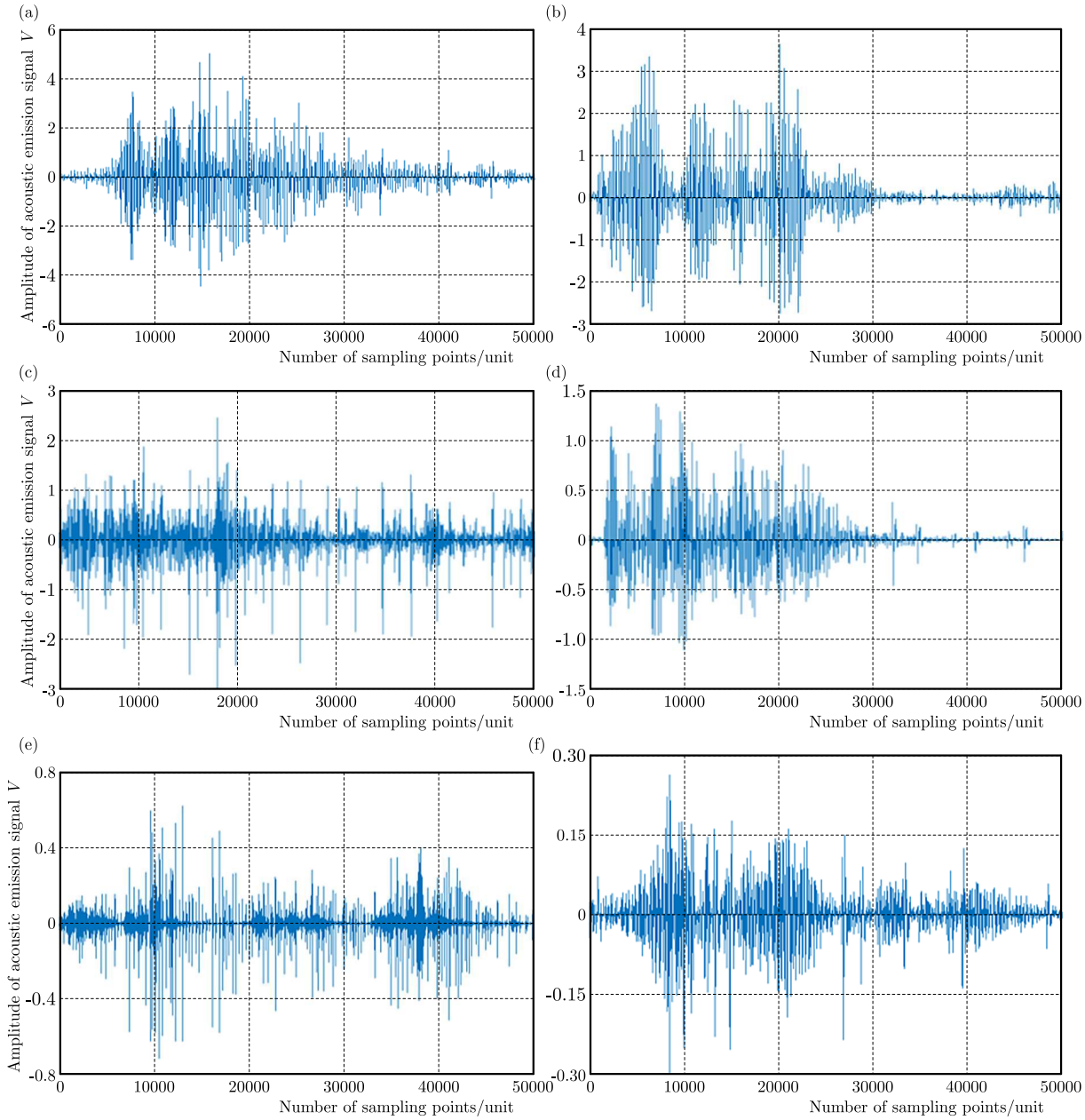

Fig. 3. X-axis acoustic emission acceleration curves for different wear degrees: (a) new pick, (b) slight wear, (c) medium wear, (d) large wear, (e) severe wear, (f) failure pick

2.3. Analysis and recognition of characteristic signals

2.3.1. Wavelet packet analysis of vibration signal

Three-layer wavelet packet decomposition is used to decompose vibration acceleration time domain signals of the pick in six states, and the signals are decomposed into eight frequency bands. After the signal decomposition, each node is de-noised as (3.0), (3.1), (3.2), (3.3), (3.4), (3.5), (3.6), and (3.7). The frequency band range of each node after the signal decomposition is shown in Table 1. Figure 4 depicts the wavelet packet decomposition diagram of each state (part of the picture). The abscissa is the number of sampling points in each frequency band, and the ordinate is the signal energy in the corresponding frequency band after the wavelet packet decomposition.

Table 1. Corresponding frequency band of each node signal

Number	Frequency [kHz]	Number	Frequency [kHz]
(3.0)	0-12.5	(3.4)	50-62.5
(3.1)	12.5-25	(3.5)	62.5-75
(3.2)	25-37.5	(3.6)	75-87.5
(3.3)	37.5-50	(3.7)	87.5-100

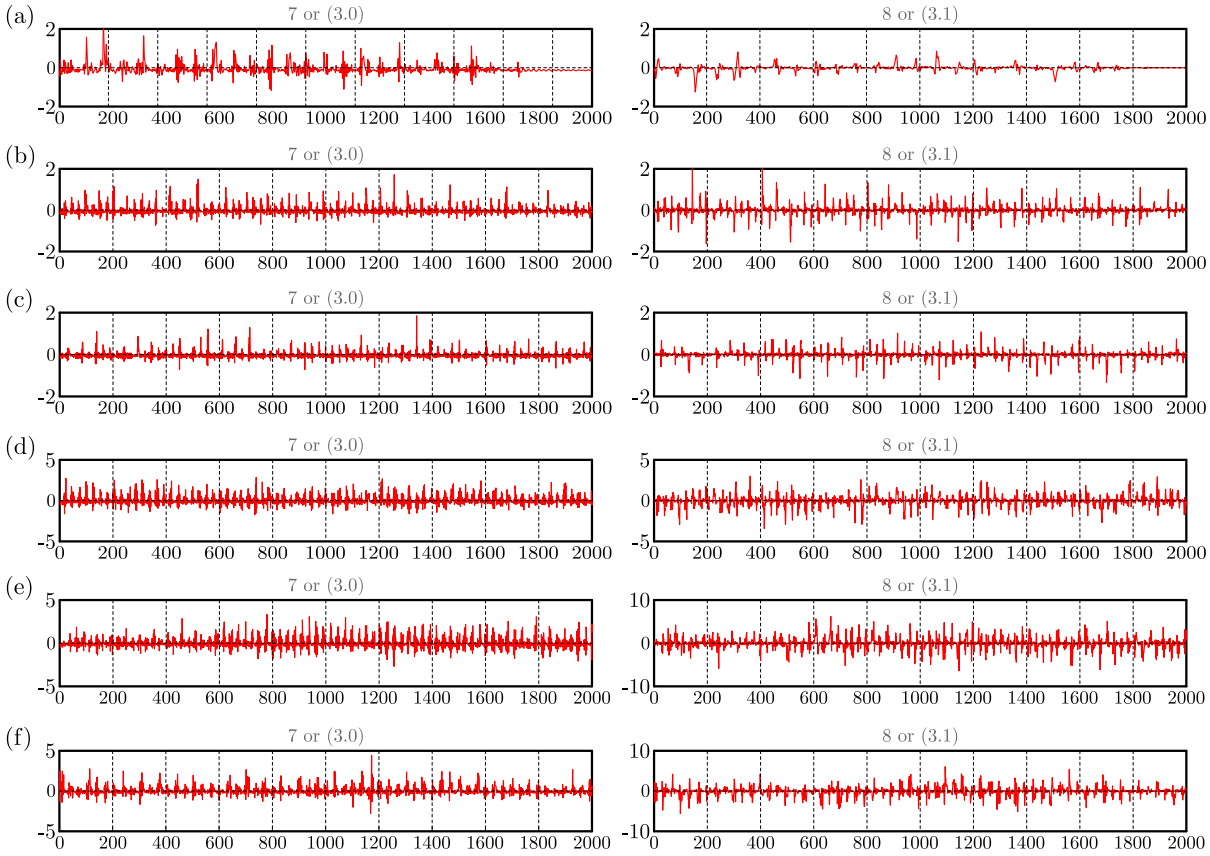

Fig. 4. Wavelet packet decomposition diagrams: (a) new pick, (b) slight wear, (c) medium wear, (d) large wear, (e) severe wear, (f) failure pick

It is evident from Fig. 4 that the signal intensity in (3.0)-(3.3) frequency band is small, whereas both the signal intensity and energy value in (3.4)-(3.7) frequency band are large with an obvious vibration amplitude. With the aggravation of the pick wear degree, the peak value and the energy value of the same frequency band also increase gradually. With deterioration of the pick wear degree, the amplitude of the vibration acceleration signal increases continuously with obvious changes, which can realize the recognition of different pick wear degrees.

The energy of each frequency band range of A1-A6 picks is calculated, and the energy values of each frequency band of 6 picks obtained with different wear degrees are shown in Fig. 5.

It is evident from Fig. 5 that the vibration energy of six picks with different wear degrees in the same frequency band exhibits a gradual increasing trend, among which the energy values in the frequency bands of 50-62.5 Hz, 62.5-75 Hz, 75-87.5 Hz and 87.5-100 Hz are higher and the change rule is obvious. Therefore, the sum of these four frequency energy bands is selected as the feature samples. Some of the data samples are shown in Table 2.

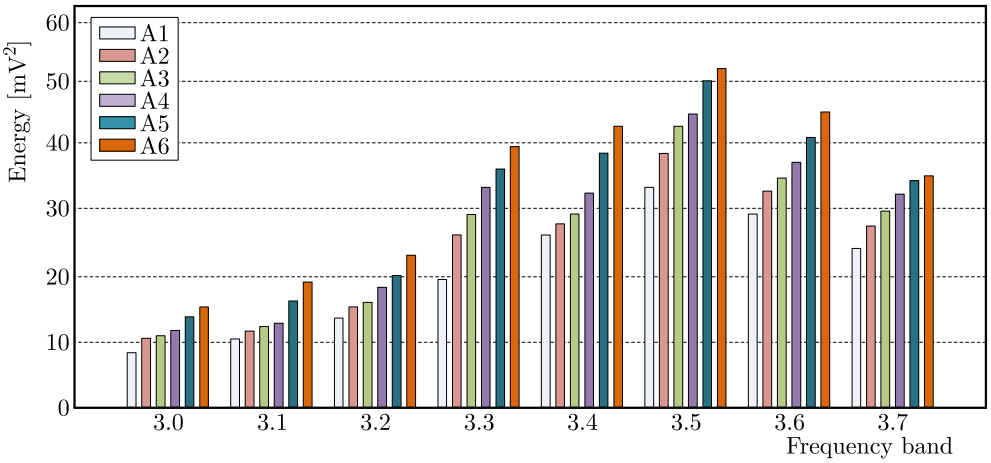

Fig. 5. Energy values of X-axis frequency band

Table 2. Sum of the energy for different pick vibration acceleration signal samples [mV^2]

Number	A1	A2	A3	A4	A5	A6
1	100.0061	112.3315	126.2487	145.2145	171.9594	209.9130
2	100.7538	112.8459	126.4478	146.5461	171.1254	210.6678
⋮	⋮	⋮	⋮	⋮	⋮	⋮
49	114.6851	126.6147	147.5921	171.8481	209.1217	226.6507
50	114.9854	126.5984	147.8459	172.0114	209.1584	226.9761

2.3.2. Wavelet packet analysis of the acoustic emission signal

In line with the aforesaid vibration signals, DB9 wavelet basis is selected, and the wavelet packet decomposition of the pick in each state (part of the picture) is shown in Fig. 6. By comparing the decomposition diagrams of the eight frequency bands of A1-A6 picks, it is noticed that the signal intensity is higher in frequency band (3.1)-(3.3), the acoustic emission signal amplitude is more obvious, and the energy value is higher. The peak value and the energy value of the same frequency band increase gradually with the aggravation of pick wear.

In order to analyze the acoustic emission wavelet packet signal characteristic samples, the energy of each frequency band range of A1-A6 cutter is calculated, and the energy values of each frequency band of six cutters with different wear degrees are given. Figure 7 reveals that the vibration energy shows a trend of gradual decline. Among these, the energy values of 12.5-25 kHz, 25-37.5 kHz and 37.5-50 kHz frequency bands are relatively high and have obvious changing rules. Therefore, the energy and values of the above 3 frequency bands are selected as the feature samples. Some of the feature samples are shown in Table 3.

Table 3. Sum of the energy for different picks acoustic emission signal samples [mV^2]

Number	A1	A2	A3	A4	A5	A6
1	64.5960	49.1954	38.0999	29.0012	24.5987	16.8302
2	64.5881	49.1548	38.0451	28.9445	24.5146	16.4791
⋮	⋮	⋮	⋮	⋮	⋮	⋮
49	48.8031	37.9921	28.7279	23.5145	16.8762	11.0043
50	48.7894	37.8489	28.6145	23.1547	16.6016	10.9641

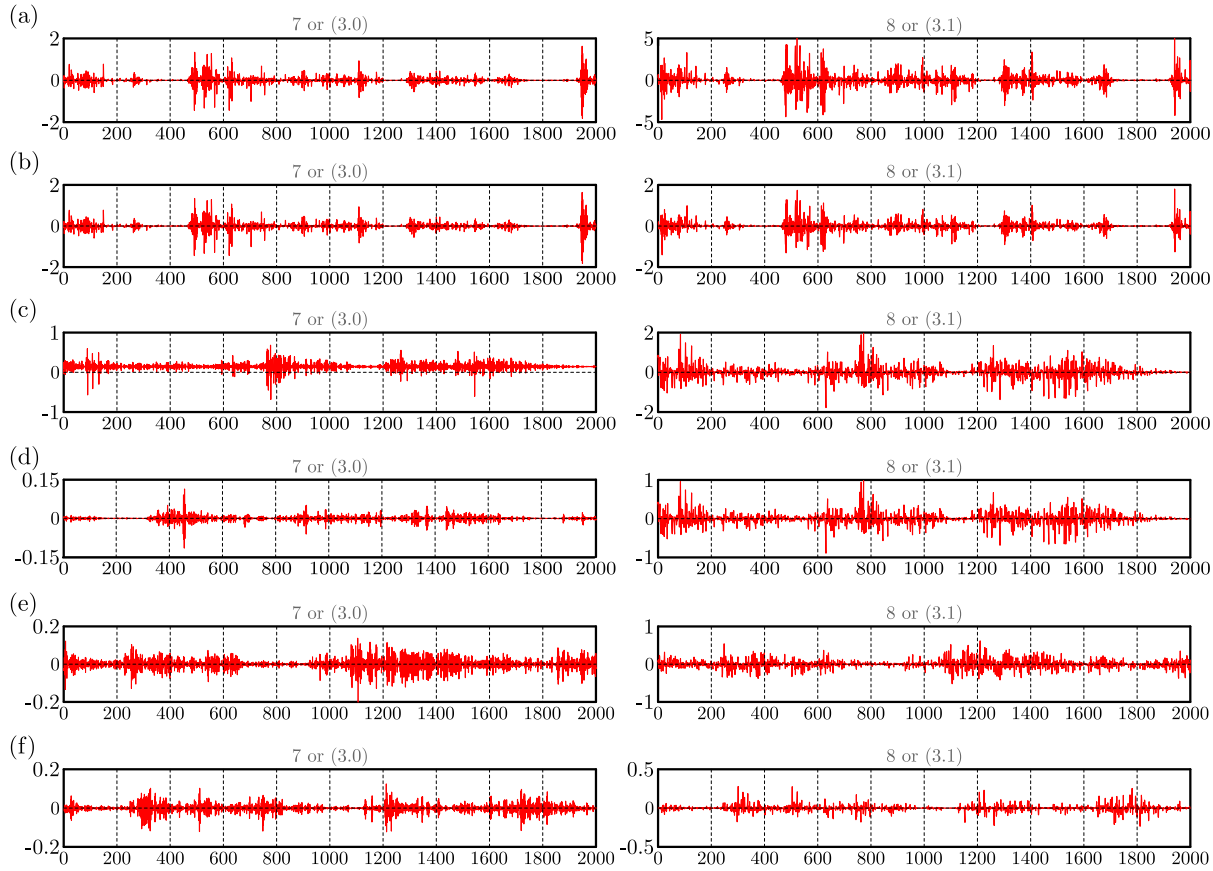

Fig. 6. Wavelet packet decomposition of different picks: (a) new pick, (b) slight wear, (c) medium wear, (d) large wear, (e) severe wear, (f) failure pick

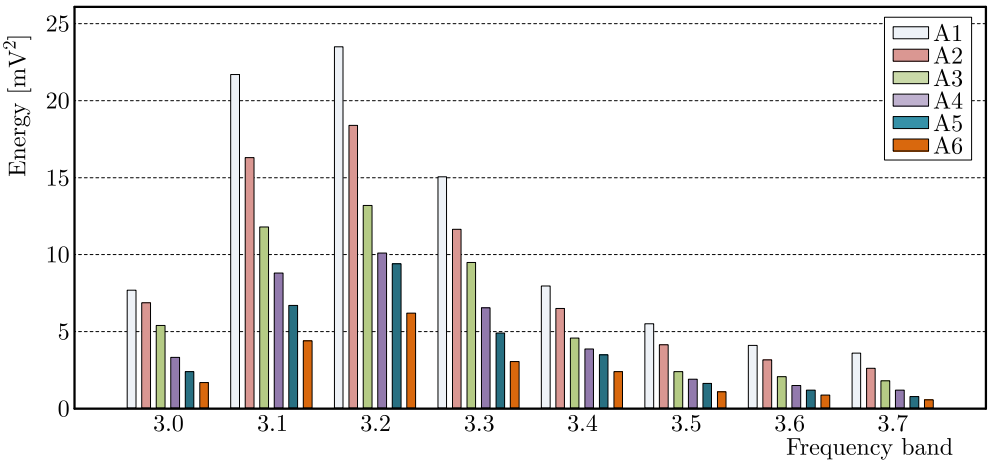

Fig. 7. Energy values of X-axis frequency band

3. Construction of the pick wear prediction model

3.1. Construction of the Grey-Markov chain model

The most basic model used in the Markov analysis is

$$\mathbf{x}(k+1) = \mathbf{x}(k) \times \mathbf{P} \tag{3.1}$$

where $\mathbf{x}(k)$ is the state vector of the predicted object at time $t = k$. $\mathbf{x}(k+1)$ is the state vector of the predicted object at time $t = k+1$ and $\mathbf{P}$ is the one-step state transition probability.

3.1.1. Partitioned prediction state

According to the predicted value of the original data, the relative value can reasonably be divided into several states with the following state interval

$$\mathbf{Q} = \frac{\mathbf{x}(t)}{\mathbf{X}(t)} \qquad \mathbf{E}_i = [Q_{i1}, Q_{i2}] \qquad i = 1, 2, \ldots, k \tag{3.2}$$

where Q_{i1} is the upper limit of the residual value in the state interval and Q_{i2} is the lower limit of the residual value of the state interval.

3.1.2. Calculate the state transition probability matrix

After determining the state of the predicted state sequence, the original data can be divided into multiple states according to the non-stationary random use property of the Markov chain, and the expression $\mathbf{E}_i$ of each state is given by

$$\begin{aligned} &\mathbf{E}_i = [\mathbf{E}'_{1i}, \mathbf{E}'_{2i}] \qquad \mathbf{E}'_{1i} \in \mathbf{E}_i \qquad \mathbf{E}'_{1i} = \mathbf{x}(t) + \mathbf{A}_i \\ &\mathbf{E}'_{2i} = \mathbf{x}(t) + \mathbf{B}_i \qquad i = 1, 2, \ldots, n \end{aligned}$$

where P_{ij} is the one-step transition probability from state $\mathbf{E}_i$ to state $\mathbf{E}_i$

$$P_{ij} = \frac{M_{ij}}{M_i} \tag{3.3}$$

where for $i, j = 1, 2, \ldots, n$, $0 \leqslant P_{ij} \leqslant 1$, $\sum_{i=1}^{n} P_{ij} = 1$ and

$$\mathbf{P}(k) = \begin{bmatrix} P_{11}(k) & P_{12}(k) & \cdots & P_{1n}(k) \\ P_{21}(k) & P_{22}(k) & \cdots & P_{2n}(k) \\ \vdots & \vdots & \ddots & \vdots \\ P_{n1}(k) & P_{n2}(k) & \cdots & P_{nn}(k) \end{bmatrix}$$

3.1.3. Markov test

When

$$\widehat{x}^2 = 2 \sum_{i=1}^{n} \sum_{j=1}^{n} f_{ij} \left| \frac{p_{ij}}{p_j} \right|$$

if $\widehat{x} \succ x_{\alpha}^2 \left((n-1)^2 \right)$, then this data meets the Markov test.

3.1.4. Calculate the predicted value of the Markov model

In the state $\mathbf{E}'_j$, where the predicted located state sequence is determined, the predicted value of the Grey-Markov model can be obtained according to the median relative value of state $[Q_{i1} + Q_{i2}]/2$, as follows

$$y(k) = \frac{Q_{i1} + Q_{i2}}{2} + x^{(0)}(k) \tag{3.4}$$

3.2. Accuracy test of the Grey-Markov model

In order to test whether the model is qualified, the ratio of the residual error, relative error and posterior difference between the two is calculated, and each result meets the requirements of series. The accuracy test index is:

— Mean relative error

$$\overline{\Delta} = \frac{1}{n}\sum_{t=1}^{n}\frac{|\varepsilon(t)|}{x(t)}\cdot 100\% \tag{3.5}$$

where $\varepsilon(t)$ is the data residual sequence.

— Posterior difference ratio

$$C = \frac{S_2}{S_1} \tag{3.6}$$

where S_1 is the standard deviation of the original sequence, and S_2 is the standard deviation of the residual sequence.

— Small error probability

$$P = \{\varepsilon(t) - \overline{\varepsilon}(t)\} \prec 0.6745S_1 \tag{3.7}$$

where $\varepsilon(t)$ is the data residual sequence, $\overline{\varepsilon}(t)$ is the mean value of the residual sequence.

The test results are shown in Table 4.

Table 4. Model test results

Feature samples	Residual	Error probability	Posterior value ratio	Relative error
Energy and vibration signal within 50-100 Hz	22.33	1	0.013	0.0015
Energy and emission signal from 50 Hz to 100 Hz	25.53	1	0.006	0.00076

It is observed from the table that for the mean value of the residual error and the relative error of each characteristic sample, the posterior error ratio $C = S_2/S_1 < 0.35$, the error probability P is 1, which proves that the model accuracy at the first-level is good.

4. Prediction of the pick wear state based on the Grey-Markov model

4.1. Vibration signal prediction model

The energy and feature samples of the vibration acceleration signal are synthesized into feature vectors $\mathbf{x}^{(0)}$

$$\mathbf{x}^{(1)} = [100.00, 100.75, 101.64, 102.19, \ldots, 226.00, 226.33, 226.65, 226.98]$$

The matrix $\mathbf{B}$ and vector $\mathbf{Y}_n$ are obtained according to the Grey-Markov rule as follows

$$\mathbf{B} = \begin{bmatrix} -100.3750 & 1 \\ -101.1950 & 1 \\ -101.9150 & 1 \\ -102.3700 & 1 \\ \vdots & \vdots \\ -225.8372 & 1 \\ -226.1626 & 1 \\ -226.4880 & 1 \\ -226.8134 & 1 \end{bmatrix}$$

$$\mathbf{Y}_n = [100.75, 101.64, 102.19, 102.55, \ldots, 226.00, 226.33, 226.65, 226.98]$$

$$\mathbf{x} = \begin{bmatrix} a \\ u \end{bmatrix} = (\mathbf{B}^{\mathrm{T}}\mathbf{B})^{-1}\mathbf{B}^{\mathrm{T}}\mathbf{Y} = \begin{bmatrix} -0.0030 \\ 95.8188 \end{bmatrix}$$

The solution

$$\widehat{x}^{(1)}(t+1) = \Big(100.75 + \frac{95.8188}{0.0030}\Big)\mathrm{e}^{0.0030t} - \frac{95.8188}{0.0030} \qquad t = 1, 2, \ldots, n$$

The state transition matrix is

$$\mathbf{P} = \begin{bmatrix} 0.8261 & 0.1739 & 0 & 0 & 0 \\ 0.0625 & 0.8625 & 0.0750 & 0 & 0 \\ 0 & 0.0769 & 0.9011 & 0.0220 & 0 \\ 0 & 0 & 0.0250 & 0.9500 & 0.0250 \\ 0 & 0 & 0 & 0.0800 & 0.9200 \end{bmatrix}$$

The residuals E_1, E_2, E_3, E_4, E_5 of five error states are divided according to 1-300 groups of data. The partition state of the residual range is shown in Table 5. By using the above formula, the predicted values of the vibration acceleration signal energy are obtained, and some of the data are shown in Table 6.

Table 5. Division of error status

Status	E_1	E_2	E_3	E_4	E_5
Residual error range	$[-10.4549 : -6.2492]$	$[-6.2492 : -2.0434]$	$[-2.0434 : 2.1623]$	$[2.1623 : 6.3681]$	$[6.3681 : 10.5738]$

Table 6. Grey-Markov model partial prediction results

Sample data	True value	Predicted value	Relative error
1	100.0061	100.0061	0.00%
2	100.7538	94.2241	6.48%
3	101.6388	98.7219	2.87%
4	102.1881	99.0149	3.11%
5	102.5543	99.3087	3.16%
⋮	⋮	⋮	⋮
298	226.3253	225.5419	0.35%
299	226.6507	226.2579	0.17%
300	226.9761	226.9761	0.00%

Figure 8 displays the comparison between the predicted and actual energy and values of each state of vibration acceleration signal predicted by the Grey-Markov model and the actual values.

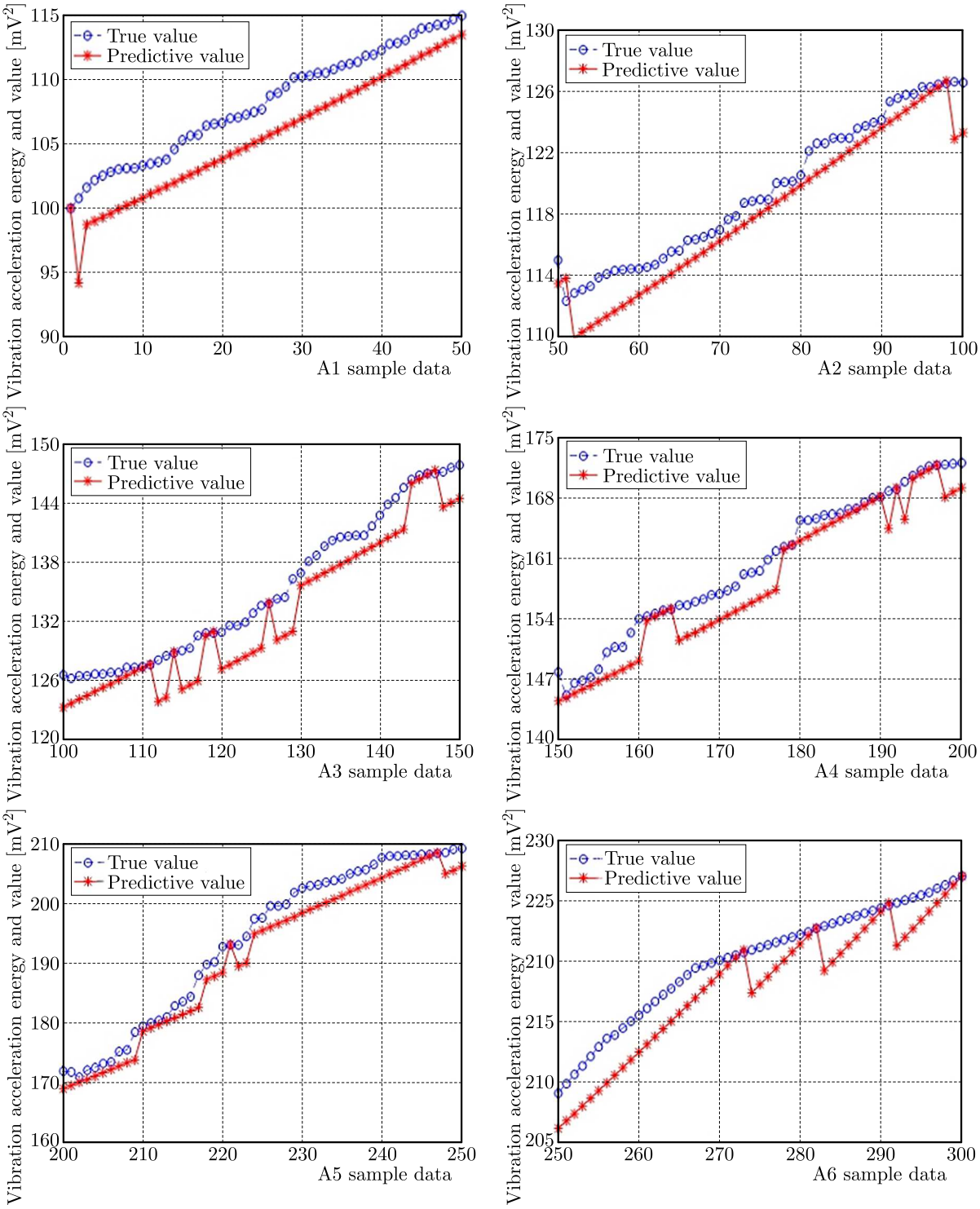

Fig. 8. Comparison diagrams of Grey-Markov real values and predicted values of the vibration signal

It is noted from Fig. 8 that the overall Grey-Markov model for each interval of the pick wear state data prediction is relatively accurate, when 1 to 50 group of data is taken as a reference

and the Grey-Markov model is used to predict such 250 groups of data, with an average relative error of 1.43%.

4.2. Acoustic emission signal prediction model

The energy and characteristic samples of acoustic emission signal are synthesized into characteristic directions $\mathbf{x}^{(0)}$

$$\mathbf{x}^{(1)} = [64.5960, 64.5881, 64.5314, 64.1547, \ldots, 11.0485, 11.0112, 11.0043, 10.9641]$$

The matrix $\mathbf{B}$ and vector $\mathbf{Y}_n$ are obtained according to the Grey-Markov rule as follows

$$\mathbf{B} = \begin{bmatrix} -64.5921 & 1 \\ -64.5598 & 1 \\ -64.3431 & 1 \\ -64.1260 & 1 \\ \vdots & \vdots \\ -11.0855 & 1 \\ -11.0299 & 1 \\ -11.0078 & 1 \\ -10.9842 & 1 \end{bmatrix}$$

$$\mathbf{Y}_n = [64.5881, 64.5314, 64.1547, 64.0972, \ldots, 11.0485, 11.0112, 11.0043, 10.9641]$$

$$\mathbf{x} = \begin{bmatrix} a \\ u \end{bmatrix} = (\mathbf{B}^{\mathrm{T}}\mathbf{B})^{-1}\mathbf{B}^{\mathrm{T}}\mathbf{Y} = \begin{bmatrix} 0.0054 \\ 65.4765 \end{bmatrix}$$

The solution

$$\widehat{x}^{(1)}(t+1) = \Big(64.5881 + \frac{65.4765}{0.0054}\Big)\mathrm{e}^{0.0054t} - \frac{65.4765}{0.0054} \qquad t = 1, 2, \ldots, n$$

The state transition matrix is

$$\mathbf{P} = \begin{bmatrix} 0.9744 & 0.0256 & 0 & 0 & 0 \\ 0.0435 & 0.7826 & 0.1739 & 0 & 0 \\ 0 & 0.0732 & 0.8455 & 0.0813 & 0 \\ 0 & 0 & 0.1515 & 0.7879 & 0.0606 \\ 0 & 0 & 0 & 0.1600 & 0.8400 \end{bmatrix}$$

The residuals E_1, E_2, E_3, E_4, E_5 of the five error states are divided according to 1-300 groups of data. The partition state of the residual range is shown in Table 7. The predicted values of energy and acoustic emission acceleration signal in the frequency domain obtained by using the above formula are shown in Table 8.

Table 7. Division of error status

Status	E_1	E_2	E_3	E_4	E_5
Residual error range	$[-2.4877 : -1.4916]$	$[-1.4916 : -0.4956]$	$[-0.4956 : 0.5004]$	$[0.5004 : 1.4964]$	$[1.4964 : 2.4924]$

From Fig. 9, it is evident that the average relative error of the prediction of the Grey-Markov model is 1.64%. The results show that the average relative error of the Grey-Markov model is marginal and acceptable for this sample size. The aforesaid predictions of each feature sample data based on the Grey-Markov model prove that the Grey-Markov model gives a small relative error and a high prediction accuracy.

Table 8. Grey-Markov model partial prediction results

Sample data	True value	Predicted value	Relative error
1	64.5960	64.5960	0.00%
2	64.5881	64.4557	0.20%
3	64.5314	64.1054	0.66%
⋮	⋮	⋮	⋮
298	11.0112	10.6160	3.59%
299	11.0043	10.5453	4.17%
300	10.9641	10.4750	4.46%

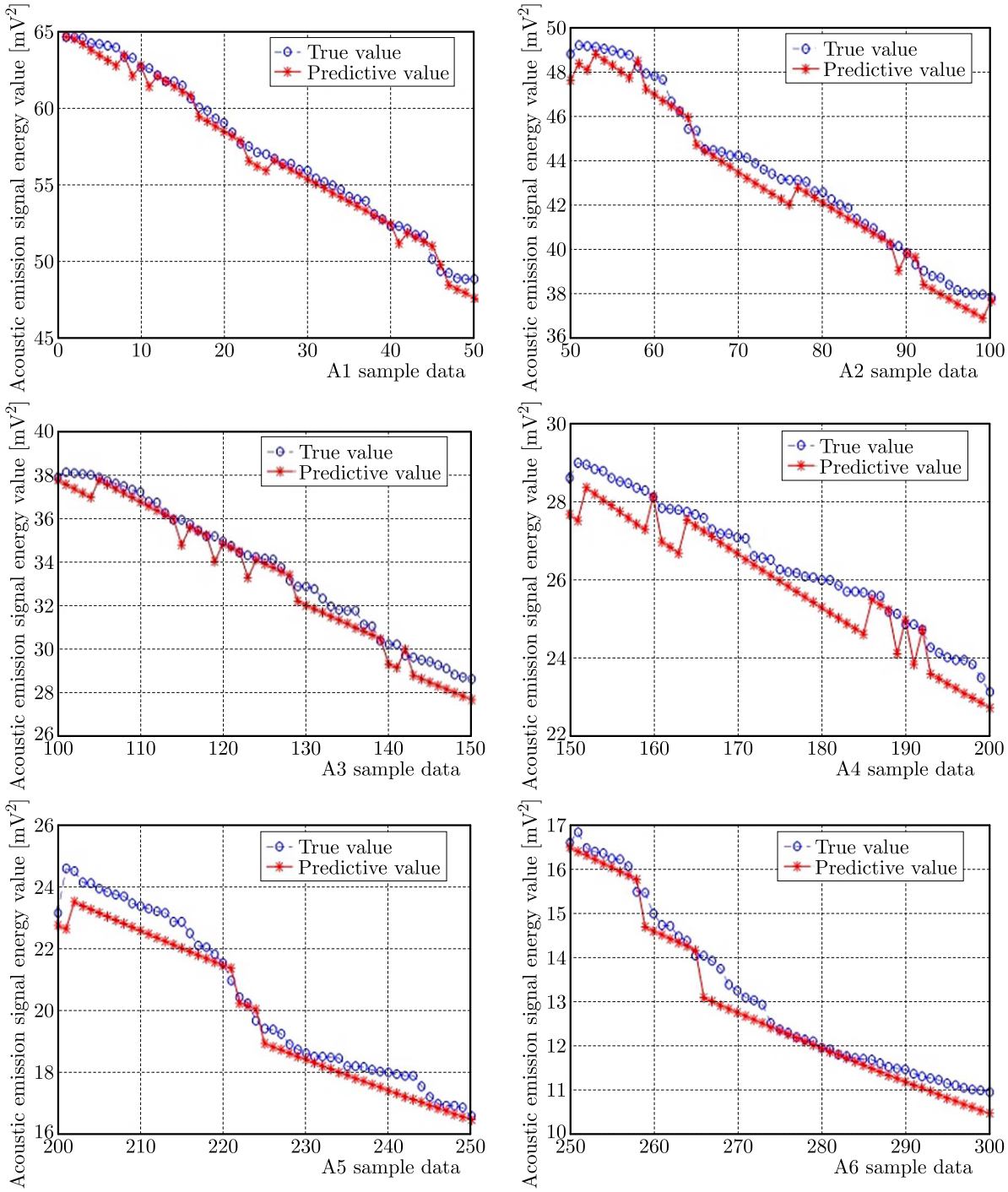

Fig. 9. Comparison of Grey Markov predicted values and real values of AE signal

5. Conclusion

- The characteristic signals of different wear picks in the pick process are obtained by pick experiments. With a change in the pick wear state, the peak value of the pick vibration acceleration in the time domain for six pick wear states increases continuously, whereas the peak value of the acoustic emission signal continuously decreases.
- The present Grey-Markov chain prediction model decides about picks in the cutting process based on characteristic signals and certain pick wear parameters of the data used in this model. The results show that the predictions based on the degree of vibration signal and the acoustic emission signal have an average relative error of 1.43% and 1.64%, respectively, indicating a high prediction accuracy for the state of the pick wear prediction.

Acknowledgment

The research was supported by the National Natural Science Foundation of China (51774161).

References

1. Bagri S., Manwar A, Varghese A., Mujumdar S., Joshi S.S., 2021, Tool wear and remaining useful life prediction in micro-milling along complex tool paths using neural networks, *Journal of Manufacturing Processes*, **71**, 679-698

2. Boing D., Castro F.L., Schroeter R.B., 2020, Prediction of PCBN tool life in hard turning process based on the three-dimensional tool wear parameter, *The International Journal of Advanced Manufacturing Technology*, **106**, 3, 779-790

3. Chen J.J, Wang Y.F., Zhang Y., Yang S.B., Zhang X.Q., 2020, Investigation on tool wear mechanism during dry cutting 304 stainless steel, *CIRP Annals*, **20**, 1, 36-44

4. Fan Y.M., Ghayesh M.H., Lu T.F., 2020, Enhanced nonlinear energy harvesting using combined primary and parametric resonances: Experiments with theoretical verifications, *Energy Conversion and Management*, **221**, 113061

5. Hu M., Ming W.W., An Q.L., Chen M., 2019, Tool wear monitoring in milling of titanium alloy Ti-6Al-4 V under MQL conditions based on a new tool wear categorization method, *The International Journal of Advanced Manufacturing Technology*, **104**, 4117-4128

6. Lan H., Xia Y. M., Miao B., Fu J., Ji Z.Y., 2020, Prediction model of wear rate of inner disc cutter of engineering in Yinsong, Jilin, *Tunnelling and Underground Space Technology*, **99**, 103338

7. Li X.R., Zhu J.M., Tian F.Q., Pan H.F., 2020, Discrimination and prediction of tool wear state based on Grey theory, *Journal of Testing and Evaluation*, **48**, 6, JTE20180302

8. Lubis S., Darmawan S., Rosehan, Winata W., Zulkarnain M., 2020, Tool wear analysis of ceramic cutting tools in the turning of gray cast iron materials, *IOP Conference Series: Materials Science and Engineering*, **857**, 012003

9. Łuczak B., Firlik B., Staśkiewicz T., Sumelka W., 2022, Numerical algorithm for predicting wheel flange wear in trams – validation in a curved track, *Proceedings of the Institution of Mechanical Engineers, Part F: Journal of Rail and Rapid Transit*, **48**, 3, 751-770

10. Ma Z., Xu X.W., Huang X.H., Ming W.W., An Q.L., Chen M., 2022, Cutting performance and tool wear of SiAlON and TiC-whisker-reinforced Si3N4 ceramic tools in side milling Inconel 718, *Ceramics International*, **48**, 3, 3096-3108

11. Ouafik Y., 2020, Numerical analysis of a frictional contact problem for thermo-electro-elastic materials, *Journal of Theoretical and Applied Mechanics*, **58**, 3, 673-683

12. Shadfar M., Molatefi H., 2017, A study on transient wear behavior of new freight wheel profiles due to two point contact in contact in curve negotiation, *Journal of Theoretical and Applied Mechanics*, **55**, 2, 621-634

13. Shen X., Chen X.S., Fu Y.B., Cao C.Y., Yuan D.J., Li X.H., Xiao Y.S., 2022, Prediction and analysis of slurry shield TBM disc cutter wear and its application in cutter change time, *Wear*, **498-499**, 204314

Manuscript received April 13, 2022; accepted for print December 10, 2022

JOURNAL OF THEORETICAL AND APPLIED MECHANICS
61, 2, pp. 305-316, Warsaw 2023
https://doi.org/10.15632/jtam-pl/161477

ON THE DEFORMATION OF POROUS SPHERICAL BODIES UNDER RADIAL SURFACE TRACTION

Simona De Cicco
University of Naples Federico II, Department of Structures for Engineering and Architecture, Naples, Italy
e-mail: simona.decicco@unina.it

The paper deals with the linear theory of elastic materials with voids based on the concept of volume fraction. In this model, the interstitial pores are vacuous and can contract or stretch. The change in the volume fraction is measured by a scalar function, so that independent kinematical variables are four: the components of displacements and the volume fraction function. The equilibrium problem of elastic spherical bodies under radial surface traction is solved. The solution is given in closed form and applied to study three special cases. Explicit formulas of the displacement, stress distribution and volume fraction function are given.

Keywords: linear elasticity, materials with voids, equilibrium theory, spherical solids

1. Introduction

The equilibrium and motion of solid bodies bounded by a spherical surface are classical problems in the theory of elasticity. At the beginning of the nineteenth century, many scientists investigated various problems concerning spheres and spherical shells. We mention among others Poisson (1829) who, in the second section of his Mémoire, studied vibrations of an elastic sphere, and Clebsch (1862), who addressed the problem of radial vibrations. The equilibrium problem of a spherical shell subjected to a given distribution of load was solved by Lamé (1854). A complete solution of the "Lamé's problem" was obtained by Lord Kelvin (Thompson, 1863) using series involving spherical harmonics. In his famous treatise, Love (1926) introduced a method of solving the Lamé's problem in terms of series of spherical harmonics regarding these functions as functions of Cartesian coordinates and avoiding transformations to polar coordinates. In more recent years, a representation of solutions in terms of series and quadrature was presented by Kupradze (1979). The method has been applied to solve several cases of boundary value problems in three-dimensional elasticity and thermoelasticity for spheres and spherical cavities in a infinite medium.

The attention given to the topic is due to its practical applications in engineering, geotechnical sciences, geophysics and earth sciences.

In this paper, we address the equilibrium problem of spherical bodies under the action of given surface traction in the context of the linear theory of elastic materials with voids introduced by Cowin and Nunziato (1983). Differently from the well-known Biot (1941) consolidation theory, where the open pore spaces are filled with a liquid or gas, in the Cowin-Nunziato model the pores are empty, containing nothing of mechanical significance. Both theories were formulated to describe mechanical behaviour of porous materials and play an important role in engineering, soil mechanics and biomechanics.

The basis of Cowin-Nunziato theory is the concept of volume fraction. The bulk density is explicated as the product of two fields, the matrix material density field and the volume fraction field. The volume fraction corresponding to the void volume is taken as an independent kinematic parameter. In consequence, the theory of materials with voids is characterized by four

independent kinematical variables, three components of the displacement and a change in the volume fraction. Consequently, for the mechanical equilibrium an additional balance equation is required. Moreover, extra boundary conditions must be added. The model is suitable to describe the behaviour of rocks, ceramics, pressed powders as well as concrete.

The theory has been subject to intensive study, and a great number of contributions regarding the fundamentals and applications has been published. Basic results and extended references may be found in the book by Ciarletta and Ieşan (1993). Theorems concerning the existence and uniqueness of the solution were established by Ieşsan (1985). Using a semi-inverse method, the Saint-Venant problem was solved by Dell'Isola and Batra (1977). Magnucki and Malinowski (2004) derived an explicit expression for the critical load of compressed porous beams. Stress concentration problems were investigated by De Cicco and De Angelis (2019). Thermoelastic deformations of porous anisotropic cylinders were studied by De Cicco and Ieşan (2013). Puri and Cowin (1985) analysed behaviour of plane harmonic waves in a medium with voids.

A contribution to the topic under consideration was given by Cowin and Nunziato (1983). They solved the problems of thick walled spherical and circular cylindrical shells under internal and external pressure. The salient feature of the solution is that the stress field is not affected by the porosity and is identical with that predicted by classical elasticity. In this problem, we generalize the pressure vessel problem proposed by Cowin and Puri (1983).

The outline of the paper is as follows. In Section 2, we present the basic equations of the equilibrium theory of elastic materials with voids. In Section 3, we derive the generalized analytical solution for a class of problems for which the kinematical variables are functions of the radial coordinate r. In Section 4, the solution is applied to study three special cases.

All the results are expressed in explicit form and generalize the solutions of analogous problems in the classical elasticity. It is worth to note that in the two cases studied, the stress distribution is not affected by a change in the volume fraction, whereas in the third case the porosity influences both the displacement and stress field.

2. Preliminaries

We consider a regular region B of three-dimensional Euclidean space occupied by a linearly elastic material with voids. The region B is referred to a system of Cartesian coordinates $O\{\mathbf{e}_1, \mathbf{e}_2, \mathbf{e}_3\}$. We denote by ∂B the boundary of B and by $\mathbf{n}$ the outward unit normal vector of ∂B. We denote by ρ the mass density in the deformed configuration and assume that ρ has the decomposition $\rho = \sigma\widehat{\rho}$, where $\widehat{\rho}$ is the density of the matrix material and σ is the volume fraction field. In the undeformed state we have $\rho_0 = \sigma_0\widehat{\rho}_0$, where ρ_0, $\widehat{\rho}_0$ and σ_0 are the mass density, density of the matrix material and the volume fraction field in the reference configuration, respectively. We introduce the notation $\psi = \sigma - \sigma_0$ (see Appendix). The independent kinematic variables are components of the displacement u_i $(i = 1, 2, 3)$ and a change in the volume fraction ψ. The governing equations of the linear theory of elastic materials with voids are given by the geometrical equations

$$\mathbf{E} = \frac{1}{2}(\nabla\mathbf{u} + \nabla\mathbf{u}^{\mathrm{T}}) \tag{2.1}$$

where $\mathbf{u}$ is the displacement field over B, $\nabla\mathbf{u}$ is the gradient of $\mathbf{u}$, $\nabla\mathbf{u}^{\mathrm{T}}$ is the transpose of $\nabla\mathbf{u}$, and $\mathbf{E}$ is the strain tensor. The equilibrium equations are

$$\operatorname{div}\mathbf{T} + \mathbf{f} = \mathbf{0} \qquad \operatorname{div}\mathbf{h} - p + q = \mathbf{0} \tag{2.2}$$

where $\mathbf{T}$ denotes the stress tensor, $\mathbf{f}$ the body force, $\mathbf{h}$ the equilibrated stress vector, p the intrinsic equilibrated body force and q the extrinsic equilibrated body force.

In some microstructural theories as well as in specific problems of classical elasticity, there arise stress systems equivalent to two oppositely directed forces at some point, known as double force systems without moments. The terminology is justified by the fact that such systems have no net force and no resulting moment. In classical elasticity, the double force systems were identified as singularities and were discussed by Love (1926).

Now we consider the problem of an elastic sphere forced into a spherical hole of slightly smaller diameter in an infinite elastic medium. The stress distribution consists of three double force systems without moment along three mutually perpendicular axes and is called the center of dilation or center of compression. In the theory of granular materials Goodman and Cowin (1972) showed the existence of an equilibrated stress resulting in either a center of compression or center of dilation.

In equation $(2.2)_2$, $\operatorname{div}\mathbf{h}$ and p can be associated with the center of dilation. The vector $\mathbf{h}$ could be interpreted as a single double force system, whereas the term p can be considered the center of dilation, but one of them acts at a distance. Other possible interpretations were suggested by Jenkins (1975) in the context of theory of granular materials and by Mackenzie (1950) who considered a porous material with spherical voids.

The second equation of (2.2) was first suggested by Goodman and Cowin (1972) and then derived from a variational argument by Cowin and Goodman (1976) (see also Appendix). It has been a subject of detailed discussions regarding the physical meaning and specific interpretations. A comparison with analogous equations arising in microstructural theories was formulated by Nunziato and Cowin (1979) and Cowin and Nunziato (1983).

The constitutive equations are

$$\mathbf{T} = 2\mu\mathbf{E} + \lambda \operatorname{tr}\mathbf{E}\mathbf{I} + \beta\psi\mathbf{I} \qquad \mathbf{h} = \alpha\nabla\psi \qquad p = \beta \operatorname{div}\mathbf{u} + \zeta\psi \tag{2.3}$$

where $\mathbf{I}$ is the identity tensor, and μ, λ, β, α and ζ are constitutive coefficients. Assuming that the internal energy density is a positive definite form, the following inequalities hold

$$\begin{aligned} &\mu > 0 \qquad \alpha > 0 \qquad \zeta > 0 \\ &2\mu + 3\lambda > 0 \qquad (2\mu + 3\lambda)\zeta > 3\beta^2 \end{aligned} \tag{2.4}$$

The boundary conditions at a regular point of ∂B are expressed by

$$\mathbf{t} = \mathbf{T}\mathbf{n} \qquad h = \mathbf{h}\cdot\mathbf{n} \tag{2.5}$$

where t is the surface traction and h the equilibrated surface force. The dot denotes scalar product. With the help of equations (2.3) and (2.1), equilibrium equations (2.2) become

$$\mu\Delta\mathbf{u} + (\mu+\lambda)\nabla \operatorname{div}\mathbf{u} + \beta\nabla\psi = 0 \qquad \alpha\nabla\psi - \zeta\psi - \beta \operatorname{div}\mathbf{u} = 0 \tag{2.6}$$

where Δ is the Laplacian.

3. Elastic porous spheres

In this Section, we shall consider the equilibrium of a porous body bounded by a spherical surface under the action of given surface tractions. We assume that the region B is referred to the interior of a sphere of radius a, i.e. $B = \{\mathbf{x}|\ x_1^2 + x_2^2 + x_3^2 < a^2\}$. The system of Cartesian coordinates $O\{x_1, x_2, x_3\}$ is chosen so that the origin O is in the center of the sphere. In the following, for our convenience, the displacement vector and the volume fraction function will be expressed in spherical coordinates (r, φ, ϑ) related to the Cartesian coordinates by the expressions

$$r = \sqrt{x_1^2 + x_2^2 + x_3^2} \qquad \varphi = \arccos\frac{x_3}{r} \qquad vt = \arctan\frac{x_2}{x_1}$$

We denote by $(u_r, u_\varphi, u_\vartheta)$ the components of the displacement vector $\mathbf{u}$. We have

$$\begin{aligned} &u_r = u_r(r,\varphi,\vartheta) \qquad u_\varphi = u_\varphi(r,\varphi,\vartheta) \\ &u_\vartheta = u_\vartheta(r,\varphi,\vartheta) \qquad \psi = \psi(r,\varphi,\vartheta) \\ &0 \leqslant r < a \qquad 0 \leqslant \varphi < \pi \qquad 0 \leqslant \vartheta < 2\pi \end{aligned} \tag{3.1}$$

Now, we restrict our attention to the class of problems with spherical symmetry. In consequence, all the quantities are independent of φ and ϑ and depend only upon the variable r. Precisely, we suppose that

$$u_r = u(r) \qquad u_\varphi = u_\vartheta = 0 \qquad \psi = \psi(r) \tag{3.2}$$

The components of the strain tensor in spherical coordinates are given by

$$e_{rr} = u' \qquad e_{\varphi\varphi} = e_{\vartheta\vartheta} = \frac{1}{r}u \qquad e_{r\varphi} = e_{r\vartheta} = e_{\varphi\vartheta} = 0 \tag{3.3}$$

where the prime stands for derivation with respect to r.

The constitutive equations become

$$\begin{aligned} &\sigma_{rr} = (2\mu+\lambda)u' + 2\lambda\frac{1}{r}u + \beta\psi \qquad \sigma_{\varphi\varphi} = \sigma_{\vartheta\vartheta} = 2(\mu+\lambda)\frac{1}{r}u + \lambda u' + \beta\psi \\ &\sigma_{r\varphi} = \sigma_{r\vartheta} = \sigma_{\varphi\vartheta} = 0 \qquad h_r = \alpha\psi' \qquad h_\varphi = h_\vartheta = 0 \\ &p = \beta\Big(u' + \frac{2}{r}u\Big) + \zeta\psi \end{aligned} \tag{3.4}$$

From (3.2) and (3.3), equilibrium equation (2.6) can be written in the form

$$u'' + \Big(\frac{2}{r}u\Big)' + \nu\psi' = 0 \qquad \alpha\Big(\psi'' + \frac{2}{r}\psi'\Big) - \zeta\psi - \beta\Big(u' + \frac{2}{r}u\Big) = 0 \tag{3.5}$$

where

$$\nu = \frac{\beta}{2\mu+\lambda'}$$

The boundary conditions reduce to

$$\sigma_{rr} = t_r \qquad \sigma_{\varphi r} = t_\varphi \qquad \sigma_{\vartheta r} = t_\vartheta \qquad h = h_r \tag{3.6}$$

where t_r and h_r are prescribed constants.

From the first equation of (3.5) we get

$$u' + \frac{2}{r}u + \nu\psi = B_1 \tag{3.7}$$

in which B_1 is an arbitrary constant. By considering equation (3.7), the second equation of (3.5) become

$$\psi'' + \frac{2}{r}\psi' - \xi^2\psi = \frac{\beta}{\alpha}B_1 \tag{3.8}$$

where

$$\xi^2 = \frac{1}{\alpha}\Big(\zeta - \frac{\beta^2}{2\mu+\lambda}\Big)$$

We note that $\xi^2 > 0$.

Equation (3.8) has solution

$$\psi = C_1 i_0(\xi_r) + C_2 k_0(\xi_r) - \frac{\beta}{\alpha\xi^2} B_1 \tag{3.9}$$

where C_1 and C_2 are arbitrary constants and i_n and k_n are spherical modified Bessel functions of the first and second kind, respectively.

When $n = 0$ and $\xi r > 0$, the following identities hold

$$i_0 = \sqrt{\frac{\pi}{2\xi r}} I_{1/2}(\xi r) = \frac{\sinh \xi r}{\xi r} \qquad k_0 = \sqrt{\frac{\pi}{2\xi r}} K_{1/2}(\xi r) = \frac{e^{-\xi r}}{\xi r} \tag{3.10}$$

where $I_{n+1/2}$ and $K_{n+1/2}$ are modified Bessel functions of a non-integer order and e is the Nepero number. Taking into account the relation

$$1 + \frac{\nu\beta}{\xi^2\alpha} = \frac{\zeta}{\alpha\xi^2} \tag{3.11}$$

from (3.7) and (3.9), we obtain

$$u = \frac{\zeta}{3\alpha\xi^2} B_1 r - B_2 \frac{1}{r^2} - \nu C_1 i_1(\xi r) + \nu C_2 k_1(\xi r) \tag{3.12}$$

in which B_2 is an arbitrary constant. In (3.12) the spherical modified Bessel functions i_1 and k_1 take the following expressions

$$\begin{aligned} i_1(\xi r) &= \sqrt{\frac{\pi}{2\xi r}} I_{3/2}(\xi r) = \frac{\xi r \cosh \xi r - \sinh \xi r}{\xi^2 r^2} \\ k_1(\xi r) &= \sqrt{\frac{\pi}{2\xi r}} K_{3/2}(\xi r) = \Big(\frac{1}{r\xi} + \frac{1}{\xi^2 r^2}\Big) e^{-\xi r} \end{aligned} \tag{3.13}$$

In the next Section we consider some applications of general solution (3.9) and (3.12) of the problem. We will study special cases related to the equilibrium of an elastic sphere.

4. Related problems and applications

4.1. Solid sphere loaded with purely radial pressure

In boundary conditions (3.6), let

$$t_r = t = \text{const} \qquad t_\varphi = t_\vartheta = 0 \qquad h = 0 \tag{4.1}$$

For $r = 0$, the functions u and ψ must be finite, so that

$$B_2 = 0 \qquad C_1 = 0 \qquad C_2 = 0 \tag{4.2}$$

The functions u and ψ reduce to

$$u = \frac{\zeta}{3\alpha\xi^2} B_1 r \qquad \psi = -\frac{\beta}{\alpha\xi^2} B_1 \tag{4.3}$$

From (4.3), (3.3) and (3.4) we find

$$e_{rr} = e_{\varphi\varphi} = e_{\vartheta\vartheta} = \frac{\zeta}{3\alpha\xi^2} B_1 \tag{4.4}$$

and

$$\sigma_{rr} = \sigma_{\varphi\varphi} = \sigma_{\vartheta\vartheta} = \frac{\zeta(2\mu + 3\lambda) - 3\beta^2}{3\alpha\xi^2} B_1 \qquad (4.5)$$
$$h_r = h_\varphi = h_\vartheta = 0 \qquad p = 0$$

We introduce the notation

$$c = \frac{\zeta(2\mu + 3\lambda) - 3\beta^2}{3\alpha\xi^2} \qquad (4.6)$$

It follows from (4.5), (4.1) and boundary conditions (3.6) that

$$B_1 = \frac{1}{c} t \qquad (4.7)$$

From (4.3), we obtain a solution of an analogous problem in the classical theory of elasticity. In fact when $\beta = 0$, then

$$u = \frac{1}{2\mu + 3\lambda} \qquad \psi = 0 \qquad (4.8)$$

Solution (4.3) enables us to calculate the bulk modulus of a material with voids. From (4.4) and (3.4) we get

$$\psi = -\frac{\beta}{\zeta} \operatorname{tr} \mathbf{E} \qquad (4.9)$$

By constitutive equations (3.4) and equations (4.5), we obtain

$$t = K \operatorname{tr} \mathbf{E} \qquad (4.10)$$

where

$$K = \frac{\zeta(2\mu + 3\lambda) - 3\beta^2}{3\zeta} \qquad (4.11)$$

The constant K is the bulk modulus of an elastic material with voids. Now we introduce the notation

$$K^* = \frac{\zeta(2\mu + 3\lambda) - 3\beta^2}{3\beta} \qquad (4.12)$$

From (4.3), (4.11) and (4.12), the functions u and ψ can be written in an explicit form

$$u = \frac{1}{3K} tr \qquad \psi = -\frac{1}{K^*} t \qquad (4.13)$$

For $\beta = 0$, we have $1/K^* = 0$ and K reducing to

$$K^0 = \frac{2\mu + 3\lambda}{3} \qquad (4.14)$$

The elastic constant K^0 is the bulk modulus in classical elasticity. We note that $K > 0$ and $K < K^0$. In fact

$$K^0 - K = \frac{\beta^2}{\zeta} > 0$$

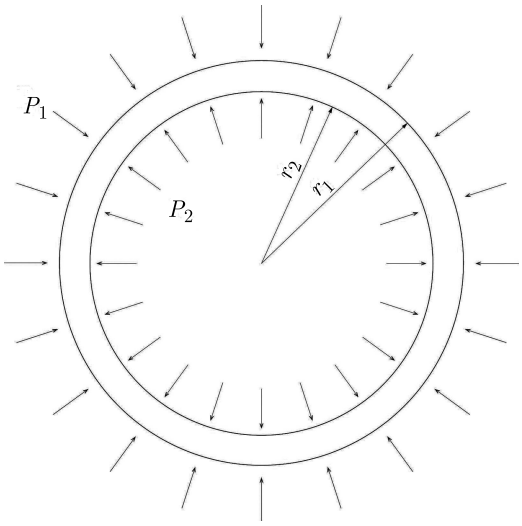

Fig. 1.

4.2. A shell bounded by concentric spherical surfaces

We consider a body bounded by concentric spherical surfaces under the action of internal and external pressure. We denote by r_1 and r_2 the radius of the external and internal boundaries, respectively. Let p_1 be the pressure on the external spherical surface and p_2 the pressure on the internal spherical surface (Fig. 1).

Boundary conditions (3.6) become

$$\begin{aligned} &\sigma_{rr} = -p_1 \qquad \sigma_{\varphi r} = \sigma_{\vartheta r} = 0 \qquad h_r = 0 \qquad \text{on} \quad r = r_1 \\ &\sigma_{rr} = -p_2 \qquad \sigma_{\varphi r} = \sigma_{\vartheta r} = 0 \qquad h_r = 0 \qquad \text{on} \quad r = r_2 \end{aligned} \tag{4.15}$$

From (3.4) and (3.9), it follows that

$$h_r = \alpha\xi[C_1 i_1(\xi r) - C_2 k_1(\xi r)] \tag{4.16}$$

For $r \neq 0$, the function i_1 and k_1 assume finite and non-zero values, so that boundary conditions (4.15) imply

$$C_1 = C_2 = 0 \tag{4.17}$$

Taking into account (3.9), (3.12), (3.4) and (4.6), the stress component σ_{rr} has the form

$$\sigma_{rr} = cB_1 + 4\mu\frac{1}{r^3}B_2 \tag{4.18}$$

With the use of (4.15), we find

$$B_1 = \frac{1}{c}\frac{p_2 r_2^3 - p_1 r_1^3}{r_1^3 - r_2^3} \qquad B_2 = \frac{p_1 - p_2}{4\mu}\frac{r_1^3 r_2^3}{r_1^3 - r_2^3} \tag{4.19}$$

From (3.9), (3.12), (3.4) and (4.19), we obtain the solution in an explicit form

$$\begin{aligned} u &= \frac{1}{r_1^3 - r_2^3}\Big[\frac{1}{3K}(p_1 r_1^3 - p_2 r_2^3)r - \frac{1}{4\mu}(p_1 - p_2)\frac{r_1^3 r_2^3}{r^2}\Big] \\ \psi &= \frac{1}{K^*}\frac{p_1 r_1^3 - p_2 r_2^3}{r_1^3 - r_2^3} \end{aligned} \tag{4.20}$$

Further

$$\begin{aligned}
&\sigma_{rr} = \frac{1}{r_1^3 - r_2^3}\Big[(p_1 - p_2)\frac{r_1^3 r_2^3}{r^3} - p_1 r_1^3 + p_2 r_2^3\Big] \\
&\sigma_{\varphi\varphi} = \sigma_{\vartheta\vartheta} = -\frac{1}{r_1^3 - r_2^3}\Big[\frac{1}{2}(p_1 - p_2)\frac{r_1^3 r_2^3}{r^3} + p_1 r_1^3 - p_2 r_2^3\Big] \\
&h_r = 0 \qquad\qquad p = 0
\end{aligned} \tag{4.21}$$

Relations (4.20) and (4.21) generalize the solution of the analogous problem in the classical elasticity (Love, 1926).

4.3. A sphere with a rigid core

Now, we consider a spherical porous body B of radius r_1 in which a concentric rigid sphere of radius r_2 has been inserted. The body is in equilibrium under the action of uniform pressure $-t$ ($t > 0$), Fig. 2.

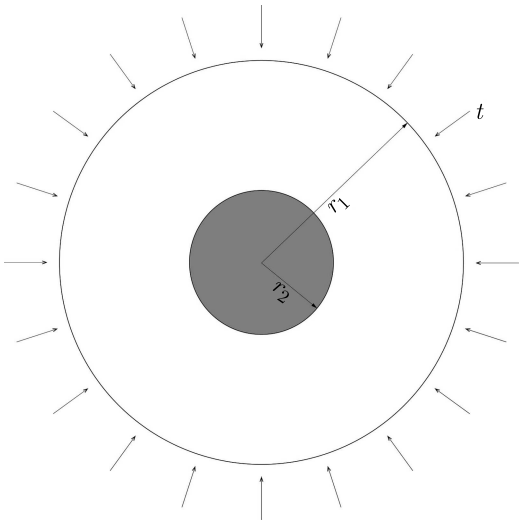

Fig. 2.

The boundary conditions are

$$\begin{aligned}
&\sigma_{rr} = -t \qquad h_r = 0 \qquad \text{for} \quad r = r_1 \\
&u = 0 \qquad \psi = 0 \qquad \text{for} \quad r = r_2
\end{aligned} \tag{4.22}$$

We introduce the following functions

$$\begin{aligned}
&Q_1(\xi r) = \frac{i_0(\xi r)k_1(\xi r_1) + k_0(\xi r)i_1(\xi r_1)}{i_1(\xi r_1)} \\
&Q_2(\xi r) = \frac{i_1(\xi r)k_1(\xi r_1) - i_1(\xi r_1)k_1(\xi r)}{i_1(\xi r_1)}
\end{aligned} \tag{4.23}$$

It follows from (3.4), (3.9) and (3.12) that boundary conditions (4.22) are satisfied if and only if

$$\begin{aligned}
&C_1 = \frac{k_1(\xi r_1)}{i_1(\xi r_1)}C_2 \qquad C_2 = -\frac{1}{D}t \\
&B_1 = \frac{\alpha\xi^2}{\beta}Q_1(\xi r_2)C_2 \qquad B_2 = \Big[\frac{\zeta}{3\beta}Q_1(\xi r_2)r_2^3 - \nu Q_2(\xi r_2)r_2^2\Big]C_2
\end{aligned} \tag{4.24}$$

where

$$D = Q_1(\xi r_2)\Big(K^* + \frac{4\mu\zeta}{3\beta}\frac{r_2^3}{r_1^3}\Big) - 4\mu\nu Q_2(\xi r_2)\frac{r_2^3}{r_1^3} \tag{4.25}$$

Replacing constants (4.24) in relations (3.9), (3.12), (3.3) and (3.4), the solution can be rewritten in an explicit form. The kinematic variables are

$$\begin{aligned} u &= -\frac{t}{D}\Big\{\frac{\zeta}{3\beta}Q_1(\xi r_2)\Big(r - \frac{r_2^3}{r^2}\Big) + \nu\Big[Q_2(\xi r_2)\frac{r_2^2}{r^2} - Q_2(\xi r)\Big]\Big\} \\ \psi &= -\frac{t}{D}[Q_1(\xi r) - Q_1(\xi r_2)] \end{aligned} \tag{4.26}$$

The components of the stress are expressed by

$$\begin{aligned} \sigma_{rr} &= -\frac{t}{D}\Big\{Q_1(\xi r_2)\Big(K^* + \frac{4\mu\zeta}{3\beta}\frac{r_2^3}{r^3}\Big) + 4\mu\nu\Big[Q_2(\xi r)\frac{1}{r} - Q_2(\xi r_2)\frac{r_2^2}{r^3}\Big]\Big\} \\ \sigma_{\vartheta\vartheta} = \sigma_{\varphi\varphi} &= -\frac{t}{D}\Big\{c\frac{k_1(\xi r_1)}{i_1(\xi r_1)} - 2\mu\Big[\frac{\zeta}{3\beta}Q_1(\xi r_2)\frac{r_2^3}{r^3} - \nu Q_1(\xi r)\Big] \\ &\quad + 2\mu\nu\Big[Q_2(\xi r_2)\frac{r_2^2}{r^3} - Q_2(\xi r)\frac{1}{r}\Big]\Big\} \\ h_r &= -\frac{t}{D}\alpha\xi Q_2(r) \qquad\qquad p = -\frac{t}{D}\alpha\xi^2 Q_1(r) \end{aligned} \tag{4.27}$$

The maximum value of σ_{rr} occurs at $r = r_2$

$$\sigma_{rr}^{max} = -\frac{t}{D}\frac{\zeta(2\mu+\lambda) - \beta^2}{\beta}Q_1(\xi r_2) \tag{4.28}$$

If we put $\beta = 0$ into equations (4.26) and (4.27), we obtain the solution of the problem in classical elastostatics

$$u^0 = -\frac{t}{D^*}\Big(r - \frac{r_2^3}{r^2}\Big) \qquad\qquad \psi^0 = 0 \tag{4.29}$$

and

$$\begin{aligned} \sigma_{rr}^0 &= -\frac{t}{D^*}\Big(2\mu + 3\lambda + 4\mu\frac{r_2^3}{r^3}\Big) \qquad\qquad \sigma_{\varphi\varphi}^0 = \sigma_{\vartheta\vartheta}^0 = \frac{t}{D^*}2\mu\frac{r_2^3}{r^3} \\ h_r &= 0 \qquad\qquad p = 0 \end{aligned} \tag{4.30}$$

where we have introduced the notation

$$D^* = 2\mu + 3\lambda + 4\mu\frac{r_2^3}{r_1^3} \tag{4.31}$$

The maximum stress occurs at $r = r_2$

$$\sigma_{rr}^{0\,max} = -\frac{t}{D^*}(6\mu + 3\lambda) \tag{4.32}$$

If we put into (4.32) $r_2 = sr_1$, $0 < s \leqslant 1$, the relation can be rewritten in the form

$$\sigma_{rr}^{0\,max} = -3t\frac{1-\nu^*}{1+\nu^*+2(1-2\nu)s^3} \tag{4.33}$$

where ν^* is the Poisson ratio.

The ratio $-\sigma_{rr}^{max}/t$ defines the stress concentration factor. For the problem under consideration, we have

$$\kappa = \frac{1}{D} Q_1(\xi r_2)\Big(K^* + \frac{4\mu\zeta}{3\beta}\Big) \tag{4.34}$$

Expression (4.34) generalizes the stress concentration factor for the analogous problem in classical elastostatics

$$\kappa^0 = \frac{3(2\mu+\lambda)}{D^*} \tag{4.35}$$

5. Concluding remarks

- In the theory presented here, the volume fraction as an independent kinematical variable serves to distinguish the mechanical behaviour of materials with voids from ordinary elastic materials. The theory is closely related to microstructural theories and can be considered a special case of the microstretch continuum theory formulated by Eringen (1999).
- We solve the problem of spherical bodies under normal pressure. The solution is obtained in a closed form, and explicit formulas for the displacement, volume fraction function and stress distribution are given.
- The solution is applied to study three special cases. The results are compared with those predicted by the classical elasticity for the same problems. It is interesting to note that in the first and second case, the stresses are not affected by the voids, whereas the radial displacement field is modified from the value predicted by the classical elasticity. Contrary to the previous cases, the third application exhibits both radial displacement and stress field influenced by the voids.
- The solution of the porous spherical shell under external and internal normal pressure coincides with that established by Cowin and Nunziato (1983) with a different approach.
- We derive the bulk modulus of an elastic material with voids and show that it is smaller than the bulk modulus of the elastic material of the skeleton. In the case of the porous sphere with a rigid nucleus, the maximum value of tensile stress and stress concentration factor are calculated.

A. Appendix

A.1. The volume fraction concept

In many branches of engineering, for example, mechanics and biomechanics, we address solids which contain pores, such as rocks, and ceramics as well as bones. The pores can be empty or filled with fluids. The exact location of the pores is impossible to describe, so that we suppose they are statistically distributed in order to create a homogenized continuum. In the N-C theory, the pores are empty, and the material is composed by a skeleton matrix and voids. The theory of materials with voids is based on the volume fraction concept.

We consider an element of volume dV_0 in a point X_0 in the reference configuration. Let dy_0 be the volume of the skeleton matrix in P_0, then we define the volume fraction field by the ratio

$$\sigma_0 = \frac{dv_0}{dV_0}$$

If we denote by σ the volume fraction field in a generic deformed configuration, the difference

$$\psi = \sigma - \sigma_0$$

is a scalar function measuring a change in the volume fraction.

In the N-C theory, the kinematic variables are four: three components of the displacement u_i $(i = 1, 2, 3)$ and a change in the volume fraction ψ. When $\psi = 0$, the theory reduces to the classical theory of elasticity.

A.2. Balance equations

The generalized theories of elasticity are characterized by a number of kinematic variables greater than three. To formulate theories that are determinate, the number of equilibrium equations must be equal to that of kinematic variables.

In the N-C theory, the additional equilibrium equation is

$$h_{i,i} - p + q = 0 \tag{A.1}$$

The equations of motion can be easily derived from the energy conservation law (Nunziato and Cowin, 1979)

$$\frac{d}{dt}\int\limits_r \rho_0\Big(e + \frac{1}{2\dot{u}_j\dot{u}_j} + \frac{1}{2}\kappa\dot{\psi}^2\Big)\, dV_0 = \int\limits_\Omega (\mathbf{f}_i\dot{\mathbf{u}}_i + q\dot{\psi})\, dV_0 + \int\limits_{\partial\Omega} (\mathbf{t}_k\dot{\mathbf{u}}_k + h\dot{\psi})\, dA_0 \tag{A.2}$$

where e is the internal energy per unit mass and k is the equilibrated inertia.

The previous equation is also true when $\dot{\mathbf{u}}$ is replaced by $\dot{\mathbf{u}} + \mathbf{a}$, where $\mathbf{a}$ is an arbitrary constant vector with all the other terms being unaltered. By subtraction, we get

$$\left(\int\limits_\Omega f_i\, dV_0 + \int\limits_{\partial\Omega} t_i\, dA_0 - \int\limits_\Omega \rho_0\ddot{\mathbf{u}}_i\, dV_0\right) - \mathbf{a}_i = \mathbf{0} \tag{A.3}$$

for all arbitrary constant vectors $\mathbf{a}$. The quantities in the square brackets are independent of $\mathbf{a}$, then it follows that

$$\int\limits_\Omega \rho_0\ddot{\mathbf{u}}_i\, dV_0 = \int\limits_{\partial\Omega} t_i\, dA_0 + \int\limits_\Omega f_i\, dV_0 \tag{A.4}$$

From the usual methods, we obtain

$$t_{ji,j} + f_i = \rho_0\ddot{\mathbf{u}}_i \tag{A.5}$$

In view of (A.4), relation (A.1) reduces to

$$\int\limits_\Omega \rho_0(\dot{e} + \kappa\dot{\psi}\ddot{\psi}\, dV_0 = \int\limits_\Omega (t_{ij}\dot{e}_{ij} + q\dot{\psi})\, dV_0 + \int\limits_{\partial\Omega} h\dot{\psi}\, dA_0 \tag{A.6}$$

If the region Ω is a tetrahedron bounded by the coordinate planes through the point X and by a plane whose unit normal is $\mathbf{n}$, we obtain

$$(h - h_i n_i)\dot{\psi} = 0 \tag{A.7}$$

Using (A.5) and (A.6) and applying the resulting equation to an arbitrary region, we obtain the load form of the conservation of energy

$$\rho_0\dot{e} = T_{ij}\dot{e}_{ij} + h_i\dot{\psi}_{,i} + p\dot{\psi} \tag{A.8}$$

where p satisfies the equation

$$h_{i,i} - p + q = \rho_0\kappa\ddot{\psi} \tag{A.9}$$

The last equation is called the balance of equilibrated force and describes dynamical changes in the void volume.

Acknowledgments

I express my gratitude to the referee for his criticism and helpful suggestions.

References

1. Biot M.A., 1941, General theory of three-dimensional consolidation, *Journal of Applied Physics*, **12**, 155-164
2. Ciarletta M., Ieşan D., 1993, *Non-Classical Elastic Solids*, John Wiley & Sons Inc., New York
3. Clebsch R.F.A., 1862, *Theorie der Elasticitat Fester Koerper*, B.G. Teubner, Leipzig
4. Cowin S.C., Goodman M.A., 1976, A variational principle for granular materials, *Zeitschrift für Angewandte Mathematik und Mechanik, ZAMM*, **56**, 281-286
5. Cowin S.C., Nunziato J.W., 1983, Linear elastic materials with voids, *Journal of Elasticity*, **13**, 2, 125-147
6. Cowin S.C., Puri P., 1983, The classical pressure vessel problems for linear elastic materials with voids, *Journal of Elasticity*, **13**, 157-163
7. De Cicco S., De Angelis F., 2019, A plane strain problem in the theory of elastic materials with voids, *Mathematics and Mechanics of Solids*, **25**, 1, 46-59
8. De Cicco S., Ieşan D., 2013, Thermal effects in anisotropic porous elastic rods, *Journal of Thermal Stresses*, **36**, 4, 364-377
9. Dell'Isola F., Batra R.C., 1971, Saint-Venant's problem for porous linear elastic materials, *Journal of Elasticity*, **47**, 73-81
10. Eringen A.C., 1999, *Microcontinuum Field Theories I: Foundations and Solids*, Springer
11. Goodman M.A., Cowin S.C., 1972, A continuum theory for granular materials, *Archive for Rational Mechanics and Analysis*, **44**, 249-266
12. Ieşan D., 1985, Some theorems in the theory of elastic materials with voids, *Journal of Elasticity*, **15**, 215-224
13. Jenkins J.T., 1975, Static equilibrium of granular materials, *Journal of Applied Mechanics*, **42**, 3, 603-606
14. Kupradze V.D., Edit., 1979, *Three-Dimensional Problems of the Mathematical Theory of Elasticity and Thermoelasticity*, North Holland
15. Lamé G., 1854, Mémoire sur l'équilibre d'elasticité des enveloppes spheriques, *Journal de Mathématiques Pures et Appliquées*, **XIX**
16. Love A.E.H., 1911, *Some Problems of Geodynamics*, Cambridge University Press
17. Love A.E.H., 1926, *Treatise on the Mathematical Theory of Elasticity*, Dover Publications Inc., New York
18. Mackenzie J.K., 1950, The elastic constants of a solid containing spherical holes, *Proceedings of the Physical Society, Section B*, **63**, 1, 2-11
19. Magnucki K., Malinowski M., 2004, Elastic buckling of porous beam, *Journal of Theoretical and Applied Mechanics*, **42**, 4, 859-868
20. Nunziato J.W., Cowin S.C., 1979, A nonlinear theory of elastic materials with voids, *Archive for Rational Mechanics and Analysis*, **72**, 175-201
21. Poisson S.D., 1829, Mémoire sur l'équilibre et le mouvement des corps élastiques, *Mémoires de l'Académie Royal des Sciences de l'Institut de France*, Paris, **8**, 357-570
22. Puri P., Cowin S.C., 1985, Plane waves in linear elastic materials with voids, *Journal of Elasticity*, **15**, 167-183
23. Thompson W., 1863, Dynamical problems regarding elastic spheroidal shells and spheroids of incompressible liquid, *Philosophical Transactions of the Royal Society of London*, **153**, 583-616

Manuscript received September 27, 2022; accepted for print December 21, 2022

JOURNAL OF THEORETICAL AND APPLIED MECHANICS
61, 2, pp. 317-330, Warsaw 2023
https://doi.org/10.15632/jtam-pl/161478

ANALYSIS OF DYNAMIC CHARACTERISTICS OF AN EXPERIMENTAL BENCH OF HIGH-PRESSURE WATER FRACTURING ASSISTED CUTTING

Zhiming Liu

School of Mechanical Electronic and Information Engineering, China University of Mining and Technology-Beijing, Beijing, China

Qiang Zhang, Yuliang Sun, Junming Liu

College of Mechanical and Electronic Engineering, Shandong University of Science and Technology, Tsingtao, China

Corresponding author Junming Liu, e-mail: junmingleo@163.com

Aiming at the problem that the cutting efficiency of a drum shearer is low when mining hard coal seams, an experimental bench of high-pressure water fracturing assisted cutting is designed. Compared with normal ones, the maximum equivalent stress of the improved experimental bench is reduced by 55.38%, and the maximum total deformation is reduced by 27.23%. According to the results of dynamic response analysis, it is concluded that the experimental bench of high-pressure water fracturing assisted cutting is stable and reliable under extreme working conditions, and meets design requirements for strength and stiffness.

Keywords: high-pressure water fracturing, experimental bench, dynamic characteristics

1. Introduction

Coal is the bottom-line guaranteed energy, and will continue to provide strong support for development of national economy and social stability. There is a large number of hard coal seam reserves in China's coal resources, and the conventional mechanical mining method has poor adaptability in the hard coal mining process (Zhang *et al.*, 2022b). How to realize safe and efficient mining of a hard coal seam is one of the research topics that has been widely concerned at present. Scholars at home and abroad search for an efficient method of mechanical cutting assisted by other means. In addition to traditional drilling and blasting, the current methods of coal breaking with assistance mainly include microwave irradiation assisted coal breaking (Hassani *et al.*, 2016), high pressure water jet assisted coal breaking (Liu, 2022b), impact pick assisted coal breaking (Zhang *et al.*, 2022a) and high-pressure water fracturing assisted coal breaking (Jiang *et al.*, 2012; Li *et al.*, 2021).

Teimoori and Cooper (2021) developed and analyzed numerical simulation of rock-microwave interaction via the finite element method to solve the electric field and magnetic field, temperature distribution and maximum principal stress. The results showed that microwave energy has potential application prospects for rock fragmentation and continuous excavation. Wang *et al.* (2021) proposed a shearer drum with an abrasive slurry jet, and studied the effects of multiple parameters on the rock-breaking ability of the abrasive slurry jet combined with picks through orthogonal experiments. Cui *et al.* (2022) studied breaking characteristics of rock samples with size of 700 mm×700 mm×700 mm by using a high-pressure foam fracturing device. The effects of well depth, seal length and foam pressure were analyzed. The results showed that when the well depth was 100-120 mm, the sealing length was 30-10 mm, and the foam pressure was 15-16.5 MPa, the rock failure mode changed from blasting pit to stripped boulder. Deng *et al.* (2022) created a physical model using rectangular and circular laser points to scan the broken

rock, and verified the accuracy of the model through a combination of experiments and numerical simulations. Li *et al.* (2021) used a hydraulic fracturing system and simulated the cutting system to cut rock samples after fracturing, and found that the cutting torque and cutting resistance were significantly reduced after fracturing. Liu *et al.* (2022a) used ASJ method to study the effect of mud properties and working parameters on rock cutting performance, and analyzed the rock cutting resistance and specific energy (SE) of ASJ-assisted conical pick. Xi *et al.* (2022) conducted orthogonal experiments of the split Hopkinson pressure bar (SHPB) device to analyze 13 parameters of the Riedel Hiermaier Thoma (RHT) material model, considering the actual size of drilling teeth and the load transmitted to the formation. Subsequently, the numerical simulation results of the SHPB test and cutting experiment were verified using a physical model. Zhang *et al.* (2022b) considered the combination of impact action and cutting action, and studied cutting characteristics of the impact pick by combining theoretical analysis, numerical simulation and an experiment. Zhao *et al.* (2021) proposed a finite element numerical modeling method for a dynamic cutting process under different ultra-high pressure loads. The cutting force, mechanical specific energy (MSE), rock failure mode and crack propagation process of heterogeneous rock with natural cracks were analyzed and compared with cutting conditions under a steady load. Deng *et al.* (2004) summarized the hydraulic fracturing mechanism of a hard coal seam through theoretical analysis and engineering practice, that is, injecting high-pressure water into the coal seam to produce cracks and weaken strength of the coal body and improve the cutting efficiency.

Among the above various methods of coal breaking with assistances, the method of high pressure water fracturing assisted cutting has broad application prospects. At present, the experimental research in the method of high-pressure water fracturing assisted cutting is mostly focused on the engineering field, and experimental devices in the related fields are mostly water jet experimental benches. There is a lack, however, an experimental device of high-pressure water fracturing assisted cutting in the laboratory. Therefore, this paper designs an experimental bench of high-pressure water fracturing assisted cutting and analyzes its structural dynamic response characteristics, which can provide a reliable experimental platform for relevant experiments.

2. Principle of the experimental bench of high-pressure water fracturing assisted cutting and a finite element model establishment

2.1. Composition and principle of the experimental bench

The structure of the experimental bench of high-pressure water fracturing assisted cutting is mainly composed of the main frame, traction slide table, propulsion slide table, mounting plate for samples, cutting drum, device for confining pressure loading and device of high-pressure water fracturing, as shown in Fig. 1.

The propulsion slide table is connected with the frame, traction slide table and the propulsion slide table through linear guide rails. Ball screw pairs are respectively installed between the propulsion slide table and the frame, and between the traction slide table and the propulsion slide table, which are driven by their respective connected servo motors. A motor for controlling the cutting drum, a reducer, speed and torque sensor, bearing seats and the cutting drum are successively installed on the traction slide table. The input and output ends of the speed and torque sensors are connected with the front and rear shafts by the internal tooth coupling, and picks are installed on the cutting drum.

The top hydraulic cylinder and side hydraulic cylinder are installed on the mounting plate. The piston rod of each hydraulic cylinder is connected with a pressing plate. When the piston rod extends, the pressure plate will apply pressure to the sample in order to simulate the confining pressure of deep coal and rock. A water tank is placed under the mounting plate to provide

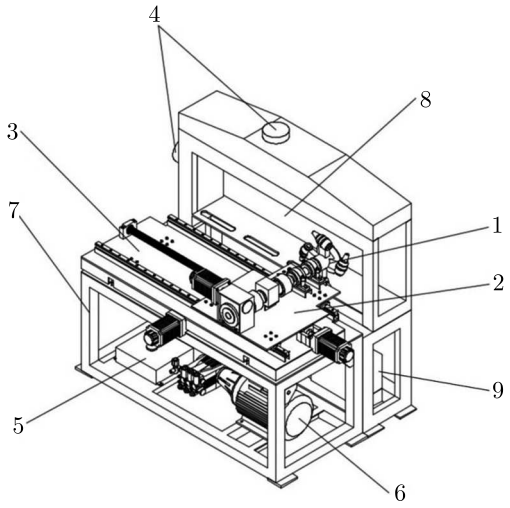

Fig. 1. Structural diagram of experimental bench of high-pressure water fracturing assisted cutting: 1 – cutting drum, 2 – traction slide table, 3 – propulsion slide table, 4 – hydraulic cylinder, 5 – hydraulic oil tank, 6 – high pressure pump, 7 – main frame, 8 – mounting plate for samples, 9 – water tank

water source for fracturing. The oil tank is installed under the main frame to provide power for the confining pressure loading device. A high-pressure pump is installed under the main frame to generate high-pressure water flow for fracturing.

The working principle of the experimental bench is as follows: Place the specimens on the mounting plate, turn on the hydraulic loading device, and apply pressure to the top and side walls of the specimens. Then start the high-pressure water pump, inject the high-pressure water into the specimens through the pipeline, and seal the water injection hole with a hole sealer. Micro cracks are generated in the specimen and then they will propagate and penetrate until the final macro cracks are generated, which leads to instability and fracture of the specimen. After the specimen is fractured by high-pressure water, the drum starts to cut it.

2.2. Establishment of the finite element model of the experimental bench

The experimental bench of high-pressure water fracturing assisted cutting studied in this paper is an assembly in which there are many connection relations between various parts. The constituent parts of the experimental bench contain many threaded holes, rounded corners and chamfers. If the finite element model is created completely according to the actual situation, it will be very complex and occupy a lot of memory resources in the calculation process. So these detail features need to be simplified. The mounting plate is not directly connected with the cutting part. This paper mainly analyzes the dynamic response of the experimental bench except for the mounting plate. Retaining the structure with large mass on the experimental bench has a great impact on the dynamic characteristics. SolidWorks is used for modeling the simplified three-dimensional experimental bench of high-pressure water fracturing assisted cutting, as shown in Fig. 2.

The simplified three-dimensional model is imported into ANSYS Workbench to establish the finite element model of the experimental bench. According to the Chinese standard of steel classification, the materials of the experimental bench mainly include aluminum alloy, cast iron and steel grades GCr15, GCr 45, 42CrMo and 40Cr, respectively. The material of the main frame, propulsion slide table and traction slide table are 40Cr steel. The material of lead screws, guide rails, nuts and sliding block is GCr15 steel. The material of nut seats, internal tooth coupling, cutting drum and main shaft is 45 steel. The material of the casing of the reducer and speed torque sensor is aluminum alloy. The material of picks, pick sleeves and pick seats is 42CrMo

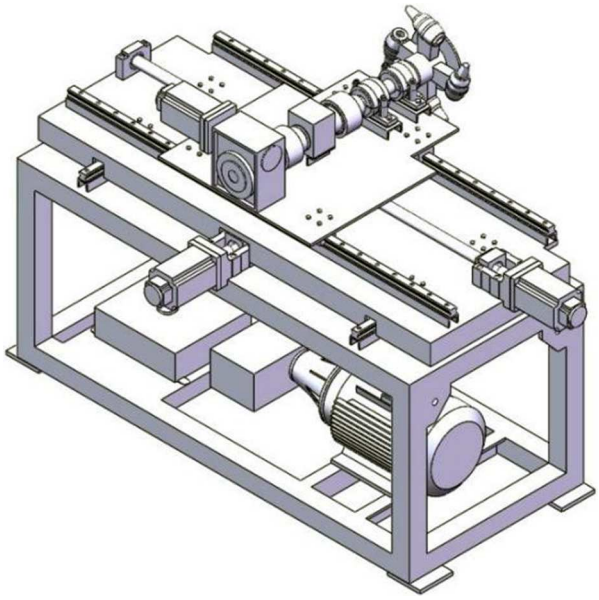

Fig. 2. Simplified three-dimensional model of the experimental bench

steel. And the material of keys, bolts, nuts and other parts installed on the experimental bench is 45 steel. The parameter settings of each material in the finite element model of the experimental bench are shown in Table 1.

Table 1. Parameters of each material in the finite element model of the experimental bench

Material type	Poisson's ratio	Density [kg/m^3]	Young's modulus [MPa]
GCR15	0.30	7810	2.08E+5
45 steel	0.27	7850	2.00E+5
42CrMo	0.28	7850	2.12E+5
40Cr	0.30	7850	2.10E+5
Aluminum alloy	0.33	2700	7.00E+4

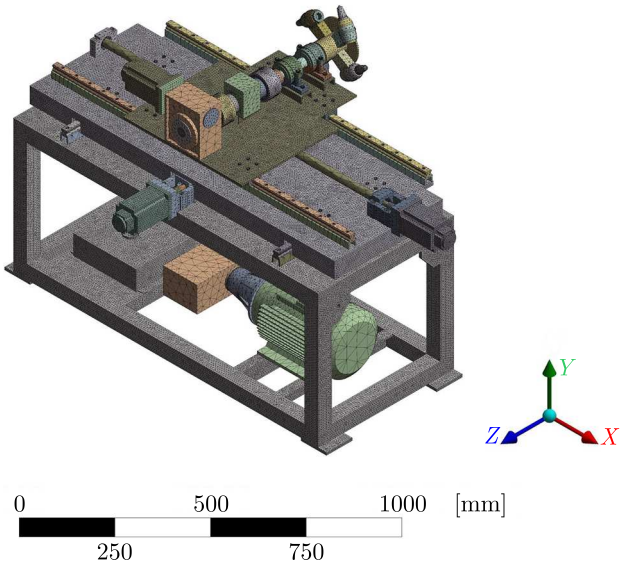

Fig. 3. Finite element model of the experimental bench

As shown in Fig. 3, after the three-dimensional model is established, it is meshed and constrained. The mesh type is selected as a tetrahedron, and the value of relevance is set to 20. The result of meshing is 1,026,377 elements. The constraint type of the contact plane between the bottom of the experimental bench and the ground is set as fixed contact. Other components such as the motor and guide rail are fixed to the experimental bench through bolts, and the contact surface type is bound contact. The rotation constraint is used for rotating components such as the cutting head.

3. Dynamic characteristics analysis of the experimental bench of high-pressure water fracturing assisted cutting

3.1. Modal analysis of the experimental bench

According to Newton's second law, motion of the experimental bench of high-pressure water fracturing assisted cutting can be expressed by a linear differential equation as

$$\mathbf{M}\ddot{\mathbf{X}}(t) + \mathbf{C}\dot{\mathbf{X}}(t) + \mathbf{K}\mathbf{X}(t) = \mathbf{F}(t) \tag{3.1}$$

where $\mathbf{M}$ is the mass matrix, $\mathbf{C}$ – damping matrix, $\mathbf{K}$ – stiffness matrix of the experimental bench, $\ddot{\mathbf{X}}(t)$ is the acceleration vector, $\dot{\mathbf{X}}(t)$ – velocity vector, $\mathbf{X}(t)$ – displacement vector, $\mathbf{F}(t)$ is the external excitation vector.

In order to determine the natural frequency and vibration mode of the experimental bench, an undamped homogeneous vibration equation of the system can be obtained by simplifying equation (3.1), that is

$$\mathbf{M}\ddot{\mathbf{X}}(t) + \mathbf{K}\mathbf{X}(t) = \mathbf{0} \tag{3.2}$$

Due to the fact that the elastic body can be decomposed into a series of simple harmonic vibrations under the state of free vibration, the solution of the equation is

$$\mathbf{X}(t) = x\mathrm{e}^{\mathrm{j}\omega t} \tag{3.3}$$

where ω is the angular frequency.

Substitute equation (3.3) and its second derivative into equation (3.2), the equation is obtained as

$$(\mathbf{K} - w^2\mathbf{M})(x)\mathrm{e}^{\mathrm{j}\omega t} = \mathbf{0} \tag{3.4}$$

Equation (2.4) is a homogeneous algebraic equation about $\mathbf{x}$ of w^2, and the only condition for this equation to have a non-zero solution is that its coefficient determinant is zero, that is

$$|\mathbf{K} - w^2\mathbf{M}| = 0 \tag{3.5}$$

or

$$d_{2n}w^2 + d_{2n-2}w^{2n-2} + \cdots + d_0 = 0 \tag{3.6}$$

The above formula is the n-th order polynomial of w^2 containing coefficients of the characteristic equation or frequency equation $d_{2n}, d_{2n-2}, \ldots, d_0$. The roots $w_1^2, w_2^2, w_3^2, \ldots, w_n^2$ of the characteristic equation are the only n eigenvalues to ensure that hypothetical solution (3.3) can be found, and its square root is the undamped natural frequency of the vibration system. Substituting any natural frequency into equation (3.4), a value corresponding to the phase $\mathbf{x}$ of the amplitude

vector can be obtained, which represents the eigenvalue of the natural frequency. And deformation characteristics of the discrete mass in the vibration equation under the corresponding natural frequency are determined.

Modal analysis can help designers to determine the natural frequency and mode shape of the structure, so as to avoid a resonance and predict the vibration mode of the structure under different loads. The experimental bench of high-pressure water fracturing assisted cutting will vibrate under the influence of an external excitation in the working process. When the external excitation frequency is close to the natural frequency of a certain order, the experimental bench may resonate and affect its stability and performance.

In order to avoid the harm for resonance, it is necessary to carry out modal analysis. The first 8 order modes are extracted in this modal analysis, and the first 8 order natural frequencies of the experimental bench are obtained after solving, as shown in Table 2. The first 8 modal shapes are extracted as shown in Fig. 4.

Table 2. The first 8 order natural frequencies of the experimental bench

Modal order	Natural frequency [Hz]	Modal order	Natural frequency [Hz]
1	34.718	5	64.318
2	40.816	6	71.821
3	50.803	7	90.130
4	56.064	8	95.295

In Fig. 4, it can be seen that the first order mode shapes show a right inclination of the upper part of the bench. The second shows a deformation of the traction unit and cutting unit. The third and the fourth show an upward deformation on the bottom of the main frame and the pump as well as the drum, respectively. The fifth and the seventh show a right inclination of the reducer and the motors. The sixth shows a torsional deformation of the bench and the eighth one shows an upward deformation on the bottom of the main frame and the pump.

In the process of cutting, the excitation frequency of the cutting force not only acts on the part for mechanical cutting, but also on the mounting plate through specimen conduction. It is also necessary to conduct modal analysis of the mounting plate. The mounting plate is not directly connected with the part for mechanical cutting, so the modal analysis is carried out separately. In this modal analysis, the material of the mounting plate is 45 steel, and the grid element size is set as 5 mm. A total of 1414169 elements are obtained, and fixed constraints are added at the bottom of the frame. The first 8 order natural frequencies of the mounting plate are obtained, as shown in Table 3.

Table 3. The first 8 natural frequencies of the mounting plate

Modal order	Natural frequency [Hz]	Modal order	Natural frequency [Hz]
1	26.576	5	102.62
2	35.299	6	127.35
3	57.191	7	137.86
4	95.391	8	156.16

During the high-pressure water fracturing stage of the experiment, the source of the excitation frequency is mainly the motor driving the high-pressure pump. The working speed of the motor is 1450 r/min, and the excitation frequency is 24.17 Hz. It will not have a great impact on the structure of the experimental bench, and it will not resonate.

During the cutting stage of the experiment, the excitation frequency mainly comes from two parts. One of them comes from rotational motion of the parts installed in the experimental bench. The maximum working speed of the motor controlling the cutting speed is 2000 r/min,

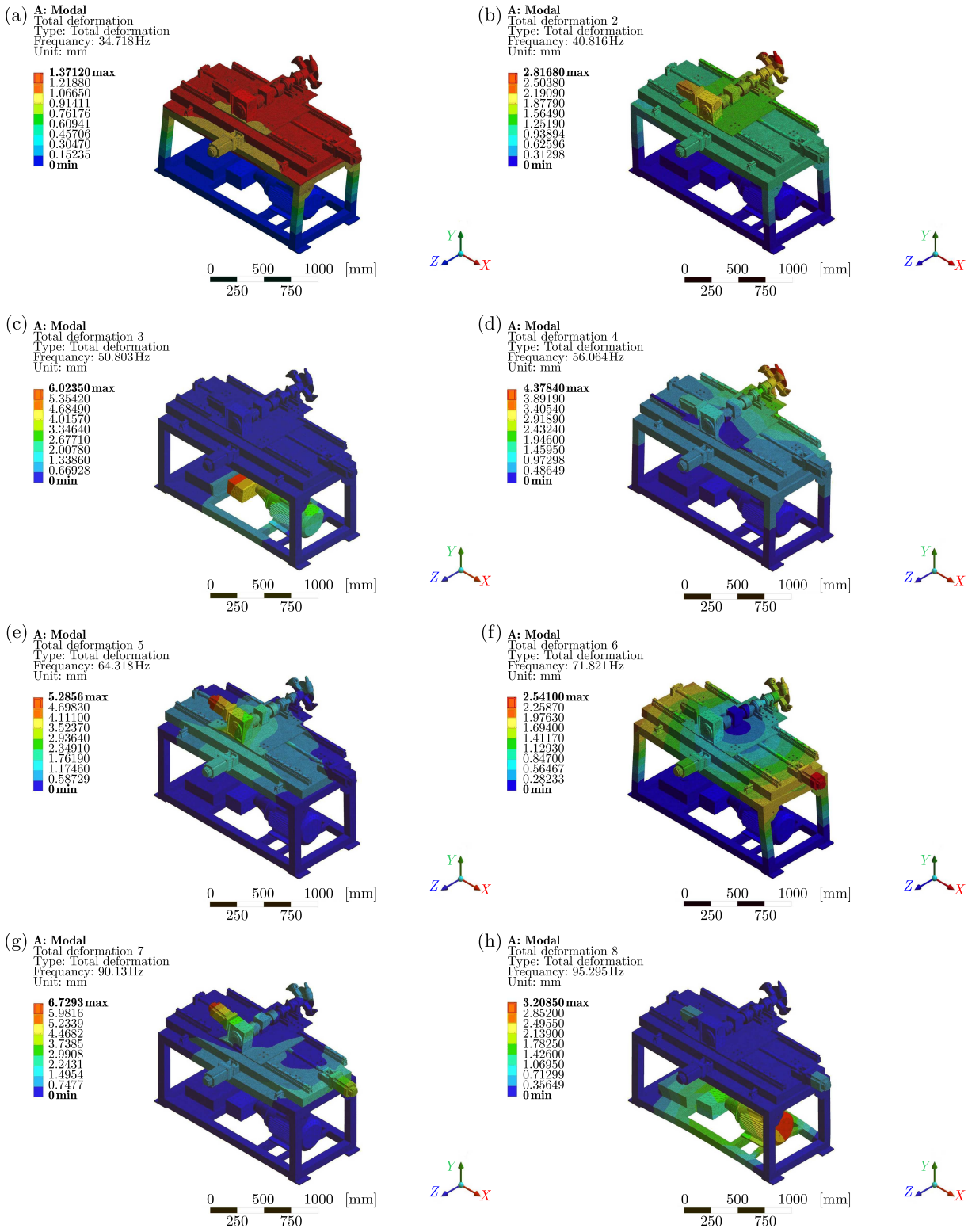

Fig. 4. First 8 order mode shapes of the experimental bench: (a) first order mode shapes, (b) second order mode shapes, (c) third order mode shapes, (d) fourth order mode shapes, (e) fifth order mode shapes, (f) sixth order mode shapes, (g) seventh order mode shapes, (h) eighth order mode shapes

and the excitation frequency is 33.33 Hz; the maximum working speed of the cutting drum and the main shaft is 41.67 r/min, and the excitation frequency is 0.69 Hz; the maximum working speed of the servo motor and lead screw in the traction sliding assembly is 1200 r/min, and the excitation frequency is 20 Hz; the maximum working speed of the servo motor and lead screw in the propulsion sliding assembly is 1500 r/min, and the excitation frequency is 25 Hz.

Another part of the excitation frequency comes from the influence of the cutting force excitation on the drum in the process of cutting. The dominant frequency of the cutting force is concentrated in a low order. It is further inferred that in the normal cutting experiment, the structure of the experimental bench of high-pressure water fracturing assisted cutting designed in this paper will not resonate due to the excitation of the load on the drum. Comparing the natural frequency and external excitation frequency of the experimental bench, the excitation frequency of the cutting motor is close to the first-order natural frequency, which may affect the structure of the experimental bench.

3.2. Harmonic response analysis of the experimental bench

The harmonic response analysis can find the steady-state response of the system under different frequency harmonic loads. In order to accurately judge the low-order resonance frequency range of the experimental bench, the harmonic response analysis is carried out. Based on the results of modal analysis, the modal superposition method is used to analyze the harmonic response of the experimental bench. The frequency range is set up between 0-120 Hz, the number of solution steps is 120, and 1000 N is applied in the X and Y direction and 500 N in the Z direction on the drum to solve the harmonic response of the experimental bench.

Through the first 8 order modes of the experimental bench, it can be found that the main frame, traction slide table and propulsion slide table are prone to large vibration. The traction slide table, propulsion slide table and main frame are selected as the research object, and the vibration amplitude-frequency response curves of are obtained, as shown in Fig. 5 and Fig. 6, respectively.

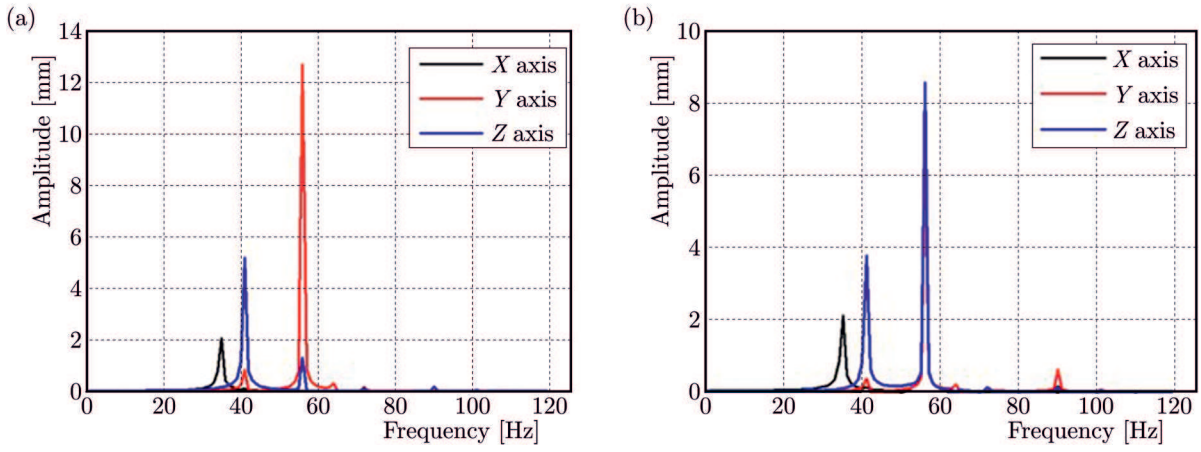

Fig. 5. Amplitude frequency response curves of: (a) traction slide table, (b) propulsion slide table

It can be seen from Fig. 5a that under the action of external loads, the amplitude peaks of the traction slide table along the X-axis, Y-axis and Z-axis appear at 35 Hz, 56 Hz and 41 Hz, respectively, and the maximum values are 2.103 mm, 12.754 mm and 5.221 mm, respectively. And it can be seen from Fig. 5b that the amplitude peaks of the propulsion slide table along the X-axis, Y-axis and Z-axis appear at 35 Hz, 56 Hz and 56 Hz, respectively, and the maximum values are 2.126 mm, 7.043 mm and 8.580 mm, respectively.

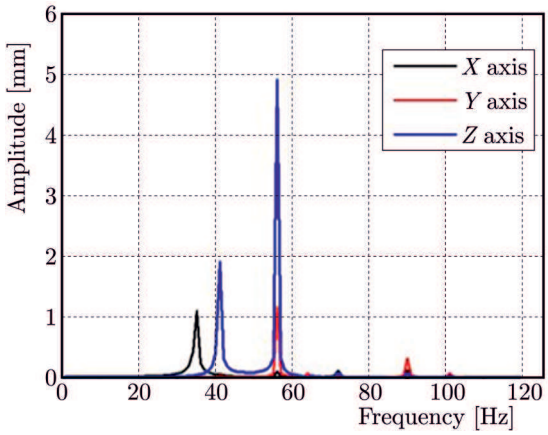

Fig. 6. Amplitude frequency response curves of the main frame

It can be seen from Fig. 7 that the amplitude peaks of the main frame along the X-axis, Y-axis and Z-axis appear at 35 Hz, 56 Hz and 56 Hz, respectively, and the maximum values are 1.114 mm, 1.167 mm and 4.918 mm, respectively.

Through the analysis of the amplitude-frequency response curves of the traction slide table, propulsion slide table and main frame along the X, Y and Z axis combined with the current operation of the experimental bench, it can be concluded that the experimental bench is prone to resonate under the action of force whose excitation frequency is close to its first-order natural frequency. Subsequent improvements to the structure of the experimental bench are required to increase its low-order natural frequency.

3.3. Transient dynamic analysis of the experimental bench

In this paper, the load spectrum of the experimental bench of high-pressure water fracturing assisted cutting under extreme working conditions is selected as the applied load, that is, the drum cuts the specimen without high-pressure water fracturing. At this time, the loads on the experimental bench are large and have a great impact on the structure. Before transient dynamic analysis, the drum cutting model of the experimental bench is established by EDEM, and the load spectrum of the experimental bench under extreme working conditions is obtained.

In this paper, the Hertz-Mindlin with bonding contact model is used to simulate the cutting process of coal and rock. Since there is no uniform standard in the parameter setting of the bond between particles, it is mostly estimated by empirical formulas

$$k_n = \frac{4}{3}\Big(\frac{2(1-\nu^2)}{E}\Big)^{-1}\Big(\frac{2}{r}\Big)^{-\frac{1}{2}} \qquad k_s = \Big(\frac{1}{2}\sim\frac{2}{3}\Big)k_n \qquad \tau = C + \sigma\tan\varphi \tag{3.7}$$

where k_n and k_s is the normal stiffness and tangential stiffness coefficient [N/m^2], r is the particle radius [m], ν is Poisson's ratio, E is the elastic modulus, σ is the normal limit stress [Pa], τ is the tangential limit stress [Pa], φ is the internal friction angle [°], C is cohesion [Pa].

The parameters used in the simulation are: (1) The shear modulus of materials of the cutting drum and coal wall are 70 GPa and 1.72 GPa, respectively, Poisson's ratio is 0.31 and 0.2, respectively, and density is 7850 kg/m^3 and 1325 kg/m^3, respectively; (2) The particles forming the coal wall are spherical particles with a radius of 10 mm. The static friction coefficient, dynamic friction coefficient and recovery coefficient between the drum and the coal wall are 0.45, 0.08 and 0.35, respectively. And the static friction coefficient, dynamic friction coefficient and recovery coefficient between the coal wall particles are 0.5, 0.2 and 0.5, respectively; (3) The contact model between particles is Hertz-Mindlin's with bonding, the contact model between the coal wall particles and drum is Hertz-Mindlin's (no slip) during cutting process.

According to the simulation results of the discrete element model, the load spectrum of the experimental bench under extreme working conditions is obtained. A group of data near the peak point of the cutting force curve is selected as the external load in the transient analysis. Specifically, the load applied to the cutting drum in this transient dynamic analysis is shown in Fig. 7. The drum is under a discrete impact condition during cutting. At the rated speed, a single pick only contacts the coal wall once per circle. According to the speed setting of the experimental bench, the paper mainly focuses on the limit load of a single pick. In order to save simulation time and improve simulation efficiency, the total simulation time is set to 0.2 s, which is divided into 40 substeps.

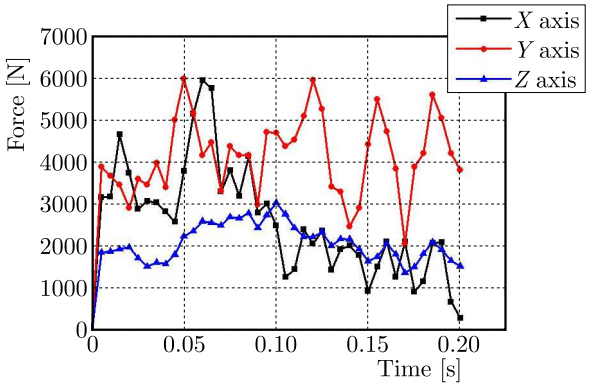

Fig. 7. Loads in transient dynamic analysis

A chance in time of the load applied to the pick tip is taken into account and a fixed constraint at the bottom of the experimental bench is added. The drum speed is set to 4.356 rad/s, and the linear speed of the traction slide is 60 mm/s. Static analysis of the experimental bench after loading is carried out, and the equivalent stress curve and total deformation curve are shown in Fig. 8.

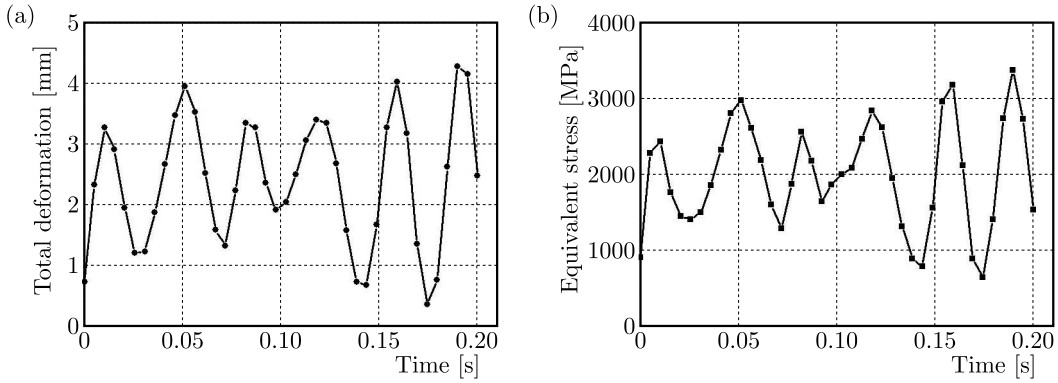

Fig. 8. The curve of (a) total deformation and (b) equivalent stress of the experimental bench with time

The maximum equivalent stress and total deformation of the experimental bench appears at 0.19 s. The equivalent stress distribution map and total deformation distribution map of the experimental bench at 0.19 s are extracted, as shown in Fig. 9.

According to Fig. 9, under the condition of time-varying loading force, the maximum equivalent stress and maximum deformation of the test bench are 335.7 MPa and 4.2659 mm, respectively. The equivalent stress and total deformation of the experimental bench in the process of cutting are large. It is necessary to improve the structure of the parts with large deformation and stress.

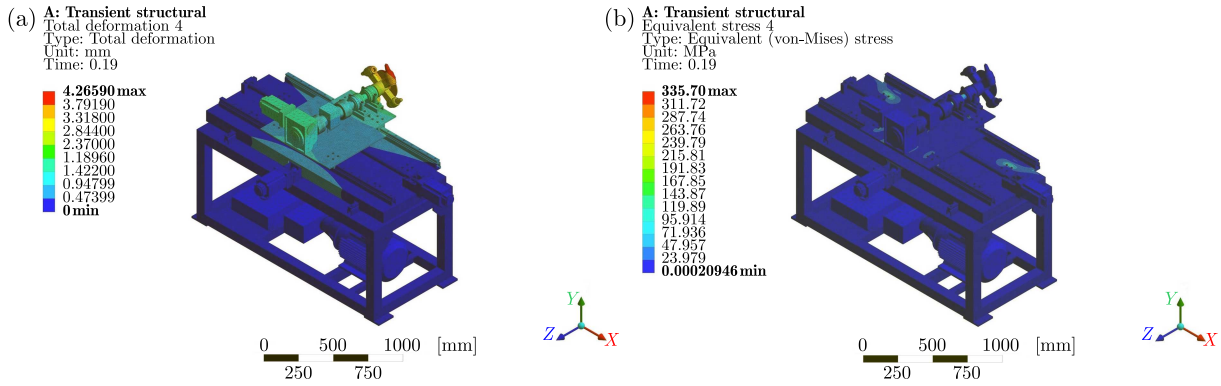

Fig. 9. Distribution nephogram of (a) total deformation and (b) equivalent stress of the experimental bench

3.4. Structural improvement of the experimental bench

According to the results of modal analysis of the traction sliding table, propulsion sliding table and frame, the vibration of the traction sliding table and propulsion sliding table is relatively large, and the low order natural frequency of the main frame has a great impact on the overall low order natural frequency of the whole experimental bench. It is necessary to optimize the structure of the experimental bench, enhance its overall natural frequency and reduce its equivalent stress and total deformation.

The experimental bench of high-pressure water fracturing assisted cutting is improved by increasing thickness of the steel plate of the support leg of the rack, and adding different forms of stiffeners at the bottom of the traction sliding table and the propulsion sliding table. The improved traction and propulsion slides are modeled using SolidWorks, as shown in Fig. 10.

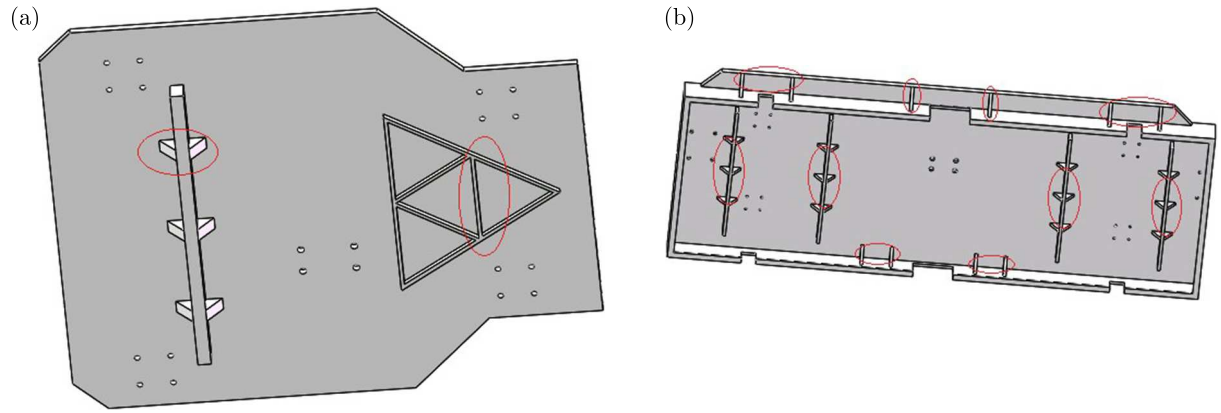

Fig. 10. Structure of the traction slide table and propulsion slide table after structural improvement: (a) traction slide table after improvement, (b) propulsion slide table after improvement

The modal analysis of the improved experimental bench is finished first, and the settings are the same as those before structural improvement. The first 8 order modes of the improved experimental bench are found. The first two order vibration modes have no obvious changes, but the vibration amplitude is reduced. After the structural improvement, the first 8 order natural frequencies are all increased. Among them, the first and second order natural frequencies are 41.066 Hz and 46.642 Hz, respectively, which are increased by 18.28% and 14.27%, respectively. The first and second order natural frequencies are greater than the external excitation frequency of the experimental bench after structural improvement, which reduces the possibility of resonance of the experimental bench.

Then, the transient dynamical analysis of the improved experimental bench is finished, and the settings of simulation are the same as those before structural improvement. The simulation results are obtained via ANSYS Workbench, and the comparison curve of the total deformation and equivalent stress changing with time before and after the structural improvement is drawn, as shown in Fig. 11.

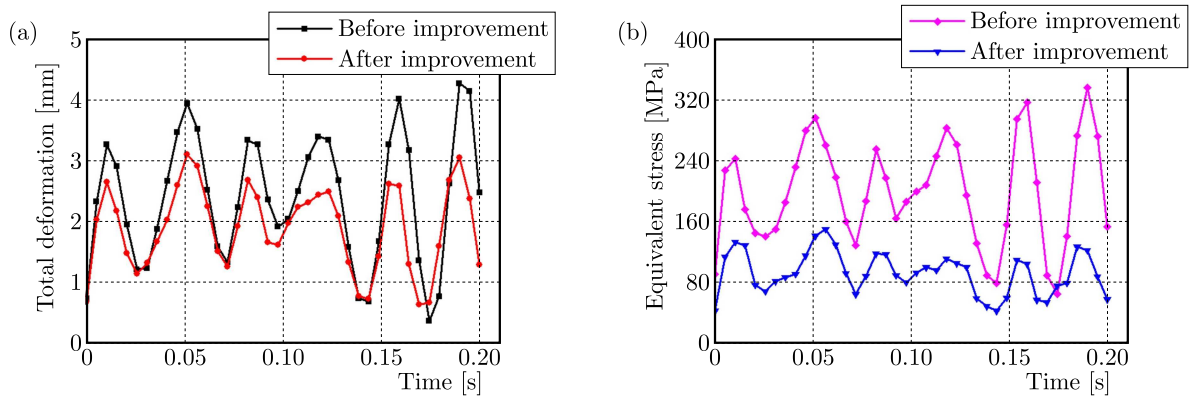

Fig. 11. Comparison diagram of (a) total deformation and (b) equivalent stress change curve before and after structural improvement of the experimental bench

It can be seen from the curves of total deformation before and after improvement in Fig. 11 that the amplitude of total deformation decreases as a whole after the structural improvement. From the curves of equivalent stress before and after the improvement, it is determined that the amplitude of equivalent stress after the improvement is greatly reduced compared with that before the improvement.

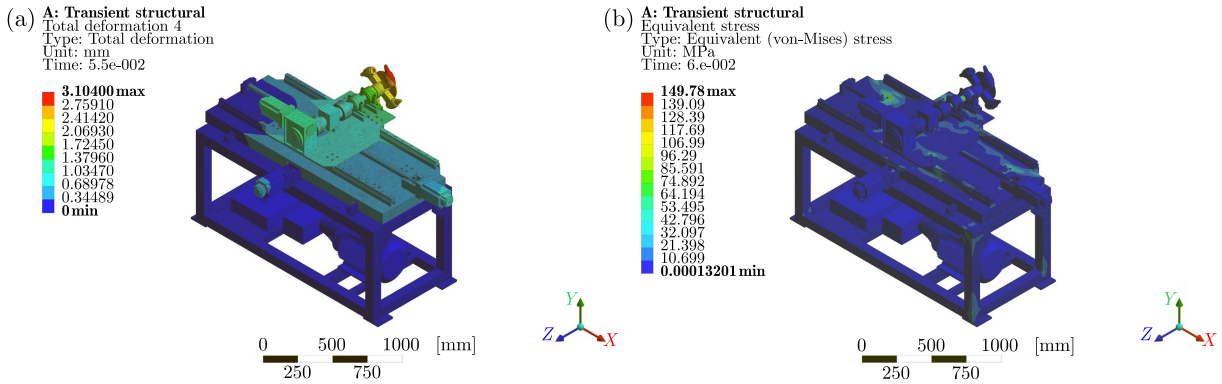

Fig. 12. Distribution nephogram of (a) maximum total deformation and (b) maximum equivalent stress of the experimental bench after structural improvement

The maximum total deformation nephogram and the maximum equivalent stress nephogram of the experimental bench after structural improvement are extracted, as shown in Fig. 12. The maximum equivalent stress after improvement is 149.78 MPa, 55.38% lower than that before improvement, which is lower than the allowable stress of its own material. The maximum total deformation of the improved experimental bench is 3.104 mm, which is 27.23% lower than that before the improvement. The overall stress distribution and deformation of the experimental bench have been greatly improved.

4. Discussion

The research presented in this article has some limitations. The damping effect is not discussed at all. In most dynamic problems (including linear dynamics and nonlinear dynamics), it is really important to define damping, but damping algorithms and parameters only approximate energy absorption characteristics of a structure. In this paper, the purpose of modal analysis is to find out the natural frequency rather than the amplitude of the structure. The purpose of transient dynamic analysis is to determine mechanical properties of the structure. It has been shown in previous studies that damping has little influence on the results of structural modal calculation and mechanical analysis, and it is very difficult to determine damping data in finite element calculation, so damping is not considered in the finite element calculation. In the future research work, we will continue to study the reliability of the experimental bench under some extreme conditions, and combine with the experimental verification. On the whole, the results indicate that the experimental bench of high-pressure water fracturing assisted cutting studied in this paper can be used as a reliable platform for carrying out experiments of high-pressure water fracturing assisted cutting, and provides a reference for the design and improvement of related experimental devices.

5. Conclusion

- In view of the lack of experimental equipment for high-pressure fracturing combined with cutting, an experimental bench of high-pressure water fracturing assisted cutting is designed. The main structure and principle are introduced, the finite element model of the experimental bench is established, and the dynamic characteristics of the experimental bench are analyzed based on the finite element method.
- The finite element model of the experimental bench is established. The first 8 order natural frequencies and modal shapes of the experimental bench are obtained in the modal analysis, and the external excitation frequencies of the experimental bench are analyzed. The results show that the excitation frequency of the cutting motor is 33.33 Hz, which is close to the first order natural frequency of 34.718 Hz, and may cause resonance. In the harmonic response analysis, the amplitude and frequency response curves of the traction slide table, the propulsion slide table and the main frame are obtained, and it is concluded that the excitation frequency that may cause the experimental bench to generate large vibration has multiple orders. However, the experimental bench is only prone to resonance at the excitation frequency close to its first order natural frequency when butting, which verifies the results of the modal analysis.
- In the transient dynamic analysis, the maximum equivalent stress of the experimental bench under the load spectrum in extreme working conditions is 335.7 MPa, and the maximum deformation is 4.2659 mm. The structure of the traction slide table, propulsion slide table and main frame are improved, and the modal analysis and transient dynamic analysis of the improved experimental bench are carried out. Compared with the experimental bench before improving, the first two order natural frequencies of the improved experimental bench increased by 18.28% and 14.27%, respectively. The overall maximum equivalent stress of the improved experimental bench is reduced by 55.38%, and the maximum deformation is reduced by 27.23%. The overall improvement effect of the experimental bench is remarkable.

Foundation Support

1. Subproject of national key R&D plan project No. 2020YFB1314200; 2. National Natural Science Foundation of China No. 52174120; 3. Taishan Scholar Program of Shandong Province No. tsqn201909113.

References

1. Cui M., Zhai Y.H., Ji G.D., 2011, Experimental study of rock breaking effect of steel particles, *Journal of Hydrodynamics, Ser. B*, **23**, 2, 241-246
2. Cui S., Liu S.Y., Li H.S., Zhou F.Y., Sun D., 2022, Critical parameters investigation of rock breaking by high-pressure foam fracturing method, *Energy*, **258**, 124871
3. Deng G.Z., Wang S.B., Huang B.X., 2004, Research on behavior character of crack development induced by hydraulic fracturing in coal-rock mass (in Chinese), *Chinese Journal of Rock Mechanics and Engineering*, **23**, 20, 3489-3493
4. Deng R., Liu J.P., Kang M.Q., Zhang W., 2022, Simulation and experimental research of laser scanning breaking granite, *Optics Communications*, **502**, 127403
5. Hassani F., Nekoovaght P.M., Gharib N., 2016, The influence of microwave irradiation on rocks for microwave-assisted underground excavation, *Journal of Rock Mechanics and Geotechnical Engineering*, **8**, 1, 1-15
6. Jiang Z.M., Feng S.R., Fu S., 2012, Coupled hydro-mechanical effect of a fractured rock mass under high water pressure, *Journal of Rock Mechanics and Geotechnical Engineering*, **4**, 1, 88-96
7. Li H.S., Liu S.Y., Zhu Z.C., Liu H., Zhang D., Guo C., 2021, Experimental investigation on rock breaking performance of cutter assisted with hydraulic fracturing, *Engineering Fracture Mechanics*, **248**, 107710
8. Liu S.Y., Cui S., Li H.S., Zhou F., Xu B., Hu Y., 2022a, Impact characteristics of rock breaking using a conical pick assisted with abrasive slurry jet, *Engineering Fracture Mechanics*, **271**, 108647
9. Liu Z.H., Ma Z.K., Liu K., Zhao S., Wang Y., 2022b, Coupled CEL-FDEM modeling of rock failure induced by high-pressure water jet, *Engineering Fracture Mechanics*, **277**, 108958
10. Teimoori K., Cooper R., 2021, Multiphysics study of microwave irradiation effects on rock breakage system, *International Journal of Rock Mechanics and Mining Sciences*, **140**, 104586
11. Wang F.C., Li L.C., Zhou X., Lin J., Guo C.W., 2021, New application of abrasive slurry jet in coal rocks breaking and prediction model of its rock breaking ability, *Arabian Journal for Science and Engineering*, **46**, 8, 7227-7237
12. Xi Y., Wang W., Fan L.F., Zha C.Q., Li J., Liu G.H., 2022, Experimental and numerical investigations on rock-breaking mechanism of rotary percussion drilling with a single PDC cutter, *Journal of Petroleum Science and Engineering*, **208**, Part B, 109227
13. Zhang Q., Wang C., Tian Y., 2022a, Numerical and experimental study on crushing properties of hard coal using impacting-cutting technique, *Shock and Vibration*, **2022**, 7091553
14. Zhang Q., Wang C., Tian Y., 2022b, Study on shearer drum structure design and coal-breaking performance based on multi-impact picks for hard coal, *Environmental Earth Sciences*, **81**, 7, 189
15. Zhao Y., Zhang C.S., Zhang Z.Z., Gao K., Li J.S., Xie X.B., 2021, The rock breaking mechanism analysis of axial ultra-high frequency vibration assisted drilling by single PDC cutter, *Journal of Petroleum Science and Engineering*, **205**, 108859

Manuscript received April 27, 2022; accepted for print January 23, 2023

JOURNAL OF THEORETICAL AND APPLIED MECHANICS
61, 2, pp. 331-342, Warsaw 2023
https://doi.org/10.15632/jtam-pl/163077

TREND ANALYSIS OF RAIL CORRUGATION IN METRO LINES CONSIDERING FRICTION MEMORY AND INTERFACE EFFECTS

Zhiqiang Wang, Zhenyu Lei
Institute of Rail Transit, Tongji University, Shanghai, China
e-mail: wangzq@tongji.edu.cn

In order to investigate the evolution trend of rail corrugation under the action of slip and interface effects, stick-slip vibration characteristics of a wheel-rail system in different line conditions have been analyzed in detail by establishing a complete three-dimensional coupling metro vehicle-track numerical model and considering the friction memory effect characterizing the slip rate and state dependence as well as interface effect. The results show that on a straight line, the friction memory effect has less influence on the wheel-rail contact stick-slip characteristics, and the values and variation ranges of adhesion coefficients and creepages are relatively small, indicating that it is difficult for the wheel-rail system to have stick-slip vibration, which makes it less likely to form rail corrugation. On a curved line, the fluctuation amplitudes of the inside longitudinal stick-slip characteristics and the outside transverse stick-slip characteristics are relatively large, which illustrates that the inside wheel-rail system is more prone to stick-slip vibration in the longitudinal direction, while the outside wheel-rail system is more prone to stick-slip vibration in the transverse direction, thus leading to different forms of rail corrugation. The friction memory effect reduces longitudinal and transverse creepages of both the inside and outside wheel-rail systems, demonstrating that the friction memory effect can moderate the relative wheel-rail slip and thus reduce the development rate of rail corrugation. The interface effect makes longitudinal and transverse adhesion coefficients of the wheel-rail system tend to homogenize and mostly decrease, while the corresponding creepages tend to increase. Although an increase in the creepage induces an enhanced interface slip, a smaller adhesion coefficient does not cause a significant change in the corrugation evolution. Friction memory and interface effects can cause the wheel-rail contact adhesion area ratio to increase, thus making the contact stick-slip distribution tend to homogenize, which is beneficial to reduce wear in the contact area and promote wear to homogenize.

Keywords: metro, rail corrugation, friction memory, interface layer, stick-slip characteristics

1. Introduction

Rail corrugation, as a structural damage, is prevalent in railway systems around the world, especially in metro lines. Unlike uniform wear of a rail surface material, rail corrugation has periodic characteristics and shows wavy wear along the longitudinal running surface of the rail (Sato *et al.* 2002). Rail corrugation involves both friction and vibration mechanisms of action, where friction determines its damage mechanism, while vibration determines its dynamic mechanism. The existence of rail corrugation will cause abnormal vibration and high-frequency noise of wheel-rail systems, which will easily lead to fatigue damage of vehicle/track components. Therefore, how to effectively prevent and control rail corrugation has become a major problem facing the current railway sector. The wheel-rail contact interface is subject to complex forces and a variety of forms of action, and all variable factors related to it have become the starting point for the study of rail corrugation. It is worth to mention that the formation of rail corrugation is not a single theoretical mechanism (Grassie and Kalousek 1993). Understanding the mechanism

of rail corrugation and exploring its evolution are important prerequisites for achieving effective management of rail corrugation.

Rail corrugation occurs in the contact patch area, and the wheel-rail contact behavior is closely related, so it is more intuitive to study the rail corrugation phenomenon from the micro contact perspective. The stick-slip theory suggests that unstable stick-slip vibration in the wheel--rail contact area contributes to formation and development of rail corrugation. Based on the above theory, Daniel *et al.* (2008) concluded through numerical simulations that the wheel-rail stick-slip had an effect on both long-wavelength and short-wavelength corrugations, and wear was mainly caused by transverse stick-slip vibration. Matsumoto *et al.* (2002), based on experimental and computational results, found that rail corrugation on a curved track was due to stick-slip vibration between the wheel and rail, which was associated with large creepages and vertical force fluctuations. Sun and Simson (2007, 2008) analyzed the effects of curve track parameters, wheel-rail friction characteristics and wheel/rail profile on the stick-slip process, and obtained that the fundamental frequency of the stick-slip process matched the passing frequency of the sleeper and a combined frequency of wheelset torsional and bending vibration. Yao *et al.* (2018) investigated the mechanism of generation of rail corrugation and proposed a micro wavelength--locked extension mechanism of corrugation. The initial stick-slip vibration will lead to formation of initial unevenness on the contact surface, i.e., the initial corrugation, and the evolution of it into the final corrugation also needs to satisfy the phase synchronization condition of stick-slip vibration. The literature (Yang and Li, 2019; Jin *et al.*, 2004; Wen and Jin, 2005) showed that rail surface defects, such as cracks, scratches, transverse geometric defects, etc., were able to ensure the same phase vibration of the stick-slip process, such that rail corrugation was eventually formed. In addition (Eadie *et al.*, 2002; Wang and Lei, 2021, 2022; Shen *et al.*, 2011; Guo *et al.*, 2009) also analyzed the formation process of rail corrugation in terms of contact stick-slip, and combined with field data to verify the correctness of the calculation results.

Most of the current papers using the stick-slip theory to explain corrugation characteristics consider the wheel-rail interface friction property as a constant value, which is not consistent with the variable friction situation in the actual wheel-rail contact due to the slip rate, state and third-body medium. In view of this, this paper focuses on stick-slip characteristics of wheel-rail contact in the presence of slip and interface effects, and analyzes the evolution trend of rail corrugation based on the stick-slip characteristics. Firstly, a three-dimensional coupling metro vehicle-track numerical model is different line conditions is established and the validity of the model is verified by combining the measured data. Then, the friction memory effect is introduced to characterize the slip rate and state dependent friction, and the corresponding contact stick--slip vibration characteristics and their influence on the corrugation trend are analyzed. Finally, on the basis of simultaneous consideration of the friction memory effect and interface effect, the joint action mechanism of both on the stick-slip characteristics and corrugation evolution is investigated in order to further improve the theoretical framework of stick-slip vibration of rail corrugation.

2. Numerical model

2.1. Establishment of model

Since this paper is mainly concerned with the evolution trend of rail corrugation is metro lines, a vehicle-track three-dimensional coupling numerical model applicable to metro scenarios is established by using the software Universal Mechanism, including the vehicle model, track model and wheel-rail contact model. The vehicle model consists of one vehicle body, two bogies and four wheelsets with the LM wear wheel profile, where the vehicle body and bogies as well as bogies and wheelsets are connected by spring-damping elements to simulate the secondary

and primary suspension. The vehicle body, bogies and wheelsets are all regarded as rigid bodies with 6 degrees of freedom, and the whole vehicle model has 42 degrees of freedom in total. The main structural parameters of the vehicle model are described in (Lei and Wang, 2021; Lei *et al.*, 2019). The rail type in the track model is CHN60, and a Timoshenko beam is used for simulation. The fastener is simulated by the spring-damping element; the track slab (under-rail structure) is built by the finite element method and imported into the track model and then connected to the rail and foundation by the spring-damping element. The main structural parameters of the track model are described in (Li, 2012; Lei and Wang, 2020). The wheel-rail contact model uses a modified CONTACT algorithm, which is based on the Duvaut-Lions variational principle and transforms the friction rolling contact problem into a variational inequality, so as to solve directly for the minimum residual energy expressed by the product of the force acting on the contact patch and displacement (Kalker, 1990; Jin and Xue, 1997). Meantime, the concept of friction memory is introduced in the CONTACT algorithm, which assumes that friction takes time to adapt to a new state and, therefore, there is a memory of the previous state (Vollebregt, 2014). By considering the friction memory of the previous state, the friction coefficient in the contact model is gradually normalized, and the slip rate dependence of friction is characterized through the friction law $\mu(S)$. The friction law $\mu(S)$ is distinguished from the actual friction coefficient $\mu(x)$, and the actual friction coefficient $\mu(x)$ is considered to be proportional to $\mu(x)-\mu(S)$ and the slip rate S, as shown below

$$\frac{d\mu}{dx} = -\frac{\max(S(x), S_{min})}{d_c(-V)}[\mu(x) - \mu(S(x))] \tag{2.1}$$

where d_c is the characteristic slip distance when convergence of the friction coefficient occurs, V is the vehicle running speed, S_{min} is the minimum slip rate that allows the friction coefficient to adapt in the adhesion area. It should be mentioned that the implementation of an instantaneous velocity-dependent falling friction law usually leads to numerical instabilities, and the latter can be prevented by the introduction of the mechanism of friction memory (Vollebregt *et al.*, 2021). A schematic diagram of the completed vehicle-track three-dimensional coupling numerical model is shown in Fig. 1.

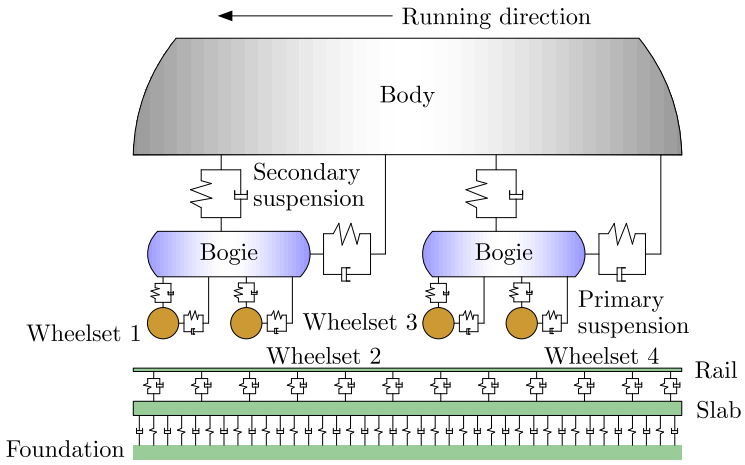

Fig. 1. Diagram of numerical model

2.2. Validation of the model

The validity of the numerical model is verified in this Section by using the measured data of rail vertical vibration acceleration of the line interval. For the test process, two sensors are arranged on a section of the measuring point, respectively on both sides of the top surface of the inner rail bottom. The INV3060S instrument is used for data acquisition, the data sampling

frequency is 2048 Hz, the speed is 56 km/h, and the software DASP-V10 is used for data analysis. The layout picture of measuring points in the field test is shown in Fig. 2. For the simulation

Fig. 2. Layout picture of measuring points

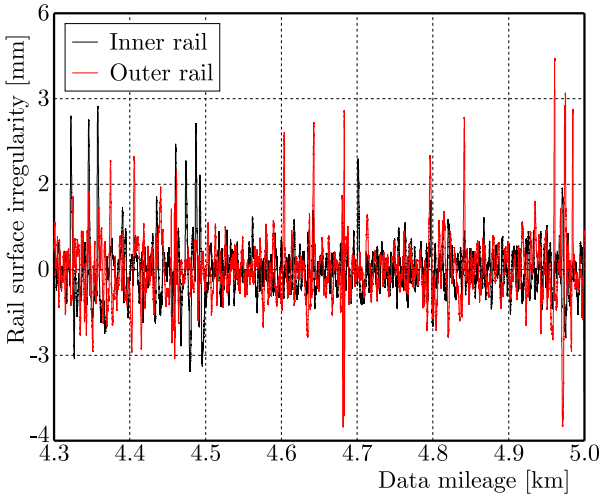

Fig. 3. Rail surface irregularities

process, firstly, the CAT (Corruption Analysis Trolley) acquisition instrument is used to measure the rail surface irregularity in the line interval, as shown in Fig. 3. Then, the measured rail surface irregularity is added to the surface of the rail model and calculation is performed. The vehicle speed in the model is taken as 56 km/h with reference to the current situation, and the rail measurement point is located on the top surface of the inner rail bottom near the track centerline side. The calculated and measured time-frequency domain results of the vertical vibration acceleration of the rail at the measurement point section are shown in Fig. 4. It can be seen that the calculated results are in good agreement with the measured results and meet engineering accuracy requirements, thus verifying validity of the numerical model.

3. Wheel-rail contact stick-slip characteristics – considering the friction memory effect

Setting d_c in Eq. (2.1) of the friction memory effect to 0.01 mm and S_{min} to 1mm/s, the friction law adopts exponentially decreasing friction, as shown in Fig. 5 (Vollebregt, 2014). By applying the numerical model and performing calculations, the longitudinal and transverse creep

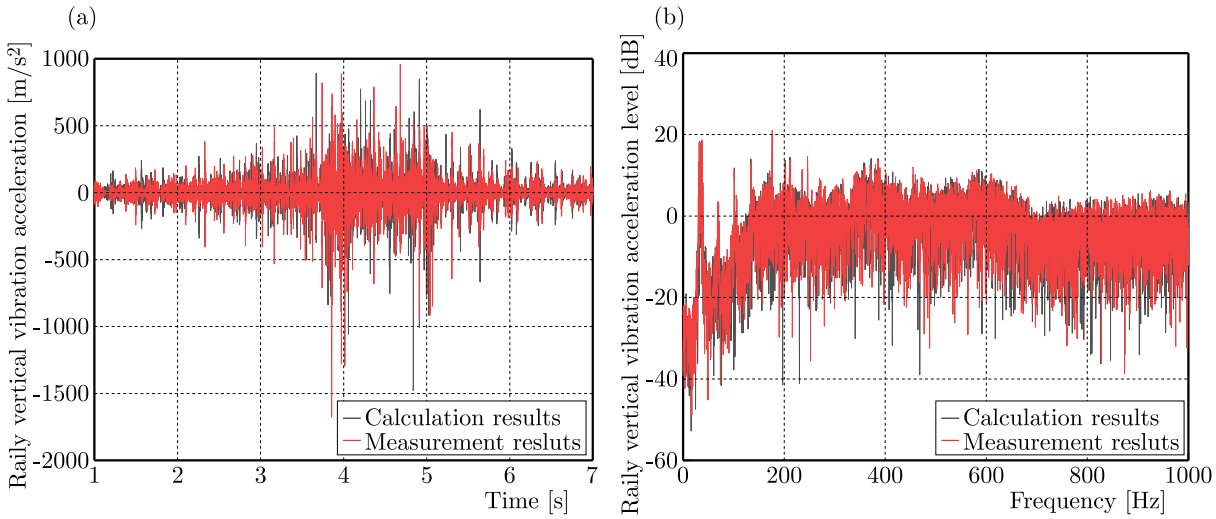

Fig. 4. Results of calculation and measurement: (a) time domain results, (b) frequency domain results

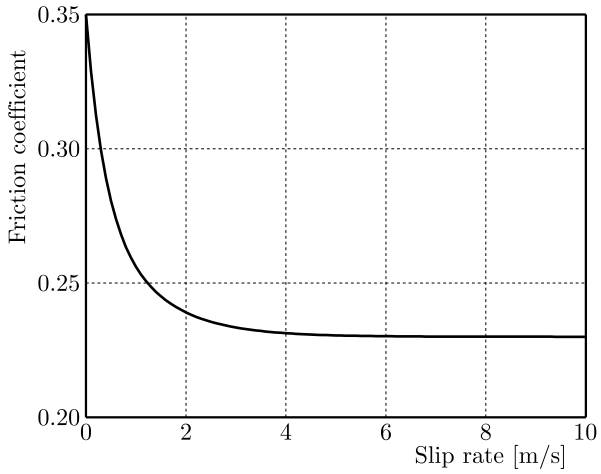

Fig. 5. Curve of the friction coefficient

forces/creepages, normal force and other parameters can be obtained during the operation of the vehicle. The creep force is compared with the normal force as shown in Eq. (3.1) to obtain the wheel-rail interface adhesion coefficient. This paper mainly focuses on the evolution trend of rail corrugation under different conditions by analyzing the relationship between the adhesion coefficient and creepage

$$\alpha_1 = \frac{F_1}{P_3} \qquad \alpha_2 = \frac{F_2}{P_3} \tag{3.1}$$

where α_1 and α_2 are longitudinal and transverse adhesion coefficients, F_1 and F_2 are longitudinal and transverse creep forces, P_3 is the normal force.

3.1. Straight line condition

In this Section, stick-slip characteristics of wheel-rail contact for the straight line condition are analyzed, and scatter diagrams of calculated longitudinal and transverse stick-slip characteristics after introducing the friction memory effect are shown in Fig. 6. As a comparison, the scatter diagrams of longitudinal and transverse stick-slip characteristics without considering the friction memory effect are shown in Fig. 7. To eliminate the influence of surface irregularities

and defects on calculation results, both the rail and wheel surfaces in the model are smooth, standard type surfaces (the same below). The vehicle speed in the model is 56 km/h and the static friction coefficient of wheel-rail contact is 0.35.

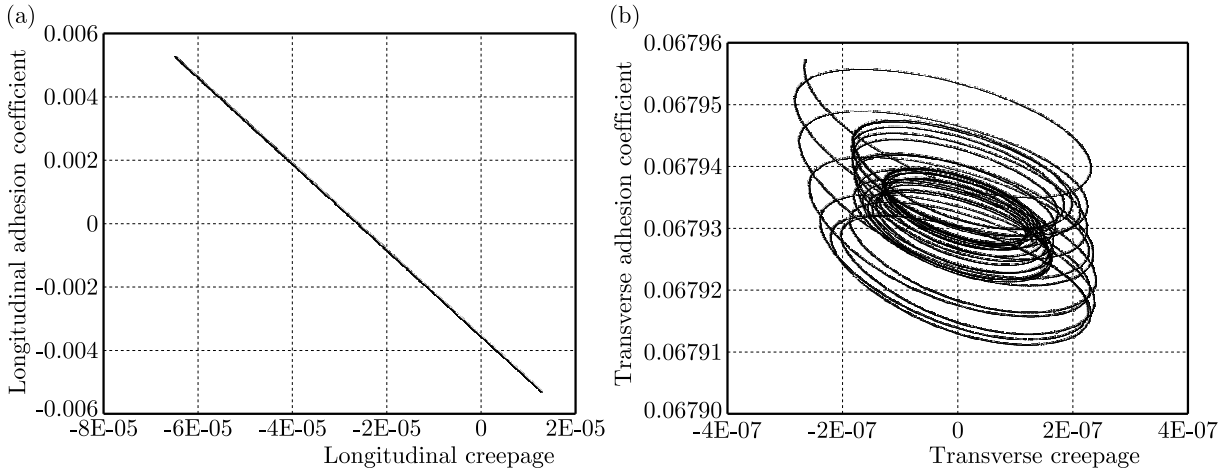

Fig. 6. Diagrams of wheel-rail contact stick-slip characteristics – straight line condition with considering the friction memory effect: (a) longitudinal stick-slip characteristics, (b) transverse stick-slip characteristics

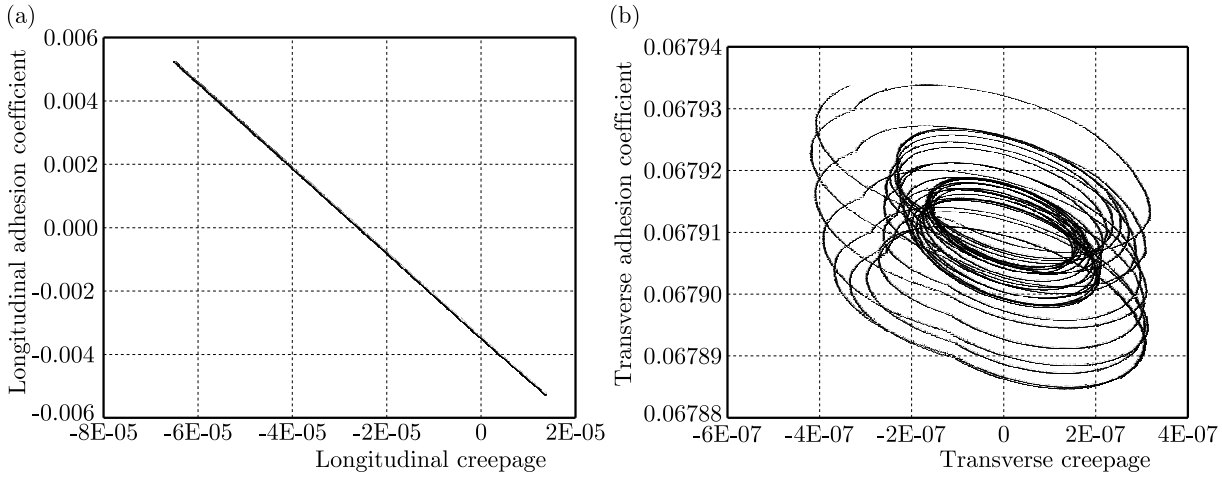

Fig. 7. Diagrams of wheel-rail contact stick-slip characteristics – straight line condition without considering the friction memory effect: (a) longitudinal stick-slip characteristics, (b) transverse stick-slip characteristics

By comparing Figs. 6 and 7, it is easy to find that the longitudinal and transverse stick-slip characteristic diagrams are similar in both cases, indicating that the introduction of the friction memory effect has a small effect on the stick-slip characteristics of wheel-rail contact on a straight line. The longitudinal adhesion coefficient shows a linear relationship with longitudinal creepage, while the transverse adhesion coefficient shows a spiral fluctuation relationship with transverse creepage, which is related to hunting motion of the wheelset. In general, for the straight line condition, the longitudinal/transverse adhesion coefficients and longitudinal/transverse creepages are small, and the corresponding variation ranges are also small, which shows that under the condition of a smooth contact interface, the stick-slip vibration is difficult to occur on the straight line, so it is not easy to induce corrugation.

3.2. Curve line condition

The scatter diagrams of wheel-rail contact stick-slip characteristics on a curved line with and without the friction memory effect are shown in Figs. 8 and 9. In the model, the track line type is a circular curve, the curve radius is 350 m, the outer rail superelevation is 105 mm, the gauge is 1435 mm, and other conditions are the same as those in the straight line condition.

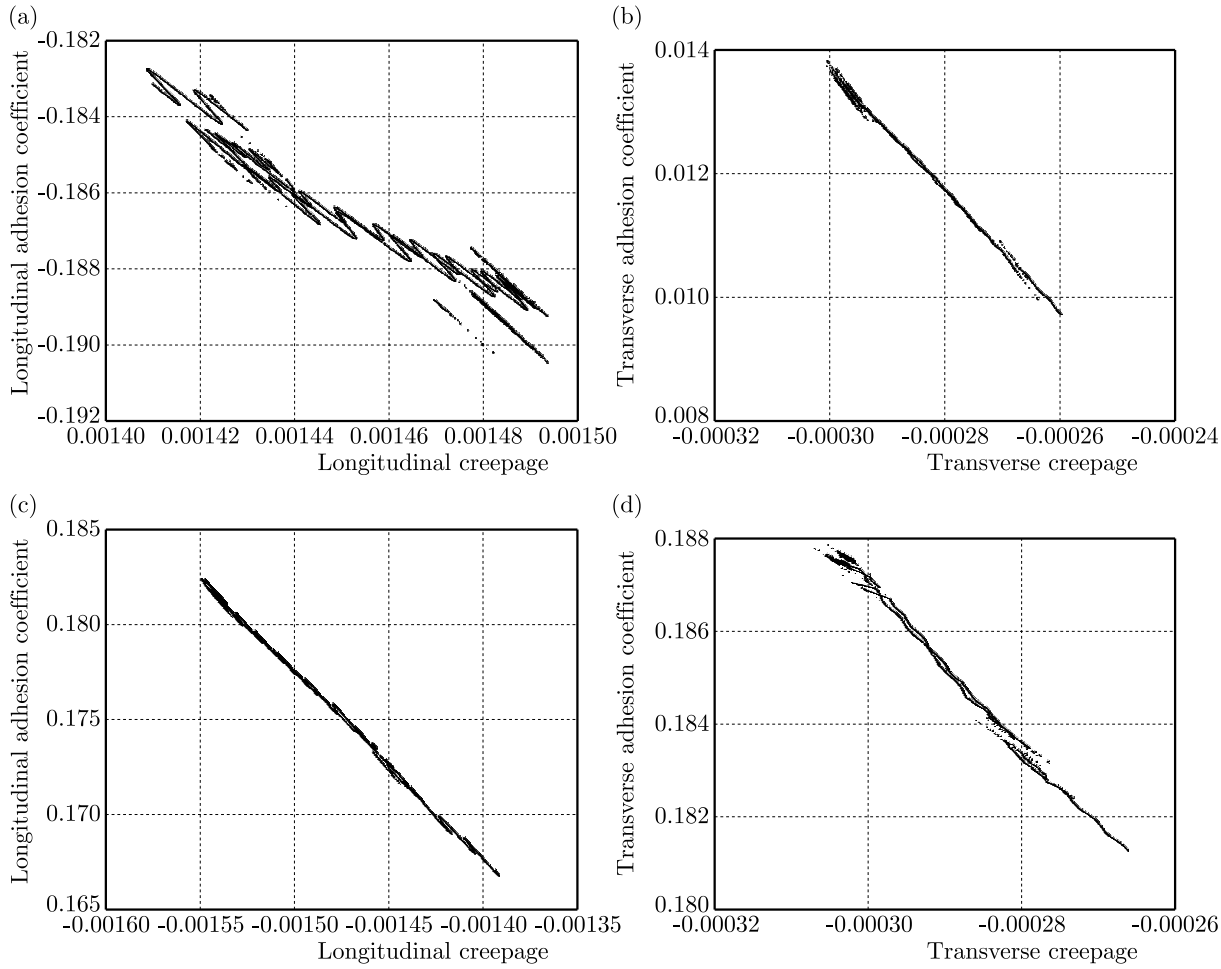

Fig. 8. Diagrams of wheel-rail contact stick-slip characteristics – curved line condition with considering the friction memory effect: (a) inside longitudinal stick-slip characteristics, (b) inside transverse stick-slip characteristics, (c) outside longitudinal stick-slip characteristics, (d) outside transverse stick-slip characteristics

From Figs. 8 and 9, it can be obtained that the longitudinal and transverse adhesion coefficients of both inside and outside wheel-rail systems are almost linearly related to the corresponding creepages on the curve line. The fluctuation amplitudes of the scatter diagram of the longitudinal stick-slip characteristics of the inner side and the transverse stick-slip characteristics of the outer side are relatively large, which indicates that the inside wheel-rail system is more prone to stick-slip vibration in the longitudinal direction, while the outside wheel-rail system is more prone to stick-slip vibration in the transverse direction, leading to different forms of rail corrugation. By comparing Figs. 8 and 9, it can be seen that after the introduction of the friction memory effect, the longitudinal and transverse creepages of the inside and outside wheel-rail systems are reduced, illustrating that the friction memory effect alleviates the slip phenomenon in the wheel-rail system. Since slip is closely related to material wear (Archard,

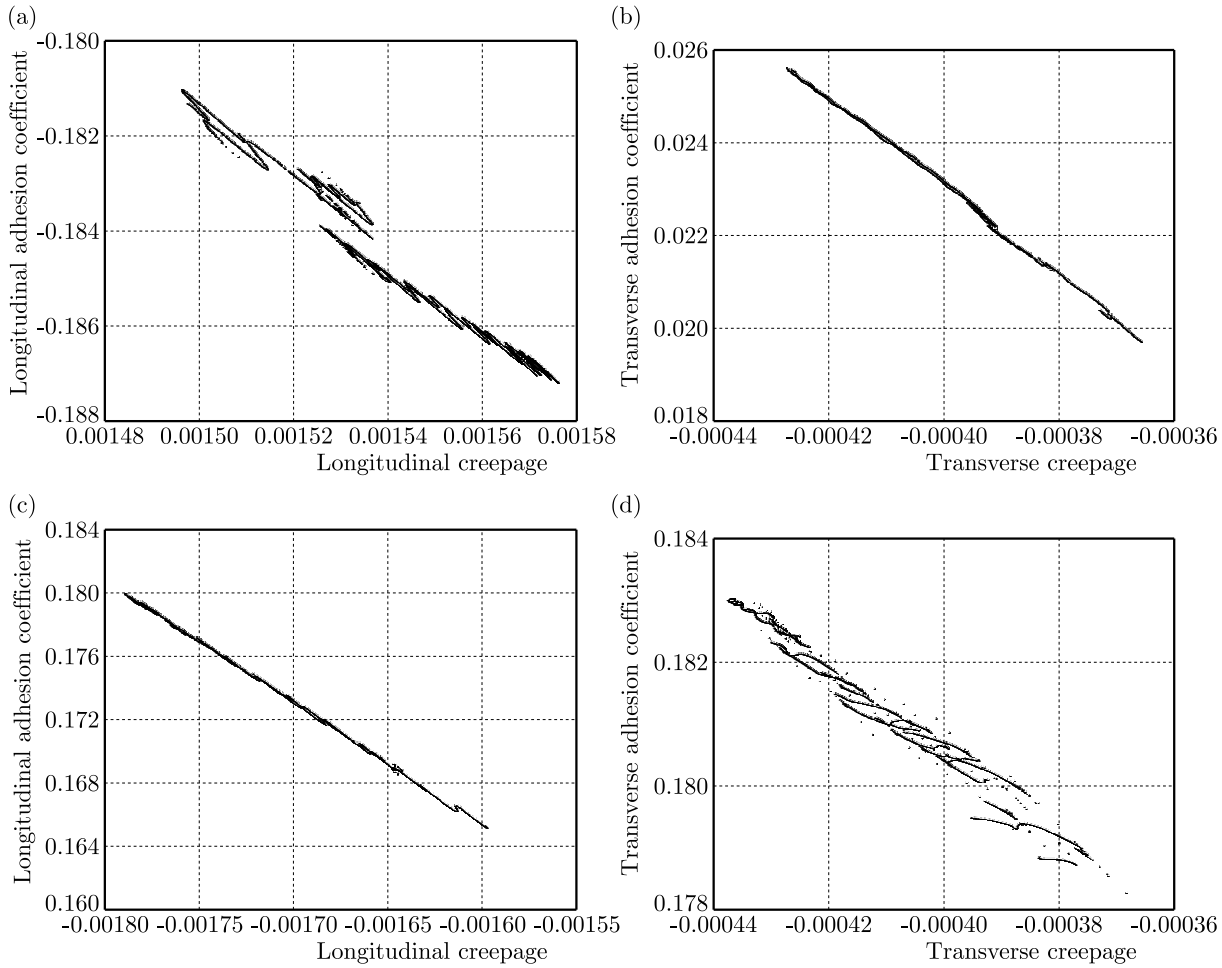

Fig. 9. Diagrams of wheel-rail contact stick-slip characteristics – curved line condition without considering the friction memory effect: a) inside longitudinal stick-slip characteristics, (b) inside transverse stick-slip characteristics, (c) outside longitudinal stick-slip characteristics, (d) outside transverse stick-slip characteristics

1953), the friction memory effect will reduce the development rate of rail corrugation in the wavelength-fixed condition of wear (Grassie, 2009).

4. Wheel-rail contact stick-slip characteristics – considering friction memory and interface effects

Based on the results in Section 3, the wheel-rail contact stick-slip characteristics under the action of the interface layer between the wheel and rail are further considered. Setting the shear modulus of the interface layer to $8.2 \cdot 10^9$ Pa and thickness to 1.25 mm for simulating an ideal natural third-body layer between the wheel and rail (Berthier *et al.*, 2004; Vollebregt, 2014), the calculated scatter diagrams of the stick-slip characteristics are shown in Figs. 10 and 11.

By comparing Fig. 10 and Fig. 6, it can be obtained that the longitudinal and transverse adhesion coefficients of the wheel-rail system on the straight line are reduced after the introduction of the interface effect, while the corresponding creepages show an increasing trend. Although an increase in the creepage drives enhanced interface slip, a relatively small adhesion coefficient does not lead to significant changes in the evolution trend of rail corrugation. Similarly, by comparing Fig. 11 and Fig. 8, it can be found that the longitudinal and transverse creepages of the

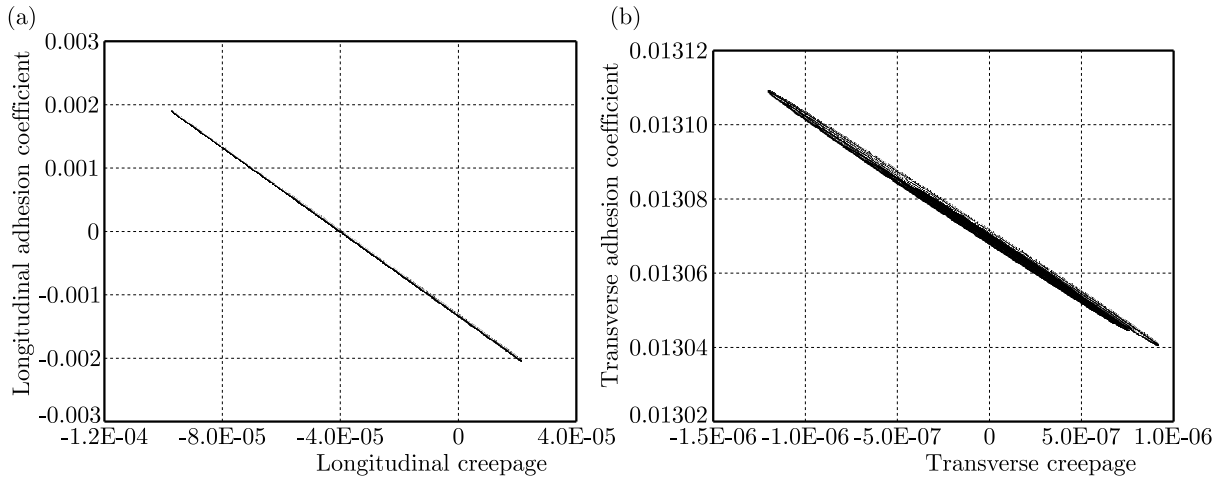

Fig. 10. Diagrams of wheel-rail contact stick-slip characteristics – straight line condition with considering the friction memory and interface effects: (a) longitudinal stick-slip characteristics, (b) transverse stick-slip characteristics

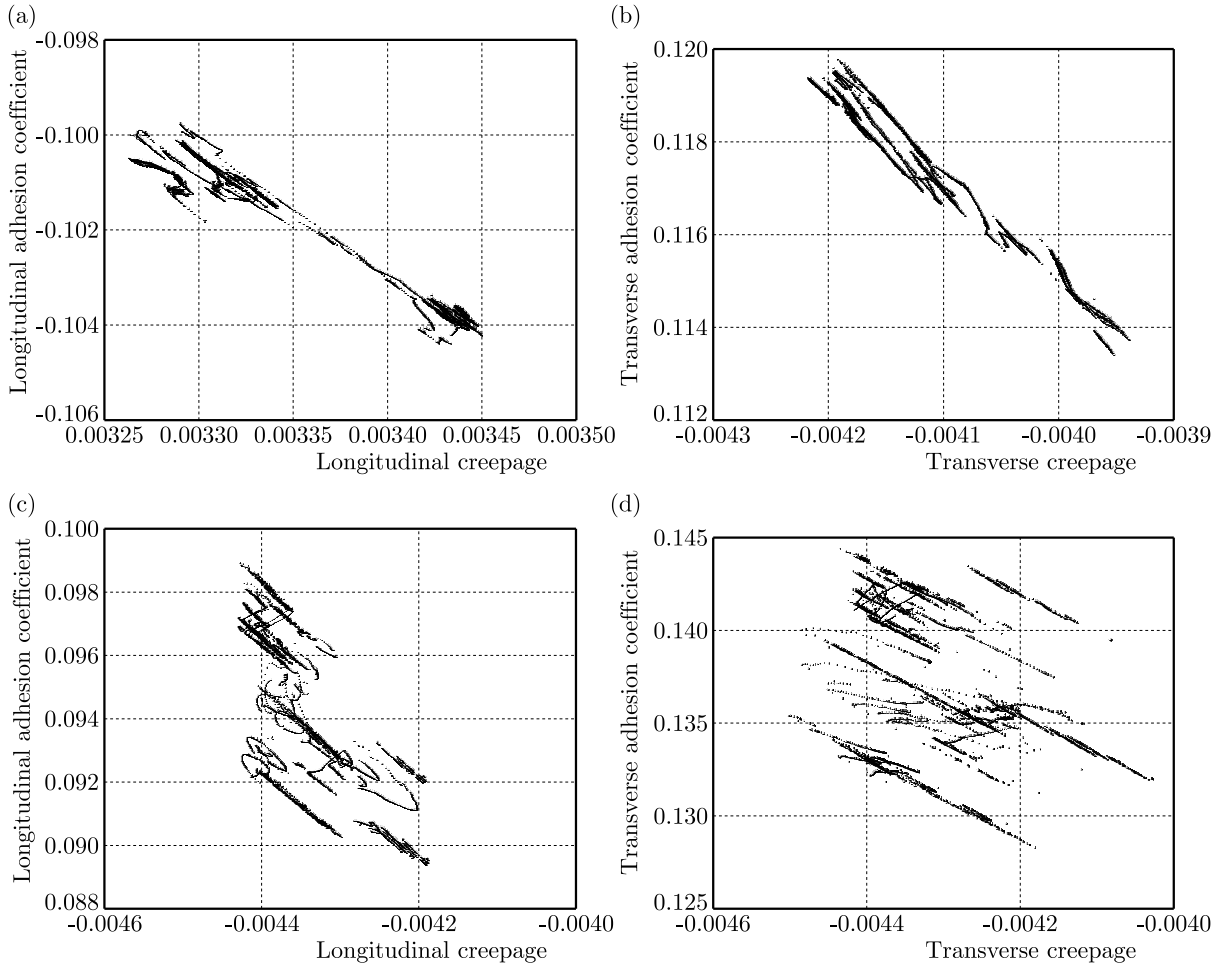

Fig. 11. Diagrams of wheel-rail contact stick-slip characteristics – curved line condition with considering friction memory and interface effects: (a) inside longitudinal stick-slip characteristics, (b) inside transverse stick-slip characteristics, (c) outside longitudinal stick-slip characteristics, (d) outside transverse stick-slip characteristics

inside and outside wheel-rail systems generally increase, while the corresponding adhesion coefficients, except for the transverse adhesion coefficient of the inside wheel-rail system, decrease. The reason for this is that the introduction of the interface layer makes the longitudinal and transverse adhesion coefficients tend to be homogeneous (around 0.100), which can also be seen from the degree of dispersion of the scattered points in Fig. 11.

In addition, by comparing Fig. 10b and Fig. 6b, it is easy to see that the adhesion coefficients are more concentrated after introducing the interface effect, which may be related to the stick-slip distribution in the contact area. In order to clarify the cause of the above phenomenon, the adhesion area ratios in the contact patch considering only the friction memory effect, friction memory and interface effects, and without any effect are respectively calculated, as shown in Fig. 12. According to Fig. 12a, when considering friction memory and interface effects, the adhesion area ratio tends to be close to 1, which is much higher than the other two cases, demonstrating that the whole contact patch is almost adhesive. The distribution form is relatively simple, and this may be the main reason why Fig. 10b is different from Fig. 6b. Meantime, it can also be seen from Fig. 12b that the introduction of friction memory and interface effects will increase the adhesion area ratio, so that the contact stick-slip distribution tends to be uniform, which will reduce wear in the contact patch and promote it to be uniform. Furthermore, in the curved line condition, it is easy to see that there are some jumpy transitions in the contact area, and the degree of jumpy transitions in the contact area of the outer rail is significantly larger than that of the inner rail (especially when friction memory and interface effects are considered at the same time). This is related to frequent side contact between the outer wheel flange and the outer rail gauge for a small radius curve.

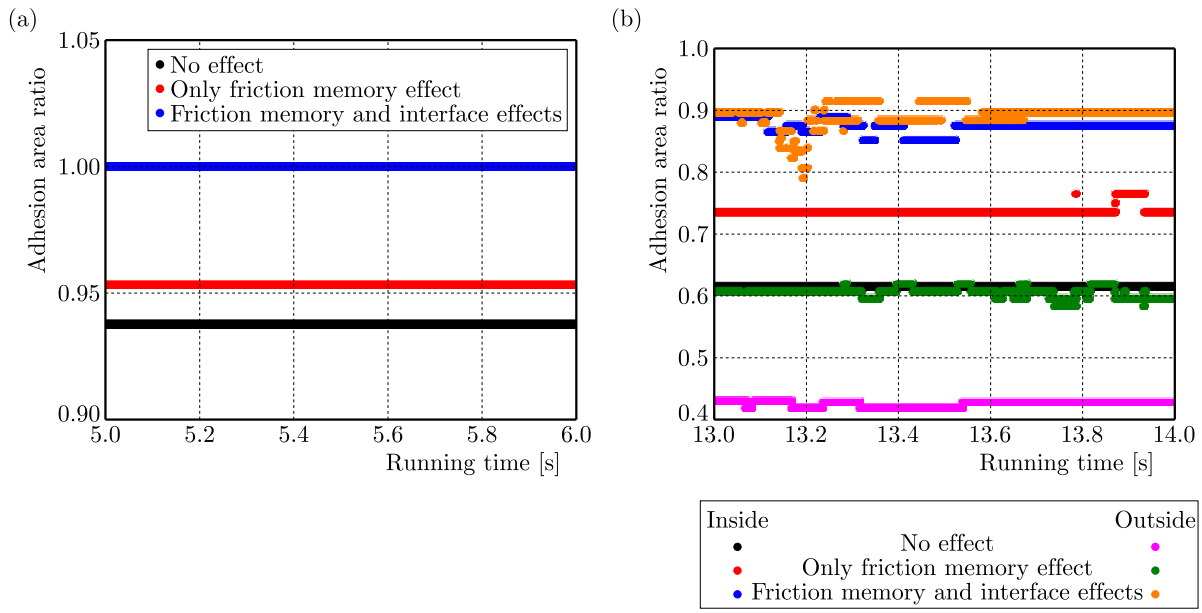

Fig. 12. Diagrams of wheel-rail contact adhesion area ratios: (a) straight line condition, (b) curved line condition

5. Conclusions

By establishing a three-dimensional coupling numerical model of a metro vehicle-track system under different line conditions, and considering the friction memory effect characterizing the slip rate and state dependence as well as the interface effect, this paper analyzes stick-slip vibration characteristics of the wheel-rail system and the evolution trend of rail corrugation in detail. The main conclusions are as follows:

- On a straight line, the introduction of the friction memory effect has little impact on a stick-slip characteristics of wheel-rail contact, and values and variation ranges of adhesion coefficients and creepages are relatively small, which indicates that the wheel-rail system is difficult to generate stick-slip vibration, and thus it is not easy to produce rail corrugation.
- On a curved line, fluctuation amplitudes of the inside longitudinal stick-slip characteristics and outside transverse stick-slip characteristics are relatively large, which illustrates that the inside wheel-rail system is more prone to stick-slip vibration in the longitudinal direction, while the outside wheel-rail system is more prone to stick-slip vibration in the transverse direction, thus leading to different forms of rail corrugation. The introduction of the friction memory effect reduces longitudinal and transverse creepages of both the inside and outside wheel-rail systems, demonstrating that the friction memory effect alleviates the slip phenomenon, thereby reduces the development rate of rail corrugation.
- The introduction of the interface effect leads to homogenization of longitudinal and transverse adhesion coefficients of the wheel-rail system and most of them show a decreasing trend, while the corresponding creepages show an increasing trend. Although the increase of the creepage will enhance the interface slip, the smaller adhesion coefficient will not cause significant changes in the corrugation evolution.
- The introduction of friction memory and interface effects will increase the adhesion area ratio in the wheel-rail contact patch, thus making the contact stick-slip distribution tend to be uniform, which will reduce wear in the contact patch and promote it to be uniform.

References

1. Archard J.F., 1953, Contact and rubbing of flat surfaces, *Journal of Applied Physics*, **24**, 8, 981-988
2. Berthier Y., Descartes S., Busquet M., Niccolini E., Desrayaud C., Baillet L., Baietto-Dubourg M.C., 2004, The role and effects of the third body in the wheel-rail interaction, *Fatigue and Fracture of Engineering Materials and Structures*, **27**, 5, 423-436
3. Daniel W.J.T., Horwood R.J., Meehan P.A., Wheatley N., 2008, Analysis of rail corrugation in cornering, *Wear*, **265**, 9-10, 1183-1192
4. Eadie D.T., Kalousek J., Chiddick K.C., 2002, The role of high positive friction (HPF) modifier in the control of short pitch corrugations and related phenomena, *Wear*, **253**, 1-2, 185-192
5. Grassie S.L., 2009, Rail corrugation: characteristics, causes, and treatments, *Proceedings of the Institution of Mechanical Engineers Part F-Journal of Rail and Rapid Transit*, **223**, 6, 581-596
6. Grassie S.L., Kalousek J., 1993, Rail corrugation: characteristics, causes and treatments, *Proceedings of the Institution of Mechanical Engineers, Part F: Journal of Rail and Rapid Transit*, **207**, 1, 57-68
7. Guo M.H., Zhang X.H., Shen G., 2009, Study on rail corrugation mechanism in curved track of metro, *Modern Urban Transit*, **4**, 60-62+1
8. Jin X.S., Wen Z.F., Wang K.Y., Zhang W.H., 2004, Effect of a scratch on curved rail on initiation and evolution of rail corrugation, *Tribology International*, **37**, 5, 385-394
9. Jin X.S., Xue B.Y., 1997, Application of three-dimensional non-Hertzian rolling contact theory to wheel/rail interactions – compilation and application of TPLR, *Journal of Southwest Jiaotong University*, **32**, 4, 53-58
10. Kalker J.J., 1990, *Three-Dimensional Elastic Bodies in Rolling Contact*, Vol. 2, Springer Science & Business Media
11. Lei Z.Y., Wang Z.Q., 2020, Generation mechanism and development characteristics of rail corrugation of Cologne egg fastener track in metro, *KSCE Journal of Civil Engineering*, **24**, 6, 1763-1774

12. Lei Z.Y., Wang Z.Q., 2021, Contact and creep characteristics of wheel-rail system under harmonic corrugation excitation, *Journal of Vibration and Control*, **27**, 17-18, 2069-2080

13. Lei Z.Y., Wang Z.Q., Li L., Geng C.Z., 2019, Rail corrugation characteristics of the common fastener track in metro, *Journal of Tongji University (Natural Science)*, **47**, 9, 1334-1340

14. Li X., 2012, *Study on the Mechanism of Rail Corrugation on Subway Track*, Southwest Jiaotong University, Chengdu

15. Matsumoto A., Sato Y., Ono H., Tanimoto M., Oka Y., Miyauchi E., 2002, Formation mechanism and countermeasures of rail corrugation on curved track, *Wear*, **253**, 1-2, 178-184

16. Sato Y., Matsumoto A., Knothe K., 2002, Review on rail corrugation studies, *Wear*, **253**, 1-2, 130-139

17. Shen G., Zhang X.H., Guo M.H., 2011, Theoretical study on rail corrugation on curved track of metro systems, *Journal of Tongji University (Natural Science)*, **39**, 3, 381-384

18. Sun Y.Q., Simson S., 2007, Nonlinear three-dimensional wagon-track model for the investigation of rail corrugation initiation on curved track, *Vehicle System Dynamics*, **45**, 2, 113-132

19. Sun Y.Q., Simson S., 2008, Wagon-track modelling and parametric study on rail corrugation initiation due to wheel stick-slip process on curved track, *Wear*, **265**, 9-10, 1193-1201

20. Vollebregt E.A.H., 2014, Numerical modeling of measured railway creep versus creep-force curves with CONTACT, *Wear*, **314**, 1-2, 87-95

21. Vollebregt E.A.H., Six K., Polach O., 2021, Challenges and progress in the understanding and modelling of the wheel-rail creep forces, *Vehicle System Dynamics*, **59**, 7, 1026-1068

22. Wang Z.Q., Lei Z.Y., 2021, Formation mechanism of metro rail corrugation based on wheel-rail stick-slip behaviors, *Applied Sciences-Basel*, **11**, 17, 8128

23. Wang Z.Q., Lei Z.Y., 2022, Formation mechanism of rail corrugation on the small radius curve of metro based on stick-slip torsional vibration, *Journal of Southeast University (Natural Science)*, **52**, 5, 998-111

24. Wen Z.F., Jin X.S., 2005, Effect of track lateral geometry defects on corrugations of curved rails, *Wear*, **259**, SI, 1324-1331

25. Yang Z., Li Z.L., 2019, A numerical study on waves induced by wheel-rail contact, *International Journal of Mechanical Sciences*, **161-162**, 105069

26. Yao H.M., Shen G., Gao L.J., 2018, Formation mechanism of worn profile rail corrugation based on experimental verification, *Journal of Tongji University (Natural Science)*, **46**, 10, 1427-1432

Manuscript received December 20, 2022; accepted for print February 9, 2023

JOURNAL OF THEORETICAL AND APPLIED MECHANICS
61, 2, pp. 343-354, Warsaw 2023
https://doi.org/10.15632/jtam-pl/162991

STUDY ON TENSILE FRACTURE FAILURE OF A STEEL PLATE WITH A SURFACE CRACK

Zhewen Chong, Jing Tao
School of Mechanical and Electrical Engineering, Hubei Polytechnic University, Huangshi, China
e-mail: 1340274972@qq.com; 605119917@qq.com

Yuehui Xie, Dongrong Wu
PipeChina Southwest Pipeline Co., Ltd, Jinniu District, Chengdu, China
e-mail: glitterx@163.com; 1743072567@qq.com

Tao Li
School of Mechanical and Electrical Engineering, Hubei Polytechnic University, Huangshi, China
e-mail: 30504935@qq.com

In order to study the effect of different surface crack parameters on the fracture failure of steel plate, the model was established by FEM. The results showed that the edge surface crack has the greatest influence on the fracture failure of the steel plate, and for non-edge surface cracks, the central surface crack has the greatest influence on the fracture failure of the steel plate. The larger the a/t and the smaller the a/c, the easier the steel plate fracture failure occurs. The a/c has a certain influence on the variation law of K and the position where K_{max} appears.

Keywords: steel plate, surface crack, stress intensity factor (SIF), fracture failure

1. Introduction

With the development of industrial production and large-scale steel structures, the market demand for steel plates is increasing day by day, and new requirements are also being put forward for the production quality of steel plates, not only to improve the yield of steel plates, but also to improve their quality. During the production and use of steel plates, surface cracks will inevitably occur due to material defects, rolling deformation and other factors (Yuan *et al.*, 2021). The surface cracks seriously affect the quality and yield of steel plates. The existence of cracks will accelerate the fracture failure, which may lead to major accidents (Wen, 2020). A steel plate with surface cracks as presented in Fig. 1. Hence, it is necessary to further study the fracture failure of steel plates containing crack defects.

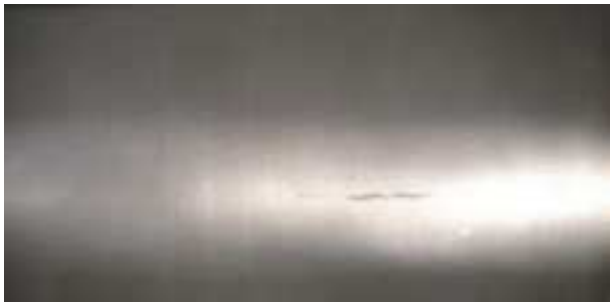

Fig. 1. The steel plate with a surface crack

In recent years, some scholars have done a lot of research on the fracture failure of steel plates and their repair, but there are relatively few studies on the fracture failure with surface crack defects. Dolbow *et al.* (2000) improved the extended finite element method (XFEM), then considered a discontinuous and a near tip strengthening function, applied it to the plate fracture problem, and verified the accuracy and practicability of the new formula. Lin and Smith (1999) analyzed a plate with a surface crack by using the finite element method. By estimating the stress intensity factor at the crack tip, the effects of the stress intensity factor on sensitivity of the crack shape, grid orthogonality and J-integral path independence were discussed. Saber *et al.* (2020) studied the influence of cutout size, position and geometry on the AISI1045 steel plate fatigue life and crack propagation path. The research showed that the cutout size and position were important parameters affecting crack propagation paths, and the increase or decrease in fatigue life could be predicted by cutout characteristics. Cheng *et al.* (2021) studied the fatigue crack propagation mechanism of carbon steel plate by using molecular dynamics (MD) and extended finite element methods (XFEM). Zhang *et al.* (2019) studied the effect of corrosion on fracture toughness of steel plates and found that the uniform and pitting corrosion damage would reduce the residual fracture toughness of corroded steel. Zhang *et al.* (2018) used Abaqus software to study deformation behavior of typical steel and analyzed the displacement change of the material during the shearing process. He *et al.* (2020) studied the causes of abnormal tensile fractures of steel plates through metallographic microscopes, scanning electron microscopes and energy dispersive spectrometers, and concluded that the main reason for abnormal tensile fractures were surface cracks. Zhang *et al.* (2021) used a fully coupled elastoplastic damage model with stress-state dependence to predict edge fracture during punching of high-strength steel plates. The results showed that the model prediction results were in good agreement with the experimental results. Chandra *et al.* (2020) used single edge notched tensile (SENT) specimens to evaluate the ductile tearing resistance of interstitial free steel plates and investigated the critical crack tip opening angle (CTOA) as well as the crack initiation parameters. Di Gioacchino *et al.* (2021) used a side-grooved Charpy test to evaluate the splitting and fracture properties of high-toughness steel plates. The research showed that the modified geometry could prevent the accumulation of plastic deformation under upper shelf energy temperature and improve the accuracy of impact performance measurement. Lee *et al.* (2022) used the finite element method and an experimental method to study the cause of random crack formation and propagation in high-alloy steels. The results showed that the alloy steel slabs were subjected to large thermal stresses during cooling. When chromium and boron were added, the possibility of a steel plate fracture increased. Omiya *et al.* (2022) studied the influence of material strength and notch shape on crack initiation and propagation characteristics of an AHSS sheet of a car body structure. The research showed that the crack generation and propagation behavior largely depended on the material strength and notch root radius. Li *et al.* (2020) studied the reinforcement effect of a fiber-reinforced polymer (FRP) on steel plates with surface cracks and proposed the optimal bond length and repair layer number. Liu *et al.* (2023) proposed an analytical model based on linear elastic fracture mechanics to evaluate fatigue performance of prestressed CFRP strip-reinforced steel plates. The research revealed that the proposed model coild better predict the stress state, stress intensity factor amplitude, fatigue crack growth life and the minimum pre-stress in the CFRP strip required for crack cessation under different strengthening conditions for various members.

However, those studies mainly focused on the fracture failure of steel plates and their repairs, while there are few studies on the fracture failure of steel plates with surface crack defects. The failure of steel plates with different crack positions, crack depth ratios and crack aspect ratios is not sufficiently analyzed. Hence, a steel plate with a surface crack is taken as the research object, and the influence of different crack positions, crack depth ratios and crack aspect ratios on the fracture failure is analyzed.

2. Theoretical method

2.1. *J*-integral and stress intensity factor

Rice (1968) proposed that the J-integral did not depend on the integral path around the crack. The J-integral is a fracture parameter to deal with nonlinear fracture problems. It does not need to calculate the elastic-plastic stress and strain fields near the crack tip, and it can be used for elastic and plastic evaluation. The J-integral can be expressed as

$$J = \int_{\Gamma} \left(w dy - T \frac{\partial u}{\partial x} ds \right) \tag{2.1}$$

where Γ is a curve surrounding the crack tip. The integral is calculated in a counter clockwise sense taking from the lower crack surface and continuing along the path Γ to the upper crack surface. w is strain energy density, u is the displacement vector, T depends on the outward normal n_j along Γ, $T = \sigma_{ij} n_j$, and ds is an arc length increment along Γ.

For cracks in linear elastic materials under mode I loading, the relationship between the J-integral and stress intensity factor K_I is as follows

$$K_I^2 = E' J \tag{2.2}$$

For the model subject to plane strain loading, E' can be expressed by equation $(2.3)_1$, and for the model subject to plane stress loading, E' can be expressed by equation $(2.3)_2$

$$E' = \frac{E}{1-\nu^2} \qquad E' = E \tag{2.3}$$

where E is Young's modulus, ν is Poisson's ratio.

2.2. Crack propagation criterion

In the elastic-plastic state, the stress and strain near the crack tip can be uniquely determined by the J-integral. When the stress and strain field at the crack tip reaches the critical state of crack growth, the J-integral also reaches the critical value, and the crack will be unstable and start to grow. Therefore, the J-integral can be used as a fracture criterion for elastic-plastic cracked bodies. The J-integral fracture criterion can be expressed as

$$J \geqslant J_{IC} \tag{2.4}$$

where J_{IC} is the characteristic parameter of the material, also called the fracture toughness.

For the stress intensity factor, when it reaches the K_{IC} value, the crack will also appear unstable and then initiate crack propagation. The fracture criterion can be expressed as

$$K \geqslant K_{IC} \tag{2.5}$$

where K_{IC} is the characteristic parameter of the material, also called the fracture toughness.

3. Materials and methods

3.1. Steel plate geometric model and parameters

The finite element model of a steel plate is established with Q235. The main parameters of the steel plate are: length $L = 1000\,\text{mm}$, width $W = 500\,\text{mm}$, thickness $t = 12\,\text{mm}$, density $\rho = 7800\,\text{kg/m}^3$, Young's modulus $E = 210\,\text{GPa}$, Poisson's ratio $\mu = 0.3$, yield strength

$\sigma_s = 243\,\text{MPa}$, and tensile strength $\sigma_b = 465\,\text{MPa}$ (Zhang, 2020). Considering the tensile fracture failure of the steel plate with crack defects, the tensile load is set as $\sigma = 10\,\text{MPa}$. The tensile load is set at one end of the steel plate, and the other end is set with a fixed constraint. The steel plate model with a surface crack and a sectional view of the steel plate are presented in Fig. 2.

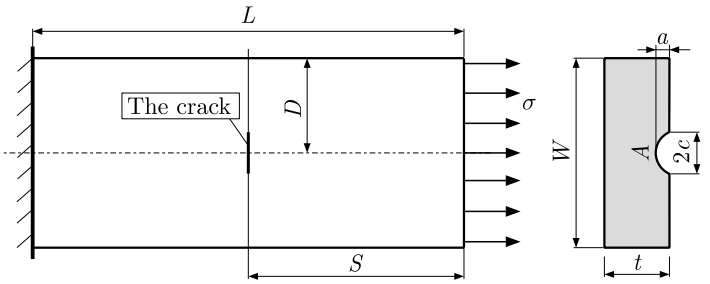

Fig. 2. Steel plate model with a surface crack and a sectional view of the steel plate

3.2. Finite element model

The steel plate with a surface crack has been implemented into the finite element software. In the process of crack propagation, any crack with an initial shape will gradually form a semi-elliptical crack (Shahani *et al.*, 2010; Anderson, 2017). Therefore, the semi-elliptical surface crack is used in the analysis. The actual field picture of the semi-elliptical crack is shown in Fig. 3a. The geometry of the semi-elliptical surface crack is shown in Fig. 3b. The dimension

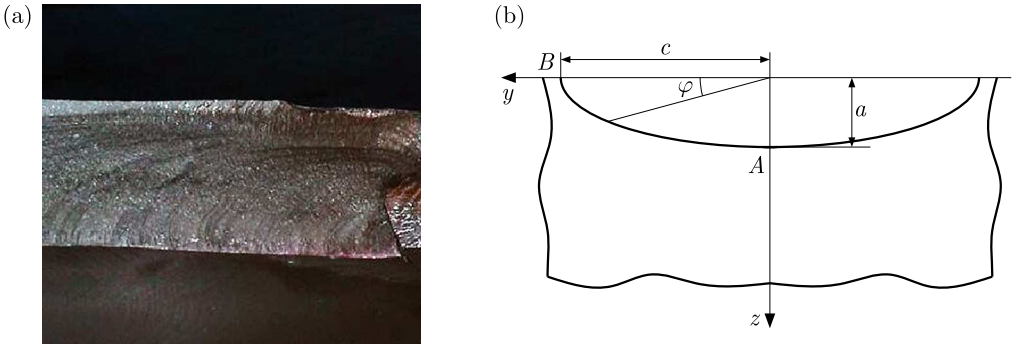

Fig. 3. The semi-elliptical crack: (a) actual photograph of a semi-elliptical crack and (b) semi-elliptical surface crack characterization

parameters φ, a and c are the crack angle, crack depth and a half of the crack length, respectively. For the surface crack, the surface point B is for the crack angle of 0°, and the deepest point A of the crack is for the crack angle of 90°. The crack depth ratio $a/t = 0.5$ and the crack aspect ratio $a/c = 0.5$ are defined for the initial crack located in the middle of the steel plate, as shown in Fig. 2. For the steel plate model with surface cracks, eight-node reduced-integration "brick" elements (C3D8R) have been adopted for the overall model. In order to eliminate singularity, the singular elements (Barsoum, 1975; Henshell and Shaw, 1975) were adopted for the crack front, and ten-node quadratic tetrahedron elements (C3D10) were used in the transition area between the crack front and the steel plate. The stress intensity factor (SIF) of the surface crack was calculated by using the contour integration method (Chong *et al.*, 2021). The finite element mesh of the steel plate is shown in Fig. 4.

In order to verify the effect of mesh number on the analysis results (Figiel and Kamiński, 2009), the mesh independence has been verified based on the initial cracking model of the steel plate. Three finite element models with different mesh numbers were established for analysis. The

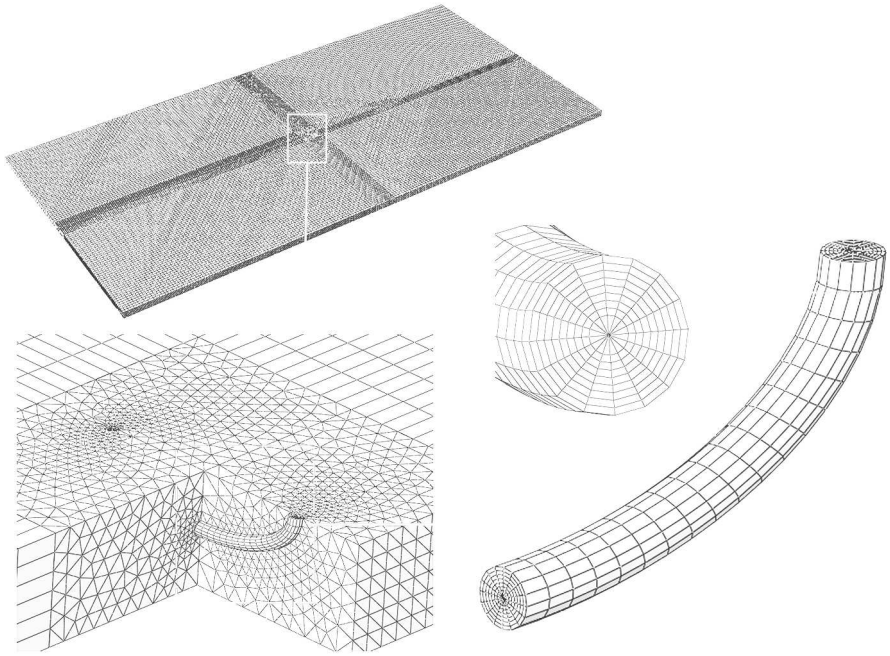

Fig. 4. Finite element mesh of the steel plate

mesh numbers in Mesh 1, Mesh 2 and Mesh 3 were 104188, 186451 and 399282, respectively. The SIF of the surface crack K with different mesh numbers is shown in Fig. 5. It can be clearly found that the crack SIFs of Mesh 1, Mesh 2, and Mesh 3 are almost the same, and the difference between them is very small. Therefore, increasing the number of meshes has little effect on the calculation results. The number of Mesh 2 meets the requirements of calculation accuracy. Considering the large number of meshes, the analysis time is long. Hence, Mesh 2 is a mesh generation standard to achieve accurate results.

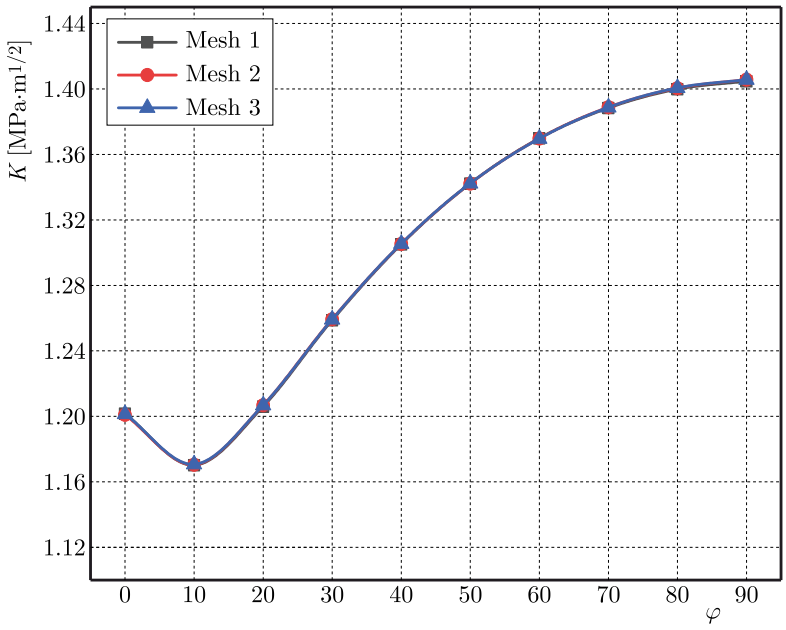

Fig. 5. The SIF of a crack for different meshes

3.3. Model validation

To verify the precision of the finite element calculation, we have calculated the SIF of the semi-elliptical surface crack with the initial crack depth ratio $a/t = 0.5$, crack aspect ratio $a/c = 0.5$. The crack is located in the middle of the steel plate, that is, $S/L = 0.5$, $D/W = 0.5$.

For an infinite center cracked plate subjected to uniform tensile stress at infinity, the stress intensity factor can be expressed as

$$K = \sigma\sqrt{\pi a} \tag{3.1}$$

where σ is the stress, a is the crack length.

For finite-sized components in the project, the stress intensity factor needs to be modified based on the above formula, so it can be expressed as

$$K = \sigma\sqrt{\pi a} f(a, W, \ldots) \tag{3.2}$$

where $f(a, W, \ldots)$ is a geometric correction coefficient.

Due to complexity of the problem, the analytical solution is still difficult to obtain for three--dimensional surface cracks. However, in order to meet the needs of solving practical engineering problems, Newman and Raju (1984) used the finite element method and numerical fitting to give an empirical formula for calculating the surface crack stress intensity factor. The theoretical calculation formula for the SIF K of a plate with semi-elliptical surface cracks can be expressed as (Newman and Raju, 1984)

$$K = \frac{\sigma\sqrt{\pi a}}{E(k)} F_s\Big(\frac{a}{c}, \frac{a}{t}, \frac{c}{w}, \varphi\Big) \tag{3.3}$$

where

$$E(k) = \sqrt{1 + 1.464\Big(\frac{a}{c}\Big)^{1.65}} \qquad F_s = \Big[M_1 + M_2\Big(\frac{a}{t}\Big)^2 + M_3\Big(\frac{a}{t}\Big)^4\Big] g f_\varphi f_w$$

$$M_1 = 1.13 - 0.09\frac{a}{c} \qquad M_2 = -0.54 + \frac{0.89}{0.2 + \frac{a}{c}}$$

$$M_3 = 0.5 - \frac{1}{0.65 + \frac{a}{c}} + 14\Big(1 - \frac{a}{c}\Big)^{24} \qquad g = 1 + \Big[0.1 + 0.35\Big(\frac{a}{t}\Big)^2\Big](1 - \sin\varphi)^2$$

$$f_\varphi = \sqrt[4]{\Big(\frac{a}{c}\Big)^2 \cos^2\varphi + \sin^2\varphi} \qquad f_w = \sqrt{\sec\Big(\frac{\pi c}{2W}\sqrt{\frac{a}{t}}\Big)}$$

Compared with the calculation results from equation (3.3), the finite element model results are very close, and the errors for different crack angles φ are less than 5%. The errors between simulation results and calculation formula are shown in Fig. 6.

4. Results and discussion

4.1. Effects of crack position on the SIF of a surface crack

The initial crack depth ratio is $a/t = 0.5$, and initial crack aspect ratio $a/c = 0.5$. Considering the influence of crack position on the SIF, D/W and S/L are defined to represent the crack position, and D/W and S/L represent the width and length ratios of the position in the steel plate where the crack is located, respectively. The length ratio $S/L = 0.5$ is taken to analyze the changes in the SIF of the crack K at different crack angles φ when the width ratio is $D/W = 0$, 0.1, 0.2, 0.3, 0.4 and 0.5.

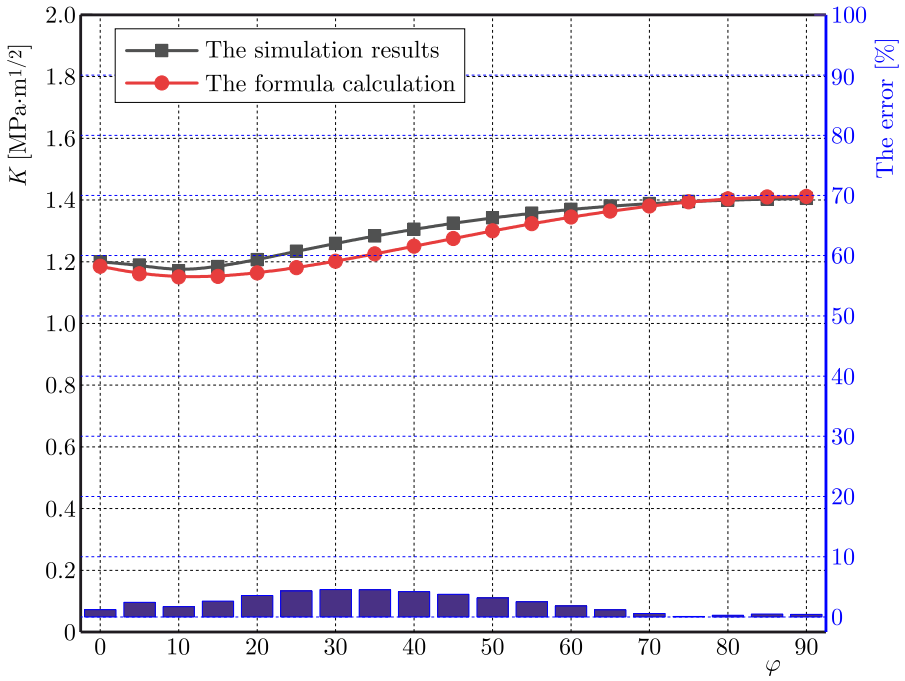

Fig. 6. The error value between simulation results and calculation formula

The variation of the crack SIF for different width ratios is shown in Fig. 7a. Firstly, K decreases and then increases gradually with an increase of φ. K gradually decreases within the crack angle range $\varphi = 0°$-$10°$, and then gradually increases within the range of $10°$-$80°$, and finally stabilizes after $80°$ when $D/W = 0$. K gradually increases within the crack angle range of $10°$-$90°$, and the increasing trend gradually stabilizes when $D/W = 0.1$-0.5. The maximum value of the SIF K_{max} for different width ratios appears at the deepest point of the crack $\varphi = 90°$. In order to further study the influence of width ratios D/W on K, K at the deepest point of the crack has been extracted for study. The variation of K at the deepest point of the crack is shown in Fig. 7b. K decreases first as the width ratio D/W increases, and then gradually increases. K gradually decreases in the range of width ratio $D/W = 0$-0.1, and gradually increases in the range of width ratio $D/W = 0.1$-0.5. K is the largest when $D/W = 0$, and the crack is an edge surface crack.

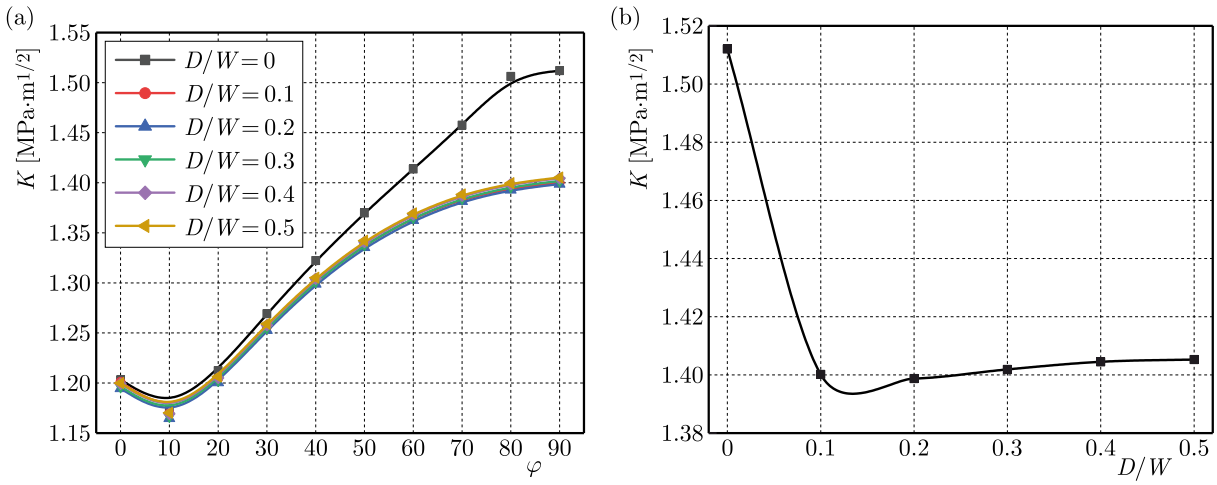

Fig. 7. The SIF of a crack for different width ratios: (a) variation of the crack SIF, (b) variation of SIF at the deepest point of the crack

As shown in Figs. 7a and 7b, the variation rule of K when the width ratio $D/W = 0$ is obviously different from that for $D/W = 0.1$, 0.2, 0.3, 0.4 and 0.5. K at the deepest point when $D/W = 0$ is much larger than that at the deepest point when $D/W = 0.1$, 0.2, 0.3, 0.4 and 0.5, indicating that the edge surface crack has the greatest influence on the fracture failure of the steel plate. K of a non-edge surface crack increases with an increase of D/W, and the maximum value of K appears at $D/W = 0.5$, that is, the central surface crack, which indicates that for a non-edge surface crack, the central surface crack has the greatest influence on the fracture failure of the steel plate.

Considering that the edge surface crack has the greatest influence on the fracture failure of the steel plate, the edge surface crack is selected to analyze the influence of different length ratios on the crack SIF, that is, the width ratio $D/W = 0$ and length ratios $S/L = 0.1$, 0.3, 0.5, 0.7 and 0.9 are taken to analyze the variation of K at different crack angles φ.

The variation of the crack SIF for different length ratios is shown in Fig. 8a. K firstly decreases and then increases gradually with an increase of φ. K gradually decreases within the crack angle range $\varphi = 0°$-$10°$, and K gradually increases within the range of $10°$-$80°$, then in tends to be stable above $80°$. The maximum value of the SIF K_{max} appears at the deepest point of the crack $\varphi = 90°$. In order to further study the influence of length ratios S/L on K, K at the deepest point of the crack is extracted for study. The variation of K at the deepest point of the crack is shown in Fig. 8b. K firstly slowly decreases as the length ratio S/L increases, then gradually decreases, and the decreasing trend becomes larger. K decreases slowly in the range of length ratios $S/L = 0.1$-0.5, and the change of K value is small. K gradually decreases in the range of length ratios $S/L = 0.5$-0.9, and the decreasing trend is larger than that in the range of $S/L = 0.1$-0.5. K is the largest when $S/L = 0.1$, indicating that the closer is to the stress end, the larger K is.

As shown in Figs. 8a and 8b, the decreasing trend of K in the range of length ratios $S/L = 0.1$-0.5 is obviously different from that in the range of $S/L = 0.5$-0.9. The trend changes at $S/L = 0.5$ indicate that this is the inflection point of the trend change. When the length ratios are $S/L = 0.1$, 0.3 and 0.5, the variation rule of K is the same, and the variation of K is small. The maximum variation difference of K is $0.01\,\mathrm{MPa{\cdot}m^{1/2}}$, indicating that the edge surface cracks when $S/L \leqslant 0.5$, which has the greatest influence on the fracture failure of the steel plate.

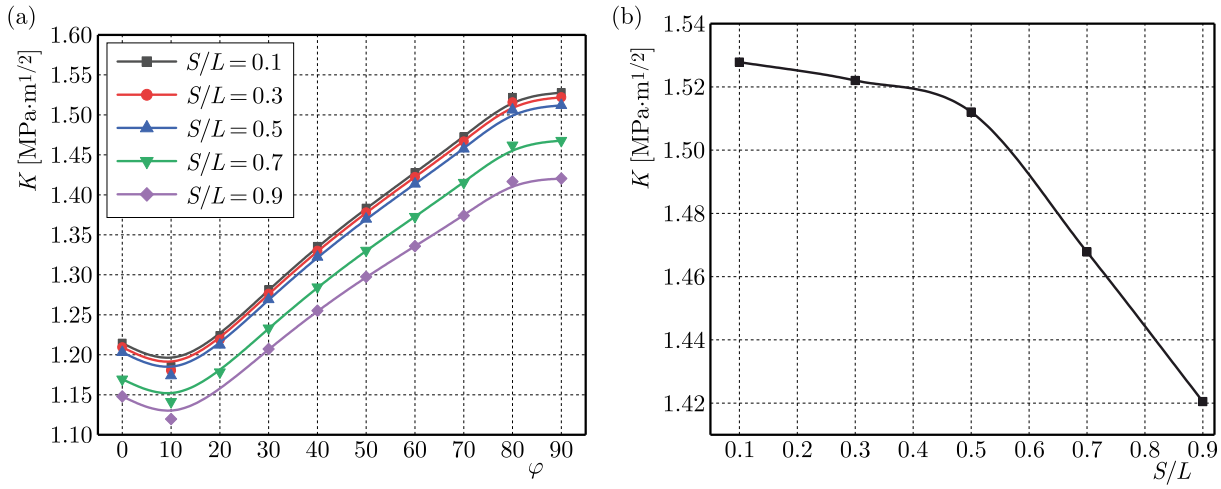

Fig. 8. The SIF of a crack for different length ratios: (a) variation of the crack SIF, (b) variation of SIF at the deepest point of the crack

Considering that the crack position has the greatest influence on the fracture failure of the steel plate when the width ratio $D/W = 0$ and the length ratio $S/L \leqslant 0.5$, the crack position

is selected in this paper when the width ratio $D/W = 0$ and the length ratio $S/L = 0.5$. The influence of different crack depth ratios and crack aspect ratios on the crack SIF is analyzed.

4.2. Effects of crack depth ratio on the SIF of a surface crack

To study the influence of crack depth ratio on the SIF of a surface crack, different depth ratios $a/t = 0.2$, 0.3, 0.4, 0.5 and 0.6 have been considered. Meanwhile, the crack aspect ratio $a/c = 0.5$ has been taken to analyze the variation of K at different crack angles φ.

The variation of the crack SIF for different crack depth ratios is shown in Fig. 9a. K firstly decreases and then gradually increases with an increase of φ. K gradually decreases within the crack angle range $\varphi = 0°$-$10°$, and gradually increases within the range of $10°$-$80°$, then it tends to be stable above $80°$. The maximum value of the SIF K_{max} appears at the deepest point of the crack $\varphi = 90°$.

In order to further study the influence of crack depth ratios a/t on K, K at the deepest point of the crack has been extracted for study. The variation of K at the deepest point of the crack is shown in Fig. 9b. K gradually increases as the crack depth ratio a/t increases, and the increasing trend of K becomes linear, indicating that the larger the crack depth ratio a/t, the more prone the steel plate is to fracture failure.

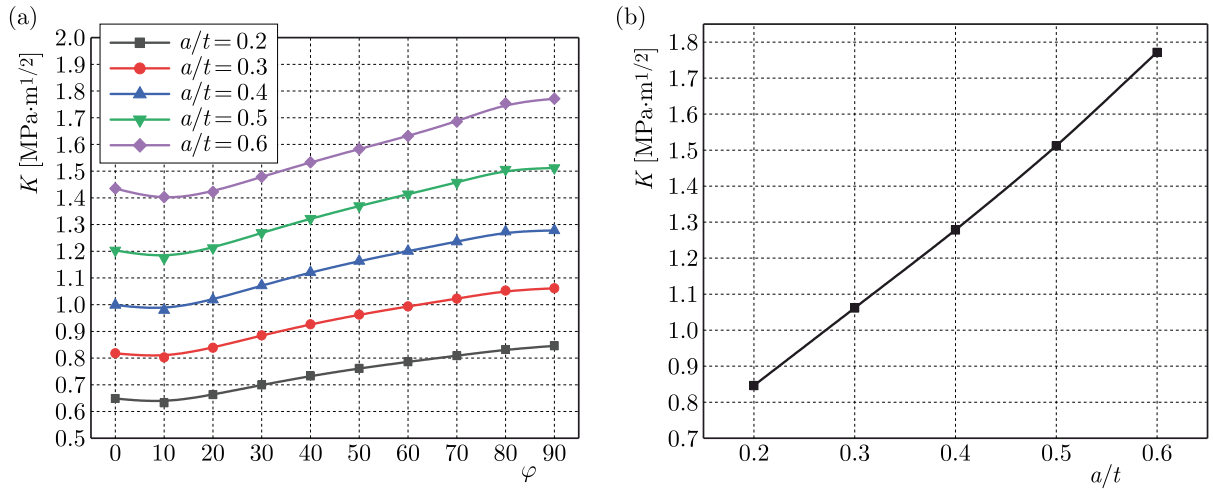

Fig. 9. SIF of a crack for different crack depth ratios: (a) variation of the crack SIF, (b) variation of SIF at the deepest point of the crack

4.3. Effects of the crack aspect ratio on the SIF of a surface crack

To study the influence of crack aspect ratio on the SIF of a surface crack, different aspect ratios $a/c = 0.3$, 0.4, 0.5, 0.6 and 0.7 have been considered. Meanwhile, the crack depth ratio $a/t = 0.5$ has been taken to analyze the variation of K at different crack angles φ.

The variation of the crack SIF for different crack aspect ratios is shown in Fig. 10a. When the crack aspect ratio is $a/c = 0.3$, K firstly rapidly increases and then decreases gradually with an increase of φ. K gradually increases within the crack angle range $\varphi = 0°$-$80°$, and then decreases gradually above $80°$. When the crack aspect ratio is $a/c = 0.4$, K first slowly increases with φ, then gradually increases, and finally gradually decreases. K increases slowly within the crack angle range $\varphi = 0°$-$10°$, and gradually increases within the range $\varphi = 10°$-$80°$, and then gradually decreases above $80°$. When the crack aspect ratio is $a/c = 0.5$, K slowly decreases with an increase of φ first, then gradually increases and tends to be stable. K decreases slowly within the range $\varphi = 0°$-$10°$, and gradually increases within $\varphi = 10°$-$80°$, then tends to be stable above $80°$. When the crack aspect ratio is $a/c = 0.6$, K firstly slowly decreases, and then

it increases gradually with an increase of φ. K decreases slowly within the range $\varphi = 0°$-$20°$, and gradually increases within $\varphi = 20°$-$90°$. When the crack aspect ratio is $a/c = 0.7$, K firstly decreases, and then increases gradually with an increase of φ. K gradually decreases within $\varphi = 0°$-$20°$, and gradually increases within the angles $\varphi = 20°$-$90°$. In order to further study the influence of crack aspect ratios a/c on K, K at the deepest point of the crack has been extracted for study. The variation of K at the deepest point of the crack is shown in Fig. 10b. K gradually decreases with an increase of the aspect ratio a/c, indicating that the smaller the crack aspect ratio is a/c, the steel plate is more prone to fracture failure.

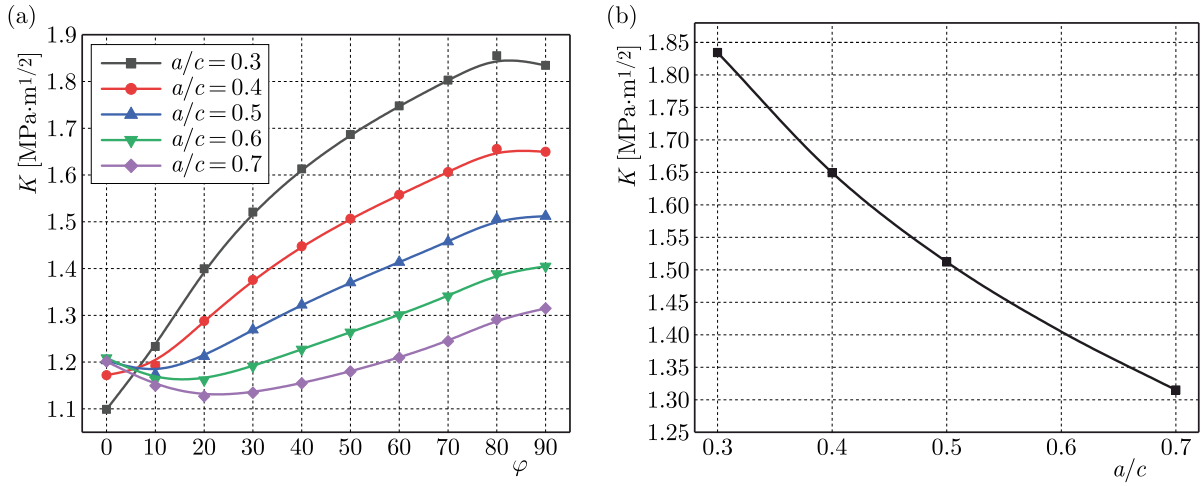

Fig. 10. SIF of a crack for different crack aspect ratios: (a) variation of the crack SIF, (b) variation of SIF at the deepest point of the crack

As shown in Figs. 10a and 10b, the variation rule of K when the crack aspect ratio is $a/c < 0.5$ is obviously different from that when $a/c \geqslant 0.5$, indicating that the crack aspect ratio has a certain influence on the variation of K at different crack angles φ. The maximum value of the SIF K_{max} appears at $\varphi = 80°$ when the crack aspect ratio is $a/c < 0.5$, and the maximum value of the SIF K_{max} appears at the deepest point of the crack $\varphi = 90°$ when the crack aspect ratio is $a/c \geqslant 0.5$, indicating that the crack aspect ratio has a certain influence on the position of the maximum value of the SIF K_{max}.

5. Conclusions

By analyzing the stress intensity factor of a steel plate with surface crack defects, the influence of different crack positions, crack depth ratios and crack aspect ratios on the stress intensity factor has been found. To a certain extent, the conclusions obtained in this paper can provide a theoretical reference for the fracture failure analysis of steel plates.

- The SIF K firstly decreases and then gradually increases with an increase of the width ratio D/W. The SIF K is the largest when $D/W = 0$, and the crack is an edge surface crack, indicating that the edge surface crack has the greatest influence on the fracture failure of steel plates. For a non-edge surface crack, K increases with an increase of the width ratio D/W, and the maximum value of K appears at $D/W = 0.5$, that is, the central surface cracks, indicating that for the non-edge surface crack, the central surface crack has the greatest influence on the fracture failure of the steel plate.
- The SIF K firstly slowly decreases as the length ratio S/L increases, then gradually decreases, and the decreasing trend becomes larger. The maximum value of K appears at $S/L = 0.1$, indicating that the closer is to the stress end, the larger K becomes. When

$S/L \leqslant 0.5$, the variation of K value is small, and the maximum variation difference of K value is 0.01 MPa·m$^{1/2}$. The change of K is large when $S/L \geqslant 0.5$, indicating that the edge surface cracks when $S/L \leqslant 0.5$, which has the greatest influence on the fracture failure of the steel plate.

- The SIF K gradually increases as the crack depth ratio a/t increases, and the increasing trend of K tends to be linear, indicating that the larger is the crack depth ratio a/t, the more prone the steel plate is to fracture failure.
- The variation rule of K when the crack aspect ratio is $a/c < 0.5$ is obviously different from that when $a/c \geqslant 0.5$, indicating that the crack aspect ratio has a certain influence on the variation rule of K at different crack angles φ. The position of the SIF K_{max} when the crack aspect ratio is $a/c < 0.5$ is different from that when $a/c \geqslant 0.5$, indicating that the crack aspect ratio has a certain influence on the position of the maximum value of the SIF K_{max}. K gradually decreases with an increase of the aspect ratio a/c, indicating that the smaller is the crack aspect ratio a/c, the more prone to fracture failure is the steel plate.

Acknowledgments

The authors are grateful for the support from the Youth Funding Project of Hubei Polytechnic University (No. 21xjz03Q) and the open project of Intelligent Transportation Technology and Equipment of Hubei Provincial Key Laboratory (No. 2020XZ109).

References

1. Anderson T.L., 2017, *Fracture Mechanics: Fundamentals and Applications*, CRC Press
2. Barsoum R.S., 1975, Further application of quadratic isoparametric finite elements to linear fracture mechanics of plate bending and general shells, *International Journal of Fracture*, **11**, 1, 167-169
3. Chandra S.K., Sarkar R., Bhowmick A.D., De P.S., Chakraborti P.C., Ray S.K., 2020, Evaluation of ductile tearing resistance of an interstitial free steel sheet using SENT specimens, *Engineering Fracture Mechanics*, **238**, 107257
4. Cheng Z., Wang H., Liu G.-R., 2021, Fatigue crack propagation in carbon steel using RVE based model, *Engineering Fracture Mechanics*, **258**
5. Chong Z., Ma T., Yu D., Wu D., Tao J., Lv H., 2021, Stress intensity factor of double cracks on seabed-spanning pipeline surface under the spring boundary, *Journal of Pipeline Systems Engineering and Practice*, **12**, 4
6. Di Gioacchino F., Lucon E., Mitchell E.B., Clarke K.D., Matlock D.K., 2021, Side-grooved Charpy impact testing: Assessment of splitting and fracture properties of high-toughness plate steels, *Engineering Fracture Mechanics*, **252**, 107842
7. Dolbow J., Moës N., Belytschko T., 2000, Modeling fracture in Mindlin-Reissner plates with the extended finite element method, *International Journal of Solids and Structures*, **37**, 48-50, 7161-7183
8. Figiel Ł., Kamiński M., 2009, Numerical probabilistic approach to sensitivity analysis in a fatigue delamination problem of a two-layer composite, *Applied Mathematics and Computation*, **209**, 1, 75-90
9. He Y., Li L., Lu Z., *et al.*, 2020, Analysis on abnormal tensile fracture of a certain high strength steel (in Chinese), *Materials Protection*, **53**, 2, 157-161
10. Henshell R.D., Shaw K.G., 1975, Crack tip finite elements are unnecessary, *International Journal for Numerical Methods in Engineering*, **9**, 3, 495-507

11. Lee Y.-S., Kim S., Jang D.-W., Lee S.-B., 2022, Mechanism of crack initiation and propagation in high-alloy steel slabs during the cooling and scarfing processes after the continuous casting process, *Mechanics of Materials*, **166**, 104240

12. Li Z., Jiang X., Hopman H., Zhu L., Liu Z., 2020, Numerical investigation on the surface crack growth in FRP-reinforced steel plates subjected to tension, *Theoretical and Applied Fracture Mechanics*, **108**

13. Lin X.B, Smith R.A., 1999, Finite element modelling of fatigue crack growth of surface cracked plates. Part I: The numerical technique, *Engineering Fracture Mechanics*, **63**, 503-522

14. Liu J., Xin H., Zhao X.-L., 2023, Prediction of fatigue crack propagation in center cracked steel plate strengthened with prestressed CFRP strip, *Thin-Walled Structures*, **183**, 110416

15. Newman Jr. J.C., Raju I.S., 1984, *Stress-Intensity Factor Equations for Cracks in Three--Dimensional Finite Bodies Subjected to Tension and Bending Loads*, National Aeronautics and Space Administration (NASA), Langley Research Center, Hampton, VA

16. Omiya M., Arakawa S., Yao Z., Muramatsu M., Nishi S., Takada K., Murata M., Okato K., Ogawa K., Oide K., Kobayashi T., Han J., Terada K., 2022, Influence of strength and notch shape on crack initiation and propagation behavior of advanced high strength steel sheets, *Engineering Fracture Mechanics*, **271**, 108573

17. Rice J.R., 1968, A path independent integral and the approximate analysis of strain concentration by notches and cracks, *Journal of Applied Mechanics*, **35**, 2, 379-386

18. Saber A., Shariati M.R., Nejad M., 2020, Experimental and numerical investigation of effect of size, position and geometry of some cutouts on fatigue life and crack growth path on AISI1045 steel plate, *Theoretical and Applied Fracture Mechanics*, **107**, 102506

19. Shahani A.R., Shodja M.M., Shahhosseini A., 2010, Experimental investigation and finite element analysis of fatigue crack growth in pipes containing a circumferential semi-elliptical crack subjected to bending, *Experimental Mechanics*, **50**, 5, 563-573

20. Wen Y., 2020, *Research on Fracture Performance of Corroded Steel Plate with Central Crack*, Xi'an: Xi'an University of Architecture and Technology

21. Yuan P., Fu D., Gao Y., *et al.*, 2021, Causes analysis and improvement measures for surface cracks of Q235B steel plate (in Chinese), *Wide ang Heavy Plate*, **27**, 6, 34-36

22. Zhang H., Xu S., Nie B., Wen Y., 2019, Effect of corrosion on the fracture properties of steel plates, *Construction and Building Materials*, **225**, 20, 1202-1213

23. Zhang K., Wang M., Liu W., Liu J., 2021, Fracture prediction for an advanced high-strength steel sheet using the fully coupled elastoplastic damage model with stress-state dependence, *Acta Mechanica Solida Sinica*, **34**, 263-273

24. Zhang Q., 2020, *Study on Mechanical Response of Q235 Steel and Constitutive Model under Cyclic Loading*, Hebei: Yanshan University

25. Zhang S.Q., Jiao S.H., Ding J.H., Zhang Q.F., Jiang H.S., 2018, Simulation study on shear crack of steel plate, *Materials Science Forum*, **941**, 480-485

Manuscript received May 1, 2022; accepted for print April 3, 2023

JOURNAL OF THEORETICAL AND APPLIED MECHANICS
61, 2, pp. 355-364, Warsaw 2023
https://doi.org/10.15632/jtam-pl/163053

IMPLEMENTATION OF A VISCOELASTIC BOUNDARY CONDITION TO YADE – OPEN SOURCE DEM SOFTWARE

Karol Brzeziński, Artur Zbiciak
Warsaw University of Technology, Faculty of Civil Engineering, Warsaw, Poland
e-mai: karol.brzezinski@pw.edu.pl

Anton Gladky
Independent Researcher, e-mail: gladky.anton@gmail.com

The paper presents implementation of a viscoelastic boundary condition to Yade software. The implemented boundary condition constraints linear displacements of bodies by applying a reaction force resulting from a solution of the Burgers rheological model. This work presents the results of one of validation tests, where the output of Discrete Element Simulation (DEM) was compared with an analytically formulated soft-contact problem. Furthermore, potential application in more complex simulations (plate load test) is demonstrated. It shows that the proposed approach allows for realistic yet efficient modeling of foundations purely within the DEM framework.

Keywords: Discrete Element Method, viscoelastic boundary condition, granular layers, pavement subsoil

1. Introduction

The subgrade impacts pavement performance and service life (Puppala *et al.*, 2009; Saad *et al.*, 2005). Hence, it is important that pavement models can accurately reflect their behavior. The subgrade can be represented by analytical or numerical models depending on the adopted methodology. For example, the Winkler foundation (Winkler, 1867) is a simple one-dimensional analytical model. Well-known engineering software, such as VEROAD and BISAR programs (Dejong *et al.*, 1973; Hopman, 1996; Zbiciak *et al.*, 2019), utilize an analytical solution of multi-layered half-space. Nevertheless, the application of purely analytical models is limited to simple geometry and load cases. Numerical methods are more versatile. The Finite Element Method (FEM) allows for modeling of complex shapes, material properties and loading scenarios. However, the size of the FEM model needs to be limited. The Discrete Element Method (DEM), introduced by (Cundall and Strack, 1979), is a numerical approach that simulates behavior of granular assemblies by analyzing movements and interactions of individual particles. Consequently, one can study various phenomena at the microstructural level. The DEM is widely applied to simulate the behavior of pavement materials, such as soil and aggregate compaction (Brzeziński and Gladky, 2022; Chen *et al.*, 2021; Gladkyy and Kuna, 2017; Pei and Yang, 2018), asphalt mixtures compaction (Zhu *et al.*, 2022), creep (Quezada and Chazallon, 2022) and rutting (Zhang *et al.*, 2022). However, it comes with a high computational cost. That is why DEM analyses often focus on a small portion of a structure, and the granular assembly needs to be embedded by some deformable boundaries. Among various approaches, the following are often utilized:

- Outer bodies are fixed in place. However, due to their contact stiffness, such a boundary shows some resilience.

- Reaction forces can be applied to outer elements (selected or automatically detected). The force is servo-controlled based on displacement or may be adjusted to satisfy a stress criterion (e.g., membrane simulation (Cheung and O'Sullivan, 2008)).
- Some of researchers use long interactions (Itasca's Particle Flow Code Documentation 7.0, 2021) to set up a two-layered boundary (Pei and Yang, 2018). The outermost layer (e.g., bottom) is fixed in place. The inner layer is bound with external particles with long deformable interactions. The analyzed granular assembly contacts only the inner layer.
- The boundary can be created by a deformable assembly of particles simulating a steel or geosynthetic net (Cheng *et al.*, 2016; Thoeni *et al.*, 2014).
- Coupling with the FEM (Orosz and Zwierczyk, 2020; Stránsky, 2013) or Finite Difference Method (Jia *et al.*, 2021) is an even more sophisticated approach. It not only allows for creating boundary conditions for a granular assembly but also efficiently models and allows for analyzing adjacent structures.

This paper proposes an easy and efficient approach for the modeling of the foundation in DEM simulations. This simple and versatile approach is similar to the Winkler foundation – the reaction force is prescribed to the element based on displacement. However, the adopted force-displacement relationship is described by a solution of the Burgers model (Zbiciak *et al.*, 2017). Hence, it can reflect basic viscoelastic phenomena: creep and relaxation. The proposed feature was implemented in Yade (Smilauer *et al.*, 2021), a popular open-source software for DEM simulations. Such a procedure can be easily programmed as a user sub-routine (e.g., Python function in the case of Yade). Nevertheless, implementation in the source code (using C++) is more efficient and ready for use right after software installation. The Burgers model can be easily degenerated within the proposed approach to simpler models (Zener, Kelvin-Voigt, Maxwell or purely elastic) by prescribing certain values to parameters of the model. Thus, it can be used to model various boundary conditions, e.g., Winkler foundation.

The paper briefly describes implementation of the viscoelastic boundary condition to Yade software. Next, an analytical formulation of a soft-contact problem is presented, and its solution is compared with the results of the DEM simulation. Finally, the results of examplary application to an engineering problem (simulation of a plate load test) are demonstrated.

2. Methods

2.1. Viscoelastic boundary implementation

Yade software conducts DEM simulation iteratively. Generally, each iteration consists of the following steps (Smilauer *et al.*, 2021):

a) Resetting of all forces acting on bodies
b) Collision detections between the bodies
c) Computing interactions between simulated objects and their properties
d) Applying forces to the bodies, based on the assumed contact laws
e) Computing new velocities and then positions of the particles.

The implemented boundary condition is a function that can be run between steps (d) and (e). Hence, the forces acting on the particles are modified before computation of new positions. The function takes a list of Id's (unique identifiers) of the bodies that should be constrained and the viscoelastic parameters (see also Fig. 1), where: k_1 – stiffness of spring 1 (the one in the Maxwell branch) [N/m]; k_2 – stiffness of spring 2 (the one in the Kelvin-Voigt branch) [N/m]; c_1 – damping coefficient of dashpot 1 (the one in the Maxwell branch). A negative value turns off the dashpot [Ns/m]; c_2 – damping coefficient of dashpot 2 (the one in the Kelvin-Voigt branch). A negative value turns off the whole Kelvin-Voigt branch [Ns/m].

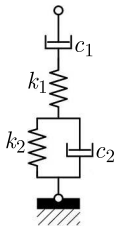

Fig. 1. Rheological scheme of the viscoelastic boundary condition

During the simulation, the initial position of the constrained body is stored in the program memory, and the current position is known from the integration conducted in the previous iteration. Thus, the model reaction can be obtained from a trivial solution to an algebraic set of equations not presented in the paper. In order to make the model more versatile, the option of dashpot deactivation was added (constraining their displacements to zero) by applying a negative value. This way, the user can switch to models simpler than the Burgers one.

2.2. Validation test – soft-contact problem

The same task was solved with two approaches to validate the proposed implementation of a viscoelastic boundary condition. First, the soft-contact problem was analytically formulated and solved with a numerical integration algorithm implemented in Python SciPy library. Next, the same issue was addressed by DEM simulation using Yade software (Smilauer *et al.*, 2021).

2.2.1. Analytical formulation

Let us consider the description of the soft-contact phenomenon in the system visualized in Fig. 2. The upper part of the model is composed of a rigid body (material point) possessing mass m_I and connected in series with a spring k_3. The lower part of the model represents linear viscoelastic boundary constraint having stiffness (spring) parameters k_1 and k_2, viscosity c_2 (damper) and equivalent mass m_{II}.

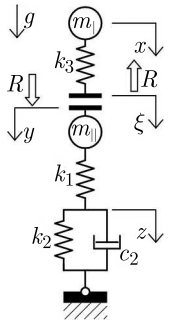

Fig. 2. Visualization of the simplified viscoelastic soft-contact model (no dashpot c_1)

The unilateral constraint between the upper and lower part of the model is visualized in Fig. 2 by two bold horizontal lines representing mass-less bumpers. The gravitational acceleration is denoted as g.

The coordinates x, ξ, y and z shown in Fig. 2 determine the displacement of material points and deformation of the rheological structure. R denotes the force of mutual interaction between the material point m_{II} and the spring k_3. The configuration shown in Fig. 2 represents such a time instant when $x = 0$ and $\xi = 0$, and $y = 0$ and $z = 0$. In the case of this configuration, both bumpers are in contact, but the spring and dashpot forces as well as the reaction R are equal to zero.

The description of the contact problem for the analyzed system may be obtained by formulation of the material points motion and evolution of the structure deformation.

The equations describing the soft-contact problem are as follows

$$\begin{aligned} &m_I\ddot{x} = m_I g - R \qquad k_3(\xi - x) = -R \\ &m_{II}\ddot{y} = m_{II} g + R - k_1(y - z) \qquad k_1(y - z) = c_2\dot{z} + k_2 z \end{aligned} \tag{2.1}$$

and

$$u = y - \xi \qquad u \geqslant 0 \qquad R(\widetilde{u} - u) \geqslant 0 \qquad \forall \widetilde{u} \geqslant 0 \tag{2.2}$$

where Eq. $(2.1)_1$ and Eq. $(2.1)_3$ describe motion of the material points m_I and m_{II}, respectively, while Eq. $(2.1)_2$ and Eq. $(2.1)_4$ represent the evolution of the structure deformation. Moreover, the system of variational inequalities (2.2) defines the relationships between the coordinate $u = y - \xi$ and the reaction R. The coordinates y and ξ denote displacements of the mass-less bumpers connected with the mass m_{II} and m_I, respectively. It can be proved that Eqs. (2.2) can be visualized via the mapping shown in Fig. 3a. (see Zbiciak and Kozyra, 2015).

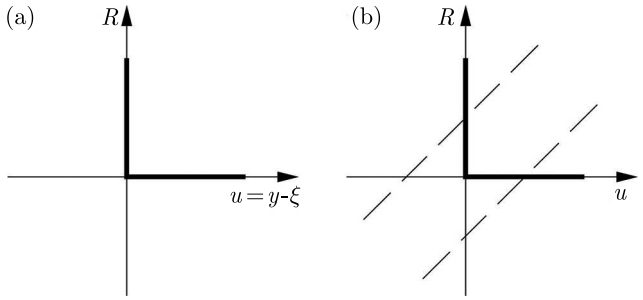

Fig. 3. Graph of the mapping expressed by Eqs. (2.2) (a) and a graphical solution leading to Eq. $(2.5)_2$ (b)

Our objective is to transform a non-linear system of Eqs. (2.1) and (2.2) to the system of explicit non-linear differential-algebraic equations (DAE). The expected system of equations should have the following form

$$\begin{aligned} &\ddot{x} = -\frac{R}{m_I} + g \qquad \ddot{y} = \frac{R}{m_{II}} - \frac{k_1}{m_{II}}(y - z) + g \\ &\dot{z} = -\frac{k_1 + k_2}{c_2} z + \frac{k_1}{c_2} y \qquad \xi = f_\xi(x, y) \qquad R = f_R(x, y) \end{aligned} \tag{2.3}$$

where Eqs. $(2.3)_{1,2,3}$ can be easily obtained using Eqs. $(2.1)_1, 3, 4$, respectively.

Let us find the functions f_ξ and f_R describing time histories of the displacement ξ and reaction R, respectively. To do so, Eq. $(2.1)_2$ should be re-written in the following equivalent form

$$R = k_3(y - \xi) + k_3(x - y) \tag{2.4}$$

Above Eq. (2.4) is a linear relation between R and $u := y - \xi$. Thus, using Eq. (2.4) and the mapping shown in Fig. 3a leads to the solution as follows

$$\begin{aligned} f_\xi(x, y) &= \begin{cases} y & \text{if} \quad x - y > 0 \\ x & \text{if} \quad x - y \leqslant 0 \end{cases} \\ f_R(x, y) &= \begin{cases} k_3(x - y) & \text{if} \quad x - y > 0 \\ 0 & \text{if} \quad x - y \leqslant 0 \end{cases} \end{aligned} \tag{2.5}$$

The graphical solution leading to Eq. $(2.5)_2$ is shown in Fig. 3b where the dashed lines represent two possible locations of the function expressed by Eq. (2.4) for $x - y > 0$ and $x - y < 0$.

2.2.2. DEM simulation

The solution of the above task has been simulated with Yade software. The upper body is modeled as a sphere of radius $r = 0.1\,\mathrm{m}$ and mass $m_I = 4.1888\,\mathrm{kg}$ (resulting from the adopted density of $1000\,\mathrm{kg/m^3}$). The lower body is a flat box of dimensions $0.1\,\mathrm{m}\times0.1\,\mathrm{m}\times0.0001\,\mathrm{m}$ and mass $m_{II} = 0.001\,\mathrm{kg}$. The Zener boundary condition is applied to the box with the following parameters: $c_2 = 1000\,\mathrm{Ns/m}$, $k_1 = k_2 = 10000\,\mathrm{N/m}$. The sphere is initially placed 0.9 m above the box (1.0 m measured to the sphere center), and it falls due to gravity ($g = 10\,\mathrm{m/s^2}$). Contact stiffness, corresponding to k_3 in Fig. 2, equals $10000\,\mathrm{N/m}$ and is independent of the contact penetration u due to the applied linear elastic contact law.

The results of this simulation are compared with the problem formulated analytically in Section 2.2.1 and solved numerically using a Python script.

2.3. Examplary application

This Section presents a more complex simulation to show an examplary application to an engineering problem – a granular layer resting on a viscoelastic foundation. The top of the layer is loaded with a circular steel plate. The simulation resembles a static plate load test often used in the construction process to determine bearing capacity of the granular layer. Nevertheless, the simulation parameters were not calibrated to the field test results. The results are presented for demonstration purposes and qualitative analysis.

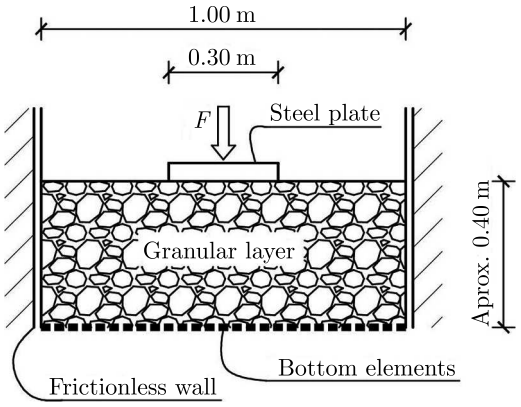

Fig. 4. Problem definition of DEM simulation of plate test

The example, shown in Fig. 4, has been simulated in the following steps:

- Frictionless, rigid, vertical walls were generated to create a vertical funnel with a square cross-section ($1.0\,\mathrm{m}\times1.0\,\mathrm{m}$).
- A discrete bottom boundary condition was created with a layer of small prismatic (box) elements (0.025 m,0.025 m,0.05 m). Hence a layer of 1600 elements was created. At the beginning of simulation, the position of the layer was fixed. However, a permanent vertical force was applied to each box to balance the gravity influence (analogous to geostatic stress often used in geotechnical simulation).
- Loose packing of spherical particles was generated above the bottom layer. Subsequently, the particles fall due to gravity ($g = 10\,\mathrm{m/s^2}$) creating a layer of thickness approximately equal to 0.4 m. The radii of the generated particles ranged between 0.008 m and 0.012 m.
- A steel plate was then placed on top of the granular layer. A cylindrical shape of the plate was achieved by clumping triangular facets into a right prism with twenty joining edges. The mass of the plate was manually prescribed as 10 kg.
- After two seconds (of simulation time), the positions of all bodies were stored as the initial positions. Furthermore, bottom elements remained fixed or were allowed to displace

vertically depending on the scenario. In the second scenario, the vertical movements were constrained by the viscoelastic boundary condition.

- The parameters of constraints applied to each bottom element were computed based on its top wall area. The adopted bedding moduli ($k_{b1} = 20\,\mathrm{N/m^3}$, $k_{b2} = 10\,\mathrm{N/m^3}$, $c_{b2} = 10\,\mathrm{Ns/m^3}$) needed to be multiplied by the top wall area ($0.025 \times 0.025\,\mathrm{m^2}$). Hence, the boundary condition was applied to the bottom element with the following parameters: $k_1 = 12500\,\mathrm{N/m}$, $k_2 = 6250\,\mathrm{N/m}$, $c_2 = 12500\,\mathrm{Ns/m}$.
- Next, the plate was loaded with a linearly increasing vertical force F that reached its maximum value $F_{max} = 17715\,\mathrm{N}$ after 1.78 s and remained constant afterwards. This load was equivalent to stress of 250 kPa since the plate diameter was 0.3 m.
- The particle displacement and reaction forces were stored for further analysis.

The granular layer consisted of only spherical particles. Nevertheless, particle interlocking was achieved by additional rolling resistance. The contact stiffness was controlled by Hertz-Mindlin's (Johnson, 1987) contact law. The remaining material parameters are summarized in Table 1.

Table 1. Material parameters adopted for simulation.

Body type	Density [kg/m^3]	Young's modulus E [GPa]	Poisson's ratio ν [–]	Friction coeff. μ [–]
Spherical particles and bottom elements	2650	1.0	0.25	0.577
Steel plate	7800	210.0	0.25	
Frictionless walls	–	210.0	0.25	0.000

3. Results

3.1. Validation test results

This Section presents a comparison of numerical (DEM) simulation of the soft-contact problem with the solution of its analytical formulation defined in Section 2.2.1. Selected results are presented in Fig. 5.

The output of the simulation reflects phenomena expected in the solution of the simulated problem. The initial position x of the mass m_I equals $-0.9\,\mathrm{m}$, and there is no contact force between the two bodies. As soon as the first body (mass m_I) contacts the second one, the contact force shortly increases, pushing the first body back towards its initial position. However, some of the energy is dissipated in the process. Hence, the displacements and the maximum forces during subsequent contact incidents diminish. After approximately 7 s of simulation, the system reaches a static equilibrium, where the elastic reaction resulting from the displacement of the bottom element balances the weight of the upper body. Moreover, the results present a very good agreement between DEM simulation and analytically formulated problems. This shows that both solutions are practically equivalent.

3.2. Results of examplary application

This Section shows the results of two scenarios of plate test simulation. In the first scenario, the bottom elements are fixed in place. Therefore, the foundation is very stiff. However, some deformation is allowed due to the elastic properties of contacts between the spherical particles and bottom elements. In the second scenario, the bottom elements can move vertically. Nevertheless, the movement is constrained by the viscoelastic boundary condition. Figure 6 shows the cross-section of the granular layer at the end of the test.

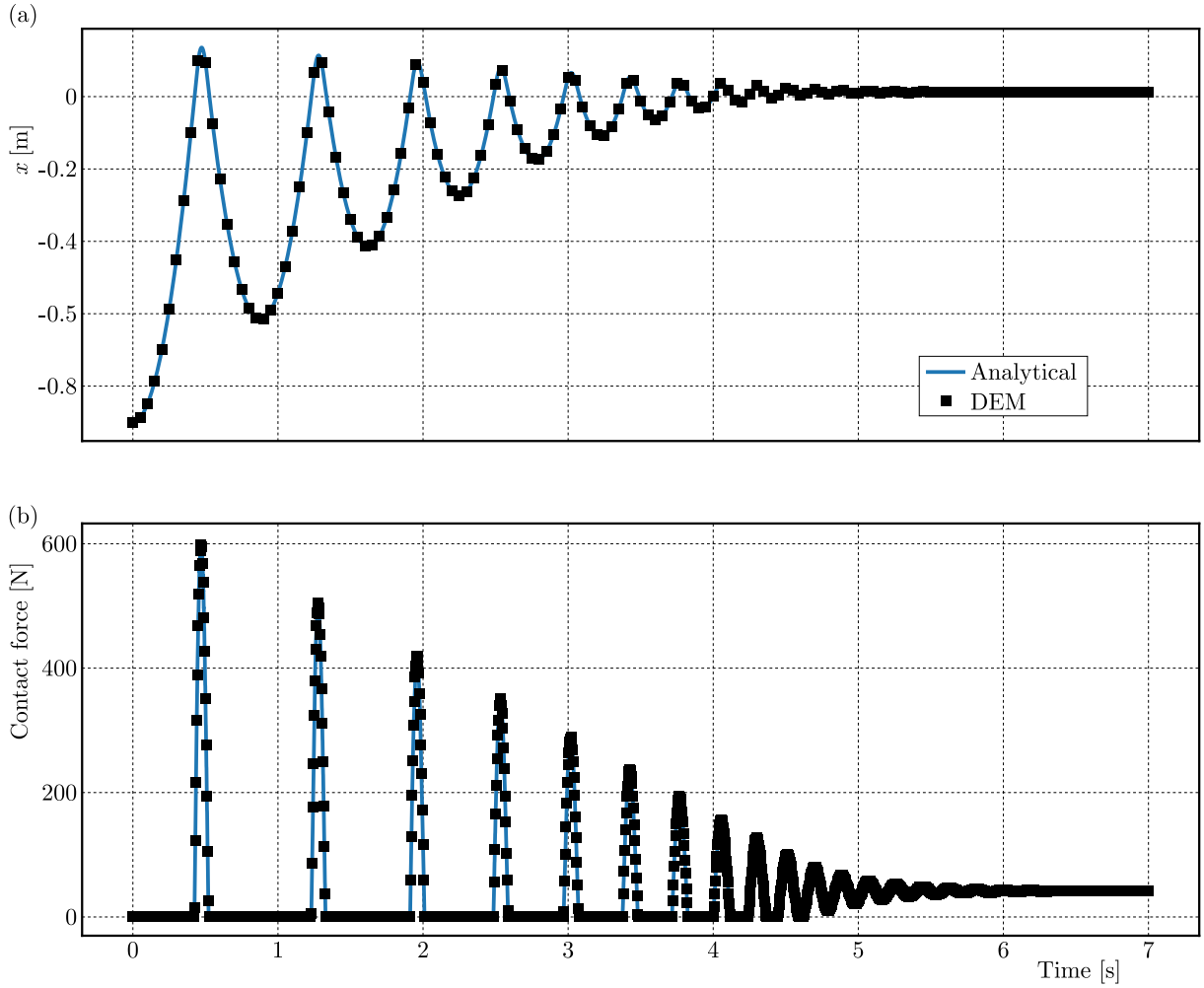

Fig. 5. Results of the soft contact problem solution obtained with an analytical formulation and numerical (DEM) simulation: (a) position of mass m_I, (b) contact force R

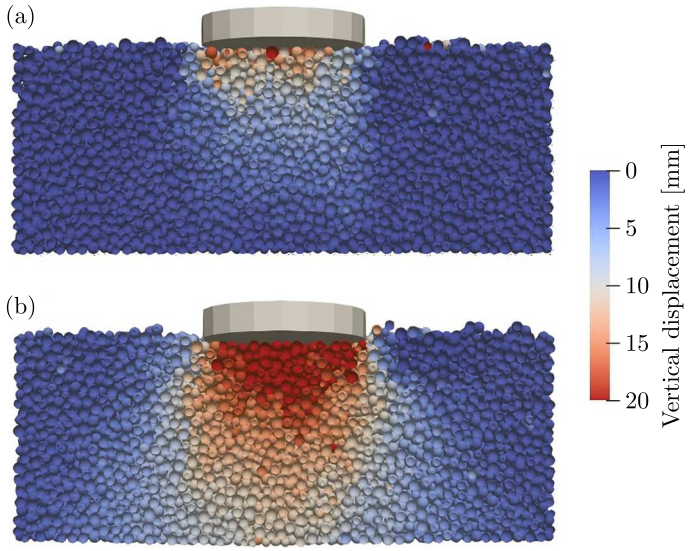

Fig. 6. Displacement of particles in plate test simulation: (a) bottom elements fixed, (b) bottom elements constrained by a viscoelastic boundary condition

In the case of the fixed boundary condition, Fig. 6a, the plate causes only indentation at the top of the layer. This simplified approach can be used to reflect the behavior of the granular material in a relatively stiff container. The results obtained with the viscoelastic boundary condition shown in Fig. 6b resemble displacements of the layer on the deformable foundation (such as an aggregate layer on the soil). This conclusion is also supported by the results presented in Fig. 7.

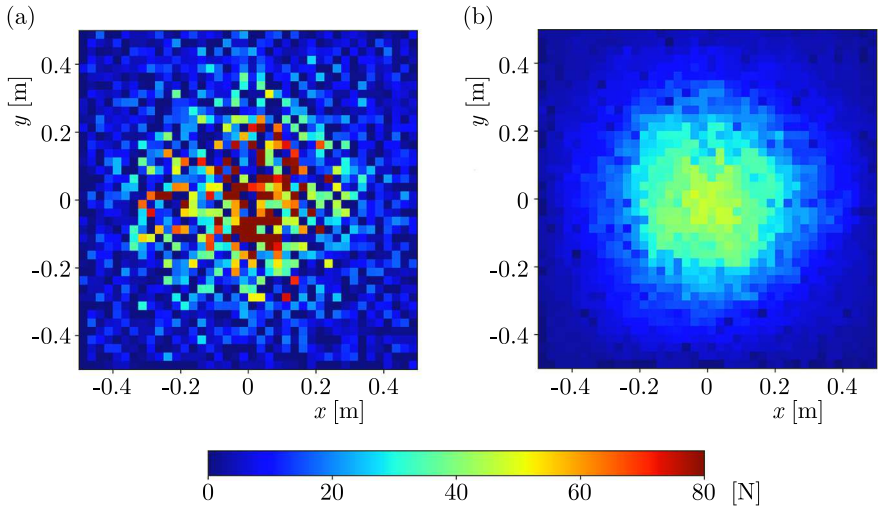

Fig. 7. Distribution of reaction forces acting on bottom elements in plate test simulation: (a) bottom elements fixed, (b) bottom elements constrained by a viscoelastic boundary condition

The reaction force in the deformable foundation is distributed more evenly (see Fig. 7b). There is a distinct circular area of load concentration below the plate that smoothly decreases towards the edges. While in the case of the fixed bottom, the reaction force distribution is much more scattered. Still, the area of the high load is approximately indicated by force concentrations. Nevertheless, the particles at the bottom could not rearrange to redistribute the load on the plate more evenly.

4. Conclusions

This paper presents an implementation of a viscoelastic boundary condition to Yade software. Two simulations have been conducted to demonstrate potential applications of the proposed feature: a one-dimensional soft contact problem and the foundation of a three-dimensional granular layer. The following conclusions can be drawn:

- The implementation works correctly. The results from DEM simulation fit the output of the analytically formulated problem.
- It can be used to simulate foundations, particularly in geotechnical issues, pavement design, compaction simulations, etc.
- The proposed approach allows for realistic yet efficient modeling of foundations purely within the DEM framework.
- The current version is limited to constraining linear displacements of the elements. It can be further developed (e.g. to constrain rotational degrees of freedom).

Acknowledgments

Research was funded by Warsaw University of Technology within the Excellence Initiative: Research University (IDUB) programme.

References

1. Brzeziński K., Gladky A., 2022, Clump breakage algorithm for DEM simulation of crushable aggregates, *Tribology International*, **173**, 107661
2. Chen Y., Jaksa M.B., Kuo Y.-L., Airey D.W., 2021, Investigating the effectiveness of Rolling Dynamic Compaction (RDC) using Discrete Element Method (DEM), *Granular Matter*, **23**, 94, 1-21
3. Cheng H., Yamamoto H., Thoeni K., 2016, Numerical study on stress states and fabric anisotropies in soilbags using the DEM, *Computers and Geotechnics*, **76**, 170-183
4. Cheung G., O'Sullivan C., 2008, Effective simulation of flexible lateral boundaries in two- and three-dimensional DEM simulations, *Particuology*, **6**, 6, 483-500
5. Cundall P.A., Strack O.D.L., 1979, A discrete numerical model for granular assemblies, *Géotechnique*, **29**, 1, 47-65
6. Dejong D., Petuz M., Korswagen A., 1973, *Computer Program, BISAR, Layered Systems under Normal and Tangential Surface Loads*, External Report AMSR-000673, Koninklijke Shell Laboratorium
7. Gladkyy A., Kuna M., 2017, DEM simulation of polyhedral particle cracking using a combined Mohr-Coulomb-Weibull failure criterion, *Granular Matter*, **19**, 3, 1-11
8. Hopman P., 1996, VEROAD: A viscoelastic multilayer computer program, *Transportation Research Record*, **1539**, 1, 72-80
9. Itasca's Particle Flow Code Documentation 7.0., 2021, http://docs.itascacg.com/pfc700/contents.html
10. Jia M., Liu B., Xue J., Ma G., 2021, Coupled three-dimensional discrete element-finite difference simulation of dynamic compaction, *Acta Geotechnica*, **16**, 3, 731-747
11. Johnson K.L., 1987, *Contact Mechanics*, Cambridge University Press
12. Orosz Á., Zwierczyk P.T., 2020, Analysis of the stress state of a railway sleeper using coupled FEM-DEM simulation, *ECMS*, 261-265
13. Pei T., Yang X., 2018, Compaction-induced stress in geosynthetic-reinforced granular base course – A discrete element model, *Journal of Rock Mechanics and Geotechnical Engineering*, **10**, 4, 669-677
14. Puppala A.J., Saride S., Chomtid S., 2009, Experimental and modeling studies of permanent strains of subgrade soils, *Journal of Geotechnical and Geoenvironmental Engineering*, **135**, 10, 1379-1389
15. Quezada J.C., Chazallon C., 2022, Discrete element modelling of hot mix asphalt complex modulus using realistic aggregate shapes, *Road Materials and Pavement Design*, **23**(sup1), 178-195
16. Saad B., Mitri H., Poorooshasb H., 2005, Three-dimensional dynamic analysis of flexible conventional pavement foundation, *Journal of Transportation Engineering*, **131**, 6, 460-469
17. Smilauer V., *et al.*, 2021, *Yade Documentation 3rd ed.*, The Yade Project, https://doi.org/10.5281/zenodo.5705394
18. Stránsky J., 2013, Open source DEM-FEM coupling. Particles III, *Proceedings of the III International Conference on Particle-Based Methods: Fundamentals and Applications*, 46-57
19. Thoeni K., Giacomini A., Lambert C., Sloan S.W., Carter J.P., 2014, A 3D discrete element modelling approach for rockfall analysis with drapery systems, *International Journal of Rock Mechanics and Mining Sciences*, **68**, 107-119
20. Winkler E., 1867, *Vortrge über Eisenbahnbau. Gehalten am königl. böhmischen polytechnischen Landesinstitute in Prag. Erstes Heft: Der Eisenbahn-Oberbau*, H. Dominicus, Prag

21. Zbiciak A., Brzeziński K., Michalczyk R., 2017, Constitutive models of pavement asphaltic layers based on mixture compositions, *Journal of Civil Engineering and Management*, **23**, 3, 378-383

22. Zbiciak A., Kozyra Z., 2015, Dynamic analysis of a soft-contact problem using viscoelastic and fractional-elastic rheological models, *Archives of Civil and Mechanical Engineering*, **15**, 1, 286-291

23. Zbiciak A., Michalczyk R., Brzeziński K., 2019, Time-temperature superposition for viscoelastic materials with application to asphalt-aggregate mixes, *International Journal of Environmental Science and Technology*, **16**, 9, 5059-5064

24. Zhang X., Chen E., Li N., Wang L., Si C., Wang, C., 2022, Micromechanical analysis of the rutting evolution of asphalt pavement under temperature-stress coupling based on the discrete element method, *Construction and Building Materials*, **325**, 126800

25. Zhu X., Qian G., Yu H., Yao D., Shi C., Zhang C., 2022, Evaluation of coarse aggregate movement and contact unbalanced force during asphalt mixture compaction process based on discrete element method, *Construction and Building Materials*, **328**, 127004

Manuscript received December 10, 2022; accepted for print February 3, 2023

JOURNAL OF THEORETICAL AND APPLIED MECHANICS
61, 2, pp. 365-378, Warsaw 2023
https://doi.org/10.15632/jtam-pl/163246

ESTABLISHMENT OF CONSTITUTIVE MODEL AND DYNAMIC PARAMETER ANALYSIS OF RUBBER CONVEYOR BELT

Hongyue Chen, Siyuan Liu

School of Mechanical Engineering, Liaoning Technical University, Fuxin, China

Corresponding author Siyuan Liu, e-mail: 1392451428@qq.com

A rubber conveyor belt is an essential piece of equipment in coal mine transportation. Its current motion and performance are directly affected by dynamic parameters. In this paper, a constitutive model has been established to study a rubber conveyor belt in order to analyze its dynamic characteristics. The covered rubber was considered as a classical solid model. The wire rope core was used as a Kelvin model, and a generalized constitutive mathematical model was established. Using Matlab, comparison of the fitting curve and the experimental curve was carried out to ensure reliability in an appropriate way. Meanwhile, the influence of different factors on dynamic parameters of rubber conveyor belts was also discussed by controlling the loading frequency and amplitude as well as external temperature. Finally, the experiment with the fitting curve was compared and verified, and the research results can provide a reference for this engineering field.

Keywords: rubber conveyor belt, wire rope core, kinetic parameters, fitting curve, mathematical model

1. Introduction

As the most economical and efficient large-scale bulk material conveying system globally, the belt conveyor system is widely used in all walks of life. One of the most commonly used systems is the rubber belt conveyor. However, with the increasing demand for conveying volume and continuous improvement of conveying efficiency, large-capacity, long-distance and high-speed conveyors have become the direction of development. However, this puts forward higher requirements for rubber conveyor belts (Yang *et al.*, 2010) due to strong nonlinearity of rubber material properties and the influence of temperature, excitation frequency and excitation amplitude. Based on the Fourier series, we propose a two-dimensional and three-dimensional boundary element formula for a compressible viscoelastic layer with any thickness, which reveals the viscoelastic effect of rubber materials due to their own asymmetry (Zéhil and Gavin, 2014). Therefore, it is essential for the constitutive model of the rubber conveyor belt and the analysis of its dynamic parameters.

As a kind of viscoelastic material, the constitutive model of a rubber conveyor belt belongs to the scope of viscoelastic mechanics. In the theory of viscoelastic mechanics, the stress-strain-time relation of a viscoelastic material can be divided into differential and integral types. The stress--relaxation behavior of rubber composites was studied using the extension index of the Collauche equation and the Maxwell-Weichert model (Maria *et al.*, 2014). In recent years, the viscoelastic constitutive relation has been significantly developed by introducing fractional derivatives. The fractional Maxwell model, the fractional Kelvin model, and the three-force superposition model were developed by Sjöberg and Kari (2002). The indentation area was measured by strain gauges, and the variation law of stress when a specific point on the rubber conveyor belt was rolled over the idler was analyzed (Jonkers, 1999). According to Spaans (2001), the energy consumption method deduced a calculation formula for indentation resistance. Lodewijks (2013) carried out a viscoelasticity test for rubber with different compositions by a dynamic mechanical analyzer

DMA, which provided a valuable reference for studying the influence of characteristics of the covering layer on the indentation resistance. Rudolphi and Reicks (2006) selected the generalized Maxwell model to characterize viscoelastic properties of the covering layer, and to fit the previous viscoelastic test results. They deduced a formula for calculating the indentation resistance.

Wang *et al.* (2007) proposed a visco-hyperelasticity model after superelasticity and viscoelasticity to test rubber materials in a wide strain range. Zhu *et al.* (2015) used a nonlinear and fractional derivative viscoelasticity (FDV) model to discuss the relationship between stiffness and damping and the excitation frequency and displacement amplitude. It was concluded that the dynamic stiffness and damping of the guide rail pad increased with the excitation frequency and decreased with an increase of the displacement amplitude. Zhang and Xia (2011) explored the energy conversion in the operation process of the belt conveyor and improved the operation efficiency through an optimization method. Qiu and Chai (2011) applied viscoelastic and Winkler basic assumptions to discuss the effects of viscoelastic characteristics, transport rate and speed on the energy loss of the transport system. Gil-Negrete *et al.* (2006) used a finite element (FE) code to predict dynamic stiffness of the filled rubber separator, evaluated dynamic stiffness of the actual liner under working conditions and used the equal effect variable amplitude value estimation, and the prediction results were reliable. Chen *et al.* (2015) deduced parameters of a conveyor belt expressed by a three-parameter constitutive model, and Liu *et al.* (2010) carried out finite element verification and optimization of viscoelasticity of the covering rubber. Cho *et al.* (2013) interpolated a temperature dependence of the rubber loss modulus by using a reasonable 4-parameter fitting method, and solved the loss of the temperature-nonlinear hysteresis and temperature distribution by using an interleaved iterative calculation scheme. Through numerical experiments, the prediction results were compared with the experimental results to verify the effectiveness of the prediction method. Hao *et al.* (2008) constructed a generalized recovery model for rubber. Tong *et al.* (2020) proposed a new nonlinear viscoelastic constitutive model to describe mechanical behavior of rubber composites. Behnke and Kaliske (2015) proposed a numerical framework for effective thermodynamic analysis of a full three-dimensional rubber tire structure (axially symmetric geometry) in steady state motion, discussed parameter identification in detail focusing on the rolling resistance and surface temperature distribution. Gholipour *et al.* (2020) first developed and solved the coupled continuous viscoelastic model based on Timoshenko's nonlocal strain gradient theory. Nguyen *et al.* (2020) proposed a structural damage diagnosis method based on the change of mechanical parameters of rubber. Chen *et al.* (2020) established and simulated a rigid-flexible coupling dynamic model of belt conveyor based on theoretical analysis.

In previous studies, many mechanical models and simulation algorithms describing dynamic characteristics of rubber conveyor belts have been obtained. It is concluded that the classical solid model and Kelvin model can well describe mechanical characteristics of rubber conveyor belts with steel wire core under a stress state, and the constitutive model of a steel wire rubber conveyor belt can better describe dynamic characteristics of operation. The ST1600 type rubber conveyor belt is regarded as the research object. The belt consists of the upper rubber cover, lower rubber cover, core rubber and a steel wire rope embedded in the core rubber, as shown in Fig. 1. This paper further improves the constitutive model by applying the previous theory and samples used in the experiment based on previous studies. Through mathematical fitting of two variables of the frequency and amplitude, this paper discusses the influence of the amplitude and frequency on the elastic modulus and damping of the rubber conveyor belt. At the same time, the frequency and amplitude are controlled by an experimental method, and the simulation results are verified to ensure reliability of the results. The dynamic characteristics of steel wire rope rubber conveyor belts are analyzed by combining the theory and experiment to analyze stress characteristics of rubber conveyor belts in industrial transportation in coal mines. Since the steel wire rope embeds the inner core rubber, the bolt body is composed of rubber. The

rubber material has some viscoelastic characteristics. It can be seen that the rubber conveyor belt has dual physical and mechanical properties. If the load changes during the operation, its elastic modulus and damping coefficient will also change. It can be seen that the self-recovery force of the rubber conveyor belt is a nonlinear relationship. Hence, the research on deformation resistance of the rubber conveyor belt has a practical application value.

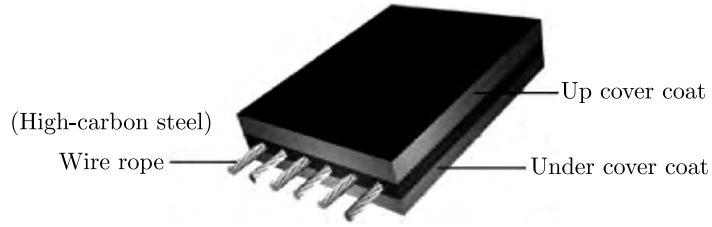

Fig. 1. Model of a rubber conveyor belt

2. Theoretical basis

In this paper, the examined object is a steel cord rubber conveyor belt. It is often used in coal mine transportation, and the typical failure mode is steel cord degumming. To study dynamic characteristics of rubber conveyor belts, it is necessary to study a mathematical model. The whole working process of the rubber conveyor belt can be understood as a steel wire core bearing a tensile force and rubber bearing the load of gravity.

2.1. Fourier series

The Fourier series is widely used in algebra, combinatorics, signal processing, probability theory, statistics, cryptography, acoustics, optics and other fields. The formula is shown in (2.1)

$$\begin{aligned} f(t) &= \frac{a_0}{2} + a_1\cos(\omega t) + b_1\sin(\omega t) + a_2\cos(2\omega t) + b_2\sin(2\omega t) + \dots \\ &= \frac{a_0}{2} + \sum_{n=1}^{\infty}[a_n\cos(n\omega t) + b_n\sin(n\omega t)] \end{aligned} \tag{2.1}$$

where

$$a_n = \frac{2}{T}\int_{t_0}^{t_0+T} f(t)\cos(n\omega t)\,dt \qquad b_n = \frac{2}{T}\int_{t_0}^{t_0+T} f(t)\sin(n\omega t)\,dt \tag{2.2}$$

The Fourier series describes the periodic function $f(t)$ as a constant coefficient a_0 and a sum of sin and cos functions of 1 times ω, sin and cos functions of 2 times ω, and sin and cos functions of n times ω. Each term has different coefficients a_n and b_n. These coefficients need to be calculated by integration. For convenience, the integration interval is generally set to the width of one cycle T. This paper studies the influence of the loading frequency and amplitude on rubber conveyor belts. The loading frequency and amplitude changes have periodic characteristics and can be treated as sinusoidal functions. Using the Fourier series to process such information enables comparison and process of data more intuitively, reduction of errors caused by repeated data processing, and improvement of data processing efficiency and reliability.

2.2. Kelvin model

The Kelvin model is an ideal spring parallel with an ideal damper with no transient elastic effect on stress or strain. As $t \to \infty$ (t – time), the creep of the Kelvin model tends to be an asymptote, which is characteristic for viscoelastic solids in stable creep. The Kelvin model is often used in conjunction with the Maxwell model, which is composed of the two units connected in series. The two units are mostly ideal dampers and ideal springs. When an external force acts on this model, the external force in the spring and the dashpot is the same. Under specific stress, the material can deform infinitely, which is characteristic for viscous fluids. The transient response of the Maxwell model is characteristic for an elastic body, while the time effect is characteristic for a viscous fluid. When applied to the model, the total stress is shared by the spring and damper, and the total strain is the sum of the two.

The application of the Kelvin model is essential for establishing the constitutive model. The establishment of the constitutive model of the steel cord rubber conveyor belt is based on the Kelvin model. It provides prerequisites for formulating a mathematical model and simulation analysis in this paper.

3. Constitutive model of the conveyor belt

In order to make the calculation straightforward, a simplified model of the rubber conveyor belt is established to analyze the stress-strain relationship. Different materials have different constitutive relations under different deformation conditions, also known as different constitutive models. In essence, it is a physical relationship. The equations established are called physical equations which comprehensively reflect the macroscopic mechanical properties of structures or materials. In a broad sense, it is a sweeping curve of a generalized force-deformation or a strength-deformation law. Various materials, components or structures may have many different reactions in various stress stages. However, if the generalized force-deformation curve is drawn, all phenomena of different reactions will have similar and corresponding geometric characteristic points on the curves. Accordingly, the application of the constitutive model, which is consistent in macroscopic scale, will be of great use in theoretical research and engineering practice.

In an ideal state, each steel wire rope inside the conveyor belt is evenly embedded, the force is the same and uniform during operation, the performance parameters of each steel wire rope are the same, and the calculation and analysis process are relatively simple. Therefore, we assume that the rubber conveyor belt is currently in an ideal working state. Under stable working conditions, the shear deformation between the steel wire rope and rubber is small and can be ignored. The sheer force between the steel wire core and rubber can also be ignored, the covering rubber is regarded as a classical solid model and the core is considered a Kelvin material.

In Fig. 2, $E_{f1}E_{fn}$ denotes the elastic modulus of each wire rope [MPa]. It represents the stress required to produce unit deformation per unit area and characterizes the ability of the material to resist elastic deformation. The larger the value, the greater the energy to resist elastic deformation. $\eta_{f1}\eta_{fn}$ stands for the damping coefficient of each wire rope; n is the total number of wire ropes, E_{m1}, E_{m2} are the elastic moduli of the rubber matrix [MPa]. The larger the damping coefficient, the greater the damping force generated by the same velocity. η_m is the damping coefficient of the rubber matrix [MPa·s]. In this paper, the Kelvin model is used to describe behavior characteristics of the steel wire which is regarded as a spring and damping element. $E_{f1}E_{fn}$ represents the elastic modulus of each steel wire and describes the ability of it to resist deformation. The larger the elastic modulus the smaller deformation and the stronger the steel wire under the same force. Since the material and geometric parameters of the wire used in the conveyor belt are exactly the same, the elastic modulus of each wire is the same,

that is, $E_{f1} = E_{f2} = \ldots = E_{fn}$. A single steel wire is loaded by the sinusoidal load, see Eq. (4.1) in Section 4.1, and the curve is fitted by the Fourier series. The parameters are shown in equations (4.2)-(4.5) to complete the calculation of elastic modulus E of the steel wire.

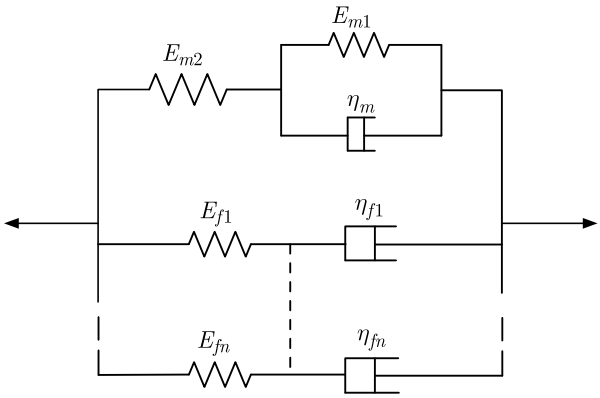

Fig. 2. Constitutive model of the rubber conveyor belt

The rubber conveyor belt and the steel wire core of the dual steel cable belong to elastic materials, rubber belongs to hyperelastic materials. The steel wire core is a skeleton, and the rubber is used as the cladding with viscoelastic properties. In this paper, mechanical characteristics of overburden rubber are regarded as in a classical solid model, and mechanical characteristics of the wire core are regarded as in the Kelvin model. A generalized constitutive model is established, which can not only reflect the relaxation and creep characteristics of the conveyor belt, but also express the transient response during loading. The load during operation can be regarded as a sinusoidal change, so the loading displacement has sinusoidal character. A smooth operation process of the steel wire reinforced rubber conveyor belt can be regarded as uniform linear motion. The rubber conveyor belt maintains a balanced state along the axial direction of the steel wire core. In the actual working process of belt, although there is tension along the axial direction, the deformation is small, which does not affect the motion state of the rubber conveyor belt, so the classical solid model and Kelvin model are used as a theoretical basis to establish the equation of equilibrium of the constitutive model

$$\begin{aligned} &\sigma = n\sigma_f v_f + \sigma_m(1 - v_f) \qquad \sigma_f = E_f\varepsilon_f + \eta_f\dot{\varepsilon}_f \qquad \varepsilon = \varepsilon_{m1} + \varepsilon_{m2} \\ &\sigma_m = E_{m1}\varepsilon_{m1} = E_{m2}\varepsilon_{m2} + \eta_m\dot{\varepsilon}_{m1} \qquad \varepsilon = \varepsilon_f \end{aligned} \tag{3.1}$$

In the formula, v_f is the volume fraction of each wire, σ is the stress of the belt [MPa], σ_f is the stress of each wire [MPa], σ_m is the stress matrix of rubber [MPa], ε is the strain of the steel wire core, which indicates deformation of the conveyor belt (dimensionless). The strain mattrix of the rubber is regarded as ε_{m1}, ε_{m2} and indicates deformation of the stressed rubber (dimensionless). The strain of each wire is regarded as ε_f which indicates deformation of the wire ubder stress (dimensionless).

The generalized constitutive mathematical model of the rubber conveyor belt is obtained by combining and simplifying the equation of the system (3.1)

$$\sigma = (E_f\varepsilon + \eta_f\dot{\varepsilon})nv_f + (-p_1\dot{\sigma} + q_0\varepsilon + q_1\dot{\varepsilon})(1 - v_f) \tag{3.2}$$

where

$$p_1 = \frac{\eta_m}{E_{m1} + E_{m2}} \qquad q_0 = \frac{E_{m1}E_{m2}}{E_{m1} + E_{m2}} \qquad q_1 = \frac{\eta_m E_{m1}}{E_{m1} + E_{m2}}$$

$\dot{\sigma}_m$ is the first derivative of σ_m with respect to time t and the $\dot{\varepsilon}$ is the first derivative of ε.

The external load dynamic strain of the conveyor belt is

$$\varepsilon = A\sin(\omega t) + \varepsilon_0 \tag{3.3}$$

where ε_0 is the initial strain, A – strain amplitude [mm].

Substituting (3.3) into (3.2), one gets

$$\begin{aligned}\sigma(t) = {} & [E_f\varepsilon_0 + E_f A\sin\omega t + \eta_f A\omega\cos(\omega t)]nv_f \\ & + \Big[q_0\varepsilon_0 + \frac{A(q_1\omega^2 p_1 + q_0)}{1+\omega^2 p_1^2}\sin(\omega t) + \frac{A(q_1 - q_0 p_1)\omega}{1+\omega^2 p_1^2}\cos(\omega t)\Big](1-v_f)\end{aligned} \tag{3.4}$$

The length of the conveyor belt is denoted by L, and the cross-sectional area by S. At the same time, it is assumed that the displacement of the loaded conveyor belt by angular excitation is

$$x = M\sin(\omega t) + x_0 \tag{3.5}$$

where x_0 – initial loading displacement [mm], M – load displacement amplitude [mm], ω – loading angular frequency [rad/s].

The following equation can express strain of the belt

$$\varepsilon = \frac{x}{L} \tag{3.6}$$

According to formula (3.6), the initial strain is $\varepsilon_0 = x_0/L$.

The following equation can express the strain amplitude

$$A = \frac{M}{L} \tag{3.7}$$

Substituting the strain amplitude and initial strain into equation (3.4), equation (3.4) becomes

$$\begin{aligned}\sigma(t) = {} & \frac{x_0}{L}[nE_f v_f + q_0(1-v_f)] + \frac{M}{L}\sin(\omega t)\Big[nE_f v_f + \frac{q_1\omega^2 p_1 + q_0}{1+\omega^2 p_1^2}(1-v_f)\Big] \\ & + \omega\frac{M}{L}\cos(\omega t)\Big[n\eta_f v_f + \frac{q_1 - q_0 p_1}{1+\omega^2 p_1^2}(1-v_f)\Big]\end{aligned} \tag{3.8}$$

Under the displacement excitation, the force of the conveyor belt will change dynamically. It can be expressed as

$$F = \sigma(t)S \tag{3.9}$$

where F is the force of the conveyor belt under the displacement excitation in [N], S is the cross-section area of the conveyor belt in [mm^2].

Substituting equation (3.8) into (3.9), we get

$$\begin{aligned}F = {} & \frac{x_0}{L}[nE_f v_f + q_0(1-v_f)] + \frac{M}{L}S\sin(\omega t)\Big[nE_f v_f + \frac{q_1\omega^2 p_1 + q_0}{1+\omega^2 p_1^2}(1-v_f)\Big] \\ & + \omega\frac{M}{L}S\cos(\omega t)\Big[n\eta_f v_f + \frac{q_1 - q_0 p_1}{1+\omega^2 p_1^2}(1-v_f)\Big]\end{aligned} \tag{3.10}$$

4. Parameter prediction and validation

4.1. Experiment preparation

The general steel cord rubber conveyor belt ST1600 that meets GB/T 9770-2013 is selected as the research object in this paper. As shown in Fig. 3, the length of the selected sample is 1100 mm, width is 75 mm, and thickness of the upper and lower covering glue is 6 mm. The thickness of the core rubber is 5 mm, there are six steel wire ropes inside, and the diameter of the steel wire core is 5 mm. Although the rubber conveyor belt is subjected to weight of the materials, friction and tension during operation, the action of these forces makes the rubber conveyor belt displace. Therefore, the displacement represents the action of various forces acting on the rubber conveyor belt. The electronic universal tensile testing machine was used to load the sample in this experiment. A sinusoidal displacement loading was used as the initial loading during this experiment. The frequency f was 0.1 Hz, the amplitude M was 1.4 mm, and the initial displacement x_0 was 1.9 mm. The loading function is given by the formula

$$x = 1.4\sin(0.2\pi t) + 1.9\,\text{mm} \tag{4.1}$$

Since the vibration frequency is about 0.1Hz under a heavy load in the actual working process, 0.1 Hz is selected as the loading frequency. There is tension in the conveyor belt installation process and an initial position is generated. In this scheme, the initial position is 1.9 mm. In this paper, the maximum width of the conveyor belt is 1.5 mm, and such limiting cases rarely occur, so the loading amplitude of 1.4 mm is selected for the study.

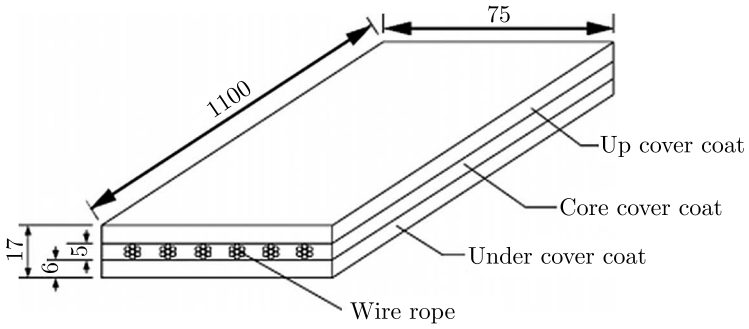

Fig. 3. Schematic diagram of the sample structure

4.2. Experimental verification

According to the relevant knowledge of material mechanics and structural mechanics, the external load equation of the wire rope is

$$F_f(t) = \frac{x_0 E_f S_f}{L} + \frac{M S_f E_f}{L}\sin(\omega t) + \frac{\omega M S_f \eta_f}{L}\cos(\omega t) \tag{4.2}$$

where F_f is the force of the wire rope under the displacement excitation in [N]; S_f is the section area of the wire rope in [mm^2].

A first-order Fourier series can fit the force-displacement curve of a viscoelastic material, and the fitting function is as follows

$$F(t) = a_0 + a_1\cos(\omega t) + b_1\sin(\omega t) \tag{4.3}$$

According to formula (4.2) and (4.3), it can be known that

$$a_0 = \frac{x_0 E_f S_f}{L} \qquad a_1 = \frac{\omega M S_f \eta_f}{L} \qquad b_1 = \frac{M S_f E_f}{L} \tag{4.4}$$

According to formula (4.4), we can get

$$E_f = \frac{a_0 L}{x_0 S_f} \qquad \eta_f = \frac{a_1 L}{\omega S_f M} \tag{4.5}$$

The displacement-force curve of a single wire rope is fitted by the Matlab cftool tool, and a_0, a_1 and b_1 can be obtained. The elastic modulus and damping coefficient of the wire rope model are calculated by using a_0, a_1 and b_1. In this paper, GB/T 9770-2013 ordinary steel wire core rubber conveyor belt ST1600 is selected, and the steel wire used in the core is the some as in GB/T 12753-2020 conveyor belt. By calculation, $E_f = 9735.3$ MPa, $\eta_f = 683.9$ MP·s.

The external load equation of the rubber conveyor belt base is given as

$$F_m = \frac{x_0 S_m q_0}{L} + \frac{M S_m (q_1 \omega^2 p_1 + q_0)}{L(1+\omega^2 p_1^2)} \sin(\omega t) + \frac{\omega M S_m (q_1 \omega^2 p_1 + q_0)}{L(1+\omega^2 p_1^2)} \cos(\omega t) \tag{4.6}$$

where F_m is the force of the rubber substrate under displacement excitation in [N]; S_m is the section area of the rubber substrate in [mm^2].

From equations (4.6) and (4.4), it can be found that

$$a_0 = \frac{x_0 S_m q_0}{L} \qquad a_1 = \frac{\omega M S_m (q_1 \omega^2 p_1 + q_0)}{L(1+\omega^2 p_1^2)} \qquad b_1 = \frac{M S_m (q_1 \omega^2 p_1 + q_0)}{L(1+\omega^2 p_1^2)} \tag{4.7}$$

Deduced from equations (4.6) and (4.7)

$$E_{m1} = \frac{L(a_1^2 x_0 + b_1^2 x_0 + a_0 b_1 M)}{S_m M(x_0 b_1 - a_0 M)} \qquad E_{m2} = \frac{a_0 L(a_1^2 x_0 + b_1^2 x_0 - a_0 b_1 M)}{S_m(a_1^2 x_0 + b_1^2 x_0^2 - 2a_0 b_1 x_0 M + a_0^2 M^2)}$$
$$\eta_m = \frac{a_0 L(a_1^2 x_0 + b_1^2 x_0 - a_0 b_1 M)^2}{a_1 S_m(a_1^2 x_0 + b_1^2 x_0^2 - 2a_0 b_1 x_0 M + a_0^2 M^2)} \tag{4.8}$$

The rubber matrix displacement-force curve is fitted with the Matlab cftool tool from which a_0, a_1 and b_1 can be obtained, and the elastic modulus and damping coefficient of the wire rope model is calculated using a_0, a_1 and b_1.

It has been calculated that $E_{m1} = 684.6$ MPa, $E_{m2} = 2059.7$ MPa, $\eta_m = 5487.4$ MPa·s.

In order to verify correctness of the theoretical model of the rubber conveyor belt, a test has been conducted in a universal tensile test machine and a digital display temperature control box. The experimental equipment and materials are shown in Fig. 4. In order to avoid the test data being affected by temperature, first, the sample is placed at a room temperature of 25°C for 12 hours. With the experimental data unaffected by temperature, the specimen is then fixed in the testing machine with a load applied to one end and a fixed clamp at the other end. The strain amplitude is controlled between 0.5 mm-3.6 mm, the frequency is 0.1 Hz, the loading changes according to the sine law, the experimental data is exported, and the exported data is put into Matlab for comparison with the theoretical curve, as shown in Fig. 5, the reliability is analyzed.

The digital display temperature control box ensures that the temperature of the experimental process is constant and ensures that the experimental results are not affected by external temperature. In the experiment, the upper and lower fixtures of the universal tensile test machine is 1000 mm. An experiment with the sinusoidal displacement loading of the conveyor belt is performed, and then the reliability of the current mechanical model is analyzed according to the experimental data. The size of the conveyor belt used for the loading test is: width 75 mm, thickness 17 mm, wire core diameter 5 mm, upper and lower cover layer rubber thickness 6 mm, upper and lower fixture interval 1000 mm, fixture clamping part 50 mm, the selected conveyor

Fig. 4. Experimental equipment and materials

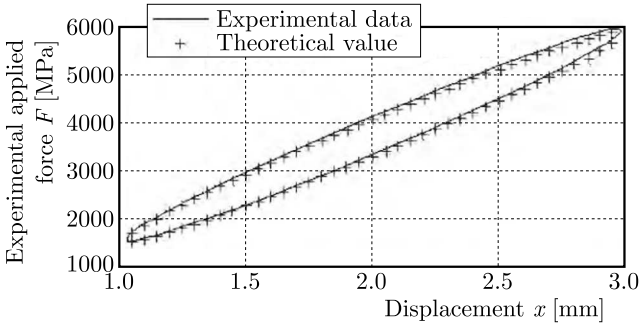

Fig. 5. Theoretical curve and the actual curve

belt specimen length 1100 mm. The calculation process of the characteristic parameters of the conveyor belt is shown in Eqs. (4.2)-(4.8). The section area of the wire is S_f, and that of the rubber substrate is S_m.

According to Fig. 5, it can be seen that the experimental and simulation results have a reasonable degree of agreement. The coefficient of coincidence of the two curves is 0.96, which can meet the accuracy requirements of the actual working conditions.

The curve error map is generated by Matlab, as shown in Fig. 6.

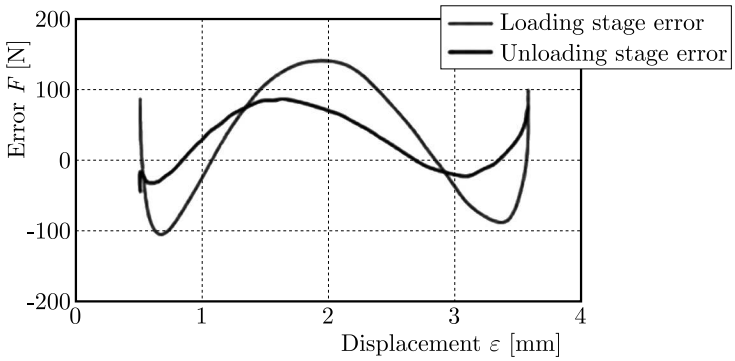

Fig. 6. Curve error diagram

It can be seen from the curve error diagram that the maximum error is 148 N, and the operation is not significantly affected. Therefore, it is adviable to explore mechanical parameters of the rubber conveyor belt described by the constitutive model and applicable in the coal transportation process.

5. Analysis of parameter changes

5.1. Amplitude and frequency changes

Since viscoelasticity is possessed by the material of the rubber conveyor belt itself, there are differences in the damping coefficient η_m and elastic moduli E_{m1}, E_{m2} of the rubber conveyor belt under different loads. It is of practical research value to explore the influence of the load on these parameters. Investigated is the influence of the load on the characteristics of rubber conveyor belt through loading amplitude and loading frequency. When the rubber conveyor belt is working normally, the elongation per unit length under the maximum load condition is 3.6 mm, and the maximum elongation in normal working conditions is between 2.0-3.6 mm. The conveyor belt has dead weight, and the elongation per unit length under no load condition is about 0.5 mm. Therefore, the minimum displacement is selected as 0.5 mm, and the maximum displacements of loading are 2.0 mm, 2.5 mm, 2.7 mm, 3.0 mm and 3.5 mm. The identification results are shown in Table 1. It can be seen that the damping coefficient η_m first decreases and then increases, and the elastic modulus E_{m1} increases slightly but rapidly. It can be seen that as the loading displacement increases, the rigidity of the conveyor belt increases as well.

According to the data in Table 1, the relationship between the loading amplitude M and the damping coefficient η_m, elastic moduli E_{m1}, E_{m2} is fitted to determine the relationship between different amplitudes and the damping coefficient η_m and the elastic moduli E_{m1}, E_{m2}.

Table 1. Parameters of the conveyor belt model for changing load amplitude

Serial number	Frequency f [Hz]	Amplitude M [mm]	Initial value x_0 [mm]	Damping coefficient η_m [MPa·s]	Elastic modulus E_{m1} [MPa]	Elastic modulus E_{m2} [MPa]
1	0.10	0.75	1.25	7349.40	1812.27	16161.88
2	0.10	1.00	1.50	5829.19	1811.64	16333.88
3	0.10	1.10	1.60	4646.56	1804.29	16949.18
4	0.10	1.25	1.75	5726.50	1789.69	19332.34
5	0.10	1.50	2.00	6189.91	1721.71	29190.33

Using Matlab software to perform quadratic polynomial fitting, the fitting results are as follows

$$\begin{aligned} \eta_m(M) &= (4.78M^2 - 12.67M + 13.92) \cdot 10^3 \\ E_{m1}(M) &= (-0.04M^2 - 0.14M + 1.98) \cdot 10^3 \\ E_{m2}(M) &= (9.32M^2 - 6.22M + 14.01) \cdot 10^3 \end{aligned} \tag{5.1}$$

The certainty coefficients between the fitted curve and the original data are 0.81, 0.88 and 0.94, respectively, and the certainty coefficients are relatively low. Therefore, verification of prediction accuracy is required.

The values of $f = 0.1$ Hz, amplitude $M = 1.45$ mm, initial displacement $x_0 = 1.95$ mm are substituted into formula (5.1) for verification and comparison of the prediction results with the identification results, as shown in Table 2.

It can be seen from Table 2 that the relative error between the identification results of the damping coefficient η_m and the prediction results is the largest. However, it is only 3.76%, which can still meet the actual needs of the project. It can be seen that the needs of predicting the belt operation by Eqs. (5.1) is satisfied.

Chen *et al.* (2017) used viscoelastic dynamics theory and the Fourier series fitting method to derive and establish the parameter identification equation of the standard solid model of a rubber conveyor belt. For a constant frequency of 0.10 Hz, the amplitudes are, respectively, 0.75 mm,

Table 2. Comparison of prediction and identification parameters

	Damping coefficient η_m [MPa·s]	Elastic modulus E_{m1} [MPa]	Elastic modulus E_{m2} [MPa]
Identification result	5816.84	1701.47	24285.60
Forecast result	5598.40	1692.90	24586.00
Relative error [%]	3.76	0.50	1.24

1.00 mm, 1.25 mm, 1.50 mm, 1.75 mm, 2.00 mm. The damping coefficient η_m is 7340.49 MPa·s, 5892.09 MPa·s, 5750.26 MPa·s, 6135.89 MPa·s, 7068.83 MPa·s, 7629.77 MPa·s. The elastic modulus E_{m1} is 1812.64 MPa, 1817.27 MPa, 1730.69 MPa, 1621.71 MPa, 1609.19 MPa, 1571.28 MPa and the elastic modulus of E_{m2} is 16160.88 MPa, 16336.15 MPa, 18322.34 MPa, 29190.33 MPa, 32789.09 MPa, 37425.32 MPa. The law of parameter change shows that the damping coefficient η_m decreases first and then increases, and the elastic moduli E_{m1} and E_{m2} both increase, but the growth rate of E_{m1} is far smaller than that of E_{m2}, which is consistent with the change law of the experimental results. The experimental method, experimental data and experimental conclusions are reliable.

Table 3. Conveyor belt model parameters for changing frequency

Serial number	Frequency f [Hz]	Amplitude M [mm]	Initial value x_0 [mm]	Damping coefficient η_m [MPa·s]	Elastic modulus E_{m1} [MPa]	Elastic modulus E_{m2} [MPa]
1	0.02	1.25	1.75	6326.46	1777.00	45124.94
2	0.05	1.25	1.75	6067.00	1758.03	38278.99
3	0.08	1.25	1.75	5810.73	1749.01	23465.56
4	0.10	1.25	1.75	5726.50	1740.69	19332.34
5	0.12	1.25	1.75	5385.27	1721.71	16856.33

The loading frequency expresses a typical change in the load during operation of the conveyor belt. Therefore, the influence of the loading frequency on the conveyor belt needs to be discussed. Here, the loading amplitude is kept constant, and the loading frequency is set to 0.02 Hz, 0.05 Hz, 0.08 Hz and 0.10 Hz. The conveyor belt is loaded at 0.12 Hz, and the identification results are shown in Table 3. It can be concluded that with an increase of the loading frequency, the damping coefficient η_m and elastic moduli E_{m1}, E_{m2} both decrease, and the change rate of E_{m2} is faster and more apparent.

According to the data in Table 3, the relationship between the loading amplitude f and damping coefficient η_m as well as elastic moduli E_{m1}, E_{m2} is fitted to determine the relationship between different amplitudes and the damping coefficient η_m and the elastic moduli E_{m1}, E_{m2}

$$\begin{aligned} \eta_m(f) &= (-8.66f^2 - 7.34f + 6.47) \cdot 10^3 \\ E_{m1}(f) &= (-1.9f^2 - 0.25f + 1.68) \cdot 10^3 \\ E_{m2}(f) &= (1183f^2 - 477.4f + 56.54) \cdot 10^3 \end{aligned} \tag{5.2}$$

In equation (5.2), the fitting coefficients between the three fitting curves and the original data are 0.98, 0.99 and 0.96, respectively. The three curves have a good fitting relationship with the original data and have a high degree of approximation. The needs for forecasting operation of the belt are met.

5.2. Temperature change

Although coal mining is mostly underground, it changes with working conditions and external environmental temperature. The wire rope rubber conveyor belt is used for underground transportation, and the operating temperature is usually not lower than 0°C and not higher than 40°C. Therefore, a loading experiment is conducted every 10°C interval between 0°C and 40°C, and the loading frequency $f = 0.1\,\text{Hz}$, amplitude $M = 1.25\,\text{mm}$ and initial displacement $x_0 = 1.75\,\text{mm}$ are selected to discuss the influence of temperature change on the conveyor belt parameters.

This experiment was conducted with a universal stretching test machine and incubator as shown in Fig. 4. First, the incubator temperature was set to 0°C, after 10 minutes to ensure the accurate temperature, then adjusted to 10°C, kept constant for 10 minutes, and then raised up to 20°C, 30°C and 40°C. The parameter identification results are shown in Table 4. It can be seen that the damping coefficient η_m and the elastic moduli E_{m1} and E_{m2} both decrease with an increase of temperature. The elastic modulus E_{m1} changes once linearly, E_{m2} quadratically. E_{m1} is less affected by temperature than E_{m2}. The damping coefficient η_m is greatly affected by temperature after it exceeds 20°C. Its change is less affected by temperature below 20°C, and the amplitude is small. Combined with the change of the conveyor belt damping coefficient η_m and the elastic moduli E_{m1} and E_{m2} for changing amplitude and frequency, it is known that although the temperature affects the dynamic parameters of the conveyor belt, its influence is smaller than the effect of amplitude and frequency.

Table 4. Conveyor belt parameters for changing temperature

Serial number	Temperature T [°C]	Frequency f [Hz]	Amplitude M [mm]	Initial value x_0 [mm]	Damping coefficient η_m [MPa·s]	Elastic modulus E_{m1} [MPa]	Elastic modulus E_{m2} [MPa]
1	0	0.10	1.25	1.75	5728.97	1743.97	19339.94
2	10	0.10	1.25	1.75	5727.68	1741.89	19336.83
3	20	0.10	1.25	1.75	5727.57	1740.84	19333.57
4	30	0.10	1.25	1.75	5724.48	1740.66	19330.41
5	40	0.10	1.25	1.75	5712.55	1740.62	19327.25

According to the data in Table 4, the relationship between the temperature T and damping coefficient η_m, elastic moduli E_{m1} and E_{m2} is fitted to true relationship between these parameters

$$\begin{aligned} &\eta_m(T) = -0.0009T^3 + 0.03692T^2 - 0.449T + 5729 \\ &E_{m1}(T) = 0.0048T^2 - 0.254T + 1744 \qquad E_{m2}(T) = -0.3189T + 19340 \end{aligned} \tag{5.3}$$

The equation (5.9), the fitting coefficient between the three fitting curves and the original data is 0.98, 0.94 and 0.91, respectively. The three curves have a good fitting relationship with the original data with a high approximation, which fulfills the needs for predicting the operation of the belf property.

6. Conclusions

- The classical solid model and the Kelvin model are used as the theoretical basis for establishing a generalized constitutive dynamical model of a rubber conveyor belt. Displacement and external load curves are obtained by Matlab and Fourier parameter identification and experiments, and the theoretical values are compared with the experimental ones to verify reliability of the method.

- The law of change of the dynamic parameters of the rubber conveyor belt is discussed by controlling the frequency and amplitude of the loading process. When the loading amplitude is kept constant and its frequency increases, the damping coefficient η_m and elastic moduli E_{m1}, E_{m2} both decrease, and changes of E_{m2} are more significant. When the loading frequency is kept constant and the loading amplitude increases, the damping coefficient η_m first decreases and then increases, and the elasticity moduli E_{m1}, E_{m2} both increase, but the increase and growth rate of E_{m1} are much smaller than these of E_{m2}. Next, the influence of temperature changes on the kinetic parameters of the rubber conveyor belt is discussed. Keeping the amplitude and loading frequency unchanged, the damping coefficient η_m and the elastic moduli E_{m1} and E_{m2} both decrease with an increase of temperature. The elastic modulus E_{m1} changes linearly, E_{m2} in a quadratic way, E_{m1} is less affected by temperature than E_{m1}. The damping coefficient η_m is greatly affected by temperature after it exceeds 20°C, and the change is smaller below 20°C, but the amplitude stays small.
- By establishing a mathematical model to analyze the variation law of dynamic parameters of the rubber conveyor belt, vibration and impacts in the actual transportation process of underground industrial production in the coal mine are mainly characterized by the frequency and amplitude of load. This paper discusses the influence of these factors on damping coefficient and elastic modulus. In long-distance transportation of the belt, the load is mainly borne in the steel wire rope. There will appear degumming between the steel wire rope and rubber. When the elastic modulus of rubber and damping coefficient of steel wire are lower, the stiffness of the conveyor belt is worse diminished, and the belt is more prone to deformation, degumming, and its service life is reduced. Therefore, it is necessary to select the most reasonable working frequency and amplitude by comparing and fitting the analytical results with experiments and verifying the reliability of fitting analysis to provide guidance for underground industrial coal minjng.

References

1. Behnke R., Kaliske M., 2015, Thermo-mechanically coupled investigation of steady state rolling tires by numerical simulation and experiment, *International Journal of Non-Linear Mechanics*, **68**, 101-131
2. Chen H.Y., Hu X.B., Zhu H.D., *et al.*, 2020, Analysis of internal stress distribution characteristics of conveyor belt, *Machine Design*, **37**, 4, 55-60
3. Chen H.Y., Wang X., Zhong S., *et al.*, 2015, Hysteresis characteristic analysis of rubber conveyor belt and parameter prediction of restoring force model (in Chinese), *Journal of China Coal Society*, **12**, 40, 2995-3001
4. Chen H.Y., Zhang K., Li E.D., 2017, Parameter identification and variation rule analysis of rubber conveyor belt, *Journal of Vibration and Shock*, **14**, 234-238
5. Cho J.R., Lee H.W., Jeong W.B., Jeong K.M., Kim K.W., 2013, Numerical estimation of rolling resistance and temperature distribution of 3-D periodic patterned tire, *International Journal of Solids and Structures*, **50**, 86-96
6. Gholipour A., Ghayesh M.H., Hussain S., 2020, A continuum viscoelastic model of Timoshenko NSGT nanobeams, *Engineering with Computers*, **38**, 1, 631-646
7. Gil-Negrete N., Viñolas J., Kari L., 2006, A simplified methodology to predict the dynamic stiffness of carbon-black filled rubber isolators using a finite element code, *Journal of Sound and Vibration*, **296**, 757-776
8. Hao H.R., Bai H.B., Hou J.F., 2008, Identification of generalized restoration force model for metal-rubber, *Vibration and Shock*, **27**, 11, 105-110

9. Jonkers C.O., 1999, The indentation rolling resistance of belt conveyors: A theoretical approach, *Fördern und Heben*, **30**, 4, 384-391

10. Liu W.W., Weng X.Q., Zhu S.J., *et al.*, 2010, Research on the optimal inversion method for determining the parameters of the rubber viscoelasticity model, *Vibration and Shock*, **29**, 8, 185-190

11. Lodewijks G., 2013, Determination of rolling resistance of belt conveyors using rubber data: Fact or fiction, *Bulk Solids Handling*, **23**, 6, 384-391

12. Maria H.J., Lyczko N., Nzihou A., Kuruvilla J., Cherian M., Sabu T., 2014, Stress relaxation behavior of organically modified montmorillonite filled natural rubber/nitrile rubber nanocomposites, *Applied Clay Science, Chinese Society of Mechanics*, **87**, 120-128

13. Nguyen T.D., Nguyen T.Q., Nhat T.N., Nguyen-Xuan H., Ngo N.K., 2020, A novel approach based on viscoelastic parameters for bridge health monitoring. A case study of Saigon bridge in Ho Chi Minh City – Vietnam, *Mechanical Systems and Signal Processing*, **141**, 106728

14. Qiu X.J., Chai C., 2011, Estimation of energy loss in conveyor systems due to idler indentation, *Journal of Energy Engineering*, **137**, 36-43

15. Rudolphi T.J., Reicks A.V., 2006, Viscoelastic indentation and resistance to motion of conveyor belts using a generalized Maxwell model of the backing material, *Rubber Chemistry and Technology*, **79**, 2, 307-319

16. Sjöberg M., Kari L., 2002, Nonlinear behavior of a rubber isolator system using fractional derivatives, *Vehicle System Dynamics*, **37**, 3, 217-236

17. Spaans C., 2001, The calculation of main resistance of belt conveyor, *Bulk Solids Handling*, **11**, 4, 809-825

18. Tong X., Xu J., Doghri I., El Ghezal M.I., Krairi A., Chen X., 2020, A nonlinear viscoelastic constitutive model for cyclically loaded solid composite propellant, *International Journal of Solids and Structures*, **198**, 4, 126-135

19. Wang R., Li S.Q., Song S.Y., 2007, Research on basic modeling of vibration isolation rubber, *Vibration and Shock*, **26**, 1, 77-80

20. Yang C.H., Mao J., Li C.L., 2010, Research on indentation resistance of conveyor belt (in Chinese), *Journal of China Coal Society*, **35**, 1, 149-454

21. Zéhil G.-P., Gavin H.P., 2014, Two and three-dimensional boundary element formulations of compressible isotropic, transversely isotropic and orthotropic viscoelastic layers of arbitrary thickness, applied to the rolling resistance of rigid cylinders and spheres, *European Journal of Mechanics A/Solids*, **44**, 175-187

22. Zhang S.R., Xia X.H., 2011, Modeling and energy efficiency optimization of belt conveyors, *Applied Energy*, **88**, 3061-3071

23. Zhu S.Y., Cai C.B., Spanos P.D., 2015, A nonlinear and fractional derivative viscoelastic model for rail pads in the dynamic analysis of coupled vehicle-slab track systems, *Journal of Sound and Vibration*, **335**, 304-320

Manuscript received May 18, 2022; accepted for print December 19, 2022

JOURNAL OF THEORETICAL AND APPLIED MECHANICS
61, 2, pp. 379-393, Warsaw 2023
https://doi.org/10.15632/jtam-pl/163290

APPLICATION OF A RING COUPLED DOUBLE-DUFFING OSCILLATOR TO A SCHEME FOR IDENTIFYING THE COULTER SIGNAL WITH A LOW SNR

Zhijie Zhao, Runcong Liu, Xiaodong Wang

Center of Materials Science and Optoelectronics Engineering, College of Materials Science and Opto-Electronic Technology, University of Chinese Academy of Sciences, Beijing, China

Corresponding author Xiaodong Wang, e-mail: xiaodong.wang@ucas.ac.cn

In order to use chaotic oscillators to identify Coulter signals with a low SNR (SNR$\leqslant 0$), a Gaussian pulse signal is used to simulate the Coulter signal, and we study the continuous synchronous mutation (CSM) phenomenon of a chaotic ring coupled double-Duffing (RCDD) oscillator to identify the signals. The maximum difference between the two state variables in the oscillator can be used to determine the anti-noise ability of the oscillator and construct a function to identify pulse amplitudes. A Simulink model is constructed to verify that the proposed method can be used to identify pulse amplitudes with a low SNR, which provides an approach for developing a technology of measuring Coulter signals with the low SNR.

Keywords: simulated Coulter signal, pulse signal identification, ring coupled double-Duffing oscillator, chaotic-transient synchronous mutation, continuous synchronous mutation

1. Introduction

In 1953, Coulter W.H. proposed the Coulter Principle when he studied the automatic detection technology of blood cells (Coulter, 1953). The Coulter Principle is also known as the Electric Sensing Zone (ESZ) method, which is an electrical method to measure size and quantity of microparticles by detecting pulse signals named Coulter signals. Based on the principle, an instrument named Coulter counter was designed and manufactured. Researchers at McGill University skillfully used the Coulter Principle for reference and proposed to apply it to detect inclusions in a liquid metal. The instrument related to this technology is called Liquid Metal Cleanliness Analyzer (LiMCA) (Doutre, 1984). Because pulse signals measured in the instruments directly reflect the information of microparticles or inclusions, whether the signals can be measured accurately is an important index to evaluate quality of the instruments. In a harsh industrial environment, strong ambient noise would annihilate the pulse signals, which makes the instruments unable to reflect the real information of microparticles or inclusions. Therefore, reducing the interference of strong noise is the key technology to improve accuracy of the instruments.

In order to reduce the interference of strong noise, the previous solutions mainly used high--sensitive electronic components, electromagnetic shielding and grounding (Guthrie and Li, 2001). However, when the pulse signals are annihilated by noise, which means pulse amplitudes are less than the those of the noise, and the signal-to-noise ratio (SNR) of the signals satisfies SNR$\leqslant 0$, modern signal processing technology cannot be used to identify weak signals with a low SNR. Weak signal detection has always been a research focus at home and abroad. Birx and Pipenberg (1992) used a chaotic oscillator to identify weak periodic signal for the first time. Since then, scholars studied the application of nonlinear systems to identify weak signal parameters. Chaotic oscillators had a very broad application in weak signal detection because

of their strong sensitivity to weak signals and good anti-noise capability (Feng *et al.*, 2012; Li H. *et al.*, 2022; Li J. *et al.*, 2014). On the other hand, the signals annihilated by noise can be reconstructed by a stochastic resonance of nonlinear system (Huang *et al.*, 2019). However, the signals detected in these previous studies are periodic signals.

Since Pecora and Carroll (1990) discovered chaotic synchronization, many achievements have been made in nonlinear synchronization (Duane *et al.*, 2017; Fu and Li, 2010; Goldobin and Pikovsky, 2005). Ye *et al.* (2009) studied a nonlinear response of Duffing oscillator to a chaotic sequence, found that the phases of the oscillator were positively correlated with the chaotic sequence. The study successfully detected an aperiodic electroencephalogram signal for the first time. Subsequently, the synchronization phenomenon in coupled oscillators excited by aperiodic signals has become a focus of study (Agrawal *et al.*, 2010; Anishchenko *et al.*, 2008; Baibolatov *et al.*, 2009; Ciszak *et al.*, 2009; Ott *et al.*, 2008). Inspired by the above research, Wu *et al.* (2011) studied the ring coupled Duffing oscillator excited by pulse signals in period-doubling bifurcation. They found that when one of the oscillators was excited by a pulse signal, the trajectory between oscillators changed from a synchronous state to an asynchronous state, and then returned to the synchronous state as the pulse passed. This phenomenon was defined as the transient synchronous mutation (TSM) phenomenon, based on which the existence of pulse signals annihilated by noise can be identified (Wu *et al.*, 2011a,b). These above researches mainly used the synchronous mutation of non-chaotic oscillators to identify aperiodic signals, and only verify the existence of pulse signals with a low SNR. Few research has been made to study the synchronous mutation of chaotic oscillators and their potential to identify the parameters of the signals.

This paper proposes an effective method to identify amplitudes of simulated Coulter signals with a low SNR by using the maximum difference ($\max(x_1 - x_2)$) between the state variables in the ring coupled double-Duffing (RCDD) oscillator with a chaotic state. The Coulter signals are measured by a Coulter counter, and a Gaussian pulse signal is used to simulate the Coulter signal, which is introduced into the RCDD oscillator. The identification function about $\max(x_1 - x_2)$ can be used to identify simulated Coulter signal amplitudes with a low SNR. Furthermore, the Simulink model of the RCDD oscillator is constructed, which verifies that the theoretical results can be applied to develop a technology for measuring Coulter signals with a low SNR, and promote the development of a nonlinear system in a measurement field.

2. Coulter signal and its simulated signal

Figure 1a is a schematic diagram of the Coulter Principle, opening a micropore on the side wall of a test tube, placing a pair of electrodes inside and outside the tube and putting them into a conductive solution. One end of the infusion tube is connected to the closed tube and the other end is connected to a pump to make the solution pass through the micropore. Applying direct current to both electrodes, the ESZ is formed near the micropore. When an insulated microparticle passes through the micropore with the solution, due to the conductivity difference between the microparticle and solution, the voltage between the two electrodes would change to form a pulse signal, which can reflect the size of the microparticle (Coulter, 1953). From Maxwell's equations, the pulse amplitude can be expressed as follows when the particle size is much smaller than the diameter of the micropore

$$\Delta U = \frac{4\rho_e I d^3}{\pi D^4} \tag{2.1}$$

where ρ_e is the resistivity of the conductive solution, d is the nominal size of the microparticle, D is the diameter of the micropore, I is the current through the micropore.

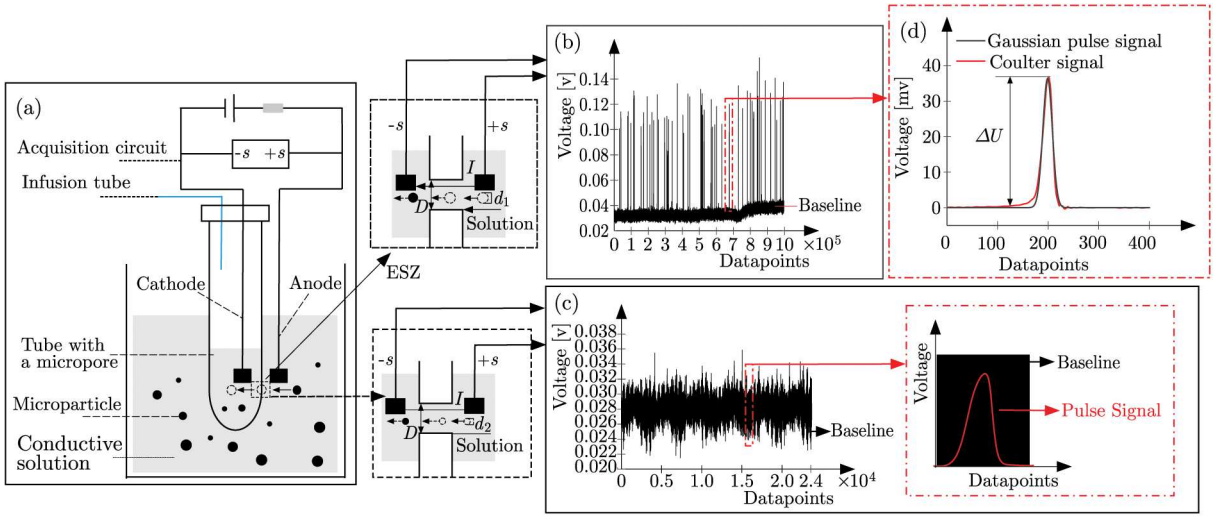

Fig. 1. (a) Schematic diagram of the ESZ method, (b) signals measured in the beaker containing microparticles with nominal size d_1, (c) signals measured in the beaker containing microparticles with nominal size d_2, (d) Gaussian pulse signal with proper parameters can mimic a Coulter signal

In the experiment of this paper, 0.9% saline was placed in two beakers with the same capacity, polystyrene standard particles with nominal sizes d_1 and d_2 were added to the two beakers, respectively, and the sizes of two microparticles met $d_1/D > d_2/D$. The real-time signals in different beakers at a stable speed in the magnetic stirrer were observed online by the Coulter counter respectively, as shown in Fig. 1b and 1c. By analyzing the measurement results, Coulter signals with obvious characteristics could be measured in the beaker containing the microparticles with size d_1. But the signals could not be measured in the beaker containing the microparticles with size d_2, because Coulter signals were annihilated in baseline. In order to improve the accuracy of the Coulter counter, Coulter signals annihilated by noise must be extracted.

In order to use chaotic oscillators to detect Coulter signals annihilated by noise, it is necessary to understand characteristics of the signals generated by microparticles with nominal size d_1. Wavelet denoising and morphological filtering were used to remove the noise in Coulter signals (Jagtiani *et al.*, 2008), and then we used the Gaussian pulse signal to simulate the Coulter signal. The function of the Gaussian pulse signal is $S_c(t) = r\exp\{-[(t-A)/B]2\}$, where r is the Gaussian pulse amplitude, A is the transient time corresponding to the Gaussian pulse peak, and B represents the dispersity of the signal, which determines width of the Gaussian pulse. Given proper values of A and B, a good fitting effect can be obtained, as shown in Fig. 1d. In this paper, white Gaussian noise is used to represent the noise in the measurement process. All the numerical experiments in this paper are prior, which means the parameters of Gaussian pulse signals are known, so as to find a method to identify parameters of pulse signals with a low SNR by using chaotic oscillators.

3. Investigation of parameters in a chaotic RCDD to study synchronous mutation

3.1. Amplitude selection of the driving force

In order to use the anti-noise ability of a chaotic Duffing system to identify amplitudes of simulated Coulter signals with a low SNR, this paper studies the synchronous mutation phenomenon in a chaotic RCDD system. The RCDD system is as follows (Wu *et al.*, 2011b)

$$\begin{aligned}\ddot{x}_1 + \xi\dot{x}_1 - x_1 + x_1^3 - k(x_2 - x_1) &= f\cos(\omega t) + S_c(t) + n(t)\\ \ddot{x}_2 + \xi\dot{x}_2 - x_2 + x_2^3 - k(x_1 - x_2) &= f\cos(\omega t)\end{aligned} \tag{3.1}$$

where ξ is the damping ratio, $f\cos(\omega t)$ is the periodic driving force. $k(x_i - x_j)$, $i \neq j$, $i, j \in \{1, 2\}$ is the coupling coefficient of the linear term between oscillators $(3.1)_{1,2}$, indicating the coupling strength between the two oscillators. $S_c(t)$ is the simulated Coulter signal and $n(t)$ is the white Gaussian noise. It is stated in the paper that when system (3.1) is chaotic, there would be no the TSM phenomenon (Wu *et al.*, 2011b). However, this is not true. In fact, the TSM phenomenon in chaotic oscillators can be controlled by setting proper parameters. We prove that the TSM phenomenon can still be observed in chaotic system (3.1) by setting different parameters in this paper.

In previous studies, when using a chaotic Duffing system to identify weak signal parameters, the damping ratio is generally selected as $\xi = 0.5$. Under different coupling coefficients, the amplitudes of the driving force are adjusted to make system (3.1) chaotic. Without a white Gaussian noise, setting parameters of system (3.1) as $\xi = 0.5$, $k = 0.1$, $\omega = 1$, the parameters of the simulated Coulter signal are $r = 0.25$, $A = 4$, $B = 1$, the calculation time of the numerical experiment is 100 s, the sampling interval is 0.01 s, and the initial value is [1,1,1,1]. The calculating time, sampling interval and initial value of all numerical experiments in this paper are the same, making the bifurcation diagram of system (3.1) changing with f, as shown in Fig. 2.

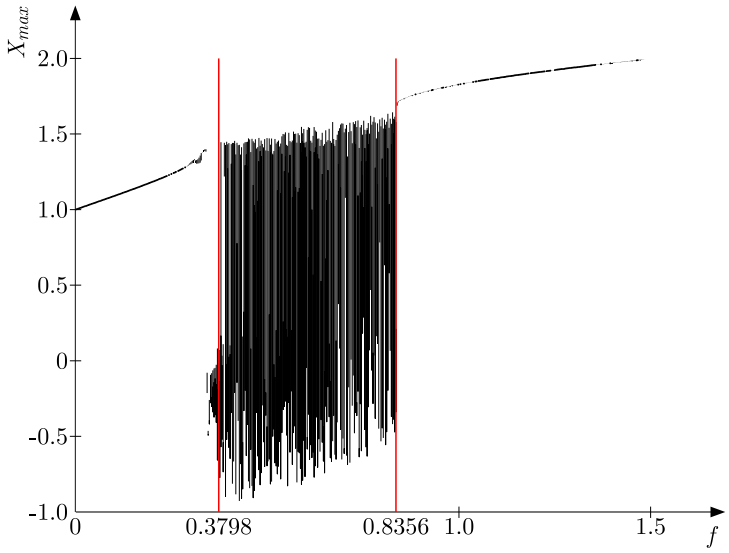

Fig. 2. Bifurcation diagram of system (3.1) via f

From Fig. 2, under a set of parameters, X_{max} label in the horizontal axis represents the maximum value of the phase trajectory of system (3.1) projected on the x-axis. If the phase of system (3.1) is periodic with the set of parameters, the number of X_{max} is finite. However, if the phase of system (3.1) is chaotic with the set of parameters, the number of X_{max} is infinite. Thus, when $k = 0.1$ and $f \in (0.3798, 0.8356)$, phases of system (3.1) are in chaos, as shown in Fig. 2. Then, combining with the controlling parameters of the nonlinear system, setting $k \in [0.1, 1]$ and making different bifurcation diagrams of system (3.1) changing with f, and selecting the intervals of f put system (3.1) in chaos. We find if f always takes a value from $(0.3896, 0.8301)$, system (3.1) is always chaotic. When k satisfies $k \in [0.1, 1]$, setting $f = 0.7 \in (0.3896, 0.8301)$, phases of oscillators $(3.1)_1$ and $(3.1)_2$ are shown in Fig. 3.

Through numerical simulations, when the parameters of system (3.1) satisfy $f = 0.7$ and $k \in [0.1, 1]$, the phases of the two oscillators are in a chaotic state, as shown in Fig. 3. When

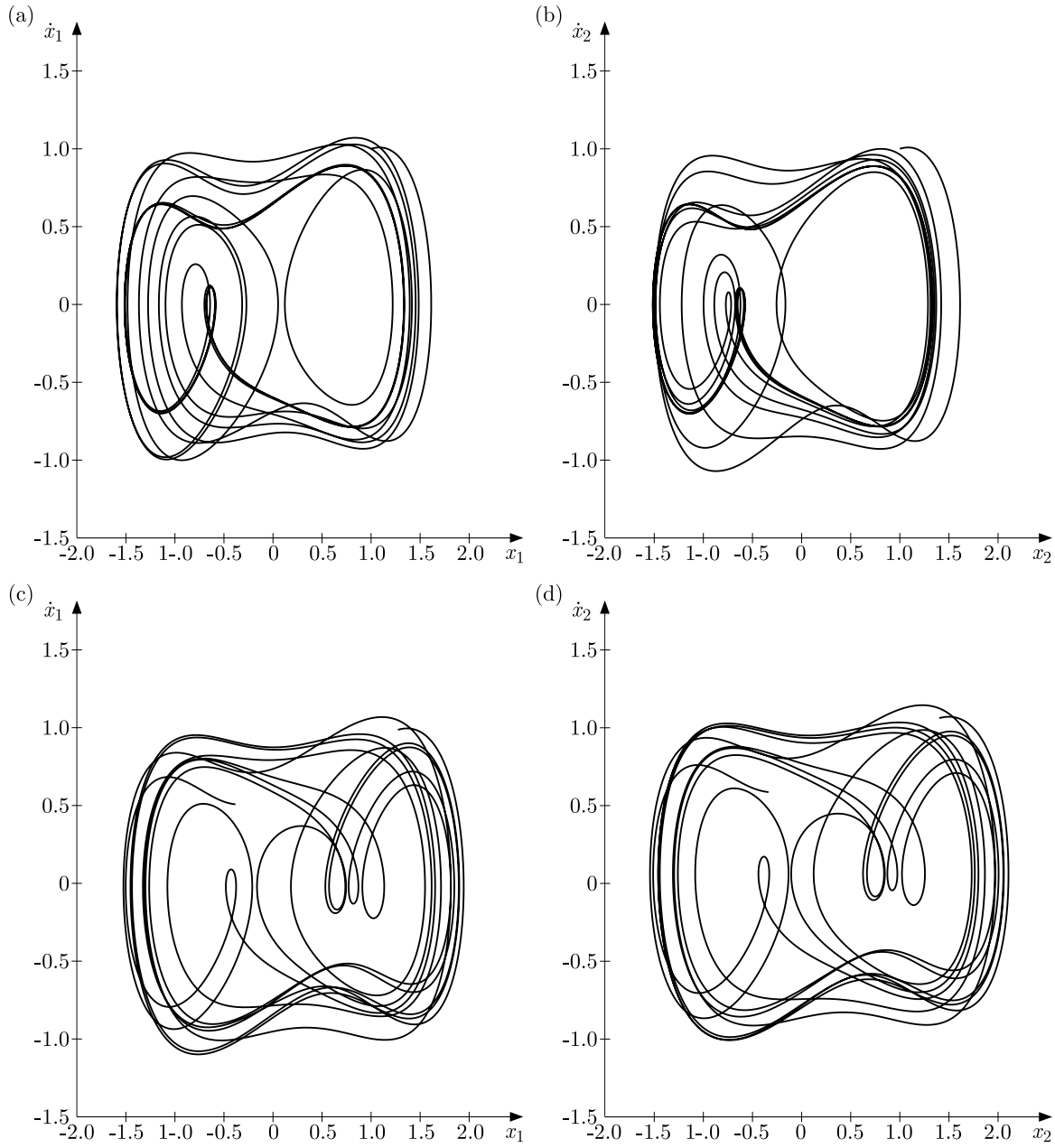

Fig. 3. Phase diagrams of system (3.1) with different values of k: (a) $k = 0.2$ – phase of oscillator $(3.1)_1$, (b) $k = 0.2$ – phase of oscillator $(3.1)_2$, (c) $k = 0.3$ – phase of oscillator $(3.1)_1$, (d) $k = 0.3$ – phase of oscillator $(3.1)_2$

$k = 0.2$, the phases of oscillators $(3.1)_1$ and $(3.1)_2$ are significantly different, so the two oscillators are in an asynchronous state, as shown in Fig. 3a and 3b. In contrast, when $k = 0.3$, the phases of oscillators $(3.1)_1$ and $(3.1)_2$ are only slightly different, which means that the two oscillators are in synchronization, as shown in Fig. 3c and 3d. Therefore, the values of the coupling coefficient determine whether the trajectories of the two oscillators are in synchronization or not.

3.2. Synchronous mutation phenomena with different values of k

Except that different coupling coefficients will affect the synchronization of the two oscillators, the solution interval will also affect the synchronous states (Woafo and Kraenkel, 2002). In this paper, when the interval is 0.01 s, the differences between the two state variables $x_1(t)$

and $x_2(t)$ in chaotic system (3.1) excited by the simulated Coulter signal are made to study the synchronous mutation phenomenon of system (3.1), and the values of k are selected from $[0.1, 1]$ to analyze the influence of different coupling coefficients on the phenomenon, as shown in Fig. 4.

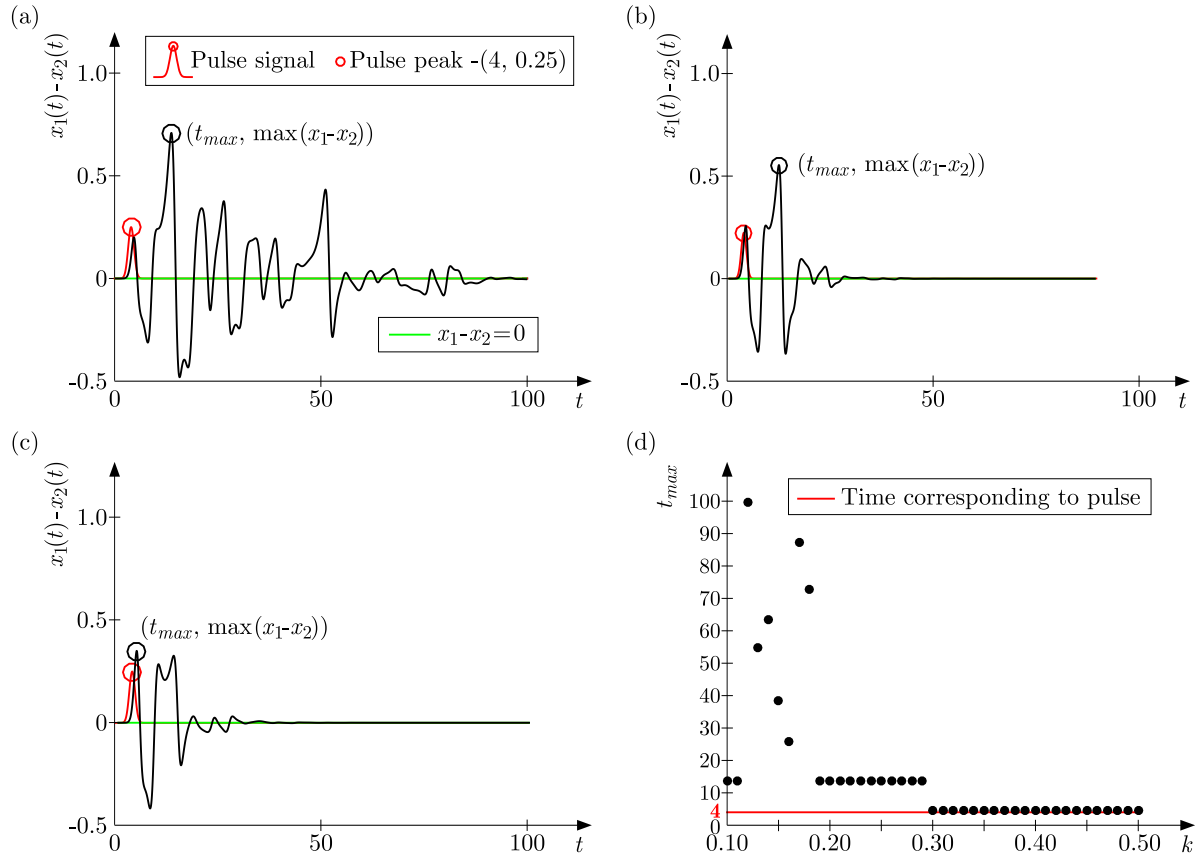

Fig. 4. (a) Synchronous mutation phenomenon with $k \in [0.1, 0.23)$, (b) synchronous mutation phenomenon with $k \in [0.23, 0.3)$, (c) synchronous mutation phenomenon with $k \in [0.3, 1]$, (d) different values of t_{max} with $k \in [0.1, 1]$

Figure 4 shows when k takes different values, the synchronous mutation phenomenon evolves gradually. When k satisfies $k \in [0.1, 0.23)$, the phenomenon persists in system (3.1), which means that the differences between the numerical solution $x_1(t)$ of oscillator $(3.1)_1$ and the numerical solution $x_2(t)$ of oscillator $(3.1)_2$ are not zero even after pulse passing, as shown in Fig. 4a. When k satisfies $k \in [0.23, 1]$, the TSM phenomenon is observed in Fig. 4b and 4c, which is due to the fact that the signal is limited and chaotic oscillators have inherent randomness, so that the two oscillators are synchronous as the signal disappears. When chaotic system (3.1) is excited by the signal and values of k belong to $[0.23, 1]$, the differences would change from a synchronous state to an asynchronous state. As the signal disappears, the differences would change from the asynchronous state to the synchronous state again, and keep staying in that state. This is defined as a chaotic transient synchronous mutation (C-TSM) phenomenon in this paper.

3.3. Reliability analysis of identifying the pulse based on the C-TSM phenomenon

Because values of k play an important role in controlling the synchronous mutation phenomenon in chaotic system (3.1), it is necessary to further analyze which value of k selected from $[0.1, 1]$ is more suitable for identifying simulated Coulter signals. It can be seen from Fig. 4 that there is a maximum value in the differences, which is defined as $\max(x_1 - x_2)$. The time

when $\max(x_1 - x_2)$ appears in Fig. 4 is always near 4 s corresponding to the pulse peak, which is defined as t_{max} . Therefore, it can be considered that $\max(x_1 - x_2)$ is caused by the pulse, and the closer $\max(x_1 - x_2)$ appears to the pulse peak, the higher reliability of $\max(x_1 - x_2)$ caused by the pulse. As shown in Fig. 4d, with an increase of k, values of t_{max} are gradually approaching the time 4 s.

When the coupling coefficient satisfies $k \in [0.3, 1]$, values of t_{max} are closer to 4 s than when the coupling coefficient is within $k \in [0.1, 0.3)$. According to the above parameter analysis, when k belongs to $[0.3, 1]$, the differences in system (3.1) exhibit the C-TSM phenomenon, which indicates that the C-TSM phenomenon is more suitable for identifying the pulses. Finally, the parameters of system (3.1) are determined as follows, the damping ratio is $\xi = 0.5$, the coupling coefficient is $k = 0.3$, and the amplitude of the driving force is $f = 0.7$. The influence of noise on the C-TSM phenomenon in chaotic system (3.1) is analyzed below.

4. Anti-noise ability of the RCDD system

4.1. Synchronization mutation phenomenon with noise

In the measurement experiment, there are various forms of noises in the environment, such as power frequency signals and interference signals similar to white noise, it is then necessary to understand the influence of noise on the C-TSM phenomenon. In this paper, white Gaussian noises with different variances are used to characterize the noise in the experiment, and the influence of the noises with different variances D on the C-TSM phenomenon are explored. Setting the variances as $D \in \{0.001, 0.01, 0.1, 1\}$, under the influences of noises, the differences between the two state variables $x_1(t)$ and $x_2(t)$ in chaotic system (3.1) excited by the simulated Coulter signal or not are made to study the synchronous mutation phenomenon, as shown in Fig. 5. From the noises with different variances and the signal with the same amplitude satisfying $r = 0.25$, we can calculate different values of the SNR.

It can be seen from Fig. 5 that under the influence of the noises, the C-TSM phenomena no longer exist in the differences, but the differences with or without the signal reveal continuous synchronous mutation phenomena, as shown by black solid lines or yellow dotted lines, respectively. The phenomenon is defined as a continuous synchronous mutation (CSM) in this paper, which means that the differences between $x_1(t)$ and $x_2(t)$ are always not zero. According to Fig. 5, there is still $\max(x_1 - x_2)$ in the CSM phenomenon with or without the signal, as shown by black circles or yellow circles, respectively.

Under the influence of noise with the same variance as in Fig. 5, by comparing t_{max} at 4 s as shown by the red circles, if there are no signals, t_{max} is relatively random, as shown by the yellow circles. Otherwise, values of t_{max} are always near the time 4 s, as shown by the black circles. Besides, $\max(x_1 - x_2)$ in the CSM phenomena with the signals is always greater than that without the signals, which means that $\max(x_1 - x_2)$ caused by the noise is not enough to exceed that caused by the signals. Therefore, with the influence of noise and signals, it can be considered that $\max(x_1 - x_2)$ is caused by the signal. Next, for different values of SNR, $\max(x_1 - x_2)$ is selected from the CSM phenomena in system (3.1) with a period-doubling bifurcation state or chaotic state. And the anti-noise ability of system (3.1) in the two states is analyzed.

4.2. Anti-noise ability of the RCDD system in the two states

Previous studies have explored the synchronous mutation phenomenon of system (3.1) in a period-doubling bifurcation. In order to analyze the anti-noise ability of system (3.1) in the period-doubling bifurcation or chaos, values of $\max(x_1 - x_2)$ are used to judge the stability of system (3.1) excited by simulated Coulter signals with and noise. The parameters are set as

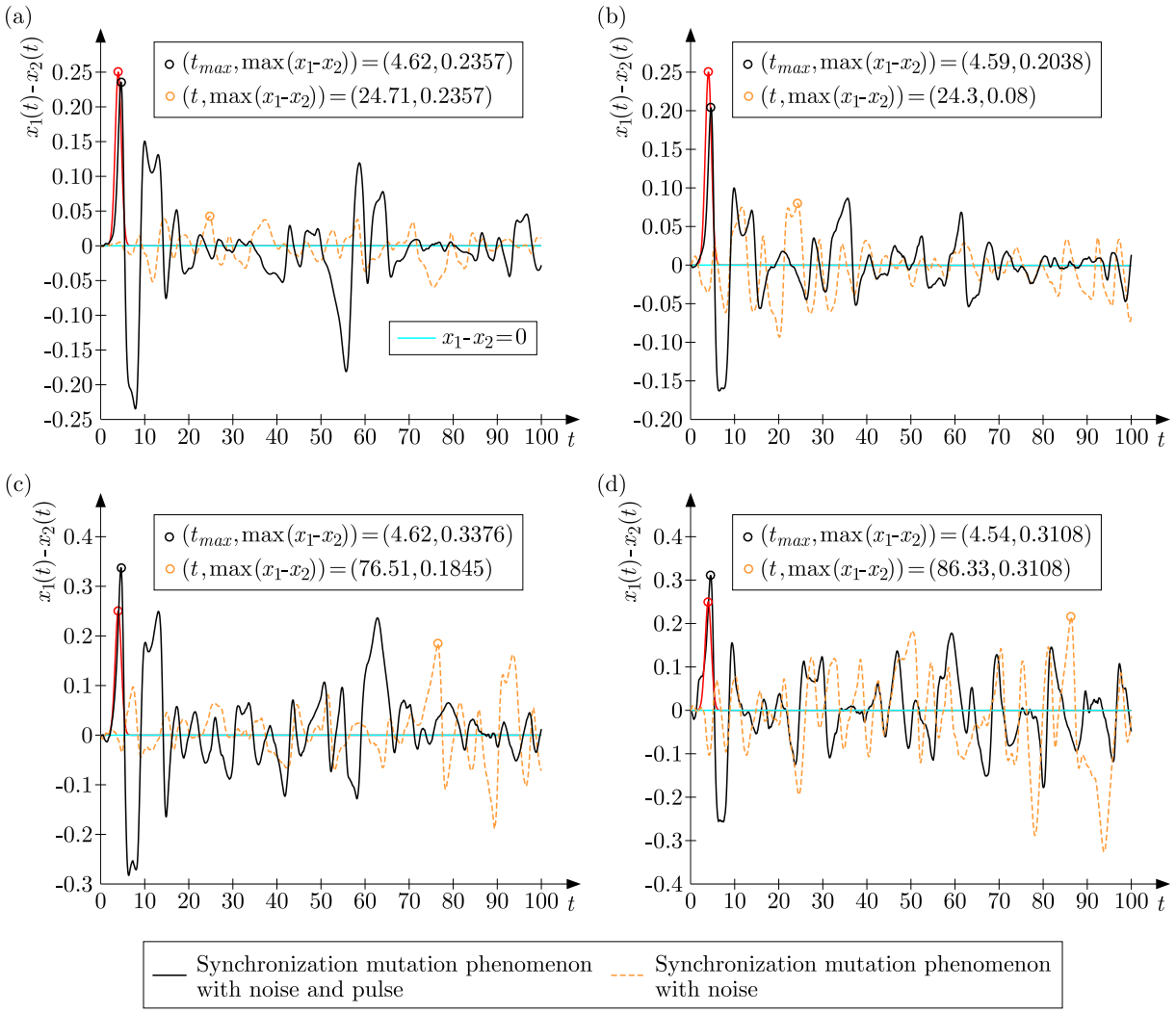

Fig. 5. Influence of noises with different variances, synchronization mutation phenomena in system (3.1) with or without pulse signal: (a) $D = 0.001$, SNR $= 41.4$ dB, (b) $D = 0.01$, SNR $= 18.3$ dB, (c) $D = 0.1$, SNR $= -4.7$ dB, (d) $D = 1$, SNR $= -27.7$ dB

$\xi = 0.35$, $k = 0.1$, $\omega = 1$, $f = 0.22$ according to Wu *et al.* (2011b), then system (3.1) would be in the period-doubling bifurcation. After adding the simulated Coulter signal to system (3.1), the synchronous mutation phenomenon with or without noise is shown in Fig. 6.

Without the noise, $\max(x_1 - x_2)$ is selected in the TSM phenomenon from Fig. 6a, which is redefined as $\max_{\mathrm{PDB-TSM}} = 2.2459$. With the noise, system (3.1) has the CSM phenomenon as shown in Fig. 6b. From Fig. 4c, $\max(x_1 - x_2)$ is selected from the TSM phenomenon of chaotic system (3.1) without the noise, which is redefined as $\max_{\mathrm{C-TSM}} = 0.19$.

When white Gaussian noises with different variances within $D \in \{0.001, 0.01, 0.1, 1\}$ and the signal are added to system (3.1), values of $\max(x_1 - x_2)$ appearing at around 4 s are selected from the CSM phenomena in system (3.1) with the period-doubling bifurcation or chaos, which is redefined as $\max_{\mathrm{PDB-CSM}}$ or $\max_{\mathrm{C-CSM}}$, respectively. Due to randomness of noise, the number of simulations for each variance is 100, and values of $\max_{\mathrm{PDB-CSM}}$ or $\max_{\mathrm{C-CSM}}$ selected each time are different. The anti-noise ability of system (3.1) in the period-doubling bifurcation or chaos is analyzed by changes of $\max_{\mathrm{PDB-CSM}}$ ($\max_{\mathrm{C-CSM}}$) compared with $\max_{\mathrm{PDB-TSM}}$ ($\max_{\mathrm{C-TSM}}$), as shown in Fig. 7.

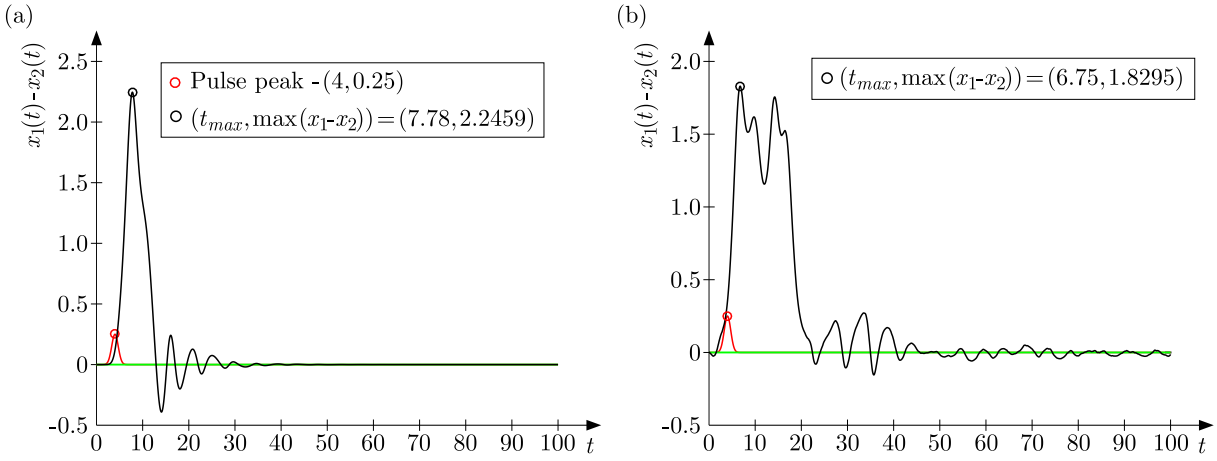

Fig. 6. Synchronous mutation phenomenon of system (3.1) in the period-doubling bifurcation: (a) without noise, (b) with noise

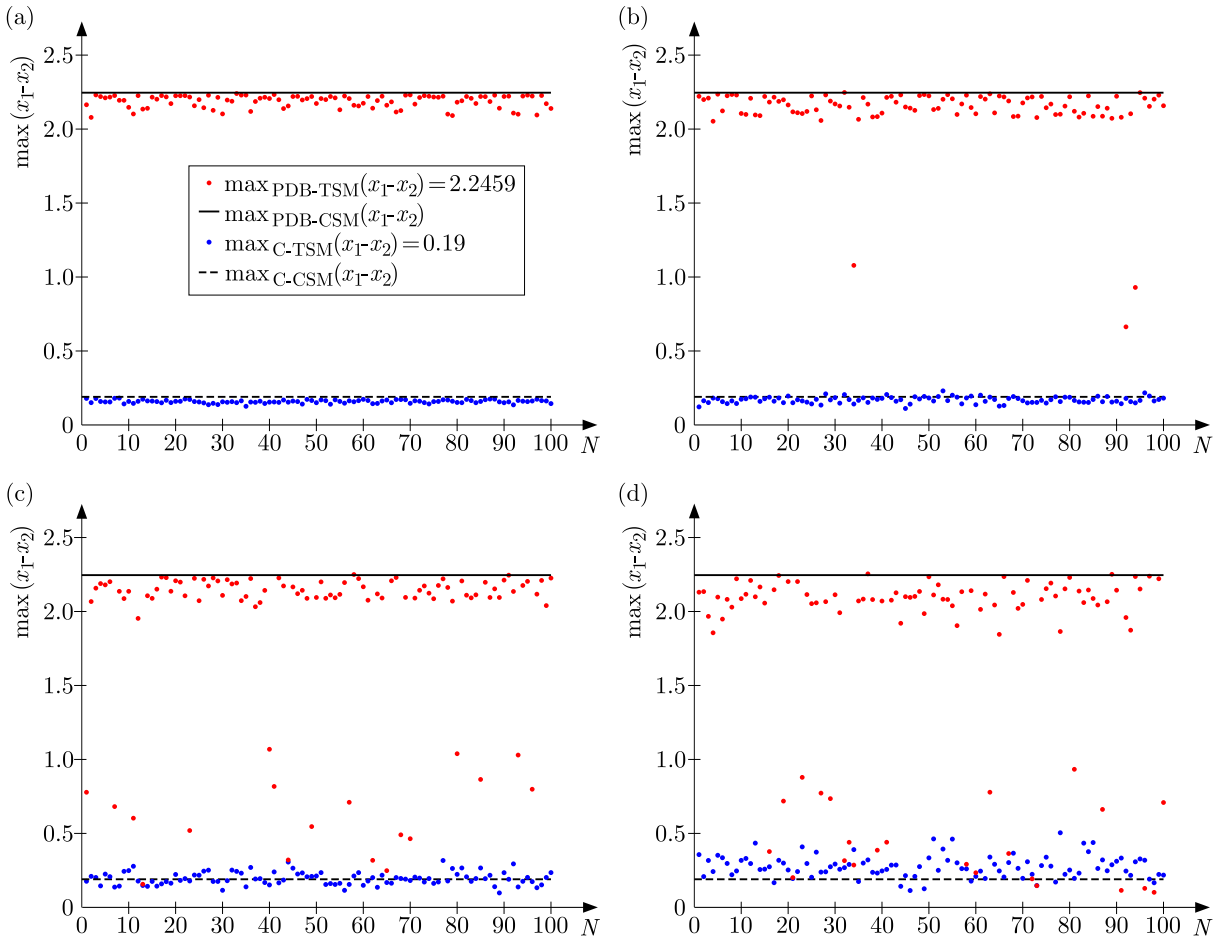

Fig. 7. Influence of noises with different variances and the signal, changes of $\max_{\text{PDB}-\text{CSM}}$ ($\max_{\text{C}-\text{CSM}}$) compared with $\max_{\text{PDB}-\text{TSM}}$ ($\max_{\text{C}-\text{TSM}}$): (a) $D = 0.001$, SNR $= 41.4$ dB, (b) $D = 0.01$, SNR $= 18.3$ dB, (c) $D = 0.1$, SNR $= -4.7$ dB, (d) $D = 1$, SNR $= -27.7$ dB

It can be seen from Fig. 7 that $\max_{\text{PDB}-\text{CSM}}$ or $\max_{\text{C}-\text{CSM}}$ would change compared with $\max_{\text{PDB}-\text{TSM}}$ or $\max_{\text{C}-\text{TSM}}$, which reflects the influence of noise on the stability of system (3.1). It can be seen from Fig. 7a and 7b that after being excited by the signal with a high SNR (SNR $>$ 0 dB), $\max_{\text{PDB}-\text{CSM}}$ ($\max_{\text{C}-\text{CSM}}$) slightly change compared with $\max_{\text{PDB}-\text{TSM}}$

($\max_{\mathrm{C-TSM}}$), which shows that noise has little influence on the solutions of system (3.1) in the period-doubling bifurcation or chaos. As can be seen from Fig. 7c and 7d, after being excited by the signal with a low SNR, the changes of $\max_{\mathrm{C-CSM}}$ compared with $\max_{\mathrm{C-TSM}}$ are smaller than those of $\max_{\mathrm{PDB-CSM}}$ compared with $\max_{\mathrm{PDB-TSM}}$, which means that the solutions of chaotic system (3.1) are more stable than those of system (3.1) with the period-doubling bifurcation. Therefore, $\max_{\mathrm{C-CSM}}$ can be better used to identify the simulated Coulter signals with a low SNR.

5. Identification of the pulse amplitude with a low SNR by using $\max(x_1 - x_2)$

Based on the above analysis, this paper uses $\max_{\mathrm{C-TSM}}$ to identify amplitudes of the simulated Coulter signals with a low SNR. For convenience, $\max_{\mathrm{C-TSM}}$ would be redefined as $\max(x_1 - x_2)$ in the rest of this paper. The signal amplitude is selected from $[0.01, 1]$, variance of noise set as $D = 1$ to make the SNR of the signal satisfy $\mathrm{SNR} \leqslant 0\,\mathrm{dB}$, and values of $\max(x_1 - x_2)$ are selected from the CSM phenomena. Repeatedly setting signal amplitudes to obtain a large number of simulation data about $\max(x_1 - x_2)$, let $\max(x_1 - x_2)$ be an independent variable and the stated signal amplitude be a dependent one. The relationships between $\max(x_1 - x_2)$ and the stated amplitude are constructed by using different combinations of elementary functions and curve-fitting programs. Through a great deal of numerical simulations, the best relationship for identifying the amplitude is a polynomial function, as shown in equation (5.1), where $\widetilde{r}$ is the identified amplitude

$$\widetilde{r} = a_n \max(x_1 - x_2)^n + a_{n-1} \max(x_1 - x_2)^{n-1} + \cdots + a_1 \max(x_1 - x_2) + a_0 \tag{5.1}$$

We find that with an increase of the polynomial order, the identified amplitudes are closer to the stated pulse amplitudes. In this paper, a 6-degree polynomial function is used as the identification function to obtain amplitudes as shown in equation (5.2). The relationship between the simulation data and the identification function, and the errors between the stated amplitudes and identified amplitudes are shown in Fig. 8a and 8b, respectively

$$\begin{aligned}\widetilde{r} = {} & 0.1114 \max(x_1 - x_2)^6 - 2.6881 \max(x_1 - x_2)^5 + 9.9167 \max(x_1 - x_2)^4 \\ & - 14.5506 \max(x_1 - x_2)^3 + 9.0598 \max(x_1 - x_2)^2 - 1.0521 \max(x_1 - x_2) + 0.0987\end{aligned} \tag{5.2}$$

The errors between the identified amplitudes and stated amplitudes can not be obtained from Fig. 8a. Therefore, the proportion of the number of identified amplitudes within the allowable error in the total number of identified amplitudes is used to estimate the probability of equation (5.2) describing how effectively the amplitudes can be identified, see Fig. 8b. The simulation results show that when the allowable error is 15%, the probability of equation (5.2) to identify amplitudes is only $\sim 48\%$, which is due to large errors when identifying the amplitudes with a low SNR. Under the influence of noise with variance $D = 1$, different stated amplitudes are set to obtain different values of the SNR and identification functions. When the allowable error is 15%, the probabilities that the functions can effectively identify the amplitudes are obtained with different values of the SNR, as shown in Table 1.

It can be seen from Table 1 that when the allowable error is 15%, as the interval of the stated amplitude or SNR shrinks, the probability of identification functions to identify amplitudes increases. If the interval of the stated amplitude is within $[0.5, 1]$, the probability can be improved to 80%, and the identification function is constructed as shown in equation (5.3), which can be used with the lowest SNR at about $-13.86\,\mathrm{dB}$

$$\begin{aligned}\widetilde{r} = {} & -22.7025 \max(x_1 - x_2)^6 + 106.7767 \max(x_1 - x_2)^5 - 197.5111 \max(x_1 - x_2)^4 \\ & + 181.2927 \max(x_1 - x_2)^3 - 85.5568 \max(x_1 - x_2)^2 + 19.7986 \max(x_1 - x_2) - 1.215\end{aligned} \tag{5.3}$$

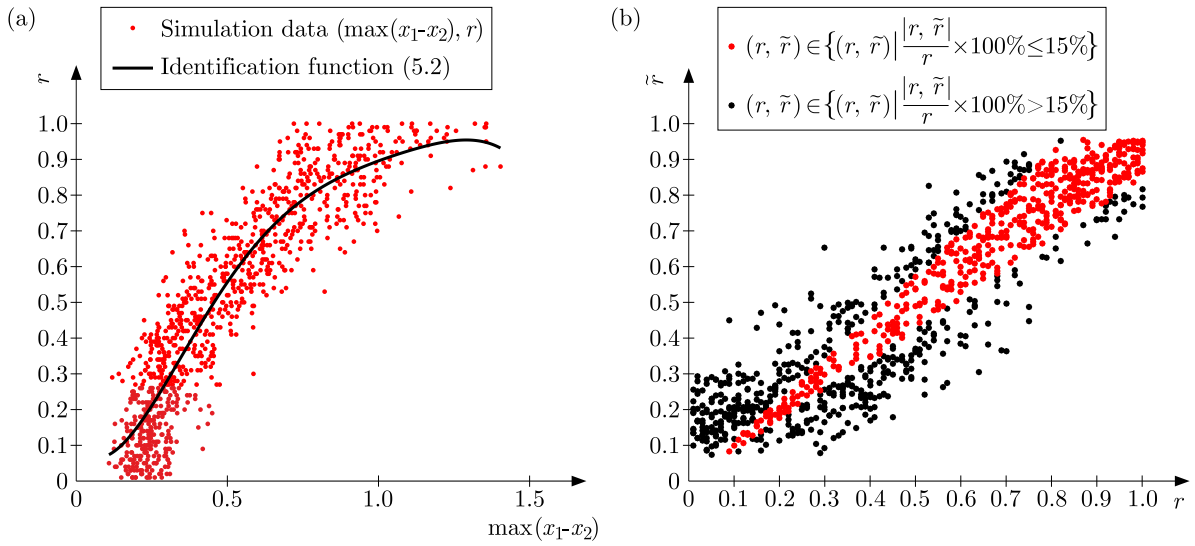

Fig. 8. (a) Simulation data and identification function (5.2), (b) errors between identified amplitudes and stated amplitudes

Table 1. Probability of different identification functions to identify amplitudes with different stated amplitudes or values of SNR

Interval of stated amplitude or SNR	Total number of identified amplitudes	Number of identified amplitudes satisfied $\lvert r-\tilde{r}\rvert/r \leqslant 15\%$	Probability
$[0.01, 1]/[-92.1\,\mathrm{dB}, 0\,\mathrm{dB}]$	1000	482	48.2%
$[0.1, 1]/[-46.05\,\mathrm{dB}, 0\,\mathrm{dB}]$	910	479	52.64%
$[0.2, 1]/[-32.19\,\mathrm{dB}, 0\,\mathrm{dB}]$	810	483	59.63%
$[0.3, 1]/[-24.08\,\mathrm{dB}, 0\,\mathrm{dB}]$	710	491	69.15%
$[0.4, 1]/[-18.33\,\mathrm{dB}, 0\,\mathrm{dB}]$	610	456	74.75%
$[0.5, 1]/[-13.86\,\mathrm{dB}, 0\,\mathrm{dB}]$	510	406	79.61%
$[0.6, 1]/[-10.22\,\mathrm{dB}, 0\,\mathrm{dB}]$	410	343	83.66%
$[0.7, 1]/[-7.13\,\mathrm{dB}, 0\,\mathrm{dB}]$	310	276	89.03%
$[0.8, 1]/[-4.46\,\mathrm{dB}, 0\,\mathrm{dB}]$	210	208	99.05%
$[0.9, 1]/[-2.11\,\mathrm{dB}, 0\,\mathrm{dB}]$	110	110	100%

6. Simulink model of the RCDD system

In order to verify if $\max(x_1 - x_2)$ selected from the CSM phenomenon can be used to identify amplitudes of simulated Coulter signals with a low SNR, a Simulink model of system (3.1) has been designed in Matlab. Rewriting system (3.1), one obtains

$$\begin{aligned} \dot{x}_1 &= y_1 \qquad & \dot{y}_1 &= -\xi y_1 + x_1 - x_1^3 + k(x_2 - x_1) + f\cos(\omega t) + \widetilde{s}_c(t) + \sqrt{D}\widetilde{n}(t) \\ \dot{x}_2 &= y_2 \qquad & \dot{y}_2 &= -\xi y_2 + x_2 - x_2^3 + k(x_1 - x_2) + f\cos(\omega t) \end{aligned} \tag{6.1}$$

The parameters in system (6.1) are $\xi = 0.5$, $\omega = 1$ and $f = 0.7$, respectively, and the coupling coefficient is still selected from the interval $[0.1, 1]$, which is taken as $k = 0.9$. $\widetilde{s}_c(t)$ and $\widetilde{n}(t)$ in system (6.1) represent the simulated Coulter signal and noise respectively, and the parameters of the signal are $r = 0.5$, $A = 4$ and $B = 1$. System (6.1) is constructed by using a Matlab/Simulink module, as shown in Fig. 9.

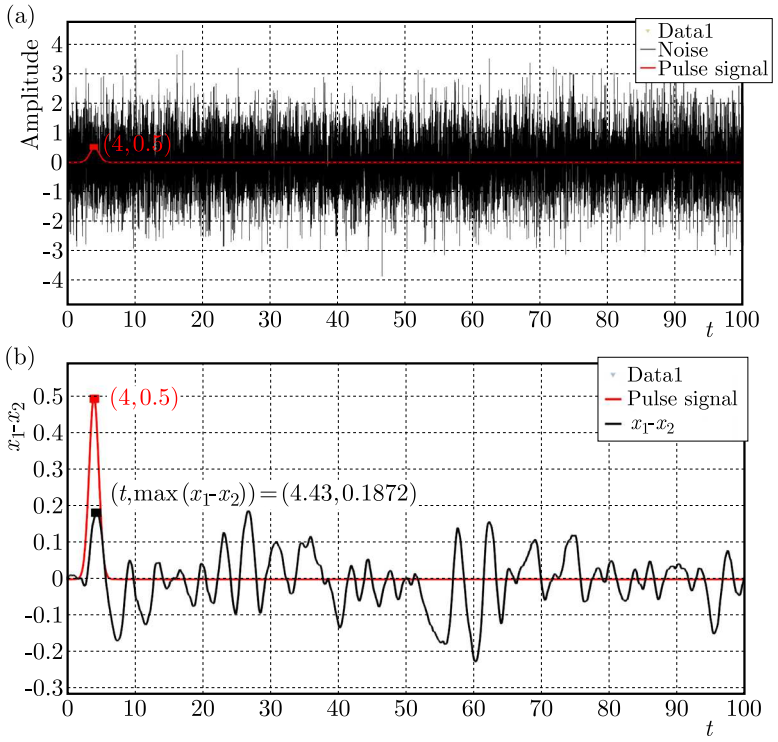

Fig. 9. Simulink model of system (6.1)

In the simulation model, Sine Waves 1 and 2 represent the driving force in system (6.1). Random Number represents the noise $\widetilde{n}(t)$. The module constructed by the Clock and Interpreted MATLAB functions represents the simulated Coulter signal. Gains 1 and 3 represent coupling coefficients k, and Gains 2 and 4 represent damping ratios ξ. The definitions of other modules can be found in Matlab/Simulink. The simulation time and sampling interval of the model are 100 s and 0.01 s, respectively, which are the same as the calculation time and sampling interval of the previous numerical simulations. Firstly, parameters of each module in the model are set according to the parameters of system (6.1), and the Random Number module is closed to verify whether the state and the synchronous mutation phenomenon in the model are consistent with the above simulation results of system (3.1) without the noise. From the output results of the modules XY graph1 and Scope, the phase of oscillator $(6.1)_1$ and the differences between the two state variables x_1 and x_2 are observed respectively, as shown in Fig. 10.

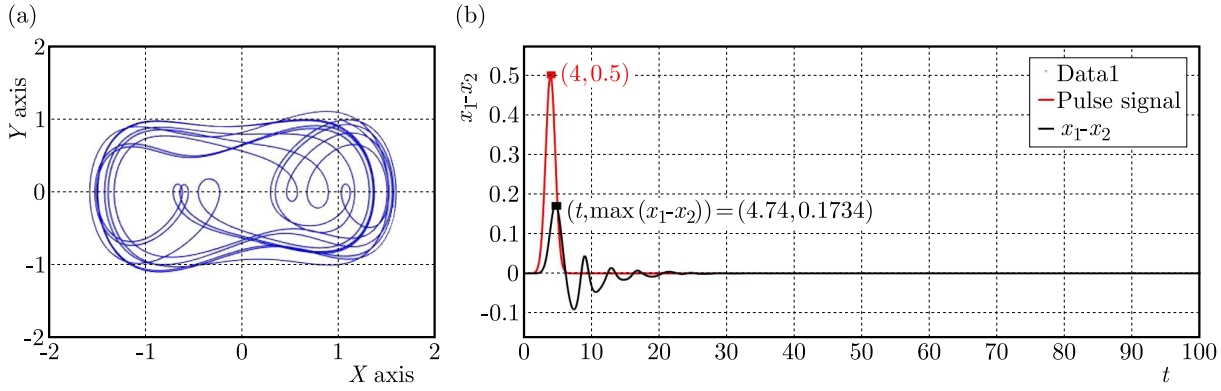

Fig. 10. (a) Phase of oscillators $(6.1)_1$ from XY graph1, (b) C-TSM phenomenon from Scope

It can be seen from Figs. 3 and 10 that phases of oscillators $(3.1)_1$ and $(6.1)_1$ are both in the chaotic state, and both differences in systems (3.1) and (6.1) reveal the C-TSM phenomena. t_{max} (4.74 s) is close to 4 s corresponding to the pulse peak, which shows that $\max(x_1 - x_2)$ in the C-TSM phenomenon of system (6.1) is caused by the pulse. Secondly, the parameters of the Random Number module as Mean = 0, Variance = 1 are set to generate the noise. The signal composed of the pulse and noise is observed by module Scope1, and its SNR is −13.86 dB, as shown in Fig. 11.

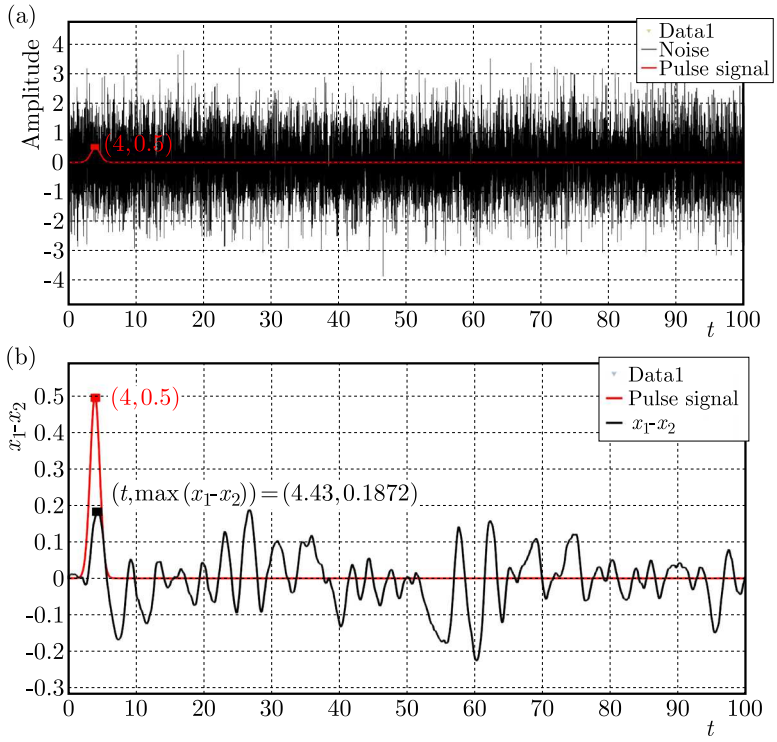

Fig. 11. (a) The signal composed of the pulse and noise from Scope1, (b) CSM phenomenon from Scope

As shown in Fig. 11a, the pulse has been annihilated by the noise. Scope is used to observe the synchronous mutation phenomenon in system (6.1) and to extract $\max(x_1 - x_2)$, as shown in Fig. 11b. Under the influence of noise, the differences have the CSM phenomenon in system (6.1), and t_{max} (4.43 s) is close to 4 s. The value of $\max(x_1 - x_2)$ selected from Fig. 11b is 0.1872 is substituted into equation (5.3) to obtain the identified amplitude $\widetilde{r} = 0.4634$. The relative error between the identified and stated amplitude is $|\widetilde{r} - r|/r \cdot 100\% = |0.4634 - 0.5|/0.5 \cdot 100\% \approx 7.3\%$. From the simulation results, it is verified that $\max(x_1 - x_2)$ in the CSM phenomenon can be used to identify the amplitude of the simulated Coulter signal with a low SNR. Meanwhile, Simulink model of system (6.1) lays the foundation for building of an electronic circuit of the RCDD system. However, parameters (e.g. amplitude and width) of Coulter signals represent physical processes and are unknown. The next study would build the electronic circuit of the RCDD system applyied to carry out a measurement experiment for detecting Coulter signals with a low SNR.

7. Conclusions

In order to use chaotic oscillators to identify amplitudes of Coulter signals with a low SNR (SNR$\leqslant$ 0), a Gaussian pulse signal is used to simulate the Coulter signal, and the synchronous mutation phenomenon of the chaotic ring coupled double-Duffing (RCDD) oscillator is studied. It is found that if the coupling coefficient is $k \geqslant 0.23$, there will appear a chaotic-transient

synchronous mutation (C-TSM) phenomenon in the oscillator excited by the simulated Coulter signal. Moreover, the maximum difference ($\max(x_1 - x_2)$) in the C-TSM phenomenon is caused by the signal. After being excited by a signal and white Gaussian noise, a continuous synchronous mutation (CSM) phenomenon occurs in the oscillator, and $\max(x_1 - x_2)$ is still caused by the signal. Under different values of SNR, $\max(x_1 - x_2)$ is selected from the CSM phenomena of the oscillator in the period-doubling bifurcation or chaos respectively, and the changes of $\max(x_1 - x_2)$ are analyzed to explore better anti-noise ability of the chaotic oscillator for a low SNR. Subsequently, $\max(x_1 - x_2)$ is used as an independent variable to construct a function to identify the simulated Coulter signal amplitude with a low SNR. The proportion of the number of identified amplitudes within the allowable error in the total number of identified amplitudes is used to estimate the probability that the function can effectively identify the amplitudes, and the lowest SNR for identification by making use of this function is -13.68 dB. A simulink model of the oscillator is constructed to verify that the values of $\max(x_1 - x_2)$ in the CSM phenomenon can be used to identify amplitudes of simulated Coulter signals with a low SNR, and it lays the foundation for study of the electronic circuit of the oscillator. The results in this paper show that the CSM phenomenon in the RCDD oscillator can be used to develop a technology for measuring Coulter signals with a low SNR.

Acknowledgements

This study was financially supported by the Beijing City Science and Technology Bureau; The Huairou Science City Achievements Implementation Special Project (Grant No. Z201100008420010); The Science and Technology Innovation Fund of Weiqiao-UCAS (Grant No. 20D101652DY) and the 'Double First-Class' Construction Fund (Grant No. 111800XX62) which greatly acknowledged.

References

1. Agrawal M., Prasad A., Ramaswamy R., 2010, Quasiperiodic forcing of coupled chaotic systems, *Physical Review E*, **81**, 2, 026202
2. Anishchenko V., Nikolaev S., Kurths J., 2008, Bifurcational mechanisms of synchronization of a resonant limit cycle on a two-dimensional torus, *Chaos: An Interdisciplinary Journal of Nonlinear Science*, **18**, 3, 037123
3. Baibolatov Y., Rosenblum M., Zhanabaev Z.Z., Kyzgarina M., Pikovsky A., 2009, Periodically forced ensemble of nonlinearly coupled oscillators: From partial to full synchrony, *Physical Review E*, **80**, 4, 046211
4. Birx D.L., Pipenberg S.J., 1992, Chaotic oscillators and complex mapping feed forward networks (CMFFNS) for signal detection in noisy environments, *Proceedings of the International Joint Conference on Neural Networks (IJCNN)*
5. Ciszak M., Montina A., Arecchi T., 2009, Control of transient synchronization with external stimuli, *Chaos: An Interdisciplinary Journal of Nonlinear Science*, **19**, 1, 015104
6. Coulter W.H., 1953, *Means for Counting Particles Suspended in a Fluid*, U.S. Patent 2,656,508
7. Doutre D., 1984, The development and application of a rapid method of evaluating molten metal cleanliness, Ph.D.Thesis, McGill University, Montreal
8. Duane G.S., Grabow C., Selten F., Ghil M., 2017, Introduction to focus issue: Synchronization in large networks and continuous media – Data, models, and supermodels, *Chaos: An Interdisciplinary Journal of Nonlinear Science*, **27**, 126601
9. Feng J., Zhang Q., Wang W., 2012, Chaos of several typical asymmetric systems, *Chaos, Solitons and Fractals*, **45**, 7, 950-958
10. Fu G.-Y., Li Z.-S., 2010, Adaptive synchronization of a hyperchaotic Lü system based on extended passive control, *Chinese Physics B*, **19**, 6, 060505

11. Goldobin D.S., Pikovsky A., 2005, Synchronization and desynchronization of self-sustained oscillators by common noise, *Physical Review E*, **71**, 4, 045201

12. Guthrie R.I.L., Li M., 2001, In situ detection of inclusions in liquid metals: Part II. Metallurgical applications of LiMCA systems. *Metallurgical and Materials Transactions B*, **32**, 6, 1081-1093

13. Huang D., Yang J., Zhou D., Sanjuán M.A.F., Liu H., 2019, Recovering an unknown signal completely submerged in strong noise by a new stochastic resonance method, *Communications in Nonlinear Science and Numerical Simulation*, **66**, 156-166

14. Jagtiani A., Sawant R., Carletta J., Zhe J., 2008, Wavelet transform-based methods for denoising of Coulter counter signals, *Measurement Science and Technology*, **19**, 6, 065102

15. Li H., Tian R., Xue Q., Zhang Y., Zhang X., 2022, Improved variable scale-convex-peak method for weak signal detection, *Chaos Solitons and Fractals*, **156**, 111852

16. Li J., Zhang L., Wang D., 2014, Unique normal form of a class of 3 dimensional vector fields with symmetries, *Journal of Differential Equations*, **257**, 7, 2341-2359

17. Ott E., Platig J.H., Antonsen T.M., Girvan M., 2008, Echo phenomena in large systems of coupled oscillators, *Chaos: An Interdisciplinary Journal of Nonlinear Science*, **18**, 3, 037115

18. Pecora L.M., Carroll T.L., 1990, Synchronization in chaotic systems, *Physical Review Letters*, **64**, 8, 821-824

19. Woafo P., Kraenkel R.A., 2002, Synchronization: Stability and duration time, *Physical Review E*, **65**, 3, 036225

20. Wu Y., Zhang S., Sun J., Rolfe P., 2011a, Abrupt change of synchronization of ring coupled Duffing oscillator, *Acta Physica Sinica – Chinese Edition*, **60**, 2

21. Wu Y., Zhang S., Sun J., Rolfe P., Li Z., 2011b, Transient synchronization mutation of ring coupled Duffing oscillators driven by pulse signal, *Acta Physica Sinica – Chinese Edition*, **60**, 10, 100509-100501

22. Ye Y., Yue L., Mandic D., Bao-Jun Y., 2009, Regular nonlinear response of the driven Duffing oscillator to chaotic time series, *Chinese Physics B*, **18**, 3, 958-968

Manuscript received December 20, 2022; accepted for print January 12, 2023

JOURNAL OF THEORETICAL AND APPLIED MECHANICS
61, 2, pp.395-406, Warsaw 2023
https://doi.org/10.15632/jtam-pl/161686

A FULLY-COUPLED THREE-DIMENSIONAL FLUID-STRUCTURE INTERACTION STUDY ON THE EXTERNALLY-PRESSURIZED COLLAPSIBLE TUBE AND THE INTERNAL FLOW

Sen Zhang

Department of Mechanics and Engineering Science, College of Engineering, Peking University, Beijing, China; and Beijing Internet Based Engineering Co., Ltd, Beijing, China

e-mail: tjuzhangsen@163.com

HaoFei Liu

Department of Mechanics, Tianjin University, Tianjin, China

e-mail: hfliu@tju.edu.cn

We study the behavior of a collapsible tube conveying a fluid subject to external pressure that could occur in many physiological applications. The method of rotating spines is developed to enable an automatic mesh adaptation when the tube is deformed largely. We examine bifurcation diagrams when the tube is collapsed under a pressure driven condition and reveal that multiple solutions exist for a range of the Reynolds number. The stability characteristic of the system is discovered by determining stability of these solutions by the eigenvalue method for the first time, which is validated by solving a time-dependent problem of the system.

Keywords: fluid structure interaction, stability, eigenvalue problem, bifurcation

1. Introduction

The flow in collapsible tubes has been widely studied for its numerous applications to physiology and medical devices in the last few decades. An intriguing feature of this system is the flow-induced self-excited oscillation. Physiological examples include respiratory wheezes during forced expiration, cervical venous hum arising through oscillations of the external jugular vein, generation of snoring noises, the Korotkoff sounds heard when the blood pressure is measured by applying an external force on an artery. We refer readers to (Heil and Jensen, 2003; Grotberg and Jensen, 2004) for a more detailed discussion of physiological applications of collapsible tube flows.

Self-excited oscillations are frequently observed in a laboratory in the "Starling resistor". Early experiments on collapsible tubes tended to investigate classification of different oscillations, influence of different system parameters on the oscillation and analyzed pressure, flow rate and tube cross-sectional area time records in many test cases (Bertram, 2003). However, flow characteristics within the tube when it is in a state of self-oscillation are lacking. This is because invasive experimental techniques measuring pressure and velocity have a great effect on the flow field. Much recent experimental work has concentrated on visualization of the flow fields using high speed particle image velocimetry. The time-varying flow field just downstream of an oscillating collapsible tube was measured by Bertram *et al.* (2008). Truong and Bertram (2009) measured the flow-field immediately downstream of a collapsible tube during oscillation onset starting from the collapsed state and identified the areas of the flow where oscillation initially occurred. The velocity fields in the flexible tube when it is on the verge of the self-oscillation state and is in the state of periodic self-oscillation has been measured (Yiasemides *et al.*, 2017).

To understand the mechanisms of self-excited oscillations of the system observed, many researchers use a two-dimensional channel in which a part of one of the sidewalls is replaced by a pre-stressed elastic membrane or a tube. When the prestress is small, the viscous pressure drop along the channel induces large-amplitude and low-frequency self-excited oscillations. Luo *et al.* (2008) analyzed the system linear stability in the absence of prestress and discovered a "cascade" stability structure for the flow-driven boundary condition (the fluid velocity is imposed at the inlet). Liu *et al.* (2012) found different oscillation modes when the system was pressure-driven (the fluid press was imposed at the inlet). Jensen and Heil (2003) employed asymptotic techniques to derive explicit predictions for stability boundaries for small-amplitude, high-frequency, self-excited oscillations in the limit of large membrane tension and identified a simple sloshing mechanism for self-excited oscillations. In three dimensions, Heil and Boyle (2010) found the sloshing mechanism which explained the development of self-excited oscillation in initially axisymmetric (or weakly buckled) three-dimensional collapsible tubes. Zhang *et al.* (2018) examined bifurcation diagrams for different collapse models in the velocity driven condition and revealed that multiple solutions exist in some range of the Reynolds number. Although Whittaker *et al.* (2010) predicted the onset of high-frequency self-excited oscillations by considering energy budget of the system, and analyzed stability of the system by direct numerical simulation which had not been done before.

In this paper, we investigate a flow-tube system in the pressure driven condition based on the model developed by Zhang *et al.* (2018). An outline of the paper is as follows. In Section 2, we introduce the model briefly. In Section 3, several methods are introduced to solve the problem including the finite element method and the eigenvalue method. In the finite element method, improved three-dimensional rotating spines are used to update the adaptive mesh deformation. In Section 4, the steady flow-tube system is solved under different pressures in a range of Reynolds numbers in the pressure driven condition, and the system buckling behavior is studied for different Reynolds numbers. The stability of some solutions is also identified by the eigenvalue method which is validated by solving the transient solution of the system. In Section 5, conclusions are included and some further researches are discussed.

2. The fluid-tube model

2.1. Model description

The model consists of a flow in a three-dimensional collapsible tube whose cross section is cylindrical initially. The tube has a thickness h^*, length L^* and inner diameter D^*. We divide the tube into the upstream part, middle part and downstream part with the length L_u^*, L_m^* and L_d^*, respectively. The upstream and downstream parts are rigid and the middle part which is subjected to an external pressure P_{ext}^* and is assumed to be collapsible as shown in Fig. 1. The tube is described by a neo-Hookean material with the density ρ_e^* and shear modulus μ_e^*. The fluid is an incompressible Newtonian fluid whose density is ρ^* and viscosity is μ^*. The flow is assumed to be laminar and the average flow velocity of the tube is U_0^*.

2.2. The governing equations

The governing equations are built by the ALE method. The fluid governing equations are built in the Eulerian coordinate system with the position vector $\mathbf{x}$, and the solid governing equations are built in two Lagrangian coordinate systems using $\mathbf{x}_e$ and $\mathbf{X}_e$, respectively. $\mathbf{x}_e$ is the position vector in the current configuration and $\mathbf{X}_e$ is the position vector in the reference configuration.

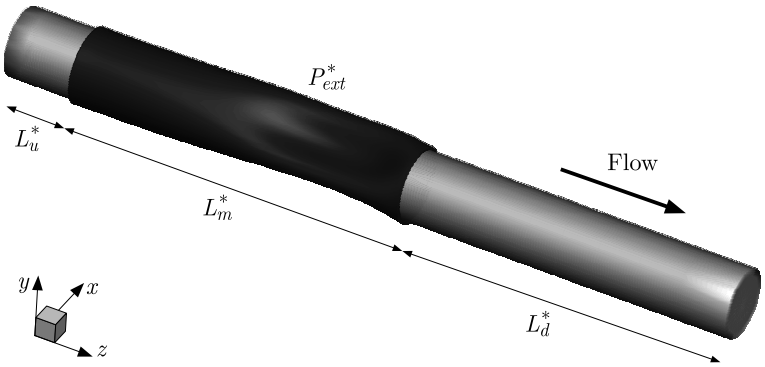

Fig. 1. Geometry of the collapsible tube

For convenience, we adopt dimensionless variables and parameters defined as follows,

$$
\begin{aligned}
&x_i = \frac{x_i^*}{D^*} \qquad x_{ei} = \frac{x_{ei}^*}{D^*} \qquad X_{ei} = \frac{X_{ei}^*}{D^*} \qquad i = 1,2,3\\
&v_i = \frac{v_i^*}{U_0^*} \qquad u_i = \frac{u_i^*}{D^*} \qquad i = 1,2,3\\
&L_u = \frac{L_u^*}{D^*} \qquad L_m = \frac{L_m^*}{D^*} \qquad L_d = \frac{L_d^*}{D^*} \qquad L = \frac{L^*}{D^*}\\
&h = \frac{h^*}{D^*} \qquad \rho_e = \frac{\rho_e^*}{D^*}\rho^* \qquad t = \frac{D^* t^*}{U_0^*}\\
&p = \frac{p^*}{\rho^* U_0^{*2}} \qquad P_{ext} = \frac{P_{ext}^*}{\rho^* U_0^{*2}} \qquad \mathrm{Re} = \frac{U_0^* D^* \rho^*}{\mu^*} \qquad \mu_e = \frac{\mu_e^*}{\rho^* U_0^{*2}}
\end{aligned}
\tag{2.1}
$$

where the quantities with a star are dimensional ones. v_i, x_i $(i = 1,2,3)$ are velocity and coordinate components of the fluid, u_i $(i = 1,2,3)$ are displacement components of the structure, and x_{ei}, X_{ei} $(i = 1,2,3)$ are coordinate components of the structure in the current and reference configuration, respectively. P is the fluid pressure, Re is the Reynolds number.

The dimensionless governing equations for the coupled fluid-structure interaction system are

$$
\begin{aligned}
&\frac{\partial v_i}{\partial t} + v_j \frac{\partial v_i}{\partial x_j} = -\frac{\partial p}{\partial x_i} + \frac{1}{\mathrm{Re}} \nabla^2 v_i\\
&\frac{\partial v_i}{\partial x_i} = 0 \qquad \det \mathbf{F} = 1\\
&\mu_e F_{iA,A} - p_e F^{-1}_{Ai,A} = \rho_e u_{i,tt} \qquad i,j,A = 1,2,3
\end{aligned}
\tag{2.2}
$$

where $\mathbf{F}$ is the deformation gradient.

2.3. The boundary conditions

We impose the following boundary conditions:

1) Parallel, axially traction-free inlet flow ($z = 0$): $v_1 = v_2 = P = 0$.
2) Zero velocity at the rigid walls ($r = R$, $0 \leqslant z \leqslant L_u$, $L_u + L_m \leqslant z \leqslant L$): $v_i = 0$, $i = 1,2,3$.
3) Parallel flow with the required flow rate at the outflow ($z = L$): $v_1 = v_2 = 0$; $\int v_3 \, dA = \pi/4$.
4) Clamped ends of the elastic tube ($z = L_u$, $L_u + L_m$): $u_i = 0$, $\dot{u}_i(t) = 0$, $i = 1,2,3$.
5) No slip condition at the interface ($L_u \leqslant z \leqslant L_u + L_m$, $r = R$): $v_i(t) = \dot{u}_i(t)$, $i = 1,2,3$.
6) External pressure on the outer wall of the tube: $\boldsymbol{\sigma} \times \mathbf{n} = -P_{ext}\mathbf{n}$, where $\mathbf{n}$ is the outward normal vector of the tube.

3. The numerical method

3.1. The adapting mesh

The finite-element method is adopted to solve the coupled nonlinear fluid-structure interactive equations simultaneously, and the method of rotating spines is used to enable an automatic mesh adaptation. To construct the adapting mesh, we once divided the fluid field in the elastic section into internal and external regions by a virtual cylindrical shell. The nodes within the cylindrical shell are fixed, and these outside the shell are movable. The spines are originating from the virtual cylindrical shell. The deformed by this method mesh is shown in Fig. 2. It can be seen when the deformation is large, the mesh in the internal section is denser than the mesh in the external section. It goes against the law that density of the mesh towards the wall should be increased to resolve the boundary layer near the tube wall.

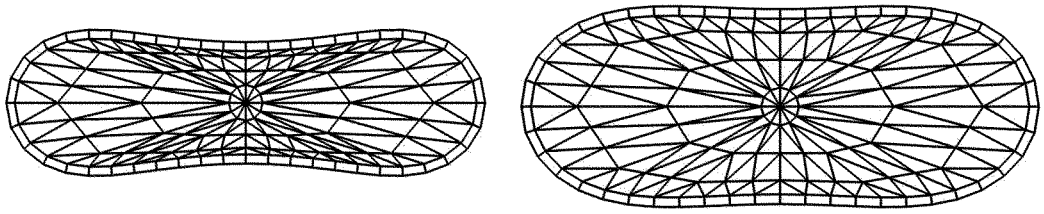

Fig. 2. The deformed mesh by the prior method

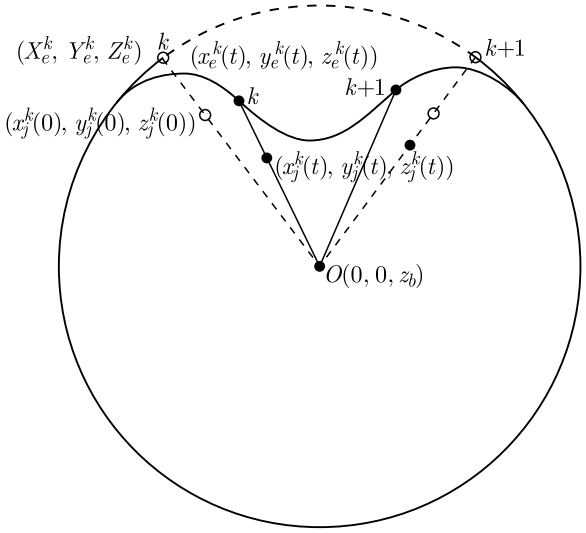

Fig. 3. A sketch of the moving rotating spines

We improve the method by cancelling the cylindrical shell and the spines originating from the center line of the tube. This method is illustrated on a circular cross section as shown in Fig. 3. The spines are straight lines which can rotate around the fixed node in the center. For example, $(x_j^k(0), y_j^k(0), z_j^k(0))$ are the initial coordinates of the (fluid) node j on the spine k which is connecting the fixed node $O(0, 0, z_b)$ in the center to the material point (X_e^k, Y_e^k, Z_e^k) on the tube wall. After deformation, (X_e^k, Y_e^k, Z_e^k) moves to $(x_e^k(t), y_e^k(t), z_e^k(t))$ according to

$$x_e^k(t) = X_e^k + u_e(t) \qquad y_e^k(t) = Y_e^k + v_e(t) \qquad z_e^k(t) = Z_e^k + w_e(t) \tag{3.1}$$

where (u_e, v_e, w_e) are the corresponding displacements. The node $(x_j^k(0), y_j^k(0), z_j^k(0))$ on the spine k moves along it according to

$$x_j^k(t) = \omega_j^k x_e^k(t) \qquad y_j^k(t) = \omega_j^k y_e^k(t) \qquad z_j^k(t) = z_b^k + \omega_j^k (z_e^k(t) - z_b) \tag{3.2}$$

where $j = 1, 2, 3, \ldots, n_k$, n_k is the total number of nodes on the spine k, and ω_j^k are the fixed scaling factors defined by

$$\omega_j^k = \frac{\sqrt{(x_j^k(0))^2 + (y_j^k(0))^2 + (z_j^k(0) - z_b)^2}}{\sqrt{(X_e^k)^2 + (Y_e^k)^2 + (Z_e^k - z_b)^2}} \tag{3.3}$$

After we obtain the coordinates of the nodes on the rotating spines, those which are not placed on the rotating lines are linearly interpolated from those on the rotating spines. The deformed mesh by the new method is shown in Fig. 4.

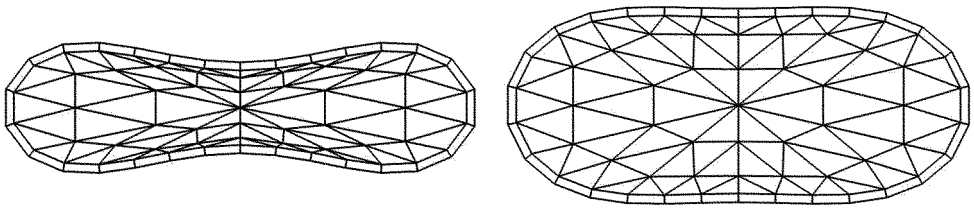

Fig. 4. The deformed mesh by the new method

3.2. Fully coupled finite-element equations

When solving the time-dependent problem, the time derivatives in the finite element equations need to be replaced by the finite time difference terms. In the solid equations, the acceleration term is expressed by the second-order partial derivative of displacement with respect to time. But it is expressed by the one-order partial derivative of velocity with respect to time in the fluid equations. In order to adopt the same time difference scheme to approximate the acceleration term, we unify the order of partial derivative with respect to time by adding the variables of solid velocity. The relationship between velocities of the solid and its displacements is

$$u_{i,t} = \alpha_i \qquad i = 1, 2, 3 \tag{3.4}$$

where α_i is the solid velocity in the x, y, z directions.

We employ the Petrov-Galerkin method to discretize governing equations (2.2). To make the order of each item in the discretization equations be the same, the element type for the flow is a 15 node triangular prism with quadratic shape functions ψ for velocities and linear shape functions φ for fluid pressure. The element type for the solid is a 20 node hexahedron with quadratic shape functions ψ^e for displacements, solid velocities and linear shape functions φ^e for the solid 'pressure'.

Coupled governing equations (2.2) when they are discretized and assembled, can be written in a matrix form as

$$\mathbf{M}\frac{d\mathbf{U}}{dt} + \mathbf{K}(\mathbf{U})\mathbf{U} - \mathbf{F}' = \mathbf{R} = \mathbf{0} \tag{3.5}$$

where $\mathbf{U} = [u_j, v_j, w_j, p_j, u_{ej}, v_{ej}, w_{ej}, p_{ej}, \alpha_{xj}, \alpha_{yj}, \alpha_{zj}]^{\mathrm{T}}$ is the global vector of unknowns, j is the number of degrees of freedom for each variable. $\mathbf{M}$, $\mathbf{K}$ are the $n \times n$ mass and stiffness matrices, respectively. $\mathbf{F}'$ and $\mathbf{R}$ is a force-like vector and residual vector with dimension n, respectively. n is the total number of degrees of freedom. $\mathbf{R}$ is denoted by

$$\mathbf{R} = [R_u, R_v, R_w, R_p, R_{u_e}, R_{v_e}, R_{w_e}, R_{p_e}, R_{\alpha_x}, R_{\alpha_y}, R_{\alpha_z}]^{\mathrm{T}} \tag{3.6}$$

where the subscripts u, v, w, p indicate the corresponding residuals of flow momentum equations in the x, y, z directions and continuity equation, respectively. Subscripts u_e, v_e, w_e, p_e indicate

the corresponding residuals of solid momentum equations and the incompressible equation. Subscripts α_x, α_y, α_z indicate the corresponding residuals of equation (3.4).

When we consider the quasi-static wall and steady flows only, the terms related to time disappear. The coupled governing equations become

$$\mathbf{K}(\mathbf{U})\mathbf{U} - \mathbf{F}' = \mathbf{R} = \mathbf{0} \tag{3.7}$$

where $\mathbf{U} = [u_j, v_j, w_j, p_j, u_{ej}, v_{ej}, w_{ej}, p_{ej}]^{\mathrm{T}}$ is the global vector of unknowns.

3.3. The stability analysis

The system shows different unsteady behavior under different parameters. To study stability of the system, there are usually two methods. One is solving the eigenvalue problem of the system, the other is solving the time-dependent problem of the system. The similarity between the two methods is that the steady solution denoted by $\overline{\mathbf{U}}$ is obtained for a given set of parameters first. The steady solution satisfies the equation

$$\mathbf{K}\overline{\mathbf{U}}\overline{\mathbf{U}} - \mathbf{F}' = \mathbf{0} \tag{3.8}$$

which is solved by the frontal method and the Newton Raphson scheme.

For the method of solving the time-dependent problem, a slightly different steady solution is used as the initial guess which has a parameter value of P_{ext}, say, 1% away from that of the steady solution in question. An implicit finite-difference second order predictor corrector scheme with a variable time step is used to deal with time derivatives (Gresho *et al.*, 1980). After doing this, the time-dependent problem can be solved as the steady problem at each time step. If as time progresses, the time-dependent solution converges to the corresponding steady solution, then the system is stable under the set of parameters. If the time-dependent solution diverges away from the steady solution or oscillates with time, it is deemed to be unstable. The critical point at which the system becomes unstable is called the neutrally stable point.

When solving the eigenvalue problem of the system, an infinitesimal perturbation denoted by $\Delta\mathbf{U}$ is applied to the steady solution. The perturbation can be written as $\Delta\mathbf{U} = \exp(\omega t)(\mathbf{U})$, where $\omega = (\omega_R + \mathrm{i}\omega_I)$ and $\overline{\mathbf{U}} = (\overline{\mathbf{U}}_R + \mathrm{i}\overline{\mathbf{U}}_I)$ are the complex eigenvalues and eigenvectors, respectively. The solution of the system can be expressed as $\mathbf{U} = \overline{\mathbf{U}} + \Delta\mathbf{U}$. We then substitute this formula into discretized matrix equation (3.5). By using of the Taylor expansion and equation (3.8), we obtain a generalized eigenvalue problem

$$\omega\overline{\mathbf{M}\widetilde{\mathbf{U}}} + \overline{\mathbf{K}}\widetilde{\mathbf{U}} = \mathbf{0} \tag{3.9}$$

where $\overline{\mathbf{M}} = \mathbf{M}(\overline{\mathbf{U}})$ and $\overline{\mathbf{K}} = \mathbf{K}(\overline{\mathbf{U}}) + \nabla_{\mathbf{U}}\mathbf{K}(\mathbf{U})|_{\overline{\mathbf{U}}}\overline{\mathbf{U}}$. They can be determined by the steady solution $\overline{\mathbf{U}}$. The above eigenvalue problem is then solved using the ARPACK(https://www.caam.rice.edu/software) software. The Arnold-frontal method employing a frontal method during along with the Arnold iteration scheme is used, for details see (Hao *et al.*, 2016). The advantage of this method is that it just needs to solve the leading few eigenvalues of the discretized system and it does not need to form large matrices $\overline{\mathbf{M}}$ and $\overline{\mathbf{K}}$ in equation (3.9). The stability of the system is decided by the signs of ω_R. If ω_R is positive, the system is unstable and if ω_R is negative, the system is stable. $\omega_R = 0$ indicates the system is at a neutral stable point, which is associated with sustained self-excited oscillations.

The eigenvalue method is adopted in the paper to study stability of the system. It is more effective than the method of solving the time-dependent problem which is used as the validation method of the eigenvalue approach.

4. Results

4.1. The bifurcation diagrams

We study the changes of the system buckling behavior due to changes in the flow rate or the Reynolds number under different external pressures. The geometrical parameters of the model are as follows

$$D^* = 0.004\,\mathrm{m} \qquad L_u = 0.5 \qquad L_m = 10.0 \qquad L_d = 4.0 \qquad h = 0.025$$

The results are presented in terms of the dimensional shear modulus and pressure, i.e. $\mu_e^* = 612000.0\,\mathrm{Pa}$, external pressures $\mu_e^* = 19.36\,\mathrm{Pa}$, $19.39\,\mathrm{Pa}$, $19.48\,\mathrm{Pa}$ and a pressure drop dp^* across the tube between $z = 0$ and 14.5.

The Reynolds numbers are varied from 40 to 210, the relationship between the Reynolds number and the pressure drop dp^* is shown in Fig. 5 for different values of the external pressure. The straight lines are obtained for axisymmetric deformation, and these remain almost the same under different external pressures. Because the cross-section of the tube keeps to be circular for axisymmetric deformation and the deformation is also small. In this condition, the pressure drop can be obtained by the following formula

$$dp^* = \frac{32 L^* \mu^{*2}}{\rho^* D^{*3}} \mathrm{Re} \tag{4.1}$$

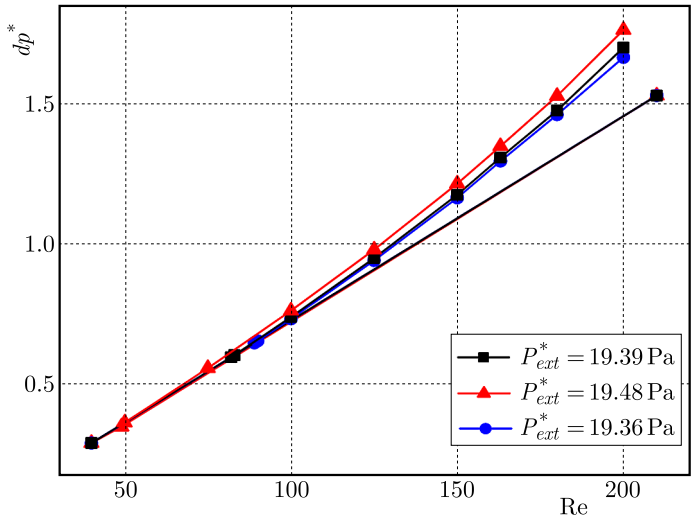

Fig. 5. The relation between Re and dp^* under different external pressures

It is linear with the Reynolds number. The other lines are obtained when the tube is collapsed. The number of pressure drops is equal to the number of solutions of the system. Take the external pressures $P_{ext}^* = 19.36\,\mathrm{Pa}$ as an example, when the Reynolds number is small, just one axisymmetric solution exists. As Re increases to $\mathrm{Re} > 89$, there are two solutions: one axisymmetric and one buckling. This trend is the same for $P_{ext}^* = 19.39\,\mathrm{Pa}$ and $19.48\,\mathrm{Pa}$ except for the critical $\mathrm{Re} = 82$ and 49, respectively. It can be seen that the critical Reynolds number is decreased as the external pressure increases. Because the tube buckles when the transport pressure (the external pressure minus the internal pressure) exceeds the critical buckling value. When the inlet pressure is imposed, the large external pressure may make the transport pressure arrive at the critical buckling value when the Reynolds number is small according to Eq. (4.1). In the pressure driven boundary condition, the number of solutions is much different with that

under the flow-driven boundary condition in which the system may have one axisymmetric solution, one axisymmetric solution with one buckling solution or two buckling solutions.

To analyse the tube deformation under different Reynolds numbers, we choose point P_2 and point Q_2 which is the intersection point of cut1 and cut2 with the cross section at $z - L_u = 5.0$, respectively, as the characteristic point shown in Fig. 6a. We can also plot a bifurcation diagram in terms of tube deformation and Re by these two points as shown in Fig. 6b. The vertical axis shows the difference of r_0 and r, where r_0 is radius of the tube and r is the distance between the characteristic point and the center of the cross section after deformation. The three overlapped straight lines are obtained when the tube is deformed symmetrically. The lines above the straight lines indicate the wall bulged out at point P_2, and the blow ones indicate the wall collapse at point Q_2. We take $P^*_{ext} = 19.48\,\text{Pa}$ as an example to show the tube deformation when Re increases. When Re is less than the critical Re, which is 49 in this situation, the tube deformation is symmetrical and small, and increases slowly as Re increases. At the critical point, the tube may buckle and the symmetrical deformation disappears. The deformation of the tube will increase rapidly as Re increases if it is on the buckling branch.

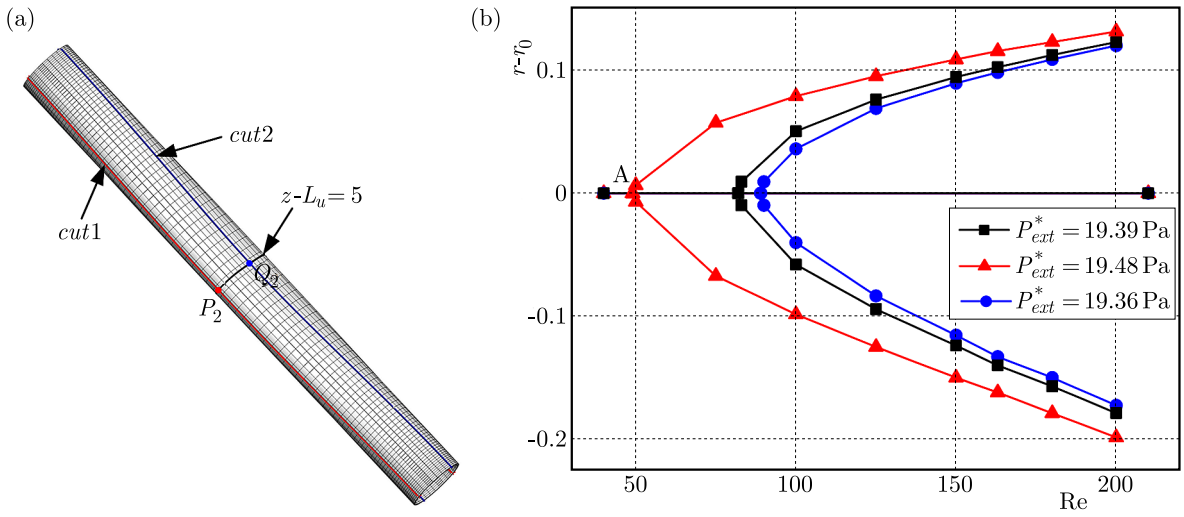

Fig. 6. (a) The sketch of the positions of characteristic points and (b) the buckling curves of the characteristic points under different external pressures

4.2. Stability analysis of the system

We investigate stability of the steady solutions obtained in Section 4.1 by the eigenvalue method described in Section 3.3. The axisymmetric deformation of the tube is small and the most likely to occur. So, the steady solution when the tube is axisymmetric is stable normally, we also validate this in some cases. We focus the attention on the buckling solutions next.

The eigenvalues of the stability problem of buckling solutions with different Re under three different external pressures when the system is in pressure driven condition are shown in Table 1. It shows that as the external pressure increases, the real part of the eigenvalue becomes smaller and smaller at the same Re. Take Re = 180 as an example, when $P^*_{ext} = 19.39\,\text{Pa}$, then the real part of the eigenvalue is 0.0096. As the external pressure increases to 19.39 Pa and 19.48 Pa, the real part of the eigenvalue decreases to 0.0086 and −0.00050, respectively. The stability of the steady solution becomes unstable from stable. It can be inferred that with an increase of external pressure, the buckling solution changes from an unstable solution to a stable one when other parameters remain unchanged. The table also shows that the real part of the eigenvalue becomes larger and larger with an increase of Re at the same external pressure. Take $P^*_{ext} = 19.36\,\text{Pa}$ as an example, when Re = 125, the real part of the eigenvalue is −0.014. As the Re increases to

150 and 163, the real part of the eigenvalue increases to −0.000203 and 0.0057, respectively. It can be observed that there is a critical Re where the real part of the eigenvalue is zero between the 150 and 163. The buckling solution with the Re below the critical Re is stable, and above the critical Re is unstable. At external pressure $P^*_{ext} = 19.39\,\text{Pa}$, the critical Re is between 150 and 163. When the external pressure $P^*_{ext} = 19.48\,\text{Pa}$, it can be considered that the critical Re is 200. Although the real part of the eigenvalue is not exactly equal to zero, considering the error of the numerical method, the real part of the eigenvalue can be approximated to zero.

Table 1. Eigenvalues of stability problem of buckling solutions with different Re under three different external pressures when the system is in the pressure driven condition

Re	$P^*_{ext} = 19.36\,\text{Pa}$		$P^*_{ext} = 19.39\,\text{Pa}$		$P^*_{ext} = 19.48\,\text{Pa}$	
	Real	Imaginary	Real	Imaginary	Real	Imaginary
125	−0.014	0.625	−0.018	0.676	−0.024	0.714
150	−0.000203	0.582	−0.00201	0.584	−0.00816	0.634
163	0.0057	0.524	0.0035	0.542	−0.00502	0.583
180	0.0096	0.486	0.0086	0.487	−0.00050	0.524
200	0.0119	0.436	0.0099	0.446	0.000091	0.476

4.3. Validation of stability of the system

In this Section, the stability of the steady-state solution is determined by solving the transient solution of the system, and the results are compared with those obtained by the eigenvalue method in Section 4.2.

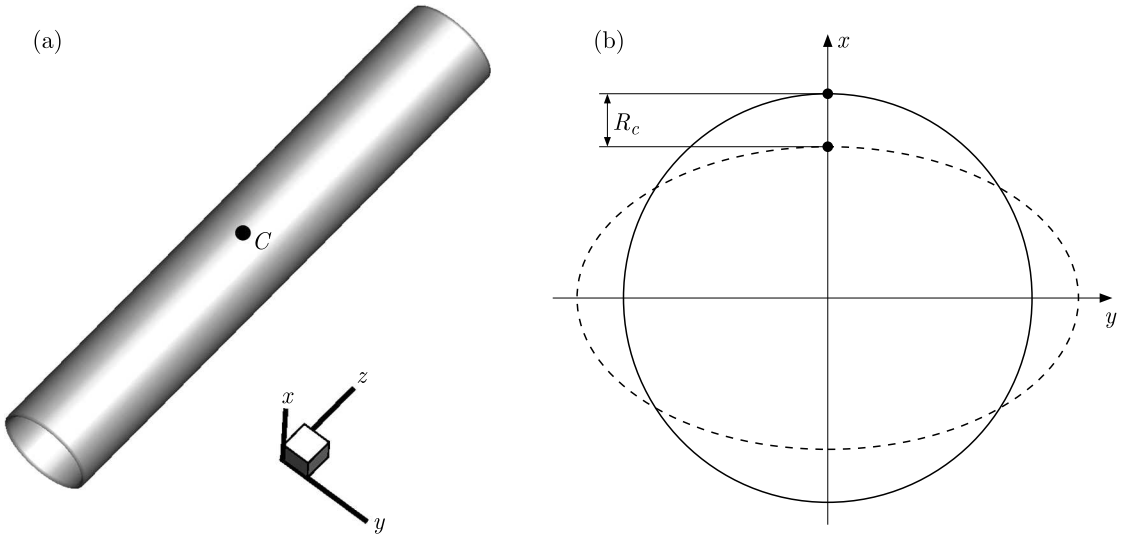

Fig. 7. The displacement of point C in the perturbation direction: (a) position of point C, (b) magnitude of displacement

The initial conditions of the transient solution are obtained by perturbing the external pressure of the steady solution. In the specific implementation, the displacement of point C on the disturbed tube, and the steady solution after the disturbance is calculated by the displacement control method as the initial gauss of the transient solution. In this way, one can avoid a too large external pressure disturbance, which leads to too large deformation of the tube and does not meet the conditions as the initial gauss of the transient solution. Point C is located at the middle of the tube collapsible section, and its coordinates are $(x = R+h, y = 0, z = L_u+0.5L_m)$, as shown in Fig. 7a. The point C is disturbed in the x direction and its displacement is R_c, as

shown in Fig. 7b. The solid line and dotted line represent the shape of the cross section at point C before and after deformation, respectively.

We will solving the transient solution of the system in three different conditions. In the first condition, Re is 150 and the external pressure P^*_{ext} is changed from 19.48 Pa to 19.49 Pa when the displacement of point C in the perturbation direction R_c is disturbed from -0.15 to -0.1625. In seeking the transient solution of the system, we set the external pressure $P^*_{ext} = 19.48$ Pa and take the steady solution of the system when $P^*_{ext} = 19.49$ Pa as the initial condition of the transient solution. In the steady buckling solution under external pressure $P^*_{ext} = 19.48$ Pa, the coordinate of point C is $(x = 0.37500, y = 0.00000, z = 5.50021)$ whose abscissa is shown by the red line in Fig. 8a. The black line in Fig. 8a shows the time varying curve of the abscissa of point C in the transient solution. It can be seen that the abscissa of point C vibrates with the position of the steady solution as the balance point. Since the energy entering the system is less than the energy dissipated in the flow field, the amplitude of vibration gradually decreases. The amplitude of the first cycle is 0.01220 and the amplitude of the last cycle is 0.00110, which is less than one tenth of that of the first cycle. It can be inferred that as time goes on, the abscissa of point C will tend to the abscissa value of the steady solution when the external pressure $P^*_{ext} = 19.48$ Pa, that is, 0.37500. Therefore, the steady solution is stable under this parameter, which is consistent with the conclusion obtained by solving the eigenvalue of the stability problem of the steady solution in Section 4.2.

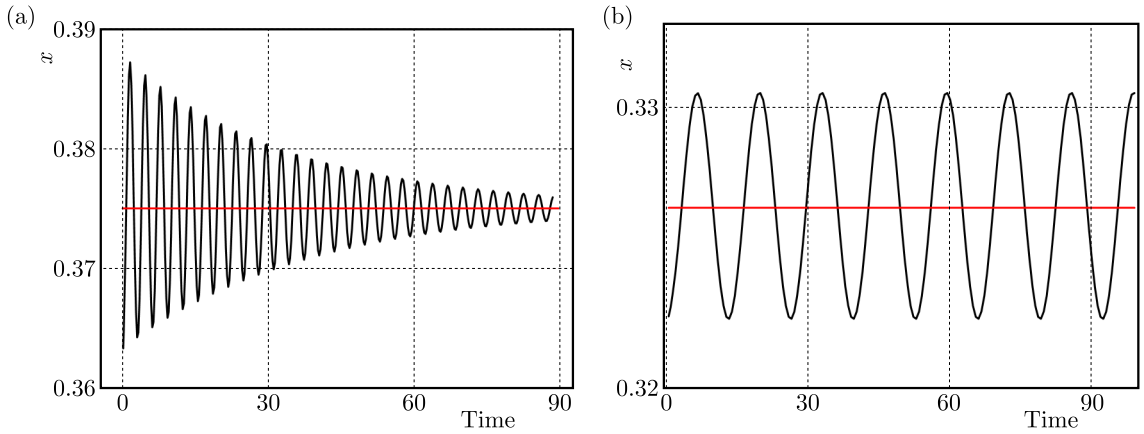

Fig. 8. The time-dependent curves of x coordinate of point C in the pressure driven condition when $P^*_{ext} = 19.48$ Pa as described by the black lines, and the red lines show the x coordinate of point C in the steady buckling solution: (a) Re = 150, (b) Re = 200

In the second condition, Re is 200 and the external pressure P^*_{ext} is changed from 19.48 Pa to 19.49 Pa when the displacement of point C in the perturbation direction R_c is disturbed from -0.198 to -0.2020. In seeking the transient solution of the system, we set the external pressure $P^*_{ext} = 19.48$ Pa and take the steady solution of the system when $P^*_{ext} = 19.49$ Pa as the initial condition of the transient solution. The black line in Fig. 8b shows the change of the abscissa of the point C of the transient solution when $P^*_{ext} = 19.48$ Pa where the red line ($x = 0.32700$) is the abscissa of the point C of the steady solution. It can be seen that the abscissa of point C vibrates with the red line and the amplitude remains unchanged over time. The system is in a critical state between stable and unstable, which is consistent with the conclusion obtained by solving the eigenvalue of the stability problem of the steady solution in Section 4.2.

In the third condition, Re is 200 and the displacement of point C is perturbed from -0.172 to -0.179 where the external pressure is changed from $P^*_{ext} = 19.36$ Pa to $P^*_{ext} = 19.39$ Pa. Take the steady solution under $P^*_{ext} = 19.39$ Pa as the initial guess to solve the transmit solution under $P^*_{ext} = 19.36$ Pa. As shown in Fig. 9, the black line in the figure is a time varying curve

of the abscissa of point C in the transient solution, and the red line ($x = 0.353$) is the abscissa of point C in the steady solution. The abscissa of point C vibrates with the red line and the amplitude is increasing with time. So, the steady solution is unstable and the conclusion is also the same as that in Section 4.2.

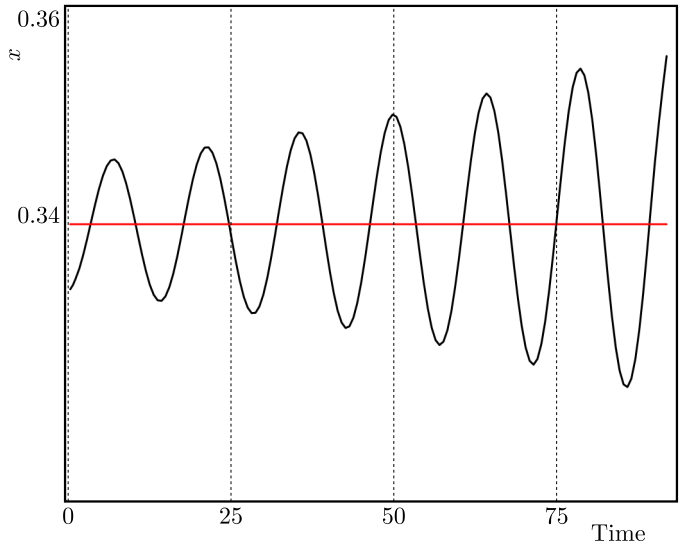

Fig. 9. The time-dependent curve of x coordinate of point C in the pressure driven condition when $P^*_{ext} = 19.36\,\text{Pa}$, $\text{Re} = 200$ as described by the black line, and the red line shows the x coordinate of point C in the steady buckling solution

It can been seen that determining stability of the steady solution by solving the transient solution derives the same conclusion with the eigenvalue method. In practical calculation, the time consumed by solving the transient solution is ten or tens times more than that in the eigenvalue method. It shows the effectiveness of the eigenvalue method.

5. Conclusion

We have carried out an extensive study on three-dimensional flows in a hyper-elastic collapsible tube in a pressure-driven condition. The rotating spines method is developed to solve the coupled fluid structure interaction problem when the tube is greatly collapsed. We found that there exists a range of Reynolds numbers when two solutions exist at the same external pressure, with one non-buckling and one buckling scenarios (Fig. 6b). This type of bifurcation diagrams for the tube buckling has not been reported before and it is very different to that in the flow-driven boundary condition (Truong and Bertram, 2009). It is the first time to determine stability of the steady solution by the eigenvalue method and the solution may be stable, unstable or in a critical state between stable and unstable in some range of Reynolds numbers. The transient solutions of the system are obtained to validate the effectiveness of the eigenvalue method to determine stability of the steady solution. By changing the core parameters of the system (Reynolds number and elastic modulus of the tube), the stability parameter space of the system with respect to the Reynolds number and elastic modulus can be determined. Analysis of the rule between system stability and its parameters, one can provide a reference for stugy of the mechanism of self--excited vibration. It also provides theoretical support for design and manufacture of auxiliary vocal devices and snoring control equipment.

Acknowledgments

This work was supported by national key research and development program (No. 2021YFB2401700) and Guangdong key research and development program (grant No. 2021B0101190001).

References

1. Bertram C.D., 2003, *Experimental studies of collapsible tubes*, [In:] *Flow Past Highly Compliant Boundaries and in Collapsible Tubes. Fluid Mechanics and Its Applications*, P.W. Carpenter, T.J. Pedley (Edit.) , **72**, 51-65, Springer, Dordrecht
2. Bertram C.D., Truong N.K., Hall S.D., 2008, PIV measurements of the flow field just downstream of an oscillating collapsible tube, *Journal of Biomechanical Engineering*, **130**, 6, 061011
3. Gresho P.M., Lee R.L., Sani R.L., 1980, On the time-dependent solution of the incompressible Navier-Stokes equations in two and three dimensions, *Recent Advances in Numerical Methods in Fluids*, **35**, 4, 205-209
4. Grotberg J.B., Jensen O.E., 2004, Biofluid mechanics in flexible tubes, *Annual Review of Fluid Mechanics*, **36**, 1, 121-147
5. Hao Y.Y., Cai Z.X., Roper S., Luo X.Y., 2016, An Arnoldi-frontal approach for the stability analysis of flows in a collapsible channel, *International Journal of Applied Mechanics*, **8**, 6, 17-29
6. Heil M., Boyle J., 2010, Self-excited oscillations in three-dimensional collapsible tubes: Simulating their onset and large-amplitude oscillations, *Journal of Fluid Mechanics*, **652**, 405-426
7. Heil M., Jensen O.E., 2003, Flows in deformable tubes and channels theoretical models and biological applications, [In:] *Flow Past Highly Compliant Boundaries and in Collapsible Tubes. Fluid Mechanics and Its Applications*, P.W. Carpenter, T.J. Pedley (Edit.) , **72**, 15-49, Springer, Dordrecht
8. Jensen O.E., Heil M., 2003, High-frequency self-excited oscillations in a collapsible-channel flow, *Journal of Fluid Mechanics*, **481**, 235-268
9. Liu H.F., Luo X.Y., Cai, Z.X., 2012, Stability and energy budget of pressure-driven collapsible channel flows, *Journal of Fluid Mechanics*, **705**, 348-370
10. Luo X.Y., Cai Z.X., Li W.G., Pedley T.J., 2008, The cascade structure of linear instability in collapsible channel flows, *Journal of Fluid Mechanics*, **600**, 45-76
11. Truong N.K., Bertram C.D., 2009, The flow field downstream of a collapsible tube during oscillation onset, *International Journal for Numerical Methods in Biomedical Engineering*, **25**, 5, 405-428
12. Whittaker R.J., Heil M., Jensen O.E., Waters S.L., 2010, Predicting the onset of high--frequency self-excited oscillations in elastic-walled tubes, *Proceedings of the Royal Society A: Mathematical, Physical and Engineering Sciences*, **466**, 3635-3657
13. Yiasemides D., Argyris A., Mathioulakis D.S., 2017, Transitory and periodic flow in a self--oscillating collapsible tube: Experimental study, *Journal of Energy Engineering*, **143**, 4, 04017001
14. Zhang S., Luo X.Y., Cai Z.X., 2018, Three-dimensional flows in a hyper-elastic vessel under external pressure, *Biomechanics and Modeling in Mechanobiology*, **17**, 1187-1207

Manuscript received November 7, 2022; accepted for print January 16, 2023

JOURNAL OF THEORETICAL AND APPLIED MECHANICS
61, 2, pp. 407-414, Warsaw 2023
https://doi.org/10.15632/jtam-pl/163169

ANALYSIS OF OUT-OF-PLANE FREE VIBRATION OF SINGLE DAMAGED CURVED BEAM BASED ON PRECISE ALGORITHM OF STRUCTURAL MECHANICS

Xiaofei Li, Zhouyang Pan, Hainan Guo, Tian Zhang
College of Transportation Engineering, Dalian Maritime University, Dalian, China
e-mail: lixiaofei@dlmu.edu.cn; panzhouyang@dlmu.edu.cn; guohainan@dlmu.edu.cn; zt20131094@dlmu.edu.cn

Based on a dynamic discrete model of an out-of-plane curved beam with a constant curvature, eigen-properties of the spatial curved beam structure in undamaged and damaged configurations are considered in this paper. In the literature, based on the equivalent section reduction method, a distributed damage modeling method is proposed. Accoding to Euler-Bernoulli beam theory, the stiffness matrix of shear, bending and torsion coupling is derived. Combined with the lumped mass matrix and the characteristic equation of the multi degree of freedom system, natural frequencies of the undamaged and damaged structures are calculated.

Keywords: out-of-plane curved beam, damaged, stiffness matrix, free vibration

1. Introduction

A curved beam structure is very important and widely used in many engineering fields. In practical engineering applications, curved beams often suffer from crack damage, which leads to structural damage. Based on Euler-Bernoulli hypothesis, if the section of a curved beam remains unchanged and is double symmetric, in-plane vibration and out-of-plane vibration are independent of each other (Zhao *et al.*, 2006). For some specific structures, such as urban ring overpass, the out-of-plane vibration is the main mode of motion, and cracks and other damage characteristics will occur in this direction, which will affect vibration characteristics of spatial curved beams (Hu *et al.*, 2007; Mao *et al.*, 2020). Therefore, vibration analysis of space curved beams with cracks is very significant for the research of crack identification, and it is more important to find accurate theoretical solutions.

Modeling a curved beam with damage is a major problem. Damage modeling of curved beams can be found in some papers (Friswell and Penny, 2002; Dessi and Camerlengo, 2015; Petroski, 1981; Pau *et al.*, 2011). Based on the above methods, researchers have published many studies on cracked beam structures with a large number of results, see for example (Wang *et al.*, 2018; Anifantis and Dimarogonas, 1983; Dimarogonas, 1996). The research on free vibration of curved beams can be divided into in-plane vibration and out-of-plane vibration studies, most of which focus on in-plane vibration, while out-of-plane vibration is relatively rare. Howson and Jemah (1999) proposed an effective method to solve the out-of-plane natural frequency of a plane structure composed of bending Timoshenko beams. Ishaquddin *et al.* (2016) studied the out--of-plane vibration of Timoshenko and Euler-Bernoulli curved beam elements. The performance of coupled and independent curved beam elements was evaluated. Caliò *et al.* (2014, 2016) carried out a primitive and extensive parametric analysis of the in-plane and out-of-plane dynamic behavior of a single arch. They studied dynamic characteristics of a space structure composed of circular arches under undamaged and damaged conditions. The influence of damage parameters

on the natural frequency of vibration was shown. Zare (2019) used on the differential quadrature element method (DQEM), to determine intrinsic frequencies of the cracked beams.

The finite element method can effectively improve computational efficiency and obtain an approximate solution close to the exact solution. However, by its principle, its total stiffness matrix is usually set into a bar matrix distributed along the diagonal, which contains a large number of zero-coupling terms, which will inevitably bring some errors. The method in this paper is a semi-analytical method that takes into account the coupling effects between non-adjacent nodes and can effectively analyze vibration modes of the damaged structure through parameter control.

This paper describes a dynamical model of a spatial curved beam structure, and investigates self-oscillation characteristics of a spatial lossless curved beam structure and a damaged structure by establishing the distributed damage model of a out-of-plane curved beam. It mainly includes two parts: 1) based on the internal force subsection function of the space statically indeterminate structure, the accurate global stiffness matrix and the concentrated mass matrix considering the rotation effect are obtained through integral calculation; 2) based on the characteristic equation of the equation of motion of the multi degree of freedom system, a MATLAB program is compiled to obtain the corresponding eigenvalues and eigenvectors of each order.

2. Theoretical analysis

Figure 1 shows a out-of-plane curved beam model. Because of the special structural form of the space curved beam, the column coordinate system should be used when analyzing the problem. The corresponding out-of-plane generalized load forms include the vertical force F_z, radial couple F_ρ and circumferential torque F_θ. These three forces correspond to three generalized displacements, namely the vertical displacement u_z, angular displacement u_ρ of the section around the radial axis, and the torsional angular displacement u_θ of the section around the circumferential axis. These three generalized displacements can be used as dynamic degrees of freedom for out-of-plane modal analysis of curved beams. Any section of the whole beam only produces three kinds of internal forces: the shear force Q_z perpendicular to the plane of the curved beam, the bending moment M_ρ around the radial axis, and the torque T_θ around the circumferential axis. The curvature radius of the curved beam is R, the section shear stiffness coefficient is k, the section area is A, the inertia moment of z axis is I_z, the polar inertia moment is I_p, the section height is h, and the section width is b. The elastic modulus of the material is E, the shear modulus is G, Poisson's ratio is ν, and the density is ρ.

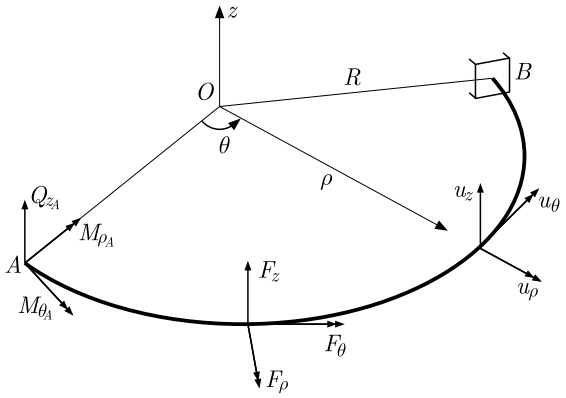

Fig. 1. Statical analysis model of a curved beam

In this paper, a distributed damage model of curved beams is studied. In order to show the weakening effect of damage on section characteristics of curved beams, the curved beams are

divided into three sections, that is, $[0, \theta_1]$, $[\theta_1, \theta_2]$ and $[\theta_2, \theta_3]$ are denoted as the cross-section area A_1, elastic modulus E_1, shear modulus G_1 in the first and third sections, and A_2, E_2, G_2 in the second section. According to the modeling characteristics of the distributed damage model, and the damage section is defined as

$$\alpha = \frac{h_d}{h} \qquad \beta = \frac{\theta_2 - \theta_1}{2\varphi} \tag{2.1}$$

where α is the damage degree coefficient, h_d is the section height of the damaged beam element, and β characterizes the section position of damage.

3. Free vibration analysis of an out-of-plane curved beam

In the undamped modal analysis of curved beam structures, the required structural characteristic matrices are stiffness matrix $\mathbf{K}$ and mass matrix $\mathbf{M}$. Calculating the mode of a curved beam belongs to solving an eigenvalue problem from the mathematical point of view. The control equation of its structural characteristics is

$$\mathbf{K}\boldsymbol{\phi} = \lambda \mathbf{M}\boldsymbol{\phi} \tag{3.1}$$

In the formula, λ is the eigenvalue corresponding to the natural vibration frequency of the structure, and $\boldsymbol{\phi}$ is the structural modal vector corresponding to the eigenvector.

3.1. Stiffness matrix integration of the damaged curved beam

According to structural mechanics, the stiffness and flexibility matrix are reciprocal matrices, and the specific relationship can be expressed as follows

$$\mathbf{K} = \mathbf{D}^{-1} \tag{3.2}$$

It can be seen from Eq. (3.2) that the stiffness matrix can be obtained by the inverse solution of the flexibility matrix. According to the node numbering principle, the number sequence of the node degrees of freedom of the curved beam structure is: 1 – vertical displacement, 2 – section rotation displacement around the radial axis, 3 – section rotation displacement around the circumferential axis. The relationship between the node force and node displacement of the whole curved beam system can be expressed as

$$\mathbf{F} = \mathbf{K}\mathbf{u} \tag{3.3}$$

Formula (3.3) is multiplied by $\mathbf{K}^{-1}$ on both sides to get

$$\mathbf{u} = \mathbf{D}\mathbf{F} \tag{3.4}$$

The solution of the flexibility matrix can be decomposed into nine forms of matrix superposition. The nine kinds of matrices are the vertical uncoupled flexibility matrix $\mathbf{D}_{zz}$, rotational uncoupled flexibility matrix $\mathbf{D}_{\rho\rho}$, torsional uncoupled flexibility matrix $\mathbf{D}_{\theta\theta}$, vertical rotational coupling flexibility matrix $\mathbf{D}_{\rho z}$, vertical torsional coupling flexibility matrix $\mathbf{D}_{\theta z}$, rotational vertical coupling flexibility matrix $\mathbf{D}_{z\rho}$, rotational torsional coupling flexibility matrix $\mathbf{D}_{\theta\rho}$, torsional vertical coupling flexibility matrix $\mathbf{D}_{z\theta}$, torsional rotational coupling flexibility matrix $\mathbf{D}_{\rho\theta}$

$$\mathbf{D} = \mathbf{D}_{zz} + \mathbf{D}_{\rho\rho} + \mathbf{D}_{\theta\theta} + \mathbf{D}_{\rho z} + \mathbf{D}_{\theta z} + \mathbf{D}_{z\rho} + \mathbf{D}_{\theta\rho} + \mathbf{D}_{z\theta} + \mathbf{D}_{\rho\theta} \tag{3.5}$$

The method in this paper is applicable to find the out-of-plane vibration solutions for all boundary conditions of curved beams, and this article takes two-end clamped out-of-plane curved

beams as the object of study. The solution of the flexibility matrix of the overall structure can be converted into a solution of the nine submatrices respectively. Since the curved beam is divided into three segments, the following are discussed respectively:

The radial unit load $P = 1$ acts on $[0, \theta_1]$. The internal force function of a statically indeterminate structure is established based on the geometric relationship of the structure:

— for $0 \leqslant \delta \leqslant \theta_p$

$$\begin{aligned} QL(\delta) &= Q_{Z_A} \\ ML(\delta) &= Q_{Z_A} R\sin\delta + M_{\rho_A}\cos\delta - T_{\theta_A}\sin\delta \\ TL(\delta) &= Q_{Z_A} R(1-\cos\delta) + M_{\rho_A}\sin\delta - T_{\theta_A}\sin\delta \end{aligned} \tag{3.6}$$

— for $\theta_p \leqslant \delta \leqslant \varphi$

$$\begin{aligned} QR(\delta) &= Q_{Z_A} + 1 \\ MR(\delta) &= Q_{Z_A} R\sin\delta + M_{\rho_A}\cos\delta - T_{\theta_A}\sin\delta + R\sin(\theta-\theta_p) \\ TR(\delta) &= Q_{Z_A} R(1-\cos\delta) + M_{\rho_A}\sin\delta - T_{\theta_A}\sin\delta + R[1-\cos(\theta-\theta_p)] \end{aligned} \tag{3.7}$$

The three internal force subsection functions of a statically determinate curved beam structure under the action of an out-of-plane unit load are:

— under the action of the unit vertical force for $\delta \leqslant \theta_{\overline{p}}$

$$\overline{QL}(\delta) = 0 \qquad \overline{ML}(\delta) = 0 \qquad \overline{TL}(\delta) = 0 \tag{3.8}$$

and for $\delta \geqslant \theta_{\overline{p}}$

$$\overline{QR}(\delta) = 1 \qquad \overline{MR}(\delta) = R\sin(\delta - \theta_{\overline{p}}) \qquad \overline{TR}(\delta) = R[1-\cos(\delta-\theta_{\overline{p}})] \tag{3.9}$$

— under the action of the unit couple for $\delta \leqslant \theta_{\overline{p}}$

$$\overline{QL}(\delta) = 0 \qquad \overline{ML}(\delta) = 0 \qquad \overline{TL}(\delta) = 0 \tag{3.10}$$

and for $\delta \geqslant \theta_{\overline{p}}$

$$\overline{QR}(\delta) = 0 \qquad \overline{MR}(\delta) = -\cos(\delta - \theta_{\overline{p}}) \qquad \overline{TR}(\delta) = -\sin(\delta-\theta_{\overline{p}}) \tag{3.11}$$

— under the action of the unit torque for $\delta \leqslant \theta_{\overline{p}}$

$$\overline{QL}(\delta) = 0 \qquad \overline{ML}(\delta) = 0 \qquad \overline{TL}(\delta) = 0 \tag{3.12}$$

and for $\delta \geqslant \theta_{\overline{p}}$

$$\overline{QR}(\delta) = 0 \qquad \overline{MR}(\delta) = -\sin(\delta - \theta_{\overline{p}}) \qquad \overline{TR}(\delta) = \cos(\delta-\theta_{\overline{p}}) \tag{3.13}$$

In Eqs. (3.6)-(3.13), θ_p is the angle of the super-static curved beam structure subject to the unit tip load, $\theta_{\overline{p}}$ is the angle beam structure subject to the tip imaginary unit load. QL, ML, TL and QR, MR, TR are the three internal force functions on the left and right sides of the action force, respectively.

The above functions are piecewise integrated and summed using the displacement integral formula

$$d_{ij} = \sum k \int \frac{\overline{Q} Q_P}{GA}\, ds + \sum \int \frac{\overline{M} M_P}{GI}\, ds + \sum \int \frac{\overline{T} T_P}{GI_\rho}\, ds \tag{3.14}$$

The obtained formula is integrated into the flexibility matrix of an order according to the coordinate numbering. According to the numbering, the obtained results are integrated into

the $3n \times 3n$ order flexibility matrix. Similarly, formulas (3.6)-(3.14) are used to calculate the displacement summation in the cases $\theta_p \in [\theta_1, \theta_2]$ and $\theta_p \in [\theta_2, \varphi]$, respectively. The interval $[\theta_1, \theta_2]$ is represented as the damaged element, and the two ends of the element are given in polar angular coordinates. The section parameters of the element are changed to characterize the section distributed damage of the curved beam structure.

According to equation (3.2), the exact stiffness matrix with damage can be obtained by inversion of the matrix **D**. The numerical distribution of the stiffness matrix **K** is shown in Fig. 2.

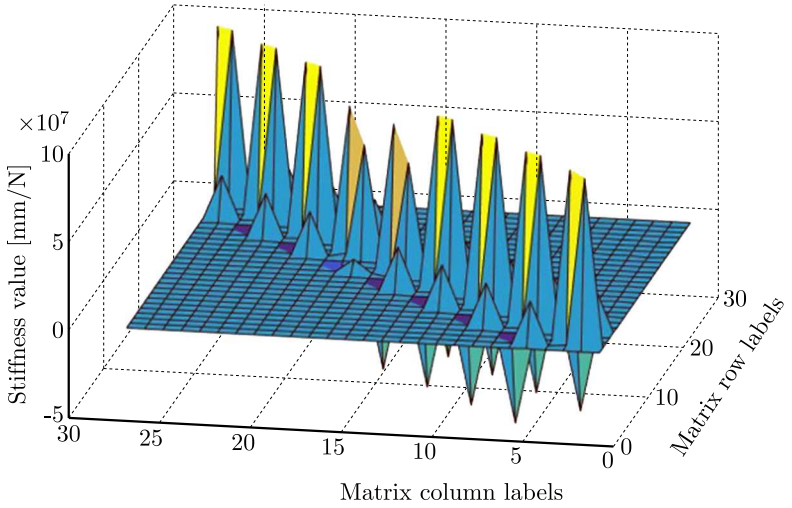

Fig. 2. Numerical distribution of the stiffness matrix with damage

It can be seen from Fig. 2 that the highest peak on the main diagonal is the coefficient related to rotational stiffness, which is much larger than other translational stiffness values. The abrupt change of the peak value is the damage position of the curved beam structure, which is due to the change of stiffness by reduction of the element section.

3.2. Mass matrix integration of out-of-plane curved beams

The dynamic model of the curved beam structure can be simplified as the mass discrete structural system shown in Fig. 3. The beam body is a non-open thin-walled section, without considering the influence of section warping. To illustrate the problem, the section form is assumed to be a rectangular section, while the corresponding stiffness characteristics of the whole beam are retained.

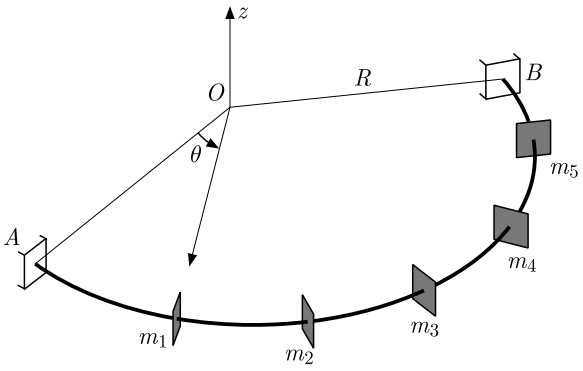

Fig. 3. Dynamic model of the curved beam

It is assumed that all the masses of curved beams are concentrated in discrete nodes. In this way, the translational mass m_i in the z direction of all nodes is the concentrated mass of the beam segment, and the mass of each arc segment is aggregated into a point mass in the node, and the distributed mass of each node is determined by the principle of statics. The mass coefficient related to rotation is given in the form of a moment of inertia about each axis. The moment of inertia of the section around axis ρ is represented by J_ρ and the moment of inertia of the section around circumferential axis θ is represented by J_θ. The lumped mass matrix of the curved beam structure containing the moment of inertia is obtained as

$$\mathbf{M} = \begin{bmatrix} m_1 & & & & & & & \\ & J_{\rho 1} & & & & & & \\ & & J_{\theta 1} & & & & & \\ & & & \ddots & & & & \\ & & & & m_n & & & \\ & & & & & J_{\rho n} & & \\ & & & & & & J_{\theta n} & \end{bmatrix} \tag{3.15}$$

4. Exemplary verification

The calculation example adopts q rectangular section constant curvature beam with section height of the intact structure $h = 15\,\text{mm}$ and width $b = 45\,\text{mm}$. The area is $A = 675\,\text{mm}^2$, central angle $\varphi = 120°$, radius of curvature $R = 1\,\text{m}$. Physical and geometric parameters are shown in Table 1.

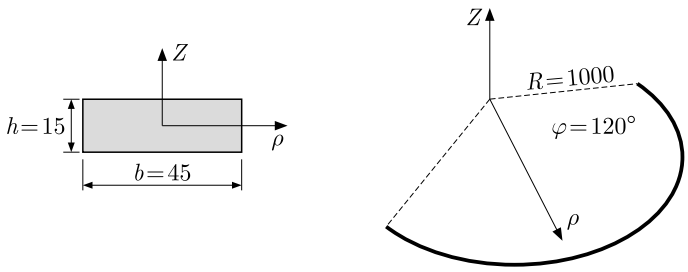

Fig. 4. Curved beam calculation diagram

Table 1. Physical and geometric parameters of the curved beam

Characteristic properties	Values
Young's modulus of elasticity E [MPa]	$2.06 \cdot 10^5$
Shear modulus of elasticity G [MPa]	$8.0 \cdot 10^4$
Inertia moment of area I [m^4]	$1.67 \cdot 10^{-5}$
Shear section coefficient k	1.2
Mass m [kg]	1803

4.1. Influence of damage on the natural frequency of the external curved beam

The frequency values of undamaged and damaged structures are found by the method presented in this paper. It is assumed that the damage location is in the middle of the span, and there are four damage coefficients ($\alpha = 0$, $\alpha = 0.16$, $\alpha = 0.33$, $\alpha = 0.5$). In order to verify the effectiveness of this method in analyzing free vibration problems of curved beams with different

damage levels, a finite element model is established for the above problems and their numerical solutions are obtained. The frequency values obtained by the two methods are listed in Table 2. By comparing the results of the two methods, it can be seen that the larger the damage degree coefficient, the smaller the natural frequency. The theoretical value is consistent with the numerical analysis results. The error values of the two methods indicate that the frequency values obtained by applying the accurate algorithm under different damage degrees maintain good stable solutions. The correctness of the method for solving the out-of-plane vibration of damaged curved beams is verified.

Table 2. Natural frequency of the circular curved beam with damage

k	Frequency $\alpha = 0$		Frequency $\alpha = 0.16$		Frequency $\alpha = 0.33$		Frequency $\alpha = 0.5$	
	present	Ansys	present	Ansys	present	Ansys	present	Ansys
1	0.50579	0.5054	0.5103	0.5099	0.5117	0.5112	0.51189	0.5114
2	1.4396	1.4376	1.4639	1.4605	1.4729	1.4695	1.4764	1.4729
3	2.9581	2.9517	2.9688	2.9576	2.9728	2.9615	2.9745	2.9631
4	4.7408	4.7272	4.8855	4.8589	4.9445	4.9172	4.9694	4.9419
5	7.4276	7.3974	7.4575	7.3920	7.4701	7.4054	7.4755	7.4112

Figure 5 shows the results of the effect of the damage degree on the inherent vibration frequency of the externally curved beam. The order and the difference of the vertical coordinate relative frequency increases with the degree of damage, indicating that the inherent frequency decreases gradually with an increase of the damage factor α.

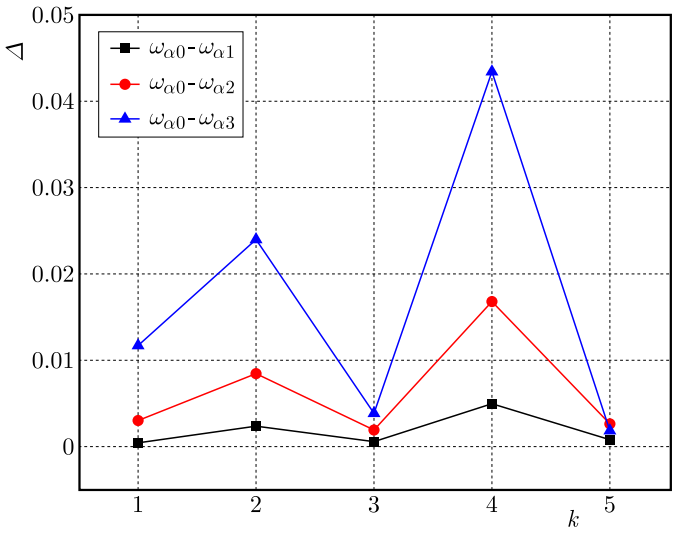

Fig. 5. Effect of the damage degree on the frequency

5. Conclusion

In this paper, a discrete dynamic model of a curved beam outside the plane is established. With the finite element model as a reference, an accurate solution can be obtained by using the proposed algorithm with fewer nodes, and has a high convergence. The paper also quantitatively analyzes the influence of damage on the natural frequency of the externally curved beam. The results show that the natural frequency of the externally curved beam decreases gradually with an increase of the damage degree. The above results show that the algorithm presented in this

paper has good adaptability to solving damage characteristics of the externally curved beam and can provide a theoretical basis for the direct problem of damage identification of the externally curved beam.

References

1. Anifantis N., Dimarogonas A., 1983, Stability of columns with a single crack subjected to follower and vertical loads, *International Journal of Solids and Structures*, **19**, 4, 281-291
2. Caliò I., Greco A., D'Urso D., 2014, Free vibrations of spatial Timoshenko arches, *Journal of Sound and Vibration*, **333**, 19, 4543-4561
3. Caliò I., Greco A., D'Urso D., 2016, Structural models for the evaluation of eigen-properties in damaged spatial arches: a critical appraisal, *Archive of Applied Mechanics*, **86**, 11, 1853-1867
4. Dessi D., Camerlengo G., 2015, Damage identification techniques via modal curvature analysis: Overview and comparison, *Mechanical Systems and Signal Processing*, **52-53**, 181-205
5. Dimarogonas A.D., 1996, Vibration of cracked structures: A state of the art review, *Engineering Fracture Mechanics*, **55**, 5, 831-857
6. Friswell M.I., Penny J.E.T., 2002, Crack modeling for structural health monitoring, *Structural Health Monitoring*, **1**, 2, 139-148
7. Howson W.P., Jemah A.K., 1999, Exact out-of-plane natural frequencies of curved Timoshenko beams, *Journal of Engineering Mechanics*, **125**, 1, 19-25
8. Hu J.S., Feng X., Zhou J., 2007, State-of-art of vibration analysis and crack identification of cracked beams, *Journal of Vibration and Shock*, **11**, 146-152+189
9. Ishaquddin M., Raveendranath P., Reddy J.N., 2016, Efficient coupled polynomial interpolation scheme for out-of-plane free vibration analysis of curved beams, *Finite Elements in Analysis and Design*, **110**, 58-66
10. Mao H., Yu G., Liu W., Xu T., 2020, Out-of-plane free vibration and forced harmonic response of a curved beam, *Shock and Vibration*
11. Pau A., Greco A., Vestroni F., 2011, Numerical and experimental detection of concentrated damage in a parabolic arch by measured frequency variations, *Journal of Vibration and Control*, **17**, 4, 605-614
12. Petroski H.J., 1981, Simple static and dynamic-models for the cracked elastic beam, *International Journal of Fracture*, **17**, 4, R71-R76
13. Wang Y.L., Ju Y., Zhuang Z., Li C.F., 2018, Adaptive finite element analysis for damage detection of non-uniform Euler-Bernoulli beams with multiple cracks based on natural frequencies, *Engineering Computations*, **35**, 3, 1203-1229
14. Zare M., 2019, Free out-of-plane vibration of cracked curved beams on elastic foundation by estimating the stress intensity factor, *Mechanics of Advanced Materials and Structures*, **27**, 14, 1238-1245
15. Zhao Y., Kang H., Feng R., *et al.*, 2006, Research progress of curved beam, *Progress in Mechanics*, **2**, 170-186

Manuscript received September 26, 2022; accepted for print March 4, 2023

INFORMATION FOR AUTHORS

Journal of Theoretical and Applied Mechanics (***JTAM***) is devoted to all aspects of solid mechanics, fluid mechanics, thermodynamics and applied problems of structural mechanics, mechatronics, biomechanics and robotics. Both theoretical and experimental papers as well as survey papers can be proposed.

JTAM accepts full-text articles (max. 12 pages) as well as the short communications with all the requirements concerning standard publications, except a volume that is limited to 4 pages.

We accept articles in English only. The text of JTAM paper should not exceed 12 pages of standard format A4 (11-point type size, standard margins – 2.5 cm, single line spacing) including abstract, figures, tables and references.

The material for publication should be sent to the Editorial Office via electronic journal system: http://www.editorialsystem.com/jtam

Papers are accepted for publication after the review process. Blind review model is applied, which means that the reviewers' names are kept confidential to the authors. Reviewer(s) declare that there is no interpersonal relation with the author(s) that would affect the opinion and recommendation of the article for publication in JTAM. The final decision on paper acceptance belongs to the Editorial Board.

Starting from January 1, 2020, the Publisher of *Journal of Theoretical and Applied Mechanics* introduces a fee for published articles.

This applies only to papers submitted after this date and accepted by the Editorial Board for publication.

A payment of 500 EUR will be a condition for commencing the editorial procedure for upcoming articles.

After qualifying your paper for publication we will require LaTeX or TeX or Word document file and figures.

The best preferred form of figures are files obtained by making use of editorial environments employing vector graphics.

Requirements for paper preparation

Contents of the manuscripts should appear in the following order:

- Title of the paper.
- Authors' full name, affiliation and e-mail.
- Short abstract (maximum 100 words) and 3-5 key words (1 line).
- Article text (equations should be numbered separately in each section; each reference should be cited in the text by the last name(s) of the author(s) and the publication year).
- References (maximum 25) in alphabetical order.
- Titles of references originally published not in English, should be translated into English.

All the data should be reported in SI units.

Cena 40,00 zł (VAT 8%)

Contents